QUANTIFICATION OF FLOW UNIT AND BOUNDING ELEMENT PROPERTIES AND GEOMETRIES, FERRON SANDSTONE, UTAH: IMPLICATIONS FOR HETEROGENEITY IN GULF COAST TERTIARY DELTAIC RESERVOIRS

ANNUAL REPORT

(January 1991 – December 1991)

Prepared by

R. S. Fisher, Noel Tyler, and M. D. Barton
Bureau of Economic Geology
W. L. Fisher, Director

and

M. A. Miller, Kamy Sepehrnoori, Jon Holder, and K. E. Gray
Center for Petroleum and Geosystems Engineering
The University of Texas at Austin
Austin, Texas 78713

For

July 1992

DISCLAIMER

50272-101

REPORT DOCUMENTATION PAGE	1. REPORT NO. GRI-92/0072	2.	3. Recipient's Accession No.

4. Title and Subtitle
Quantification of Flow Unit and Bounding Element Properties and Geometries, Ferron Sandstone, Utah: Implications for Heterogeneity in Gulf Coast Tertiary Deltaic Reservoirs

5. Report Date
July 1992

6.

7. Author(s) R. S. Fisher, Noel Tyler, M. D. Barton, M. A. Miller, Kamy Sepehrnoori, Jon Holder, and K. E. Gray

8. Performing Organization Rept. No.

9. Performing Organization Name and Address
Bureau of Economic Geology
The University of Texas at Austin
University Station, Box X
Austin, TX 78713-7508

10. Project/Task/Work Unit No.

11. Contract(C) or Grant(G) No.
(C) 5089-260-1902
(G)

12. Sponsoring Organization Name and Address
Gas Research Institute   Project Manager:
8600 West Bryn Mawr Avenue   Anthony W. Gorody
Chicago, IL 60631

13. Type of Report & Period Covered
Annual Report
1/1/91-12/31/91

14.

15. Supplementary Notes

16. Abstract (Limit: 200 words)

Outcrop mapping, field permeability measurements, petrographic analyses, petrophysical measurements, and pore-level modeling studies are being conducted on exposures of the Ferron Sandstone, east-central Utah, to develop a better understanding of the dimensions and internal arrangement of flow units, baffles, and barriers in sandstone gas reservoirs. The ultimate goals of this work are to establish methods for applying outcrop studies to reservoir characterization and to develop reservoir models that will guide infill drilling to maximize incremental gas reserve growth from fluvial-deltaic sandstone reservoirs.

Activities during the second year of this 3-year project focused on data collection and preliminary interpretations. Mapping and field permeability measurements were initiated on the seaward-stepping Ferron unit 2 sandstone. These results will provide a comparison with data collected during the 1990 field season when landward-stepping sandstones of Ferron unit 5 were examined. Framework grain and cement mineralogy and the composition of intergranular material were quantified for selected samples from unit 5. Petrophysical measurements were completed on 24 specimens from units 2, 4, and 5. Sections of the pore-level modeling code were rewritten to improve accuracy and efficiency, and scenarios were developed to model the effects of grain size, cementation, and compaction on porosity, single-phase permeability, and formation factor.

Preliminary results indicate that important differences exist in the internal geometry of landward- and seaward-stepping fluvial-deltaic sandstones. It was also found that closer spaced permeability measurements improved the resolution of permeability structure. Petrographic studies documented differences in composition between fluvial, transgressive, delta-front, and distributary-channel sandstones; these differences in rock composition are reflected by differences in the mean permeability of these facies as measured on outcrop. Initial comparisons of pore-level model results with measured petrophysical properties are encouraging and suggest that refinements based on examination of the analyzed samples will lead to a close match between observed and modeled behavior.

17. Document Analysis   a. Descriptors

Texas, Utah, Ferron Sandstone, Wilcox sandstones, depositional systems, gas reserves, reservoir heterogeneity, permeability distributions, petrophysical properties, pore-level simulator

b. Identifiers/Open-Ended Terms

c. COSATI Field/Group

18. Availability Statement
Release Unlimited

19. Security Class (This Report)
Unclassified

20. Security Class (This Page)
Unclassified

21. No. of Pages

22. Price

(See ANSI–Z39.18)   See Instructions on Reverse

OPTIONAL FORM 272 (4–77)
(Formerly NTIS–35)
Department of Commerce

RESEARCH SUMMARY

Title

QUANTIFICATION OF FLOW UNIT AND BOUNDING ELEMENT PROPERTIES AND GEOMETRIES, FERRON SANDSTONE, UTAH: IMPLICATIONS FOR HETEROGENEITY IN GULF COAST TERTIARY DELTAIC RESERVOIRS

Contractors

Bureau of Economic Geology and Center for Petroleum and Geosystems Engineering, The University of Texas at Austin.

GRI Contract No. 5089-260-1902

Principal
Investigators

Noel Tyler, M. A. Miller, K. E. Gray

Report
Period

January 1991 – December 1991

Objectives

The objectives of this research are to (1) examine outcrop exposures of fluvial-deltaic sandstones in two different sequence stratigraphic settings to determine the distribution of flow units, baffles, and barriers to gas flow in sandstone reservoirs, (2) demonstrate that such information can be used to construct realistic reservoir models that can be used to guide infill drilling to maximize incremental gas reserve growth from established fields, and (3) establish general principles for such outcrop characterization studies that can be used by other researchers and field operators.

Technical
Perspectives

The ability to predict reservoir heterogeneity in fluvial-deltaic sandstones may critically limit the amount of natural gas that can be produced from established reservoirs along the Texas Gulf Coast. This project is quantifying sandstone heterogeneity in outcrops of seaward- and landward-stepping units of the fluvial-deltaic Ferron Sandstone of east-central Utah. Field work is combined with petrologic, petrophysical, and pore network models in order to develop a predictive approach for defining the geometric distribution of reservoir properties. The expected long-term benefit of this study to the gas industry is a predictive tool that can be used to increase incremental gas reserves from established fields in a more cost-efficient manner.

Results

Sandstone architecture and permeability relations differ between landward- and seaward-stepping units of the Ferron Sandstone, largely because of differences in the geometric arrangement of component facies and in the amount and distribution of fine-grained silts and muds. A hierarchy of bounding elements that separate flow units has been recognized, and field permeability relations of bounding elements have been quantified. Within sandstone facies, permeability correlation distances generally correlate with dimensions of major macroforms or stratal types.

Sandstone compositions vary systematically between major facies. Framework grain and cement mineralogy and the type of intergranular material are different for fluvial, transgressive, delta-front, and distributary-channel sandstones. These differences affect pore structure, which is reflected in systematic differences in mean permeability of each facies.

Petrophysical analyses of flow and mechanical properties have been completed on 24 block samples from both seaward- and landward-stepping sandstones. Effects of grain size, cementation, and compaction on porosity, single-phase permeability, formation factor, and capillary pressure curves have been quantified and entered into the pore-level model. Preliminary data show that properties predicted by the model are in good agreement with measured properties in many cases.

Technical
Approach

Outcrop studies during the 1991 field season focused on the distributary-channel sandstones of Ferron unit 2 and delta-front facies of unit 5. Outcrops were selected for characterization on the basis of exposure, accessibility, and safety. Photomosaic panels were shot with a medium-format camera for preliminary mapping. Vertical transect spacings were reduced from 100-ft to 50-ft intervals; permeability measurements were taken at 0.5-ft spacings (as compared with 1-ft spacings), and detailed descriptions of each transect were recorded. Samples for petrographic and petrophysical analyses were collected as field studies progressed. Facies, stratification type, and position with respect to vertical transects were recorded for all samples collected. Petrographic methods included standard optical and scanning electron microscopy and X-ray diffraction.

Petrophysical measurements were made simultaneously under reservoir conditions. Porosity, brine and gas permeability, relative permeability, electrical conductivity, and static and dynamic moduli are measured under triaxial test conditions. Pore-level network simulations are conducted using a computer model developed and operated at the Center for Petroleum and Geosystems Engineering. Rules for pore network modification caused by grain-size variations, compaction, and cementation were developed after thin-section examination of analyzed specimens.

Project
Implications

After 2 years of research comparing and contrasting two different depositional systems, the Texas Bureau of Economic Geology (BEG) and Center for Petroleum and Geosystems Engineering (CPGE) study has made significant headway. Their air permeability measurements unequivocally differentiate among a variety of primary depositional fabrics. Even broad differences between seaward- and landward-stepping depositional packages can be clearly identified. This confirms independent analyses indicating that neither burial diagenesis nor surface weathering significantly affects air permeability measurements. Instead, we have learned that primary depositional fabric controls the architecture of flow baffles, flow barriers, and flow units. This may be the case for most clastic reservoirs buried to moderate depths. Such observations are crucial prerequisites for GRI to

continue funding an outcrop-based approach that assesses the uncertainty of volumetric calculations.

The BEG's permeability analyses further suggest that unique methods may also be available to model gas reservoir performance and to simulate development strategies. For example, jigsaw puzzle models that use channels as objects may be an appropriate approach for assessing reserves in multistory channel belts of seaward-stepping delta lobes. Alternatively, a labyrinth model approach may be more appropriate for assessing reserves in landward-stepping channel belts. Such considerations for modeling flow in Ferron depositional environments may be transportable to the Texas Gulf Coast and beyond.

Another example of a transportable concept arising from this work contrasts the continuity and connectedness of reservoir bodies within seaward- and landward-stepping distributary-channel belts. In seaward-stepping distributary-channel belts (river-dominated deltas), bedform diversity and preservation are low, connectivity is high, and continuity within reservoir bodies appears to be good. Widely spaced wells could effectively drain such reservoirs. Conversely, in landward-stepping distributary-channel belts (river-dominated, but wave-modified deltas), bedform diversity and preservation are high, connectivity between reservoirs is low, and abundant barriers lie within reservoir bodies. Such reservoirs may be optimal candidates for infill and horizontal drilling. Results such as these suggest that GRI could reclassify the data in the *Atlas of Major Texas Gas Reservoirs* to refine estimates of reserve growth potential in deltaic reservoirs.

In addition to the unique sequence stratigraphic views offered by BEG studies, the mineralogic perspectives are equally interesting. Both the original mineralogy and grain-binding cements appear to be systematically zoned within a hierarchy of depositional fabrics and environments. These observations suggest that well-site log analysts could develop transportable empirical guidelines for estimating cementation and saturation exponents on the basis of log signatures that characterize depositional environments.

Each of these results is very encouraging and suggests that an outcrop approach to understanding the flow architecture of deltaic Gulf Coast reservoirs may be quite fruitful. Furthermore, the research to date has not only drawn the attention of the international research community but has also received recognition domestically for its excellence.

The applicability of air permeability distributions to describe reservoir behavior continues to be evaluated. For example, the matching effective permeability distributions may be quite different. Capillary entry and threshold pressure data, yet to be collected and analyzed, will also elucidate the filling sequence and partitioning of these heterogeneous reservoirs. Additionally, most of the observations regarding reservoir connectivity and continuity apply to two-dimensional cross sections. Continuity and connectivity in the third dimension have yet to be documented or assessed.

CONTENTS

Figures

Tables

INTRODUCTION

Purpose

Natural gas reservoirs typically display a complex internal architecture that fundamentally controls the path of gas flow, gas recovery, and ultimately the volume of conventionally recoverable natural gas left in a reservoir at abandonment. This complexity reflects the fact that reservoirs are formed and altered by geologic processes that vary over time and space and operate over a wide range of scales. Improved efficiency in natural gas recovery, particularly in mature reservoirs, requires a more sophisticated understanding of reservoir anatomy and the spatial distribution of those petrophysical properties that affect flow.

This study addresses the predictability of flow units, baffles, and barriers to gas movement in sandstone reservoirs by combining geologic and petrographic characterization of fluvial-deltaic sandstones with laboratory measurements of petrophysical properties. Our hypothesis is that we can characterize heterogeneity through outcrop studies and petrophysical property measurements, transform this information to effective reservoir properties, and develop a realistic reservoir model that captures the three-dimensional distribution of baffles and barriers to flow in a sandstone reservoir. Our goals are to develop better methods for predicting the spatial distribution of flow units and intrareservoir barriers to gas flow in fluvial-deltaic sandstones and to demonstrate that deterministic models for sandstone gas reservoirs can be developed from outcrop studies. These models can then be used to test the effects of various reservoir development schemes on the ultimate recovery of natural gas in mature fields deposited in various depositional, tectonic, and sequence stratigraphic settings. We selected fluvial-deltaic sandstones for this study because gas reservoirs deposited in such environments account for a significant amount of total natural gas production from the Texas Gulf Coast.

The primary objective of this 3-year study is to develop methods to quantify styles and scales of sandstone reservoir heterogeneity by combining outcrop studies, petrographic and petrophysical analyses, and computer modeling. Because it is virtually impossible to determine

1

the detailed spatial distribution of petrophysical properties in the subsurface, outcrop studies are increasingly being used to provide data on sand-body geometry, positions and continuity of bounding elements between major sand bodies, the internal architecture of sandstones, and the distribution of permeability values within and between strata. This project characterizes the dimensions and distribution of flow units, baffles, and barriers by outcrop descriptions and permeability measurements. Petrographic studies augment the field work by resolving the relative importance of depositional and diagenetic processes on porosity and permeability. On the basis of field relations and air permeability values, we select samples that would act as flow units, baffles, and barriers in a gas reservoir for a suite of petrophysical property measurements. Finding ways to transform outcrop, petrographic, and petrophysical data to effective reservoir properties is our final objective.

Developing quantitative models of reservoir heterogeneity from outcrop studies requires that the permeability structure of outcrop rocks adequately reflect the permeability structure of reservoir rocks. That is, the spatial distribution of permeability, although not necessarily the absolute values of permeability, must be transportable from outcrop to subsurface. In clastic sequences this is a reasonable assumption. Studies have demonstrated the portability of outcrop observations to the subsurface (Stalkup and Ebanks, 1986; Goggin, 1988). Diagenetic effects on reservoir properties may also be important; however, such effects typically amplify primary depositional heterogeneity (van Veen, 1977; Weber, 1982, 1986).

Approach

We selected two units of the Cretaceous Ferron Sandstone, central Utah, for detailed study on the basis of outcrop exposure, accessibility, safety, and sequence stratigraphic setting. We first photograph the outcrop and map sand bodies and bounding elements on photomosaic panels; we then select sites for detailed descriptions and minipermeameter (air permeability) measurements. The first field season (1990) focused on a landward-stepping sandstone;

2

preliminary results were summarized in the first annual report for this project (Tyler and others, 1991). During the 1991 field season, we examined outcrops of both a seaward-stepping sandstone and the more seaward (distal) deposits of the landward-stepping sandstones. This outcrop selection, combined with work planned for the 1992 field season, provides detailed information on the architecture and permeability characteristics of landward- and seaward-stepping fluvial-deltaic sandstones in both proximal and distal environments.

Petrographic studies complement our understanding of permeability distributions developed from outcrop studies by evaluating the relative effects of depositional and diagenetic processes on porosity and permeability. We select samples on the basis of facies, stratification type, position along a measured permeability profile, and presumed reservoir properties. Standard petrographic examination includes quantification of framework grain and cement mineralogy, porosity, and intergranular volume by conventional thin-section petrography, examination of pore properties by scanning electron microscopy, identification of clay and carbonate mineralogy by X-ray diffraction, and various other geochemical analyses as needed to resolve the history of diagenetic events. During the past year, we collected approximately 500 samples from outcrop using a portable core plugger and approximately 40 large sandstone blocks for laboratory petrophysical analysis.

We measure petrophysical properties of samples selected to represent predominant facies, stratal types, and bounding elements between major sand bodies to determine reservoir properties of the various architectural elements. Analyses include properties related to one- and two-phase flow (porosity, air and brine permeability, relative permeability, formation factor, and saturation exponent) and static and dynamic mechanical properties (Young's modulus, Poisson's ratio, P- and S-wave velocity). Laboratory procedures were tested and refined during the first year of the project; analyses can now be routinely performed on a wide range of sample types. We have completed measurements of distributary-channel, delta-front, levee-crevasse splay, and fluvial sandstones. One significant development during the past year was the acquisition of a field core plugger capable of drilling 2 1/8-inch-diameter cylinders out of

3

tightly cemented sandstones. This drill enables us to be much more selective in our sampling. We can now obtain samples directly from described and measured vertical transects. Prior to obtaining this field core plugger we were restricted to collecting block samples near measured sections, transporting them to the laboratory, and then drilling out test cylinders.

Efforts toward scaling up from individual outcrop sample measurements to reservoir properties and finding a transform from field air permeability values to effective reservoir properties focused on improving the computer code for two-phase flow and on simulating the effects of grain-size variation, compaction, and cementation on single-phase flow.

Progress in each of these areas over the past year is described in the following sections of this report.

OUTCROP CHARACTERIZATION OF SANDSTONE ARCHITECTURE
AND PERMEABILITY STRUCTURE

Introduction

Purpose

One major goal of reservoir characterization is to determine the properties and spatial arrangement of flow units (strata through which gas will readily pass) and barriers or baffles (strata that prevent, retard, or deflect gas flow). Because accurate reservoir description is usually limited by insufficient knowledge of rock property distributions between wells, there is a tendency to stochastically model interwell reservoir architecture. However, we suggest that the distribution of geologic heterogeneities is predictable if we understand the depositional and diagenetic processes that produce flow units, baffles, and barriers sufficiently well. Characterizing outcrop exposures is one way to quantify the spatial distribution of important reservoir elements with respect to geologic processes. The more realistic models developed

from these studies can then be applied to actual reservoirs, appropriately conditioned by data specific to each reservoir.

Approach

Our primary objectives are to determine how lithology and permeability vary on the scale of outcrop exposures and how petrophysical properties and the distribution of rock types reflect depositional and diagenetic processes. We characterize outcrop heterogeneity in a manner that reflects the origin, distribution, and scale dependence of genetically related strata and lithologic discontinuities. Within genetic units we quantify permeability and the spatial distribution of permeability patterns. Lithologic discontinuities (bounding elements) typically have permeability values near or below the detection limit of our field equipment; for these units we record the dimensions, stratigraphic position, and lateral continuity of the elements.

Our sampling scheme allows us to investigate both lateral and vertical permeability structure at a variety of scales. At each sample site we measure air permeability and record depositional facies, lithofacies (rock type, facies, and bedding), grain size, fabric, and proximity to bounding elements. These data allow us to relate permeability to lithology and thereby establish discrete permeability groups unique to a specific depositional and diagenetic setting. This information provides the basis for assigning values and distributions of petrophysical properties to reservoir sandstones from similar depositional settings.

We determine lateral and vertical permeability variation by correlating permeability profiles and by constructing semivariograms. Lithologic heterogeneities such as shale breaks and other low-permeability intervals are treated separately from the analysis of sandstone permeability variation. We map the distribution of these elements on outcrop photomosaic panels and quantify their dimensions and density by probability distribution curves and other statistical techniques.

Study Area

Ryer (1981a, b; 1982, 1983) and Gardner (1991) discussed the depositional and tectonic history of the Ferron Sandstone; only a brief summary is presented here. The Ferron Sandstone is a Cretaceous fluvial-deltaic system that exposes a wide range of depositional facies from fluvial through deltaic, coastal plain, and marine. Ryer (1981a) subdivided the upper Ferron interval into seven discrete delta lobes (genetic sequences [GS] 1 through 7) that progress from seaward-stepping (GS 1 and 2) sandstones at the base to vertically stacked (GS 3 and 4) deposits in the middle and landward-stepping depositional geometries (GS 5, 6, and 7) at the top of the Ferron (fig. 1). Each unit consists of a regressive-transgressive cycle that is bounded by time-significant marine flooding surfaces. Gardner (1991) showed that systematic and predictable changes in facies arrangement and internal characteristics are related to stratigraphic position within the Ferron system. This well-documented geologic framework allowed us to quickly focus on two depositional pulses of the Ferron deltaic system that in many aspects reflect the style and scale of heterogeneity present in many Gulf Coast fluvial-deltaic gas reservoirs: the landward-stepping GS 5 and the seaward-stepping GS 2.

Data Collection

Three-dimensional exposures of the Ferron Sandstone exist where canyons dissect the western limb of the San Rafael Swell, east-central Utah. Sparse vegetation and the absence of structural complexity allow continuous examination and sampling. We examined representative facies within a seaward-stepping (GS 2) and a landward-stepping (GS 5) unit this past field season. We first selected outcrops for characterization on the basis of sequence stratigraphic setting, access, exposure, and safety. We then photographed the outcrop with a medium-format camera and compiled photomosaic panels for preliminary mapping of sand-body geometry and

6
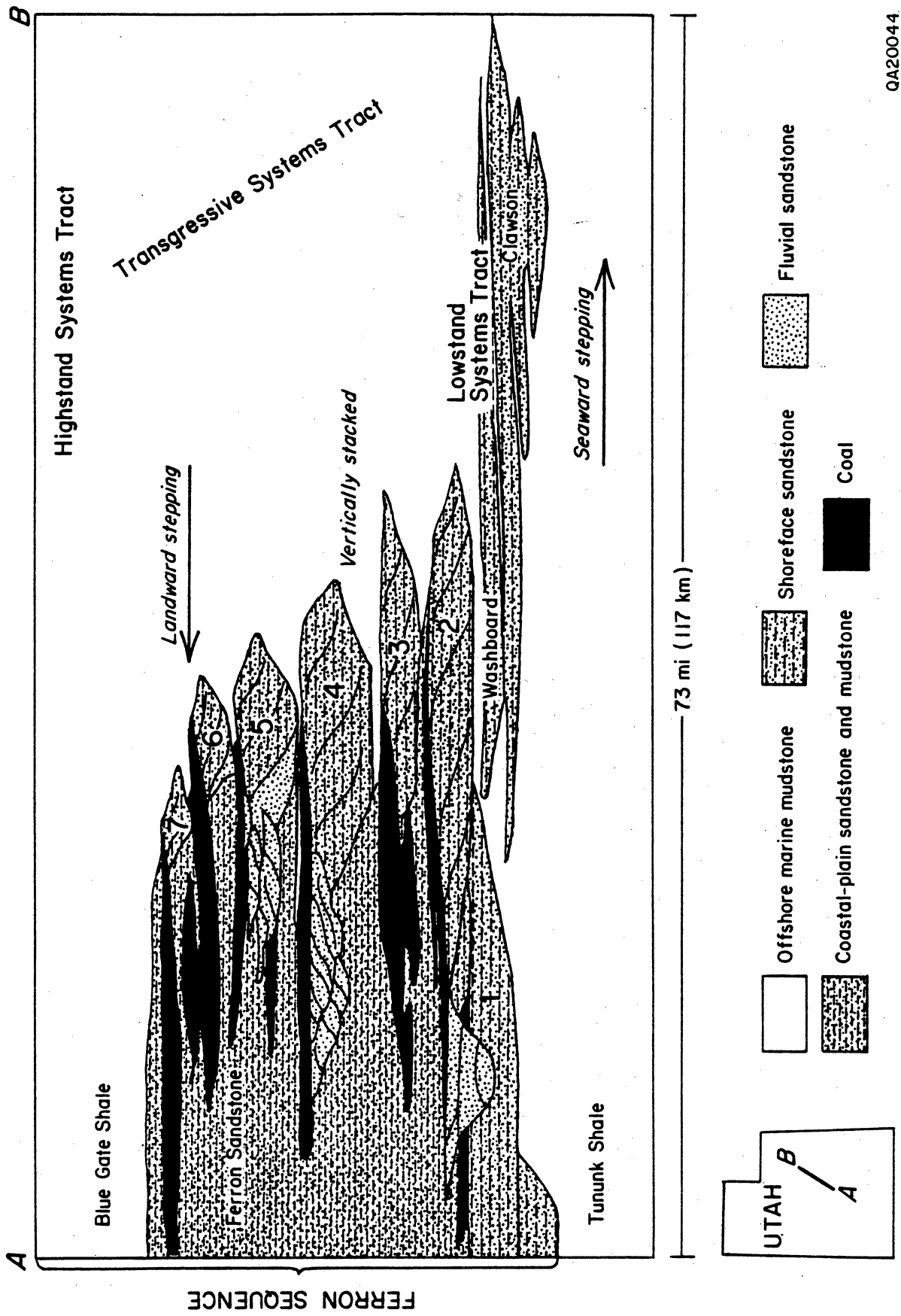
Figure 1. Schematic cross section depicting sequence stratigraphic relationships of the Ferron Sandstone in central Utah (after Ryer, 1981a, b).

bounding element relations. Locations of vertical transects and grid sites were then selected for detailed analysis.

We measured permeability along vertical transects and at grid points with a portable minipermeameter. This is a gas-flow measuring device that allows us to quickly make a large number of permeability determinations on the outcrop with minimal sample preparation. Outcrop weathering effects are minimized by choosing relatively fresh surfaces and chipping away the outer surface of the rock. To evaluate the effects of surface weathering and sample site preparation, we compared permeability values determined from chipped sample sites with values measured on 2-inch-diameter cores taken from the same site. The similarity of values (fig. 2) indicates that permeability measured at the outcrop after chipping away the surface rind compares favorably with permeability within the outcrop.

Numerous studies have demonstrated the accuracy of minipermeameter measurements in comparison with conventional measures of permeability (Weber, 1982; Goggin, 1988; Kittredge, 1988). In general, a good correspondence between minipermeameter and conventional measurements is reported over the range of approximately one to several thousand millidarcys (md). Our minipermeameter has a detection limit of about 0.1 md and can measure permeabilities as high as 2,500 md. Over the range of about 10 to 1,000 md, the minipermeameter gives the same values as the Hassler-sleeve method (fig. 3). However, values below about 10 md tend to be slightly overestimated, whereas values greater than about 1,000 md are slightly underestimated. These discrepancies do not significantly affect our results. The intent of the outcrop characterization is to resolve the permeability structure within and between sand bodies. Other samples are collected for laboratory petrophysical measurements, which have greater accuracy and precision than field measurements.

We measured more than 6,000 permeability values during the 1991 field season. Outcrop locations are shown in figure 4; the number of measurements taken, sampling schemes used, and status of the data collection phase for each facies are shown in table 1.

8
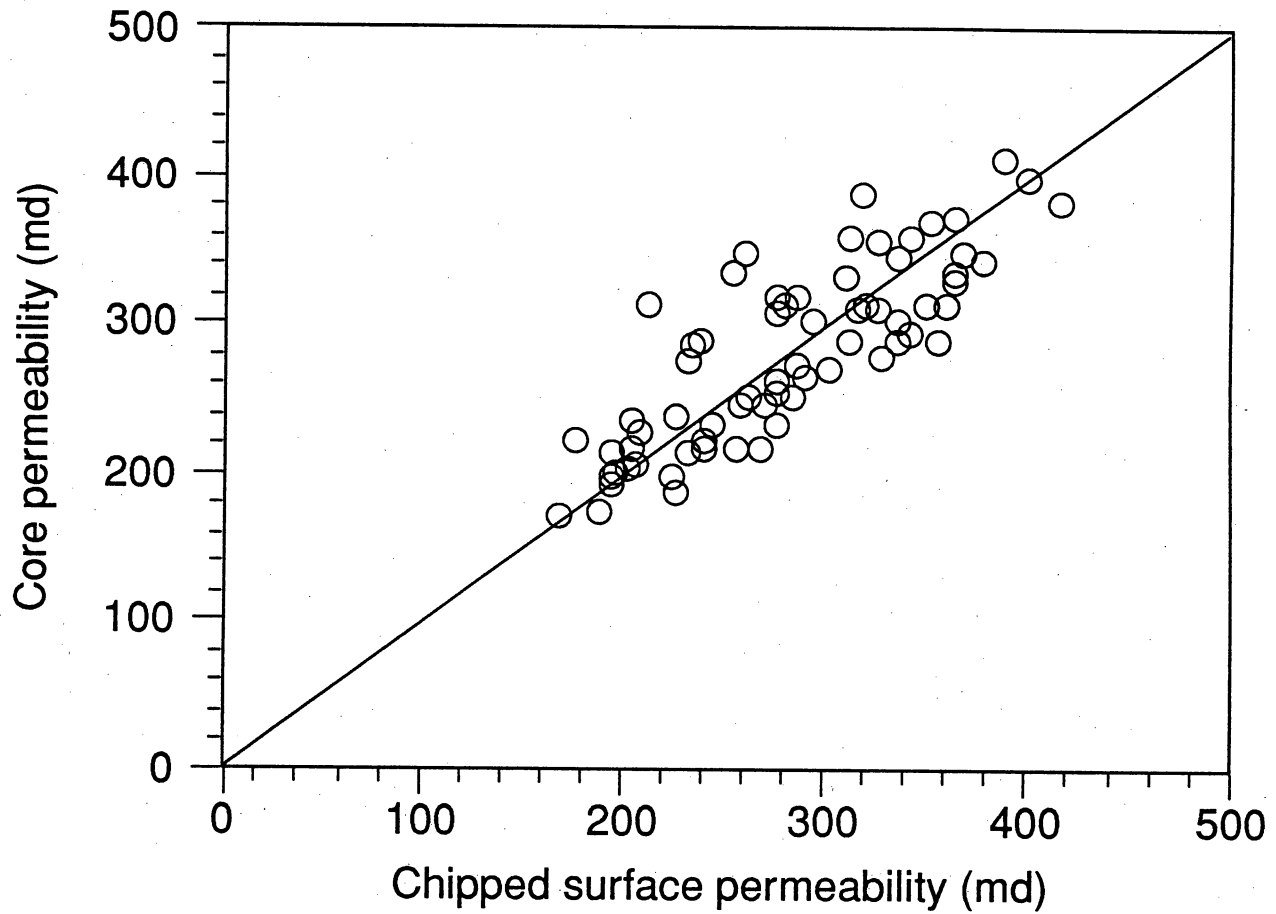
Figure 2. Comparison of permeability measurements between cored and chipped surfaces.
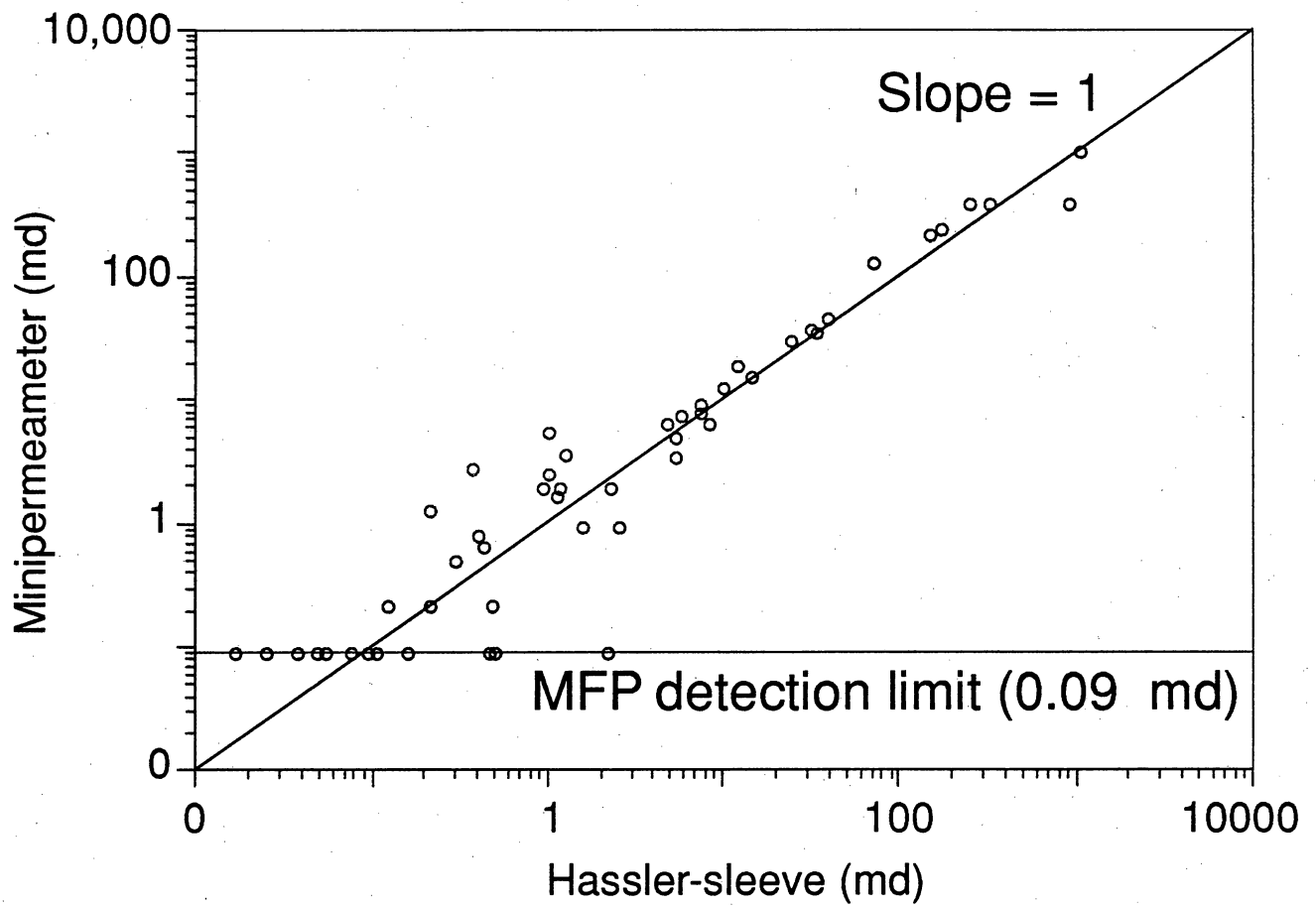
QA20055c

Figure 3. Comparison of minipermeameter- versus Hassler-sleeve-derived permeability.

QA20052c

10
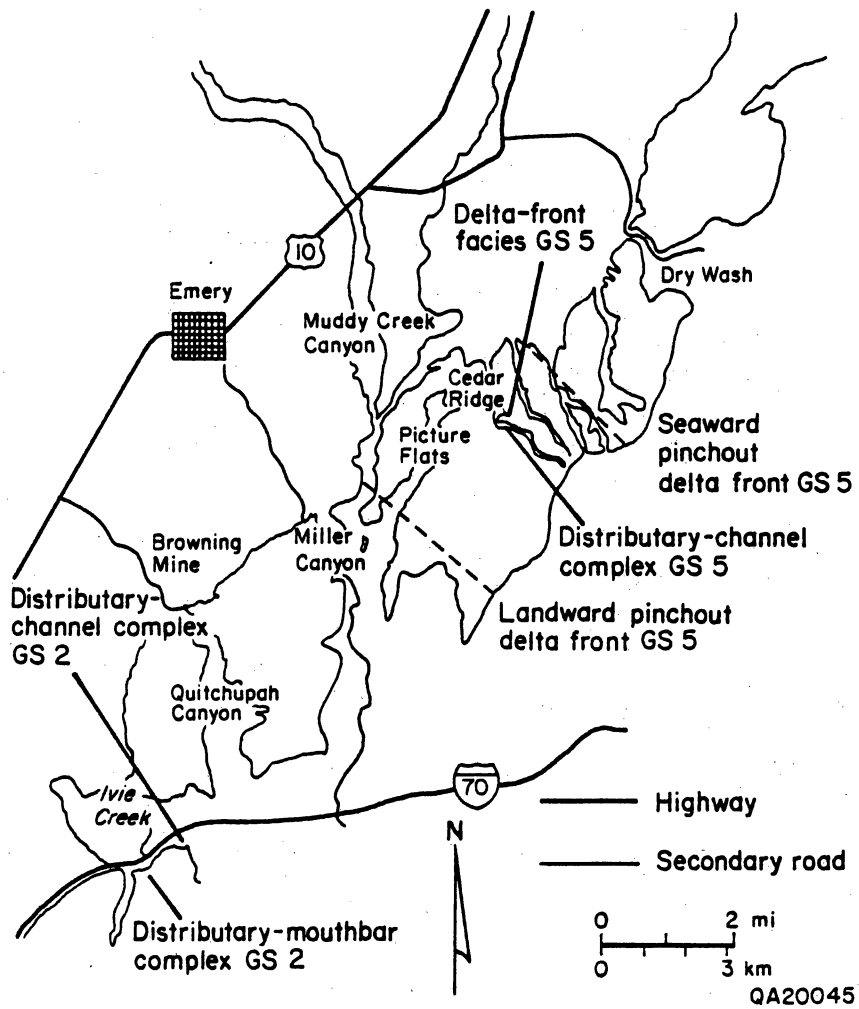
Figure 4. Map showing location of outcrops investigated during the 1991 field season. Dashed lines show the landward and seaward extent of Ferron GS 5 delta-front facies.

11

Table 1. Data collection of permeability measurements by location and depositional facies.

Location facies	Sampling scheme	Number of measurements
South of I-70 distributary channel of unit 2	10 vertical transects Grid (20 × 30 ft)	1,446 1,207
South of I-70 distributary mouth bar of unit 2	3 vertical transects	357
Cedar Ridge Canyon distributary channel of unit 5	20 vertical transects	1,627
Cedar Ridge Canyon delta front of unit 5	8 vertical transects 1 horizontal transect	634 121
Regional delta front of unit 5	12 vertical transects	626
	TOTAL	6,018

Results

Distributary-Channel and Delta-Front Architecture of GS 2

Ferron GS 2 distributary channels form sandstone belts as much as 100 ft thick and 3,000 ft wide that are composed of multiple-channel sand bodies. Individual-channel sand bodies are 3 to 30 ft thick and tens to hundreds of feet wide. In profile they consist of an erosive-based, upward-fining to -coarsening sequence (Allen, 1965) that produces a compound bar form called a macroform (Jackson, 1976; Friend, 1983; Miall, 1985). In cross section, Ferron distributary-channel belts consist of laterally restricted highly amalgamated multistory macroforms at the base that grade into meandering, moderately amalgamated macroforms near the top.

We selected a large (500 ft wide and 70 ft thick) distributary-channel complex exposed along vertical cliffs where Interstate 70 cuts through the Ferron Sandstone (fig. 4) for detailed examination. The complex is preserved as a narrow, elongate, ribbon sandstone that is incised into fine-grained delta-front and distal mouth-bar deposits. Paleocurrent directions within the channel deposits are strongly unidirectional normal to the outcrop face. Internally, the channel is composed of a series of multistoried, highly amalgamated and interconnected macroform types, each of which shows a distinct stratal architecture. Macroform variability largely results from differences in channel morphology, macroform position within the channel, and stage of channel development (Gardner, 1991).

Macroforms in the lower half of the channel are simple bar forms that have no large-scale accretion surfaces and contain a low diversity of sedimentary structures. They are characterized by 3- to 10-ft-thick, erosive-based, uniformly distributed medium- to coarse-grained sandstone sequences that consist of a sand-rich basal channel lag and crossbedded sandstone couplet. These erosive-based, lag-sandstone couplets stack to form a channel fill as much as 40 ft thick. The sand-rich nature of the channel lag results from the fixed channel position, with sand sourced from repeated erosion of underlying sand bodies. The lack of bedform types reflects erosional truncation by the overlying macroform and low preservation potential of a complete

13

waning flow sequence. This cut-and-fill macroform represents extensive sediment reworking in a low-sinuosity, fixed channel.

Macroforms in the upper half of the channel display large-scale, low-angle, inclined accretion surfaces and contain suites of unidirectional bedforms that include ripple crossbedded, horizontal/inclined bedded, and trough crossbedded strata. Thin layers of silt and clay deposited during low-flow conditions may be preserved along the channel margin or accretion surface. Under higher flow conditions, underlying sediments were eroded or reworked and a heavy mineral lag developed along channel-base, accretion, and reactivation surfaces. This macroform records channel meandering within a fixed channel belt that produces a series of low- to high-sinuosity macroforms.

Lithofacies Groups and Permeability Variation

By comparing stratal architecture with permeability values we can evaluate how depositional processes affect sandstone heterogeneity and determine what factors most significantly control permeability distributions. Three measures describe the permeability characteristics of different lithofacies groups: (1) permeability distribution type, interpreted from a cumulative frequency plot, (2) central tendency, estimated by the arithmetic mean, and (3) variance, estimated by the coefficient of variation.

Because different sedimentary processes operate in different depositional environments, we first explored permeability variation between the two volumetrically important facies in Ferron GS 2. Comparing cumulative permeability plots of distributary-channel and delta-front (distal mouth-bar) sandstones measured at the I-70 location showed that distributary-channel sandstones have a significantly higher average permeability (166 md vs. 74 md; fig. 5). Permeability in the distributary-channel facies varies considerably from less than 0.1 md to more than 1,000 md. The complex shape of the cumulative frequency plot indicates that

14
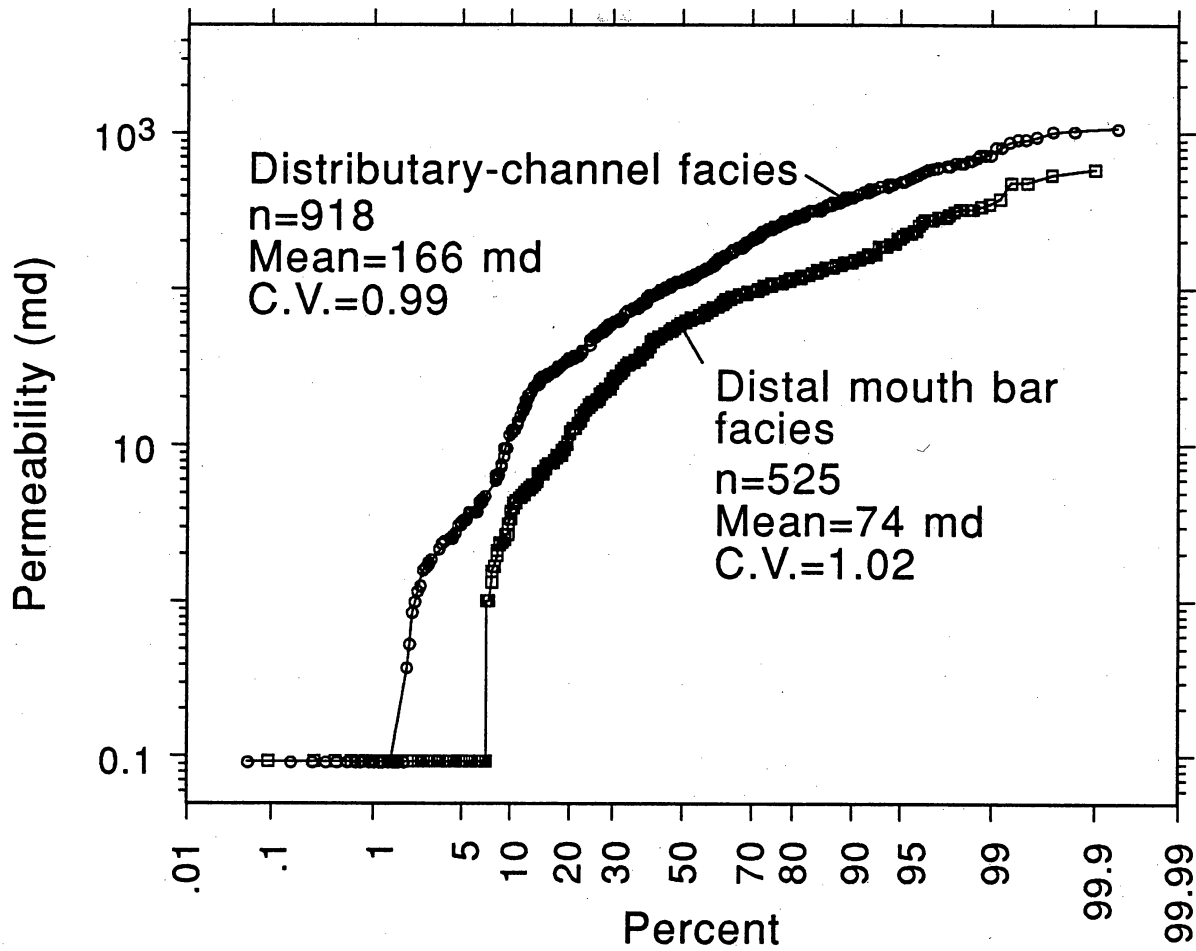
Figure 5. Cumulative frequency plot of permeability measurements from distributary-channel and delta-front facies (distal mouth bar) Ferron GS 2.

samples from a single depositional facies represent a mixture of several permeability populations.

To resolve individual permeability populations we divided the group of all distributary-channel permeability measurements into subsets according to geologic and lithologic characteristics. Much of the permeability variation in the distributary-channel samples is explained by lithofacies variation. A vertical profile (fig. 6) through distributary-channel and delta-front facies at I-70 shows the relationship between permeability, lithofacies, and depositional environment. These relationships provide a basis for separating distributary-channel samples into groups that represent different fluid-flow regimes during deposition: (1) ripple cross-stratified deposits, (2) horizontally stratified deposits, (3) trough cross-stratified deposits, (4) channel-lag deposits, and (5) fine-grained sediments and organic matter. Table 2 provides a description of lithologic characteristics, distribution, and permeability characteristics of each group.

Figure 7 shows log permeability versus cumulative percent relations for the five groups. Straight line segments on this plot indicate that ripple cross-stratified, trough cross-stratified, and horizontally stratified sandstones represent single, log-normally distributed permeability populations. Within each of these groups permeability is mainly related to grain size. Permeability of lag deposits and fine-grained, organic-rich sediments are not log-normally distributed. These patterns probably reflect a large number of permeability determinations below the minipermeameter detection limit as well as multiple populations within each group.

The range of permeability values displayed in figure 7 indicates that the five sedimentologically distinct groups form three permeability classes: (1) trough crossbedded and horizontally stratified sandstones (permeability from 10 to 1,000 md), (2) ripple stratified sandstones and fine-grained or organic-rich sediments (permeability from 0.1 to 10 md), and (3) lag deposits with intermediate permeability values (1 to 100 md).

The distribution of lithofacies and the permeability variation show a close association with the nature of the distributary-channel fill. Figures 8 and 9 compare bedform diversity and

16
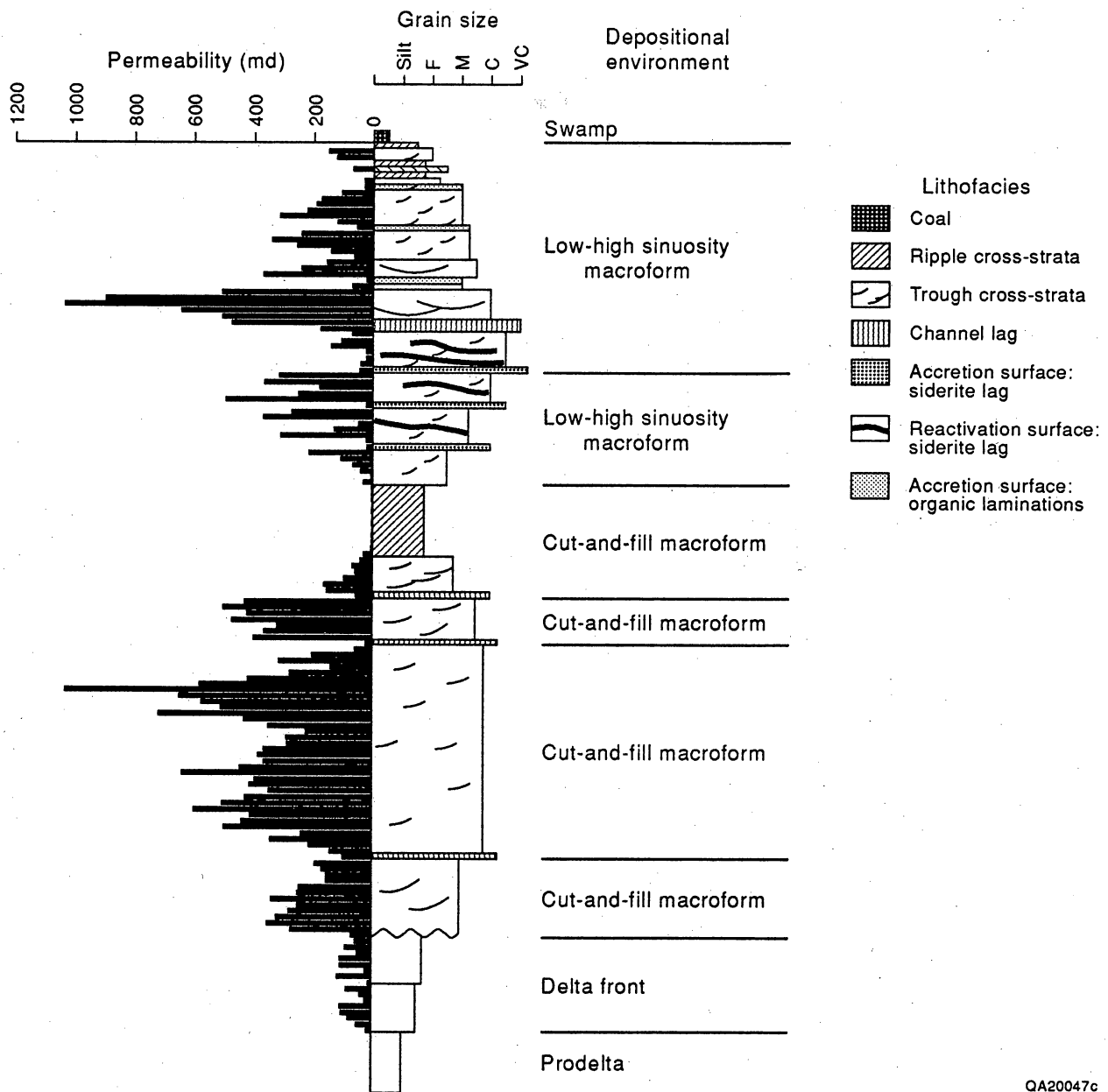
Figure 6. Vertical permeability profile, lithofacies, and depositional processes in a distributary-channel deposit.

Figure 7. Plot of log permeability versus cumulative percent for lithofacies groups from the distributary-channel facies.

18
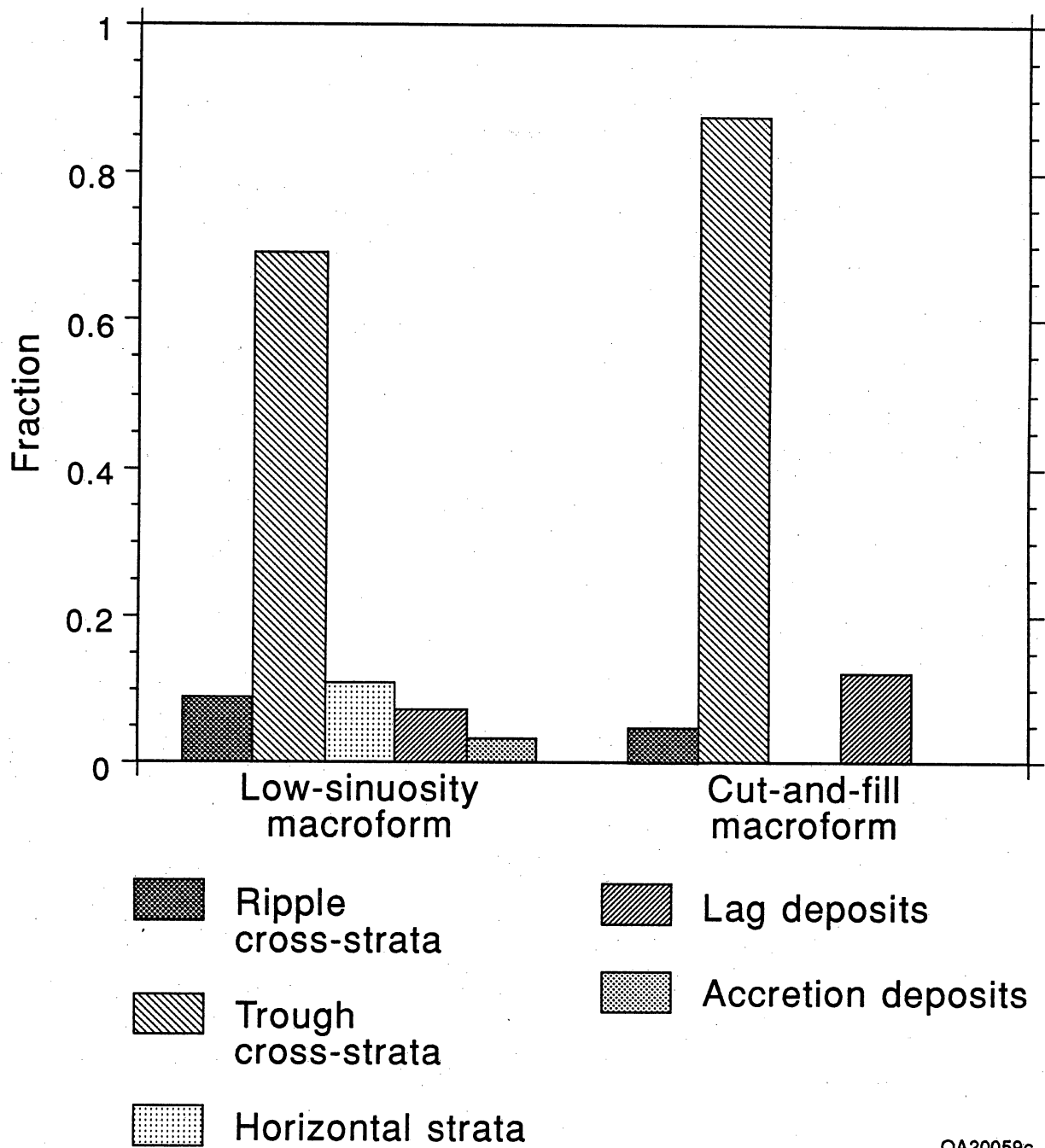
Figure 8. Plot of lithofacies diversity for cut-and-fill and low-sinuosity macroforms.

Figure 9. Cumulative frequency plot of permeability values for cut-and-fill and low-sinuosity macroforms.

QA20057c

20

Table 2. Summary of lithofacies, occurrence, and permeability characteristics of Ferron GS 2 sandstones.

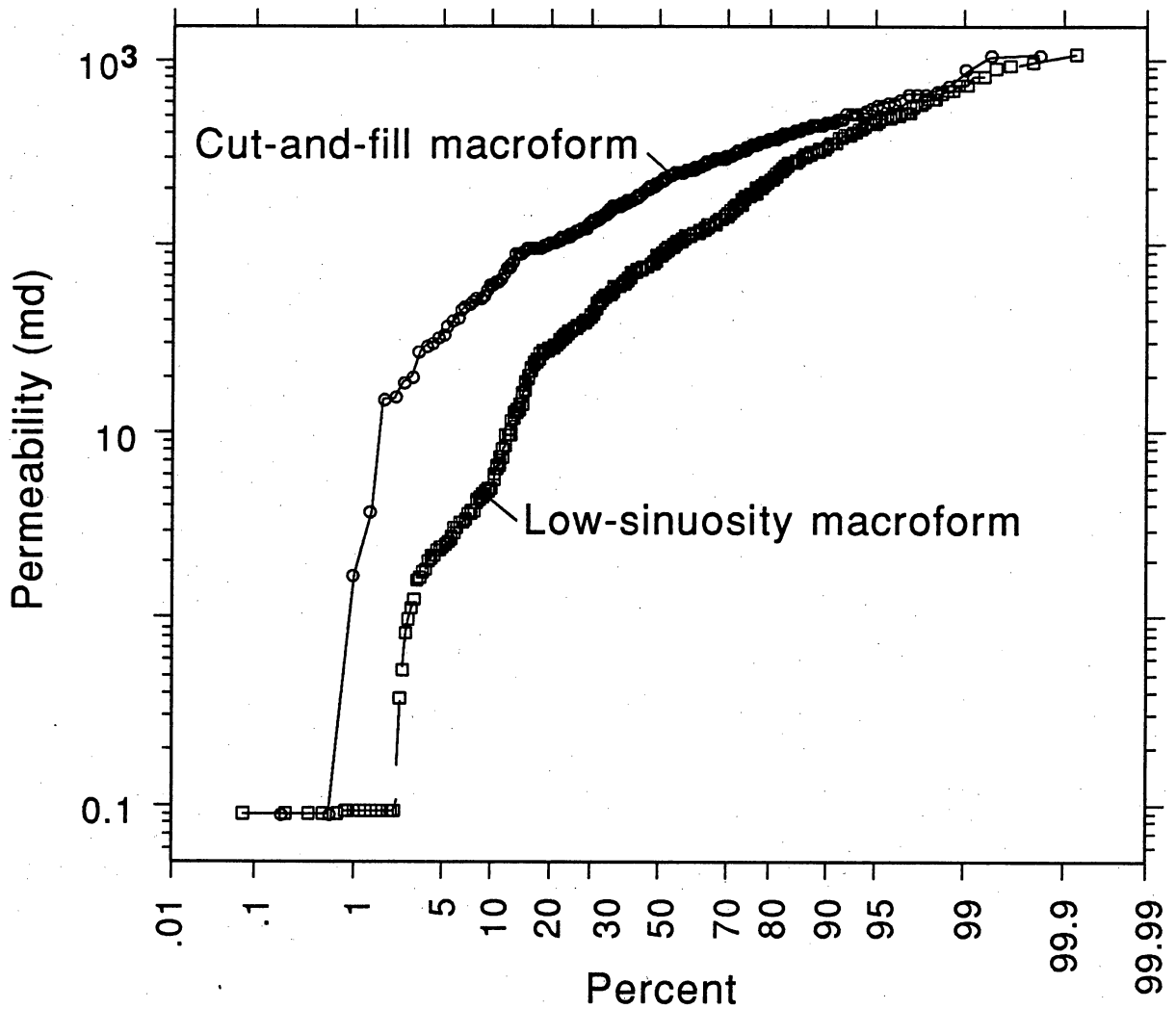| Lithofacies Group	Occurrence	Permeability Characteristics
Fine-grained to very coarse grained, poor to moderately sorted, trough cross-stratified sandstone	Very common lithology distributed throughout channel fill	Average = 204 md Range: 9 to 1,050 md Coefficient of variation = 0.81 Distribution: Log normal
Fine- to medium-grained, moderately sorted, horizontally stratified sandstone	Common lithology within accretion sets of low-sinuosity macroform type	Average = 85 md Range: 13 to 710 md Coefficient of variation = 1.05 Distribution: Log normal
Very fine grained to fine-grained, moderately sorted ripple-stratified sandstone	Deposited as final channel fill, common in low-sinuosity macroform type, uncommon in cut-and-fill macroform type	Average = 4.7 md Range: 0.09 to 13 md Coefficient of variation = 0.71 Distribution: Log normal
Medium-grained to very coarse grained, poorly sorted, sand-rich lag deposits with variable amounts of clay clast or siderite grains	Common lithology associated with lithologic discontinuities such as channel margins, accretion surfaces, and reactivation surfaces	Average = 38 md Range: 0.09 to 227 md Coefficient of variation = 1.15
Fine-grained sediments and organic laminated sandstone	Common lithology associated with accretion surfaces within low-sinuosity macroform type	Average = 2.6 md Range: 0.09 to 17 md Coefficient of variation = 1.67

21

permeability distribution, respectively, for each macroform type. Cut-and-fill macroforms, located in the lower portion of the channel, are separated by erosional discontinuities and generally lack complete stratal successions. As a result, this facies displays a low bedform diversity characterized by trough cross-stratified sandstones and sand-rich lag deposits (fig. 8). In contrast, the higher preservation potential of the low-sinuosity macroforms results in greater bedform diversity characterized by multiple bounding surfaces and a variety of sedimentary structures. These differences are reflected in a plot of log permeability versus cumulative percent for the two macroform types (fig. 9). The downward shift in the distribution curve from the cut-and-fill macroform to the low-sinuosity macroform indicates that permeability variation increases with increasing bedform diversity.

Permeability Structure

To explore spatial variability in the distributary-channel sand body we measured permeability every 0.5 ft along a series of vertical transects spaced 50 ft apart. In addition, we constructed a 20 × 30 ft sample grid and detailed transects to examine permeability variation within a single macroform. We used both correlation of permeability profiles and construction of variograms to examine permeability relations.

Permeability Correlation by Profile Comparison

We can estimate how far along the outcrop similar profiles extend by visually comparing permeability profiles. The criteria used to distinguish permeability trends from random fluctuations are (1) a trend exists if permeability consistently increases or decreases to a high or low value at a given transect as opposed to a single-point excursion, and (2) a regular trend exists if an upward-increasing or -decreasing profile related to lithologic changes persists between transects.

Figure 10 shows the relationship of stratal architecture (bounding surfaces between and within macroforms) to permeability profiles for the GS 2 distributary-channel complex. In the vertical direction permeability profiles are composed of several distinct trends: (1) a cyclic pattern in the lower channel fill, (2) an erratic upward-increasing trend in the middle channel fill, and (3) an upward-decreasing trend in the upper channel fill. The high degree of similarity between adjacent profiles indicates that the observed permeability patterns are not random but extend laterally as much as several hundred feet.

Comparison with the stratal architecture (fig. 10) demonstrates that bounding elements between macroforms define large-scale permeability trends. Cut-and-fill macroforms are characterized by a uniform permeability trend (3 to 12 ft thick) that extends laterally 100 to 250 ft. Low-sinuosity macroforms are characterized by an upward-increasing or -decreasing trend (10 to 20 ft thick) that extends laterally 200 to 350 ft. Overall, the permeability patterns in the distributary channel represent a composite of trends whose character and distribution reflect the highly amalgamated, multistoried nature of the channel fill. The classic upward-decreasing permeability trend most often modeled in reservoir simulations of channel sandstones is represented only by the final filling event in this channel complex.

Permeability Correlation by Semivariograms

Semivariograms indicate spatial similarity between separate measurements. In studies of permeability structure, we can use semivariograms to determine ranges of permeability correlation and predictability. Figures 11a and b show vertical and lateral semivariograms for the permeability data collected at 0.5-ft spacings along a series of vertical transects within the GS 2 distributary-channel complex. The results indicate that permeability measurements are related over a distance of 10 to 12 ft vertically and approximately 150 ft laterally. These dimensions correspond to the average vertical and lateral macroform dimensions (fig. 10).
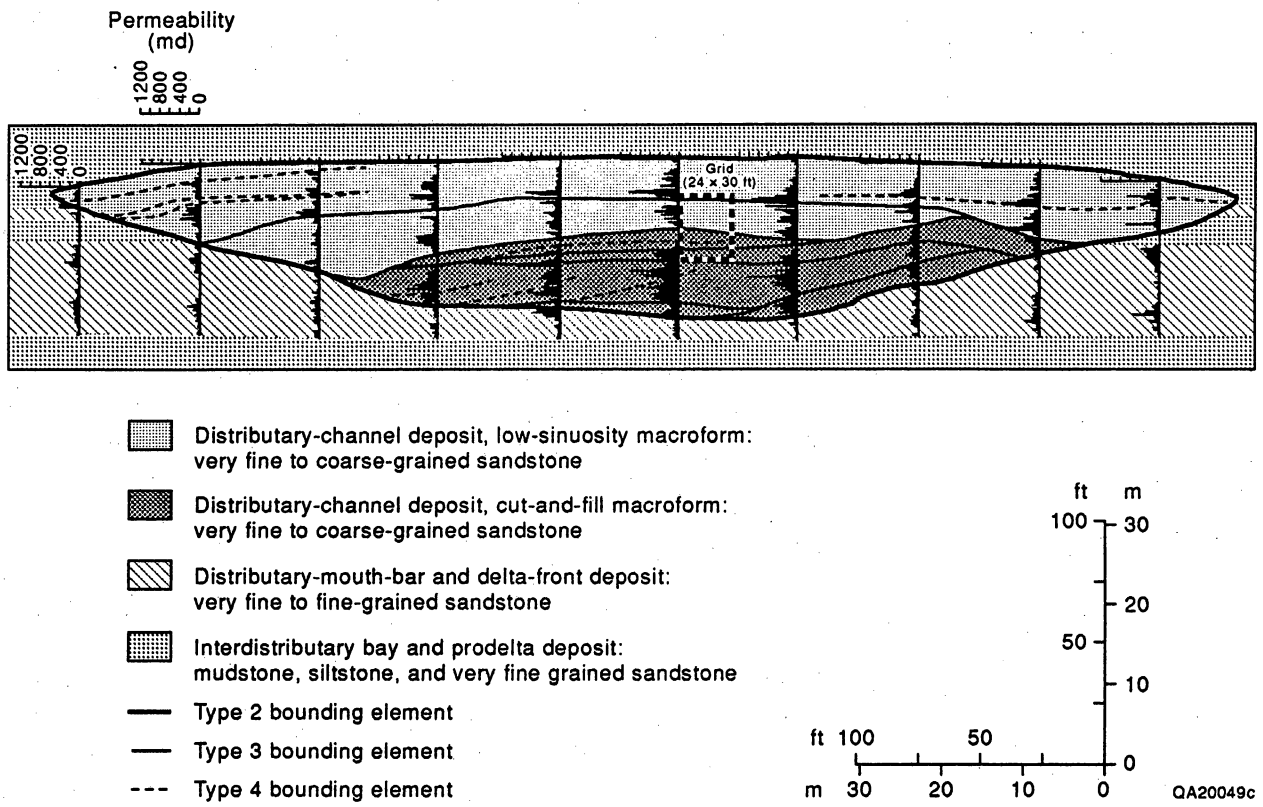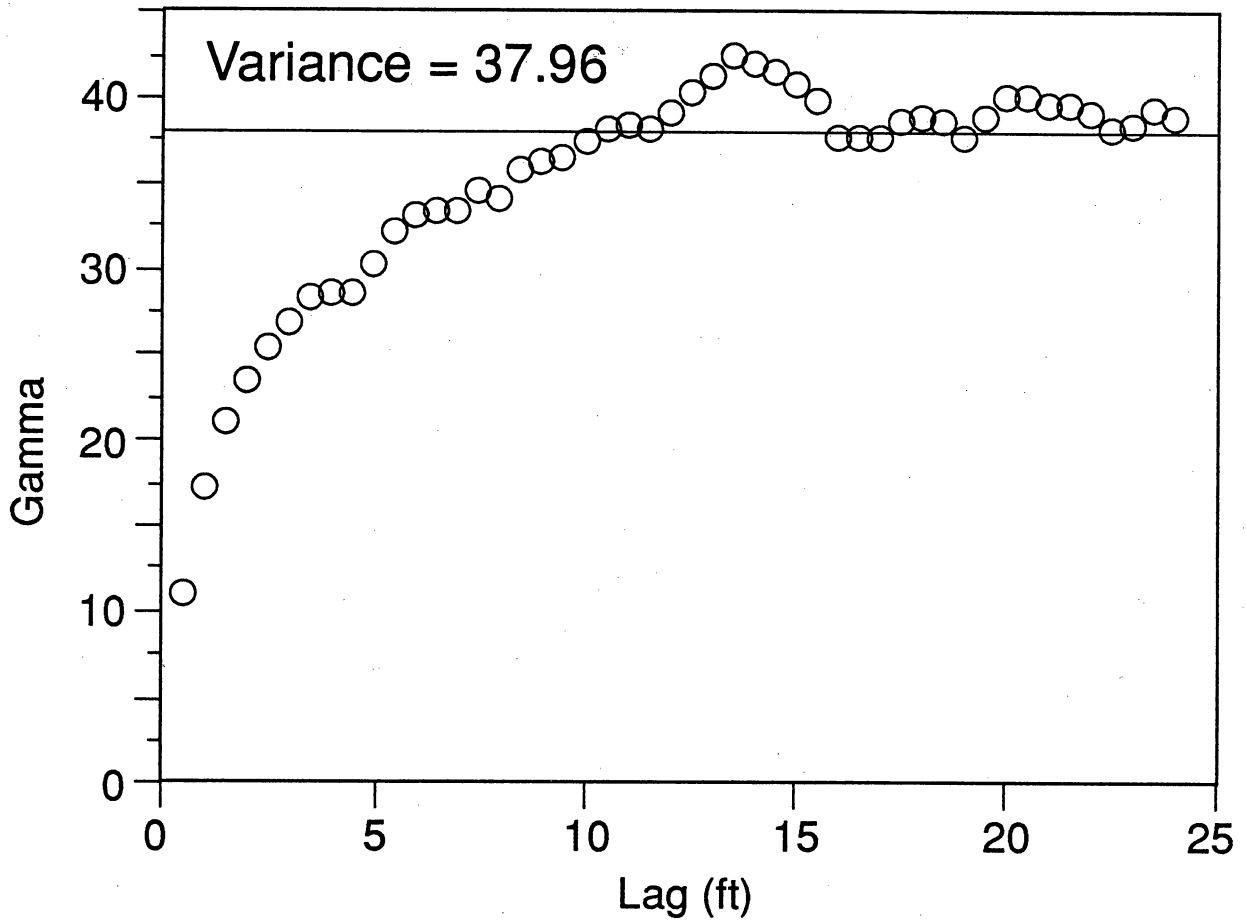
Permeability
(md)

Figure 10. Distributary-channel architecture and permeability profiles, Ferron GS 2 at I-70 location.

24
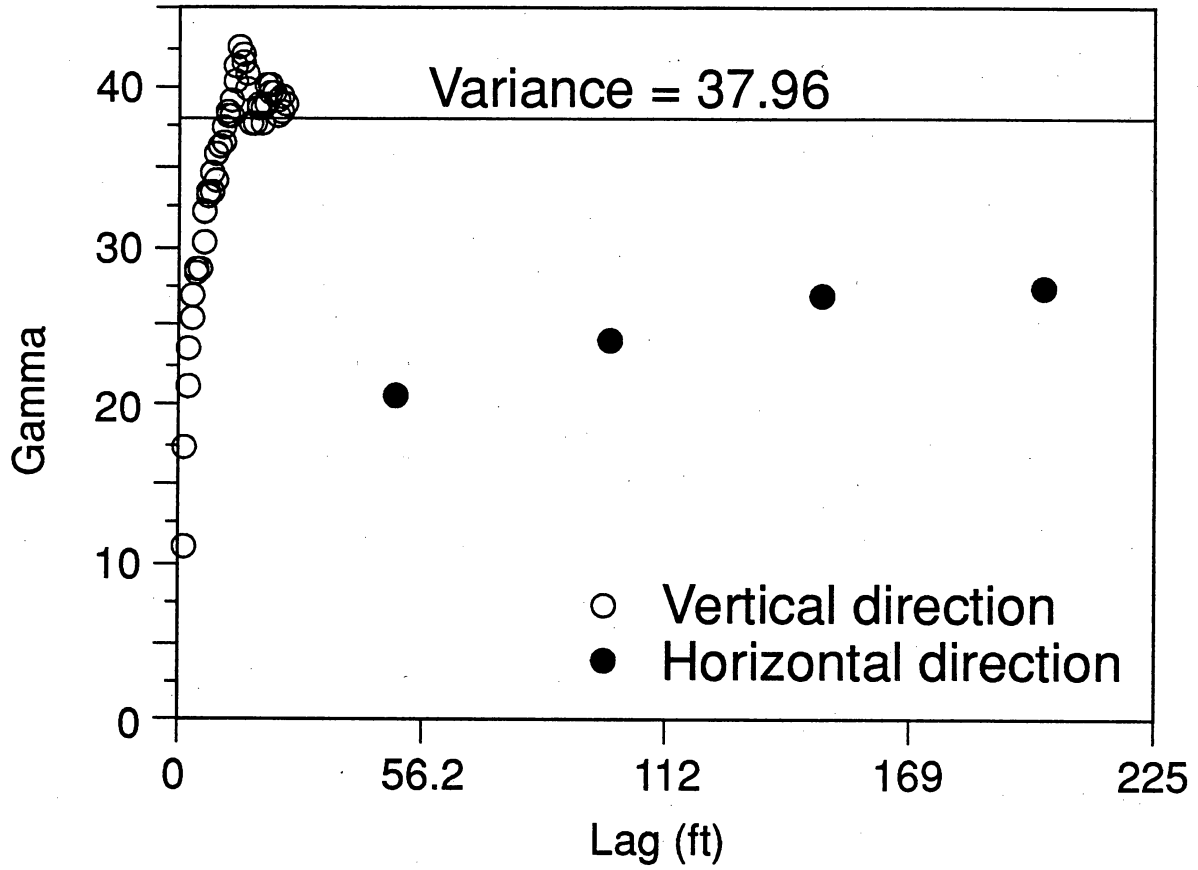
(a)

Figure 11. (a) Vertical semivariogram for distributary-channel facies. (b) Comparison of horizontal and vertical semivariograms from distributary-channel facies.

QA20051c

(b)

Figure 11. (cont.)

QA20050c

Differences in the permeability structure between the cut-and-fill macroform and the low-sinuosity macroform type are reflected in the semivariogram function. Figure 12 displays the vertical variograms for each macroform type, normalized with regard to mean permeability so that permeability variations can be directly compared. Permeability is correlated very differently for each macroform type (fig. 12). Permeability structure in the cut-and-fill macroform reflects correlation over 2 to 4 ft that reflects the contrast between the trough crossbedded sandstone and lag deposits. Permeability structure within the low-sinuosity macroform reflects several types of correlation that for distances <2 ft are related to bounding surfaces and for distances >2 ft are related to upward-increasing or -decreasing permeability trends.

Scale Dependence of Permeability

To investigate fine-scale permeability structure we constructed a 20 × 30 ft grid with measurements at 1-ft spacing and a series of 4-ft vertical transects with 0.25 ft between measurements. The grid contains both cut-and-fill and low-sinuosity macroforms. In the lower portion of the grid a cut-and-fill macroform with an erosive base, represented by a thin lag deposit, is overlaid by amalgamated trough crossbedded strata and is capped by massive to ripple-laminated strata. Erosively overlying this unit is a sequence of trough crossbedded strata with well-developed internal accretionary sets and reactivation surfaces. Grain size increases upward from fine to coarse sand. This sequence represents either downstream or lateral accretion of a low-sinuosity macroform. Near the top of the grid is part of a third macroform that eroded into the underlying sands and represents the final fill event of the distributary-channel complex.

Figure 13 shows sample grid, primary lithologic attributes and their spatial distribution, and four permeability profiles. Three vertical, scale-dependent permeability trends exist. At the largest scale permeability increases stepwise upward from base to top of the macroform. Within
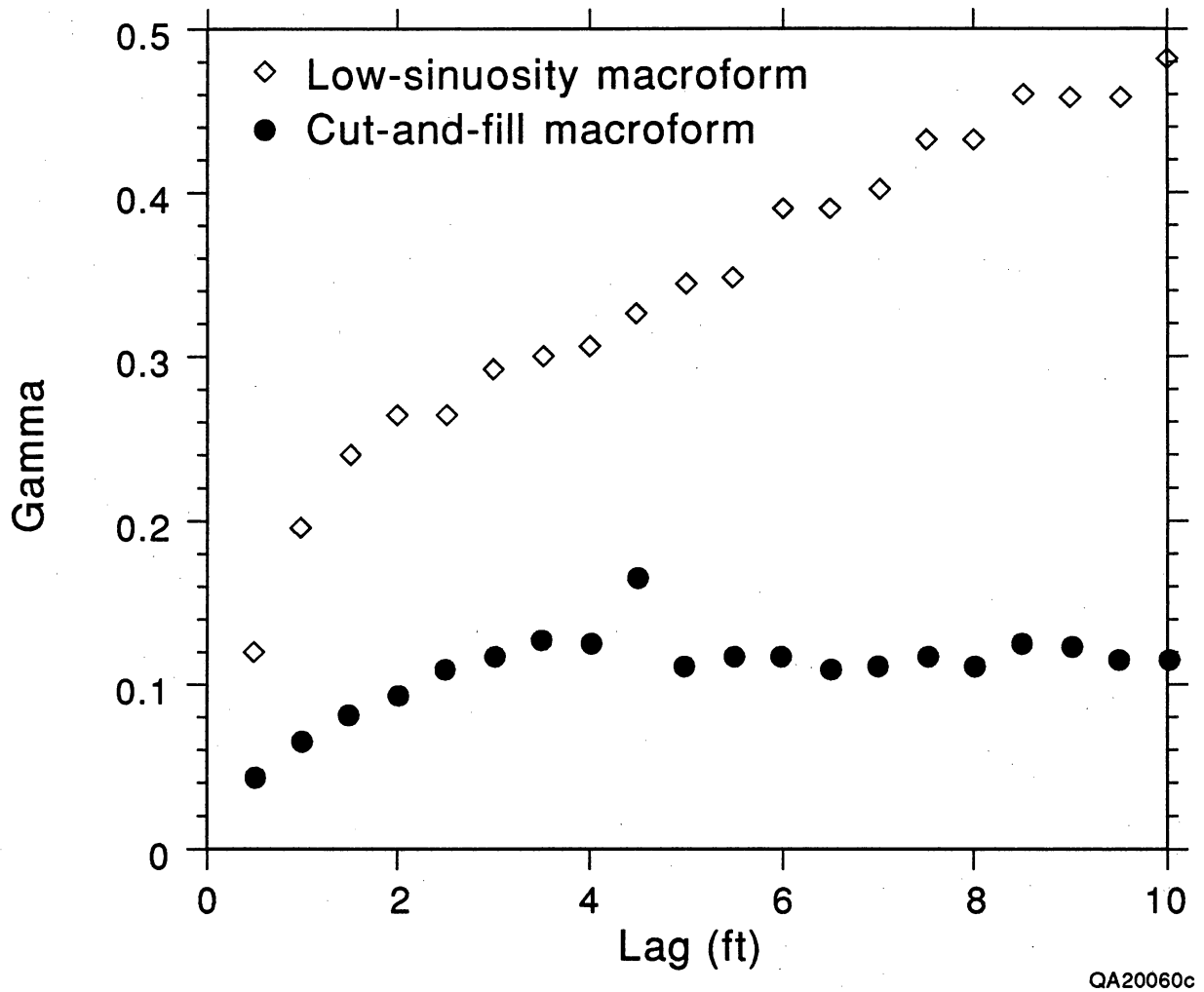
Figure 12. Normalized vertical semivariograms for cut-and-fill and low-sinuosity macroform types.
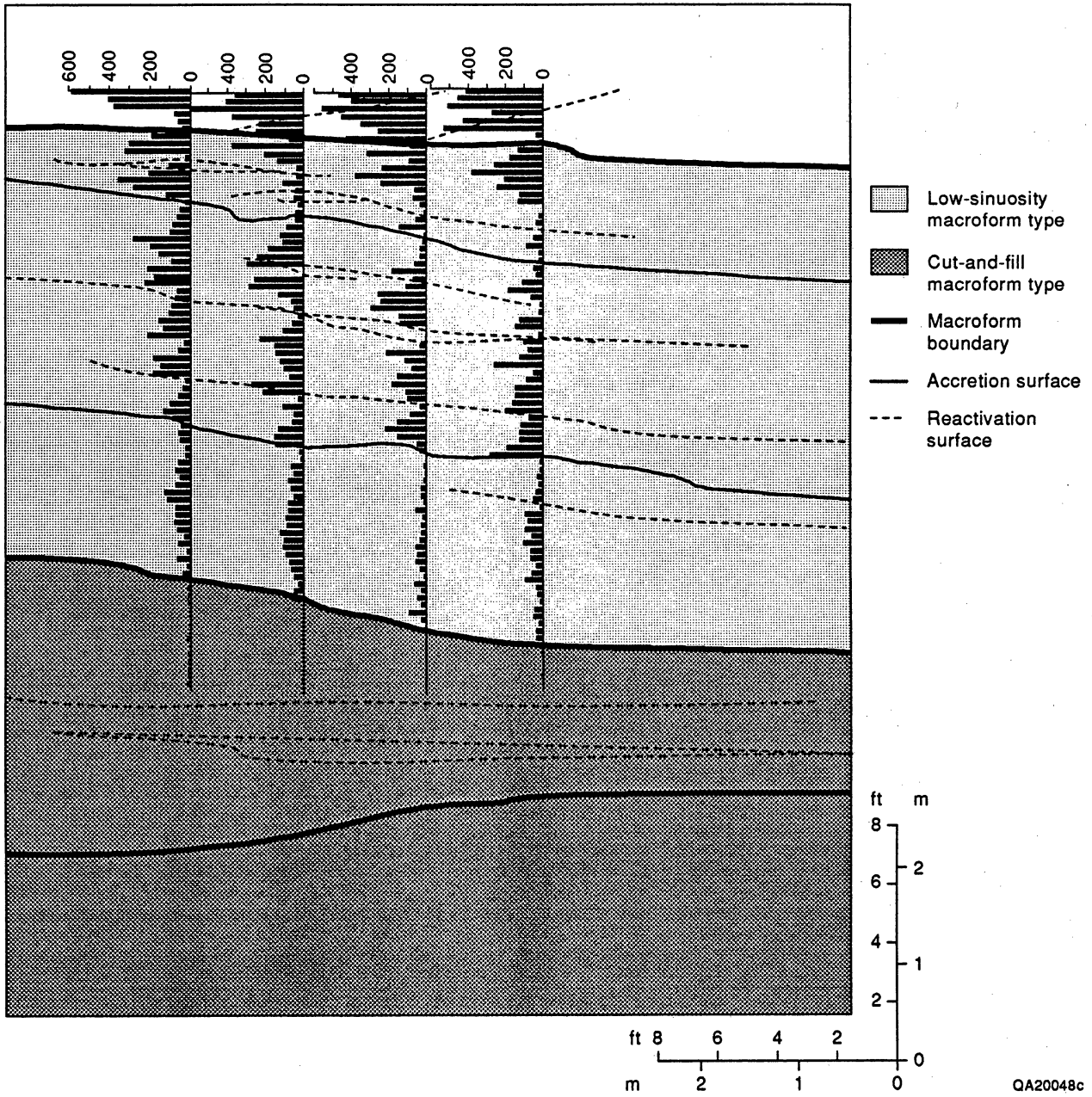
Figure 13. Detailed permeability profiles and architecture from distributary-channel facies.

the low-sinuosity macroform are distinct permeability zones 3 to 5 ft thick. Some of these zones contain small-scale permeability trends 0.5 to 1.5 ft thick. Variations in grain size, sorting, and the presence of lithologic discontinuities generally control these permeability variations. Comparison of permeability profiles indicates a high degree of lateral correlation exists with the distinct permeability zones paralleling the low-angle inclined accretion surfaces (third-order zones of heterogeneity). On the basis of the correlation of permeability variation with stratal architecture, we interpret these zones to be 50 to 75 ft long. Smaller scale permeability trends that also parallel accretionary surfaces exist within these units. These zones are related to reactivation surfaces within accretionary units. Individual zones (fourth-order) have lengths of 10 to 20 ft.

Figure 14 shows the vertical and horizontal semivariograms calculated for the sample grid. The vertical correlation range is 2 to 4 ft, and the horizontal correlation range is about 14 ft. Changes in slope of the semivariogram function reflect three scale-dependent types of vertical permeability pattern (fig. 13). From smallest to largest scale these are (1) fifth-order heterogeneity related to reactivation surfaces (2 ft), (2) fourth-order heterogeneity related to accretionary sets (6 ft), and (3) third-order heterogeneity related to macroform type (12 ft).

Distribution of Baffles

We operationally define a baffle as a discontinuous interval of low-permeability rock that would probably act as an obstacle to flow under reservoir conditions. Such intervals need not be continuous to severely affect directional permeabilities in a reservoir (Haldorsen and Lake, 1984). Because the distributions and dimensions of baffles are impossible to describe solely from core or well logs, it is important to quantify them on outcrop. Baffles within genetic units probably have characteristic shapes and distributions that are related to depositional processes. Understanding these processes will provide a basis for predicting baffle properties and distributions in sandstone reservoirs.
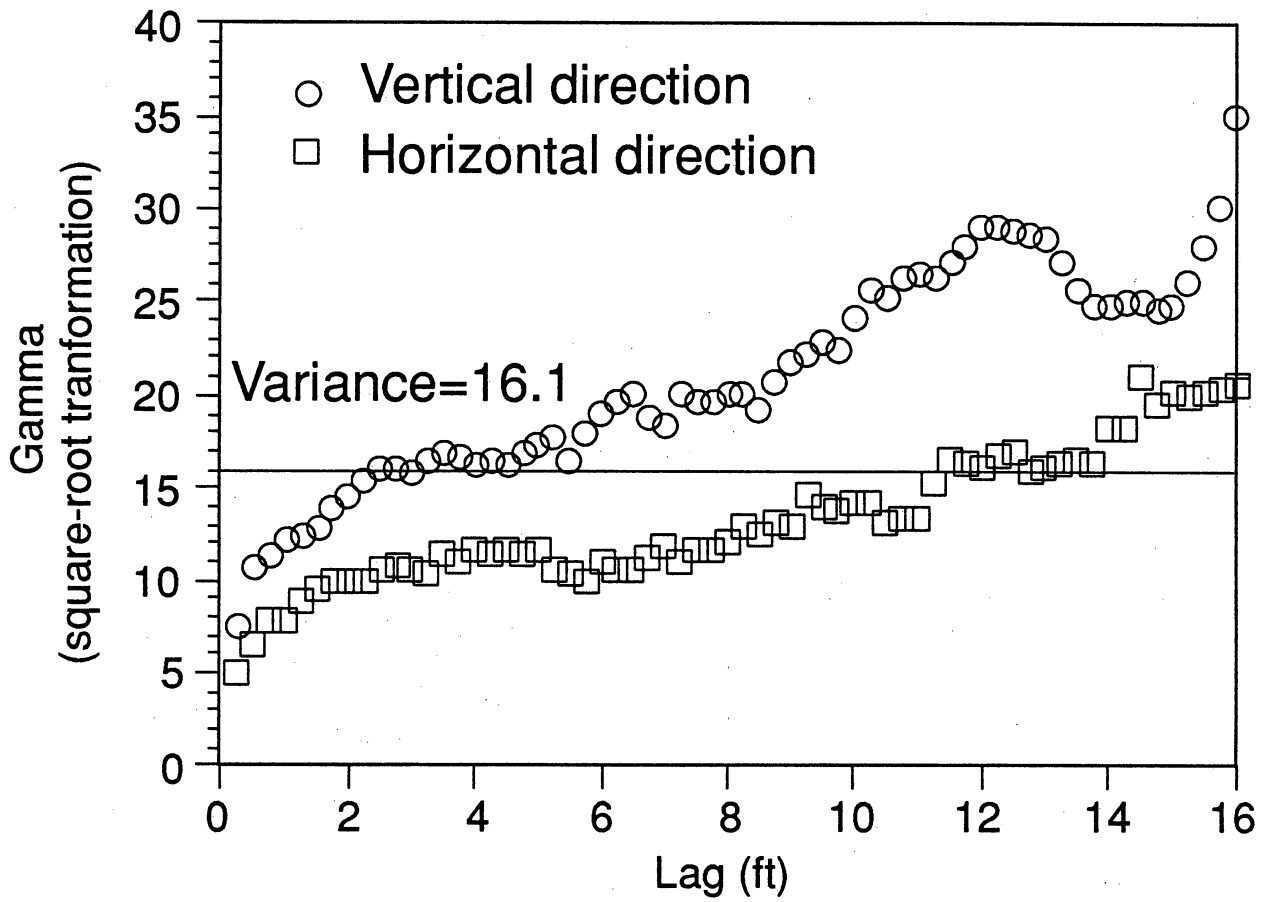
Figure 14. Horizontal and vertical semivariograms from 20 × 30 ft grid on low-sinuosity macroform, distributary-channel facies.

To characterize the geometry of baffles we mapped the distribution of low-permeability intervals on photomosaic panels. Lithologically, the low-permeability units are either thin shale layers or sandstone intervals tightly cemented by hematite and clay. Shales form thin discontinuous layers that drape lateral accretion sets and channel margins. Clay- and hematite-cemented sandstones form thin discontinuous layers along erosional surfaces such as reactivation surfaces, accretion surfaces, and channel margins (fig. 15). Individual baffles have limited lateral extent; none extend across the entire channel facies, and they rarely correlate with the adjacent transect. However, along horizons of greater lateral extent, such as channel margins, baffles regularly reappear. Figure 16 shows a cumulative frequency curve of baffle lengths; 50 percent are about 50 ft long, and few extend more than 100 ft. The spatial distribution of each baffle type shows a high dependence on macroform type; therefore, the existence of similar baffles in analogous reservoirs is predictable.

Summary

During both the 1990 and 1991 field seasons our outcrop characterization efforts concentrated on the volumetrically important distributary-channel sandstones. In 1990 we examined landward-stepping deposits of the Ferron GS 5 (Tyler and others, 1991). This past season we focused on the seaward-stepping channel deposits of Ferron GS 2.

Permeability structure within the GS 2 distributary-channel facies is closely related to the nature of the channel fill. Five distinct lithofacies have an important influence on permeability variation. Trough crossbedded and horizontally bedded strata display the highest permeabilities (10 to 1,000 md), ripple cross-strata and deposits associated with accretion and reactivation surfaces display the lowest permeabilities (0.1 to 10 md), and lag deposits have permeabilities that are intermediate between those two groups (1 to 100 md). The occurrence and distribution of these lithofacies are closely related to the two macroform types. The cut-and-fill macroform type is characterized by a thin lag deposit overlain by amalgamated trough cross-strata. The low-
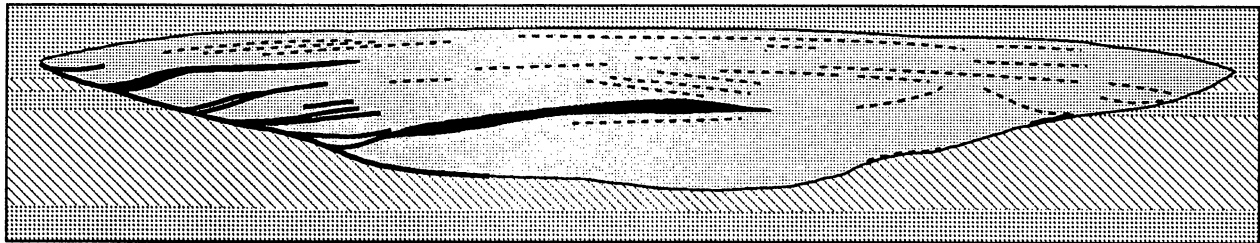
Distributary-channel facies: very fine–very coarse grained sandstone

Delta-front facies: very fine–fine-grained sandstone

Interdistributary bay and prodelta: very fine grained sandstone, siltstone, and mudstone

—— Shale layer ⎫
--- Baffle ⎬ (lithofacies with permeability less than 1.0 md)
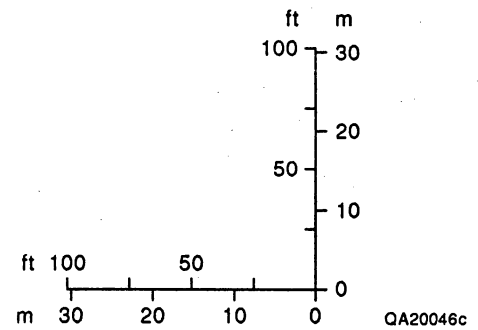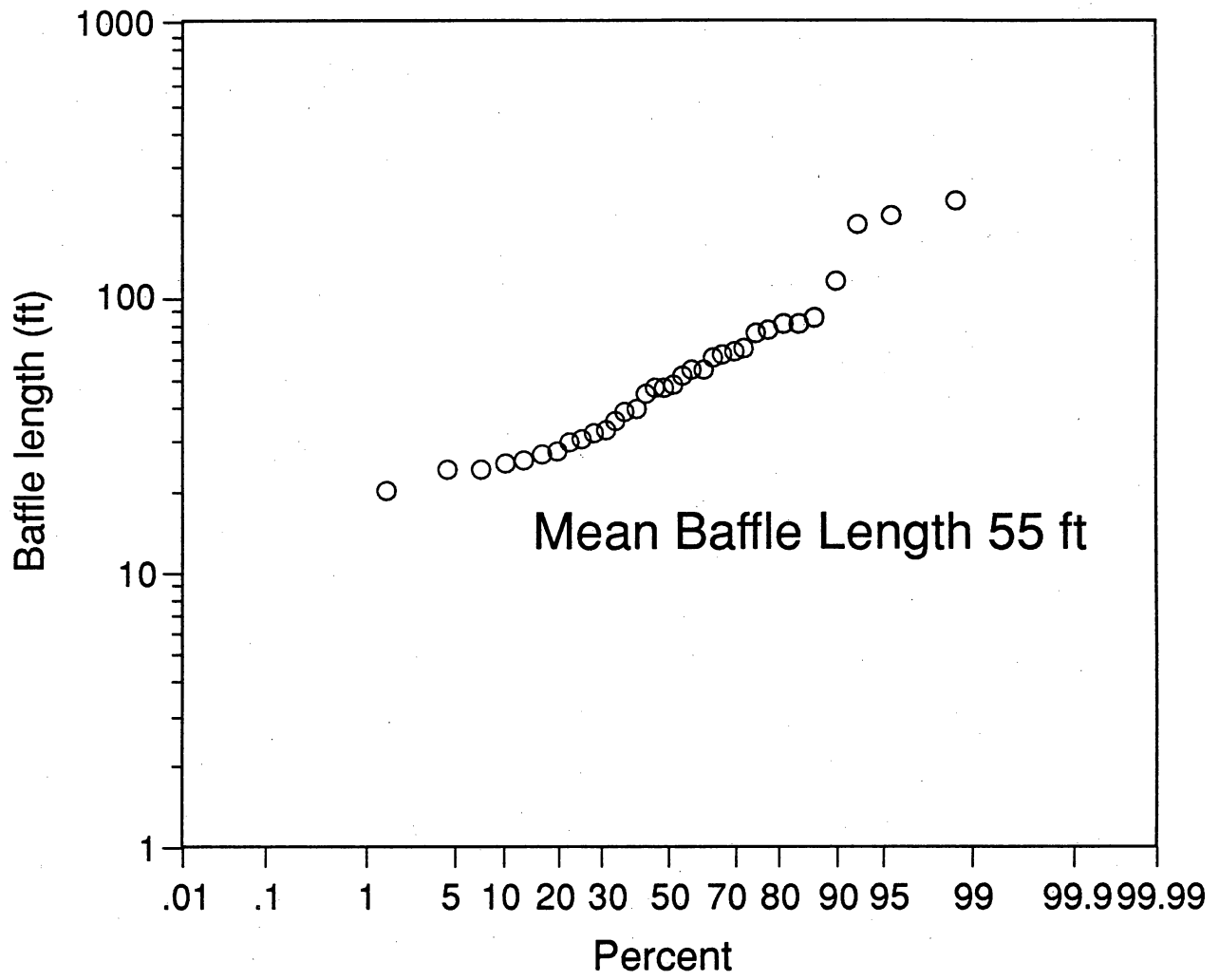
Figure 15. Distribution of baffles and shale layers within distributary-channel complex.

33

Figure 16. Cumulative frequency plot of baffle lengths for distributary-channel facies.

QA20054c

sinuosity macroform is characterized by a succession of bedforms with well-developed accretion and reactivation surfaces. On the basis of permeability characteristics of lithofacies, cut-and-fill macroforms should display good connectivity between macroforms and good continuity within macroforms, whereas low-sinuosity macroforms should display moderate connectivity and poor continuity.

PETROGRAPHIC ANALYSIS OF FERRON SANDSTONES

Purpose

Sandstone reservoirs have a long and complex history from initial sediment deposition through burial, compaction, cementation, porosity modification, and gas emplacement. Clearly we cannot expect to understand and predict the distribution of reservoir architectural elements solely by improving our understanding of depositional processes.

We conduct petrologic investigations in conjunction with outcrop studies to determine what mineralogic, textural, and diagenetic properties characterize flow units, baffles, and barriers, and to relate these properties to diagenetic history as well as depositional processes. Major objectives of this work are to (1) establish the initial mineralogic composition of Ferron sandstones from various facies and environments so we can evaluate differences between the outcrop analog and various sandstone gas reservoirs, (2) quantify changes caused by burial and diagenesis and the associated effects on porosity, pore structure, and permeability, and (3) establish predictive relations between depositional systems, lithofacies, diagenetic effects, porosity, and air permeability.

Sample Selection

During 1990 and 1991 we collected approximately 450 samples from Ferron GS 4 and 5 at outcrops in Muddy Creek Canyon, Picture Flats Canyon, and Cedar Ridge Canyon, and from Ferron GS 2 where it is cut by Interstate Highway 70. Sample selection was based on mapped facies relations and field-measured permeability; our intention was to collect sandstones that represent typical, volumetrically important sand bodies (presumed to act as flow units under reservoir conditions), sandstones near the margins of the major macroforms (commonly permeability anomalies), and bounding elements (presumed to act as baffles or barriers under reservoir conditions). Most samples are 1-inch-diameter core plugs 3 to 6 inches long that were drilled from outcrop with a portable core plugger. We also collected approximately 40 large sandstone blocks of presumed flow units, baffles, and barriers for combined petrophysical and petrographic analysis.

We visually examined each sample, measured permeability using the field minipermeameter, and prepared a thin section for petrographic examination. On the basis of preliminary microscopic examination, we selected a subset of samples and quantified framework grain mineralogy, cement mineralogy, intergranular volume, and porosity. Clay mineralogy for a suite of samples representing all facies was determined by standard X-ray diffraction techniques. Scanning electron microscopy and other chemical or isotopic analyses will be performed on a select group of samples as needed to help resolve the history of diagenetic processes.

Results

We completed petrographic examination of Ferron GS 4 fluvial samples and Ferron GS 5 transgressive, delta-front, and distributary-channel sandstones from Muddy Creek Canyon during 1991. On the basis of preliminary analyses of equivalent facies of GS 5 in Picture Flats

and Cedar Ridge Canyons, the results from Muddy Creek typify sandstone compositions throughout Ferron GS 5.

Kaolinite is the only mineral detected by X-ray analysis in the clay-sized fraction of sandstones from the fluvial facies of Ferron GS 4 and from transgressive, delta-front, and distributary-channel facies in Ferron GS 5. X-ray diffraction patterns show no expanding clay, although minor amounts (<5 percent) may be present.

Framework grain mineralogy, intergranular material, and cement compositions of Ferron sandstones from Muddy Creek vary systematically between fluvial, transgressive and delta-front, and distributary-channel sandstones. Transgressive and delta-front sandstones of Ferron GS 5 are the most quartz-rich samples examined, averaging approximately 90 percent quartz, 5 percent feldspar, and 5 percent rock fragments (fig. 17). Distributary-channel sandstones of Ferron GS 5 average approximately 80 percent quartz, 10 percent feldspar, and 10 percent rock fragments. Fluvial sandstones of Ferron GS 4 contain more feldspar minerals than GS 5 sandstones; fluvial sandstones average approximately 65 percent quartz, 20 percent feldspar, and 15 percent rock fragments. The general increase in amount of quartz from fluvial to distributary-channel to transgressive and delta-front sandstones corresponds to an increase in the amount of reworking in the depositional environment. In all sandstones examined, the most abundant lithic components are metamorphic rock fragments and chert. Where abundant, these grains significantly reduce porosity and permeability because they are deformed around more rigid framework grains during burial and compaction.

Intergranular volume (the volume percent of the rock that is occupied by matrix, cement, and void space) does not vary significantly with facies. Mean values are fluvial (23.2 percent), transgressive and delta front (23.6 percent), and distributary channel (23.5 percent). Standard deviation values (1σ) range from 4.4 to 5.8 percent. Intergranular material is predominantly cement, pore space, and pseudomatrix (clay clasts and shale fragments that deform around rigid detrital grains). Delta-front and transgressive sandstones contain little or no pseudomatrix, whereas most distributary-channel sandstones contain relatively little cement (fig. 18). Fluvial
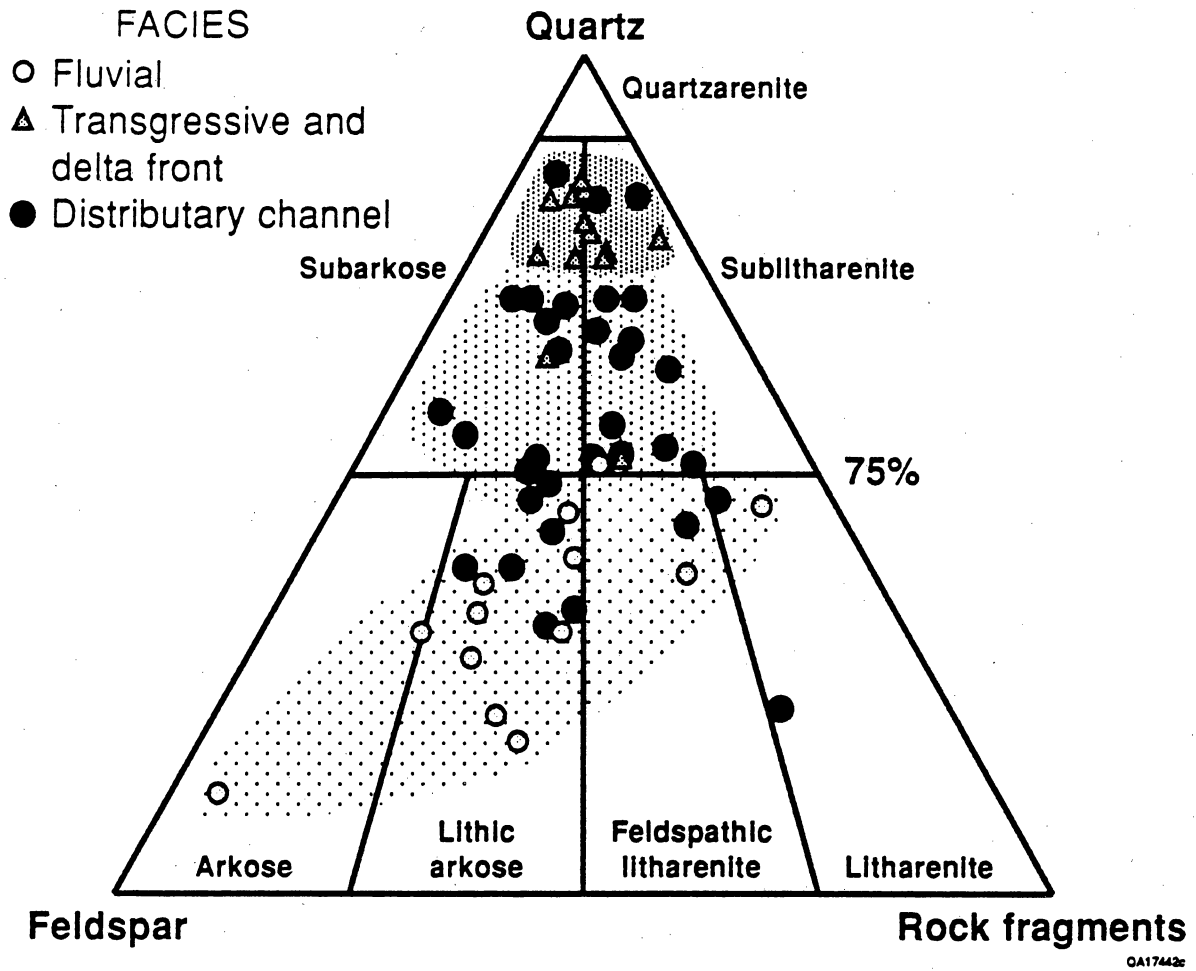
Figure 17. Trilinear plot of Ferron GS 4 and GS 5 sandstone framework grain composition (classification of Folk, 1974).
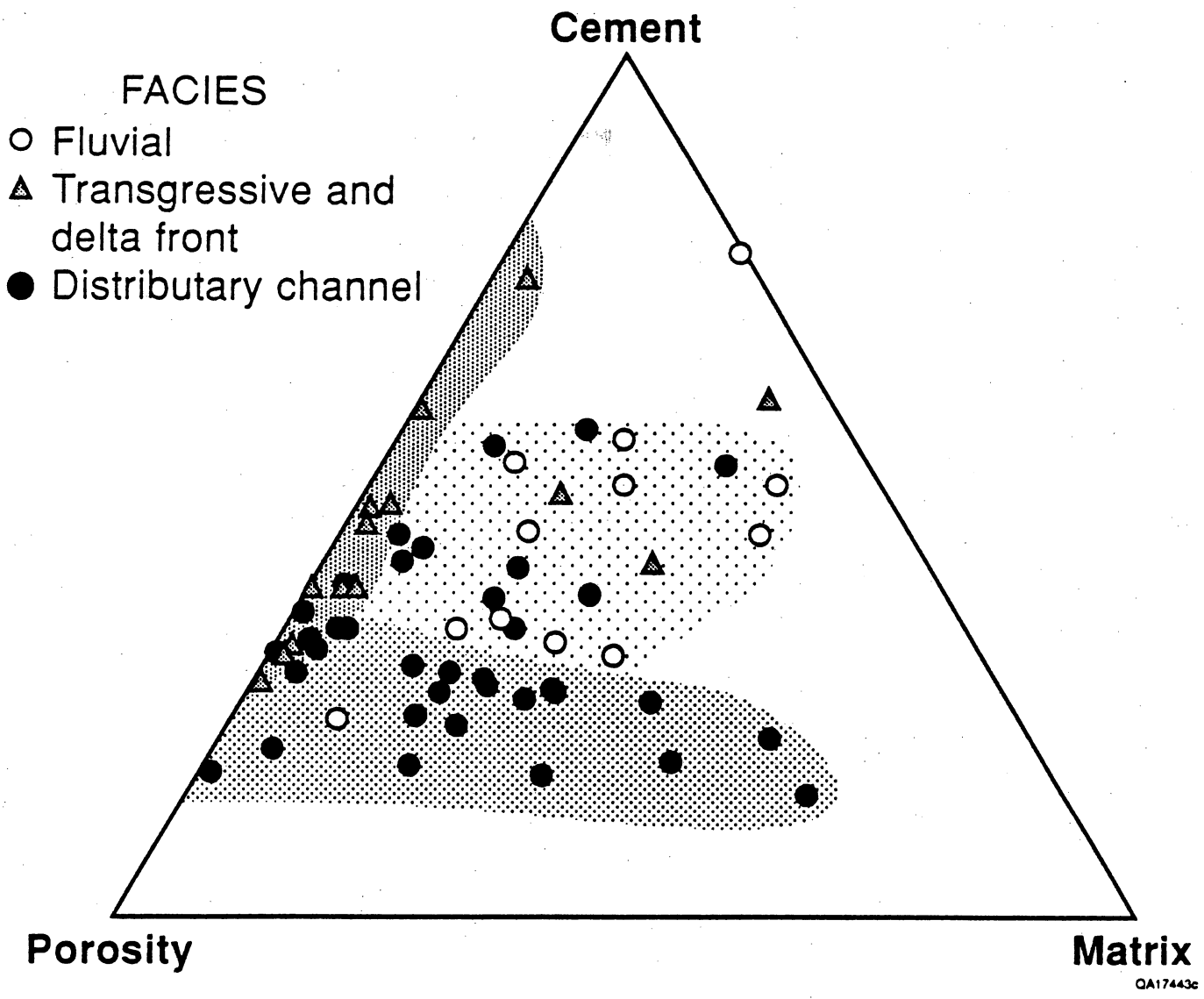
Figure 18. Trilinear plot of cement, matrix, and porosity in Ferron GS 4 and GS 5 sandstones as percentage of total intergranular volume.

sandstones contain approximately equal amounts of cement, pseudomatrix, and pore space. Pseudomatrix affects porosity and permeability in the same manner as rock fragments—compaction during burial squeezes pseudomatrix between rigid framework grains, reducing both porosity and pore-throat dimensions. Most porosity is well-connected intergranular void space. However, microporosity (micron-sized voids within kaolinite cement or leached grains) is common in fluvial sandstones, and isolated pores (secondary porosity within pseudomatrix) are common in distributary sandstones.

Quartz, kaolinite, and carbonate are the volumetrically important authigenic phases in Ferron sandstones. Delta-front and transgressive sandstones typically contain both quartz (about 70 percent of total authigenic material) and carbonate cement (about 30 percent) with only traces of kaolinite (fig. 19). Cements in fluvial sandstones are approximately 75 percent kaolinite, 15 percent carbonate, and 10 percent authigenic quartz. Distributary-channel sandstones contain approximately equal amounts of quartz cement and kaolinite with only minor amounts of carbonate. Carbonate cement is typically associated with pseudomatrix; consequently, carbonate-cemented sandstones generally have low permeability. Likewise, the microporosity associated with kaolinite significantly reduces permeability. Quartz cement rarely fills intergranular pores, and quartz cement has relatively smooth surfaces; therefore, the presence of quartz cement has minimal effect on permeability.

Thin-section porosity differs somewhat with depositional facies. Fluvial sandstones have mean porosity of 6.6 percent (4.2 percent 1σ), transgressive and delta-front sandstones have mean porosity of 10.2 percent (5.2 percent 1σ), and distributary-channel sandstones have mean porosity of 11.8 percent (3.8 percent 1σ).

Grain-Size Analyses

In addition to petrographic examination, samples collected for petrophysical measurements were analyzed for grain-size distribution to assist in understanding the geologic
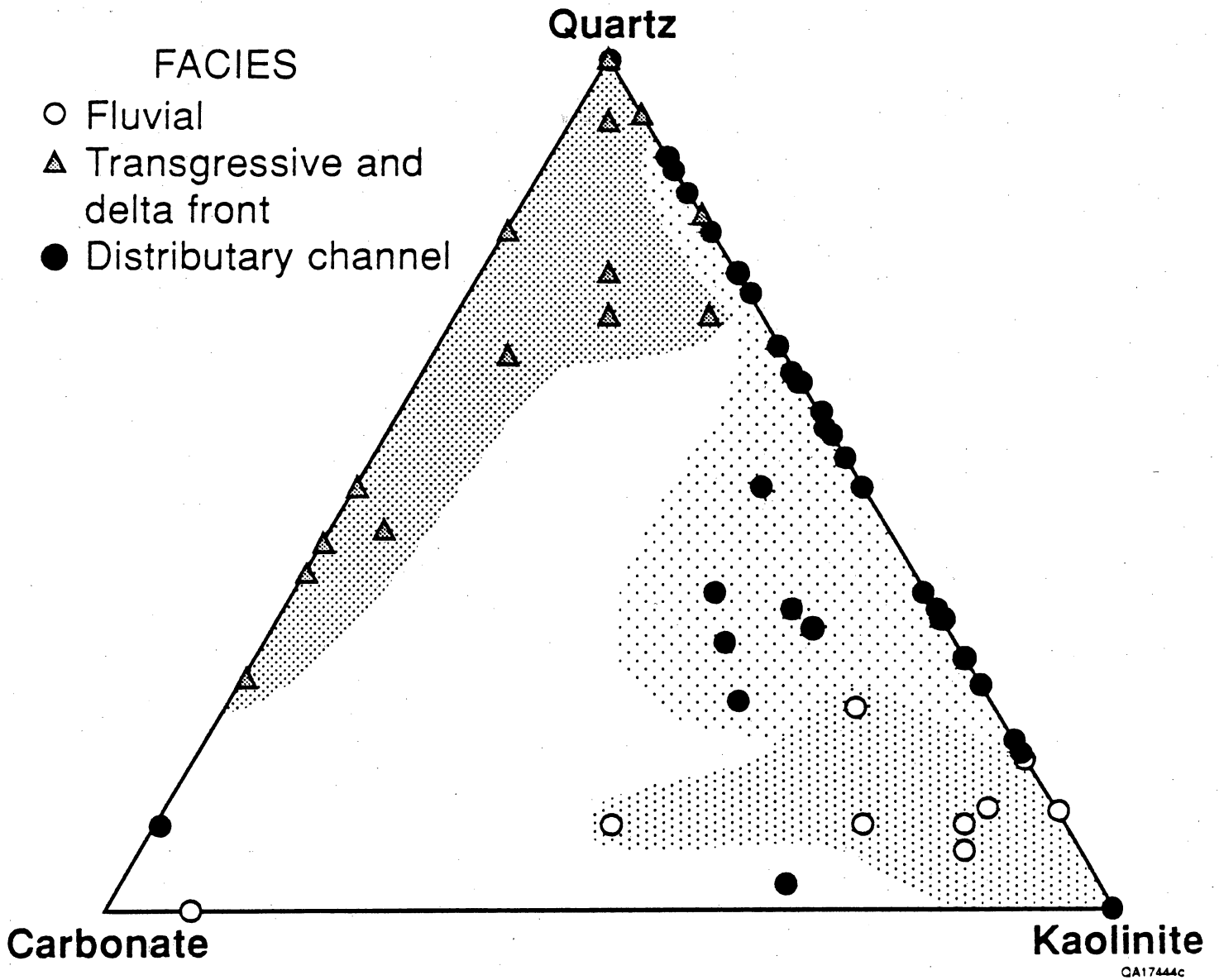
Figure 19. Trilinear plot of cement composition in Ferron GS 4 and GS 5 sandstones as percentage of total authigenic material.

controls on petrophysical properties. Table 3 lists the locations, facies, and lithologic descriptions of these samples. The next section of this report presents the results of petrophysical measurements on this sample set.

Basic textural information (percent sand, silt, and clay) was determined by sieve analysis; sand grain-size distribution was measured by determining settling velocities in distilled water. Results (table 4) show that the major facies range from 75 to 95 percent sand, 4 to 21 percent silt, and 2 to 7 percent clay-sized material. Mean grain size ranges from 3.3 to -0.3 ϕ (very fine to very coarse sand), and sorting ranges from 0.22 to 0.67 ϕ (very well to moderately well sorted).

Summary

The compositional trends exhibited by sandstones in Muddy Creek generally correspond to systematic differences in permeability between facies. Distributary-channel sandstones have the highest mean permeability (337 md) and, except where occluded by pseudomatrix, relatively high porosity compared with matrix and cement (fig. 18), and subequal amounts of kaolinite and quartz cement (fig. 19). Fluvial sandstones have the lowest mean permeability (29 md), subequal amounts of cement, matrix, and porosity (fig. 18), and relatively large amounts of kaolinite cement, which fills intergranular voids and retards fluid flow. Delta-front and transgressive sandstones have intermediate values of mean permeability (54 and 129 md, respectively), small amounts of pseudomatrix (fig. 18), and predominantly quartz cement, which results in smooth grain surfaces and little resistance to fluid flow.

Table 3. Descriptions of block samples collected for petrophysical property measurements. GS: Genetic Sequence number.

Set	Block	GS	Location	Facies	Characteristics
1	6	5	Muddy Creek	Transgressive	Highly bioturbated
2	1	5	Muddy Creek	Distributary channel	Top of contorted zone
2	2	5	Muddy Creek	Distributary channel	Horizontally laminated
2	3	5	Muddy Creek	Distributary channel	Base of channel, trough crossbedded
2	4	5	Muddy Creek	Delta front	Top of delta front
2	5	5	Muddy Creek	Distributary channel	Planar crossbedded
2	6	4	Muddy Creek	Fluvial	Top of channel
2	7	4	Muddy Creek	Fluvial	Base of channel
2	8	4	Muddy Creek	Fluvial	Indistinct bedding
2	9	5	Muddy Creek	Distributary channel	Base of channel
2	10	4	Muddy Creek	Fluvial	Top of fluvial facies
2	11	5	Muddy Creek	Distributary channel	Upper channel, planar crossbedded
2	12	5	Muddy Creek	Distributary channel	Small-scale trough crossbedded, lateral accretion point-bar deposit
2	13	5	Muddy Creek	Distributary channel	Lower channel, lateral accretion deposit
3	1	5	Picture Flats	Levee deposit	Horizontally laminated
3	2	5	Picture Flats	Delta front	Base of deposit
3	3	5	Picture Flats	Delta front	Top of delta front
3	4	5	Picture Flats	Distributary channel	Massive bedding
3	5	5	Picture Flats	Distributary channel	Top of channel, horizontally bedded
3	6	5	Picture Flats	Distributary channel	Base of channel, mud-clast-rich
3	7	5	Picture Flats	Distributary channel	Small scale trough crossbedded, lateral accretion deposit
3	8	5	Picture Flats	Distributary channel	Levee/crevasse splay deposit
3	9	5	Picture Flats	Distributary channel	Mouth-bar deposit
4	2	5	Muddy Creek	Distributary channel	Base of channel, ripple-laminated

Table 4. Results of grain-size distribution analysis of sandstone blocks collected for petrophysical measurements. Percent sand, silt, and clay were determined from sieve analyses. Mean, standard deviation, skewness, and kurtosis values are graphic moments (Folk, 1974). Pairs of samples labeled a and b for the 3-series of blocks are repeat analyses using different subsamples of the disaggregated sandstone. Comparison of results shows that moments are reproducible to within 0.1 phi unit in all cases (na indicates no material for analysis).

Sample	% Sand	% Silt	% Clay	Mean	Sorting	Skewness	Kurtosis
2-1	85	11	4	2.68	0.47	0.03	0.83
2-2	82	16	2	2.78	0.44	-0.24	0.92
2-3	86	10	4	2.27	0.38	0.46	1.07
2-4	90	8	2	2.96	0.30	0.03	1.23
2-5	81	14	5	2.49	0.26	0.09	1.16
2-6	84	14	2	2.19	0.36	0.22	1.16
2-7	90	7	3	-0.29	0.53	0.03	1.09
2-8	78	15	7	2.03	0.42	0.04	1.38
2-9	85	13	2	1.18	0.47	-0.01	0.97
2-10	75	21	4	2.51	0.36	0.00	0.91
2-11	84	13	3	1.52	0.47	0.01	1.02
2-12	84	11	5	2.40	0.33	0.10	1.00
2-13	90	8	2	1.64	0.42	0.00	0.94
3-1a	77	16	7	2.65	0.34	0.00	1.18
3-1b	77	16	7	2.71	0.31	-0.03	1.14
3-2a	95	4	1	1.76	0.34	-0.08	1.32
3-2b	95	4	1	1.76	0.30	-0.02	1.09
3-3a	84	14	2	3.28	0.19	0.13	0.95
3-3b	84	14	2	3.32	0.23	0.03	1.04
3-4a	87	7	6	1.20	0.46	-0.07	0.98
3-4b	87	7	6	1.23	0.40	-0.04	0.96
3-5a	87	8	5	2.99	0.21	-0.04	1.33
3-5b	87	8	5	3.01	0.23	0.01	1.29
3-6a	90	8	2	2.56	0.39	-0.10	1.07
3-6b	90	8	2	2.47	0.39	-0.09	1.02
3-7a	90	7	3	2.82	0.23	-0.13	1.32
3-7b	90	7	3	2.83	0.25	-0.22	1.12
3-8a	84	14	2	3.01	0.26	0.13	1.22
3-8b	84	14	2	na	na	na	na
3-9a	92	6	2	1.61	0.47	-0.09	0.98
3-9b	92	6	2	1.57	0.62	0.13	1.06

LABORATORY PETROPHYSICAL PROPERTY MEASUREMENTS

Introduction

Laboratory measurement system design and two-phase-flow test procedures developed during the first program year and the initial part of the current year have been fully implemented. Some modifications to the system described in the FY 1990 Annual Report (Tyler and others, 1991) were carried out, and the final configuration of the laboratory system is described in appendix A. The standardized sequence of petrophysical property measurements, which includes simultaneous air and gas permeability, electrical resistivity (formation factor), and P- and S-wave velocity measurements during two-phase flow of brine and nitrogen through the specimen, is also described in appendix A. System calibrations and several system performance tests are also included.

Program activity during FY 1991 focused on the measurements of petrophysical properties of representative samples of flow and baffle material from the Ferron. These simultaneous laboratory measurements of coupled petrophysical properties provide the data base for the calibration, validation, and fine tuning of pore-level network models that will be used to link pore structure—and hence the geologic controls—to petrophysical properties. The laboratory data are measured under effective reservoir conditions and are therefore of use in general in reservoir characterization, and, specifically, in correlating small-scale air permeability measurements made with a minipermeameter to appropriate relative gas permeabilities in the reservoir.

Twenty-two blocks of outcrop material from Ferron units GS 2, GS 4, and GS 5 were tested during 1991. Representative samples of distributary-channel, fluvial, levee deposit, and delta-front facies were included in this sampling; almost half of these samples were distributary-channel facies. Complete suites of petrophysical property measurements during two-phase-flow test sequences have been carried out on 28 specimens cored from these blocks. One block, from the base of a lower fluvial facies, disintegrated during coring, and no specimen was

recovered. Two specimens each, with mutually perpendicular axes, were cored from three blocks of material in which shale laminations were evident, to assess anisotropic behavior. Twenty-four of these tests were successful. In addition, one specimen of Berea sandstone was prepared from in-house material and tested for system performance documentation.

Thin-section specimens were prepared from material taken immediately adjacent to the two-phase-flow specimens. Minipermeameter measurements were carried out on 15 of the same test specimens used in the laboratory measurements. Benchtop brine permeability measurements were carried out on five of the same test specimens used for the two-phase-flow measurements and on one set of mutually perpendicular 1-inch-diameter plugs taken immediately adjacent to the 2-inch-diameter laboratory test specimens. Capillary pressure curves, measured on 1-inch-diameter plugs from within each of the 2-inch-diameter laboratory test specimens, are planned for FY 1992.

The laboratory measurements will continue into early summer of FY 1992. Twenty-five samples have been cored directly from outcrops of units GS 2 and GS 5 with the new portable coring tool. Test specimens have been prepared directly from these samples. Testing of 21 of these samples has been completed. Twenty-eight specimens are being prepared from large-diameter core material obtained by the University of Utah Research Institute, and testing of these specimens is under way.

Results

Results for the measured pore fluid storage and fluid and electrical transport properties in the Ferron specimens tested during FY 1991 are summarized in table 5; plots of permeability and formation factor variations with brine saturation are given in appendix A. The specimen listing in table 5 is subdivided into five major categories corresponding to major depositional facies. The outcrop locations and the stratigraphic units within the outcrops from which the samples were taken are also designated. The set number refers to the four sampling groups.

46

Table 5. Summary of fluid storage and transport properties from laboratory measurements during gas and/or brine flow.

Spec. #	Facies	Porosity %	k(air) md	k(brine) md	Formation Factor	Sat. Expon.	Swi %	Sgr %	kgr(Swi)	kwr(Sgr)
DISTRIBUTARY CHANNEL										
Muddy Creek Unit 5 (Set 2):										
1	Top Cont. Zone	17.3	0.8	0.5	13.5	2.3	46	40	0.33	0.07
2	Horiz. Lam.	13.0	1.9	0.8	19.5	1.5	39	22	0.49	0.05
3	Trough X-Bed	16.0	11.2	3.8	20.9	1.5	56	30	0.32	0.10
5	Planar X-Bed	21.0	115.0	43.0	11.1	2.0	55	5	0.45	0.45
9	Base of Chan.	18.1	79.0	47.0	16.3	1.5	47	30	0.19	0.12
11	Upper D.C.	17.7	16.0	8.0	15.1	2.0	50	20	0.70	0.13
12	Point Bar	16.0	12.8	5.3	14.1	1.5	60	10	0.99	0.03
13	Lower Chan.	18.0	68.0	31.1	16.2	1.5	54	23	0.17	0.15
Pictured Flats (Set 3):										
Unit 5										
4	Massive SS	15.4	16.0	10.2	11.6	3.0	58	20	0.28	0.05
5	Top of D.C.	16.3	69.3	33.9	15.8	1.6	44	30	0.47	0.05
6	D.C. Base, mud clasts	18.0	85.0	22.0	19.9	2.8	55	11	0.76	0.54
7	Sm. Scale Trough X-Bed.	18.0	217.0	54.0	13.4	1.8	45	21	0.40	0.10
8	Levee/Crevass Splay	14.3	42.4	34.1	18.4	1.5	41	13	0.38	0.08
Unit 2										
9	Mouth Bar	16.8	153.0	87.9	13.0	2.5	52	26	0.73	0.15
FLUVIAL DEPOSITION										
Muddy Creek Unit 4 (Set 2):										
6	Lower, Top of Channel	15.1	1.5	0.9	15.8	1.5	39	26	0.38	0.05
8	Fluvial	15.0	2.3	1.1	18.8	1.7	45	15	0.52	0.06
LEVEE DEPOSIT										
Pictured Flats Unit 4 (Set 3):										
1	Along Laminations	12.7	7.3	3.5	25.6	1.8	45	18	0.69	0.11
"	Across Laminations	14.0	0.1	0.0	35.5	1.2	31	25	0.23	0.14
RIPPLE LAMINATED										
Muddy Creek Unit 2 (Set 4):										
2	Along Laminations	16.0	12.3	3.5	14.2	1.7	49	10	0.90	0.07
"	Across Laminations	16.0	0.4	0.1	19.4	1.1	24	29	0.55	0.16
DELTA FRONT										
Muddy Creek Unit 5 (Set 1):										
6	Bioturbated	12.5	20.4	4.5	29.3	1.3	44	14	0.54	0.2
Pictured Flats Unit 5 (Set 3):										
2	Delta Front	12.5	0.1	0.1	20.7	2.0	35	11	0.49	0.1
3	Top of Shore Face	17.6	35.8	31.4	15.6	1.6	36	29	0.3	0.02
REFERENCE										
	Berea Sandstone	25	450	260	10.0	2.0	47	8	0.31	0.11

Set 1 is the original sample set, from which the brine-saturated specimens discussed in the FY 1990 Annual Report were taken. Sets 2 and 3 are blocks retrieved on the December 1990 field trip to the Muddy Creek and Picture Flats outcrops, respectively. The Set 4 sample is a block of ripple-laminated material taken from Muddy Creek as representative of a highly anisotropic material. The specimen numbers listed within the four sets are arbitrary designations used to catalog the data. Berea sandstone is a widely tested material, and data for this sample are included for reference. From visual evidence, this particular block of Berea has a relatively high clay content.

The formation factors listed in the tabulation refer to the brine-saturated specimens. Absolute permeabilities are listed for both the brine- and nitrogen-saturated specimens because the presence of moisture-sensitive clays in the pores of these shaly sandstones leads to systematically lower values for the brine flow than for gas flow. This clay-related alteration in permeability is not expected to vary after the specimen is saturated with brine and all relative permeability values are normalized to the brine-saturated permeabilities. The values for S_{wi}, the brine saturation at the irreducible water condition established by the flow of gas only, S_{gr}, the gas saturation at the residual gas condition established by the flow of brine only, and the corresponding values of the relative gas and brine permeabilities at irreducible water and residual gas, respectively, are also included in table 5.

Results of the minipermeameter measurements carried out on 15 of the same test specimens used for the table 5 measurements are compared with values determined from the laboratory measurements of gas-saturated specimens in figure 20. The values are plotted as a line graph of progressively larger permeability values versus sample name. The relative trends in the larger scale laboratory permeability measurements are accurately mimicked in minipermeameter permeabilities. However, the gas permeabilities determined with the minipermeameter do appear to be systematically larger than the laboratory gas permeability values. The minipermeameter readings were all taken on the unpressurized specimens prior to the laboratory measurements at simulated reservoir pressure, and the observed difference in
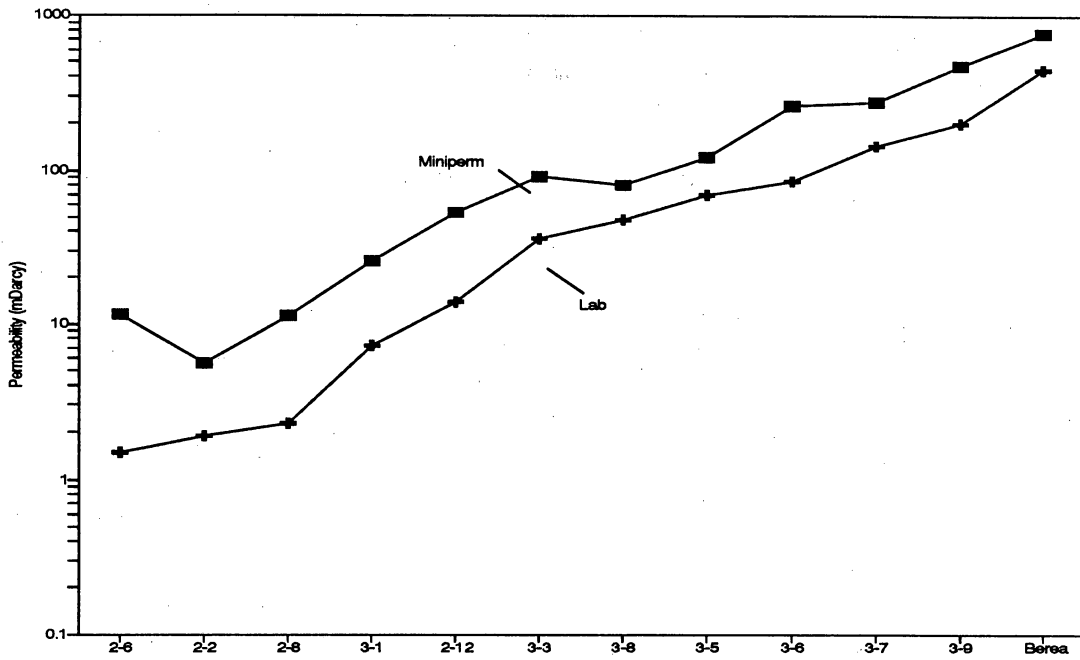
Figure 20. Comparison of laboratory and minipermeameter measurements of gas permeabilities carried out on the same specimens. The sample designations on the X-axis are the set/block numbers used in tables 3 and 5. Laboratory measurements are performed at an effective pressure of 5,000 psi.

magnitudes is probably due to compaction of these outcrop specimens during the initial labora-

tory measurement step. This conclusion is supported by a sequence of measurements carried

out on one of the specimens as a function of effective pressure, beginning with a previously

unpressurized specimen, in which progressively decreasing permeability values were observed

following the pressurization of the specimen. This test and the measurement results are dis-

cussed in appendix A.

The shear and compressional mode wave velocities measured simultaneously with the

formation factor and permeability measurements, the dynamic moduli determined from these

measurements, and their relationship to the static moduli measured during the laboratory tests

are also sensitive to pore geometry and the nature of the pore fluid. However, these data are

not being treated in the network models, and a detailed discussion of their behavior is not

included in this report. The measurement results and a limited discussion of their behavior are

included in appendix A.

PETROPHYSICAL PROPERTY TRANSFORMS AND SCALE-UP

Introduction

One of the major goals of the Ferron research project is to develop transformations

between the information that is being gathered on the outcrop (chiefly depositional

environment and air permeability) and other petrophysical properties. Because we can only

accomplish approximately 50 suites of petrophysical property measurements in the course of

this project, we planned to develop a theoretical framework within which to place our

developed transforms so that the transforms might have some general applicability. Our original

plan was to use a pore network model for this purpose. Our hypothesis was that petrographic

information being developed by the Bureau of Economic Geology could be used to link outcrop

50

permeability measurements to the petrophysical measurements through the pore network model.

This chapter describes work that was accomplished on the pore network model in 1991. Although we now believe the model to be working properly, problems in the development of the model will not allow us sufficient time to fully explore the representations of pore-level flow and pore descriptions that would have been applied to fluvial-deltaic rocks such as those we are investigating in the Ferron. Accordingly, we are proposing an alternative approach for the completion of this project that we think will provide useful insights into appropriate transformations that can be used in a predictive manner for fluvial-deltaic rocks. Details of the planned work for completion of this project are presented in the final chapter of this report.

In the following sections we describe work that was accomplished with the pore network model in 1991. We plan to continue this work with non-GRI funding and will report any results that have bearing on the Ferron study. Most of this work was accomplished by a Ph.D. student (C. Phillips) who received no GRI support.

Pore Network Model

During the past calendar year, the pore network model has been improved through the addition of a few new features, the recoding of some sections using improved algorithms, and the removal of a few errors. Most of the impetus for these improvements was the necessity to better simulate relative permeability curves.

The choices in the simulator from previous work include a network of pore bodies arranged using a three-dimensional simple cubic pattern with nearest neighbors connected by throats. Impermeable boundary conditions were used. Bodies were represented as equivalent spheres and throats as equivalent cylinders. Beta distributions were used for the size distributions. Choices in the representation of fluid-flow physics were that the phases do not mix, that is, that only one phase may be present in a pore at a given time, and that there is no

flow resistance in the bodies. Because the flow is pseudostatic, capillary forces dominate viscous forces and invasion follows pore sizes. Only one trapping rule was available in the simulator. An accessible pore was invaded only if the displaced phase was continuous to an exit face. The properties that the simulator calculated were porosity, absolute and relative permeability, capillary pressure, formation factor, and resistivity index. Of course, rules for calculating each were present in the model. Only drainage was available.

It should be mentioned that the choices implemented in the simulator were made for essentially two reasons. First, all of the choices had been previously used by other researchers (Lin and Slattery, 1982; Mohanty and Salter, 1982; Blunt and King, 1991). This is in keeping with our intention not to develop a completely new model but to use the choices of others to achieve our goal of building a simulator capable of simultaneously matching actual data for multiple petrophysical properties. Second, all of the choices used are simplifying representations when compared with the complex reality of fluid flow in actual permeable media. Indeed, a guiding hypothesis of this research is that the actual complexities can be substituted with simple representations that are able to replicate core data.

In the previous work, only one apparent problem had been noted. This problem was that the nonwetting-phase relative permeability curve was essentially zero at all saturations. Although our efforts at resolving this problem led to improvements in the model, we discuss later in this report that this behavior was correct, given the physical representations and pore-size distributions we were using.

The current model can, given input data such as pore-throat and body-size distributions, correctly calculate porosity, single-phase permeability, formation factor, resistivity index, and the capillary pressure curve using the formulas present in the model. This is not to imply that a rock identical to that specified to the simulator would exhibit the same values of properties as those of the simulator, only that the model formulas are correctly evaluated by the simulator. Periodic boundary conditions are now implemented, and uniform, log-uniform, and single-valued distributions are available. Two trapping rules have been added. An accessible pore may

be unconditionally invaded (no trapping), it may be invaded only if the displaced phase is continuous to an exit face (full trapping), or a combination of the previous two rules may be used: no trapping for throats and full trapping for bodies (partial trapping).

The porosity and single-phase permeability calculations have been verified using a previously published model. Also, if all of the throats are of the same size (as for single-sized pores), the absolute permeability can be found analytically. As expected, the model results agreed with the analytical result.

The classic paper by Kirkpatrick (1973) on percolation gives results using a three-dimensional network model simulator with a cubic lattice network of pore bodies connected by pore throats of equal conductivity. Starting with all of the bonds conducting (100 percent phase saturation), the conductivity (phase permeability) is calculated as bonds are randomly removed (throats are invaded by a second phase). There is one major difference in Kirkpatrick's simulator and ours: the invasion in the bond percolation problem is completely random. The invasion process in our simulator was temporarily altered to emulate Kirkpatrick's. The altered simulator's results matched Kirkpatrick's results well (fig. 21). A 25 × 12 × 12 network with impervious boundary conditions was used for the match. The conductivity decreases linearly until approximately 50 percent of the bonds are still in place and eventually reaches zero when about 25 percent are still in place.

After the network appeared to be functioning correctly, we added some features to see how the results could be changed. First, "periodic boundary" conditions were implemented. In the initial coding, they had been put in place but never tested. Making them work required two steps. First, the connectivity had to be verified. Second, all the functions that dealt with setting up, modifying, and solving the system of equations had to be changed because the throats on the periodic boundary were now connected to bodies whose difference in body number was potentially different from those in the previous arrangement. Basically, this required adding four diagonals to the matrix. The periodic boundary conditions did not make
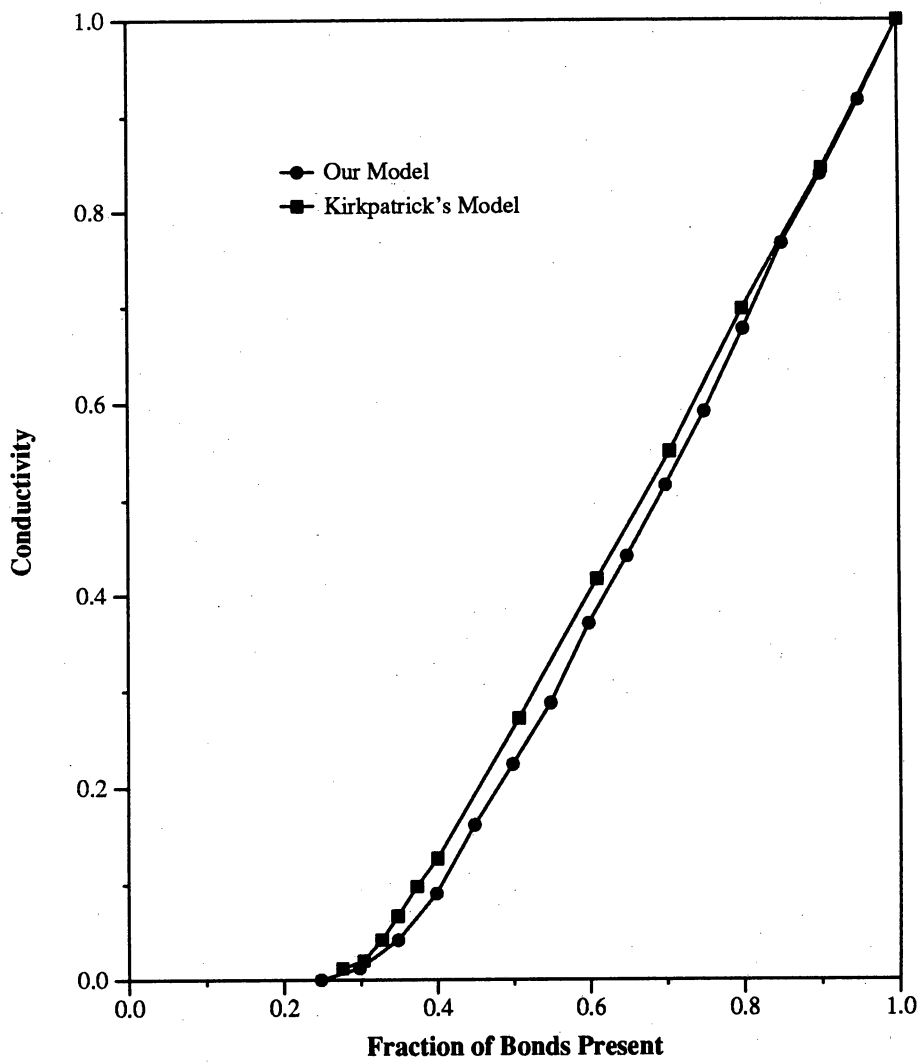
Figure 21. Match of our model's results using random invasion with Kirkpatrick's (1973) results.

much difference in the results, although they are thought to better account for the fact that the network is finite.

Another feature that was added was to ignore trapping. This has some validity in that the wetting phase is believed to be able to escape through thin films that connect pores (Mohanty and Salter, 1982). This did improve the relative permeability; although the nonwetting-phase curve was still too low, it increased markedly up to 1 at low wetting-phase saturations.

Routines were written that examined the fluid and pressure distributions in "slices" perpendicular to the macroscopic flow direction along the network. These showed not only that mass rates were equal for each slice, as required, but that the invading phase saturation decreased from the inlet to the outlet. Thinking that accessibility may be a problem, we added the ability to initially invade from both the inlet and the outlet simultaneously and to initially invade from all six faces simultaneously.

Upon examination of the number of throats in the direction of macroscopic flow and the number of bodies that were filled with the invading phase using the no-trapping case, we found that the number of bodies with invading phase for a given slice rose much faster than the corresponding number of throats. One of our basic model assumptions has been that the pore bodies control volume properties (saturation) and the pore throats control flow properties (permeability). These slice results bore out our assumption: relatively fewer invaded throats meant low permeability, and relatively more invaded bodies meant high saturation. This was well demonstrated in our relative permeability curves. As a test, two options were added whereby the pore volume could be placed entirely in either the throats or the bodies. Twelve figures (figs. 22 through 33) were constructed showing the various tests made to determine what assumptions gave relative permeability curves that appeared more typical. The differences are (a) whether trapping is in effect, (b) whether the boundary conditions are impermeable or periodic, and (c) through which faces invasion is allowed (inlet, inlet and outlet, or all six faces). On each figure, three sets of curves are shown, one where the volume is
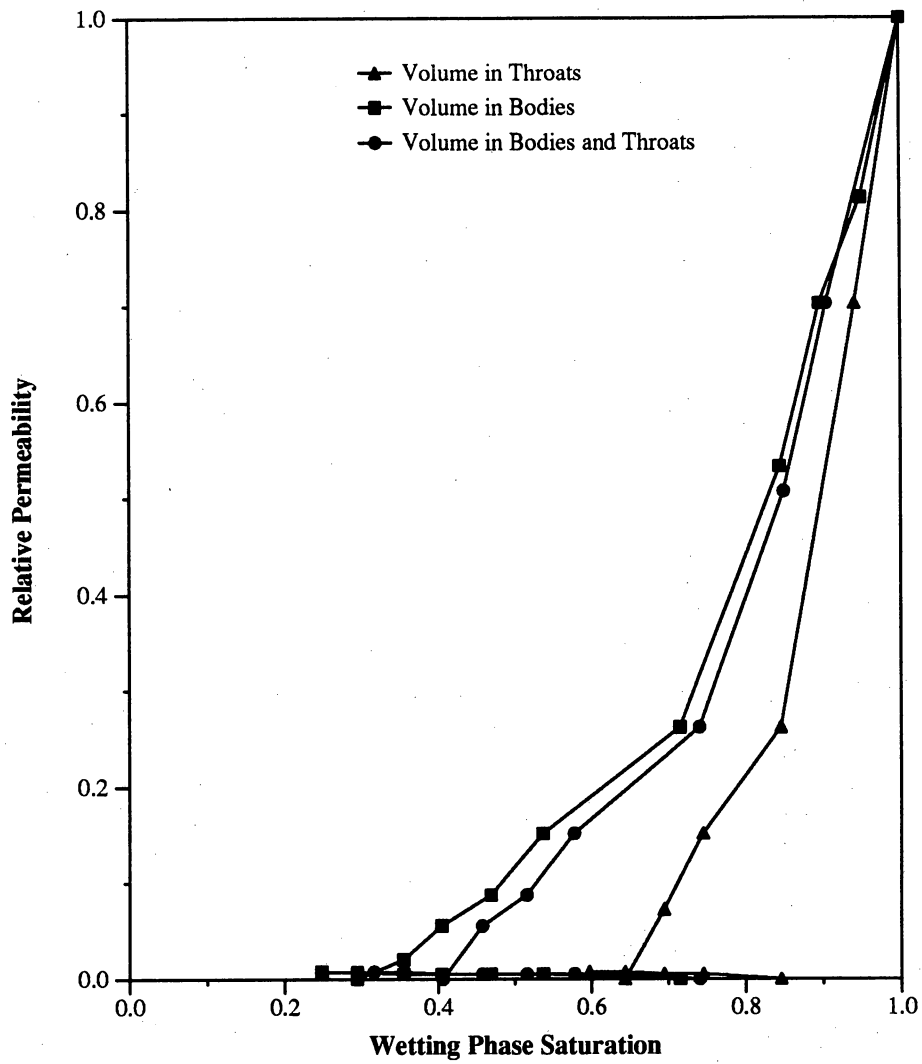
Figure 22. Relative permeability curves using a 25 × 12 × 12 network with trapping, impermeable boundary conditions, and invasion through the inlet face.
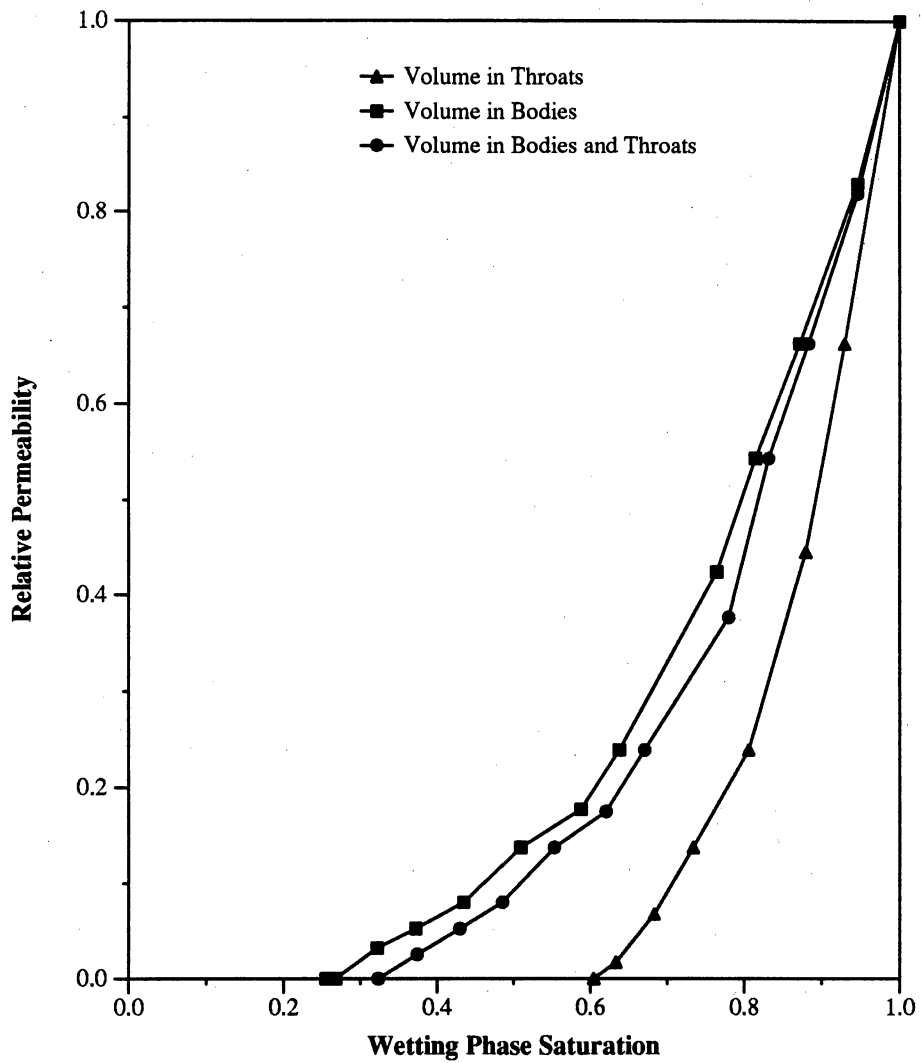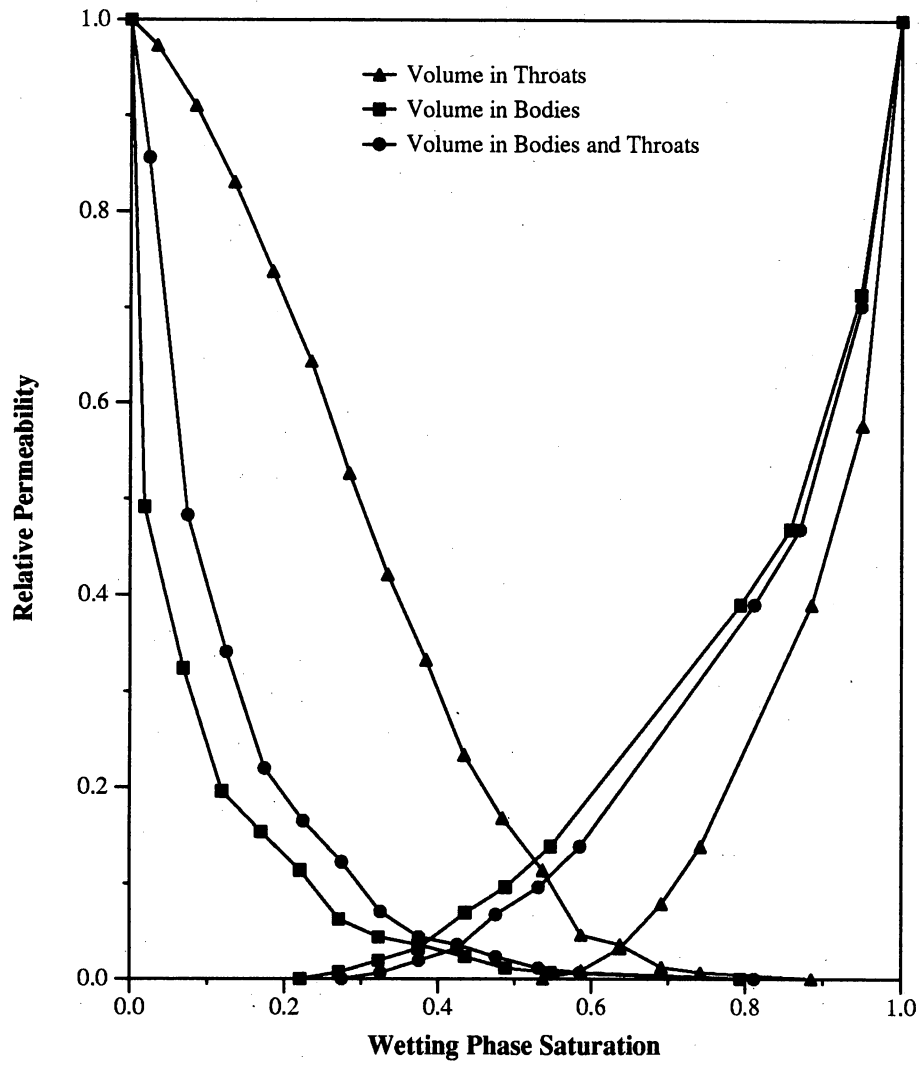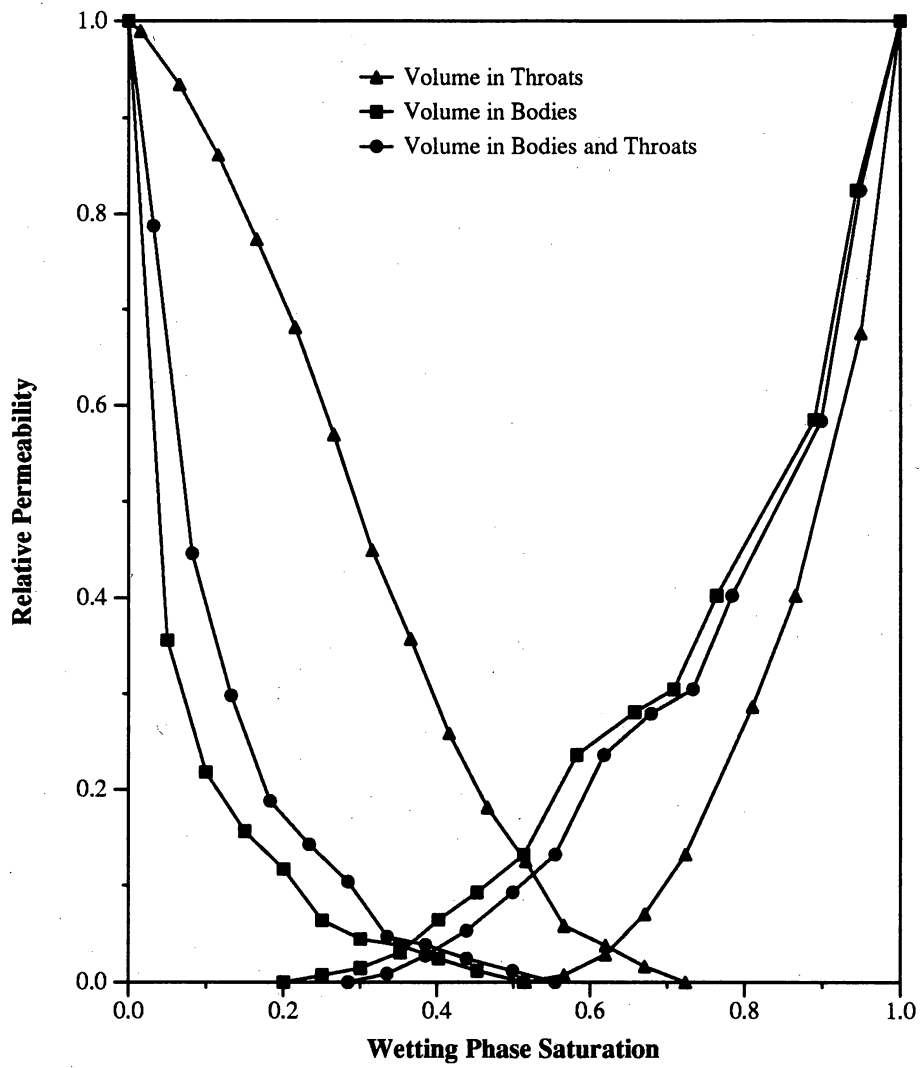
Figure 23. Relative permeability curves using a 25 × 12 × 12 network with trapping, impermeable boundary conditions, and invasion through the inlet and outlet faces.
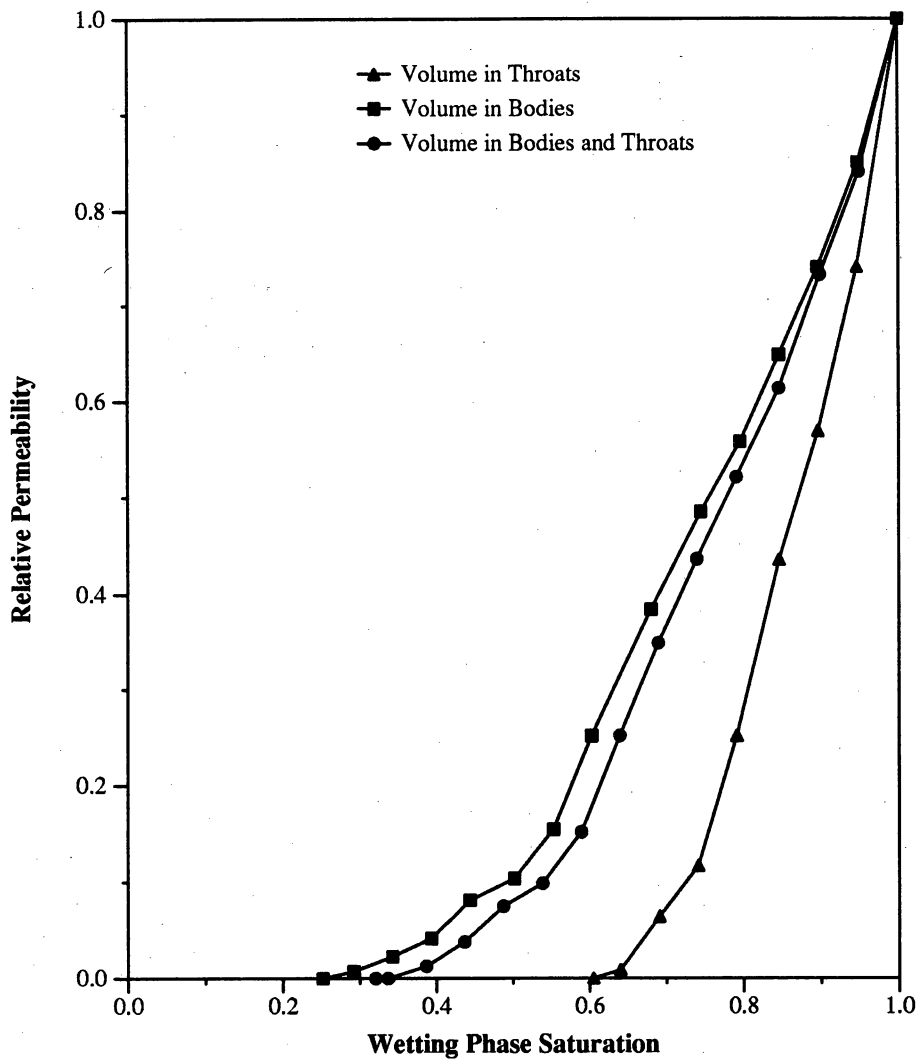
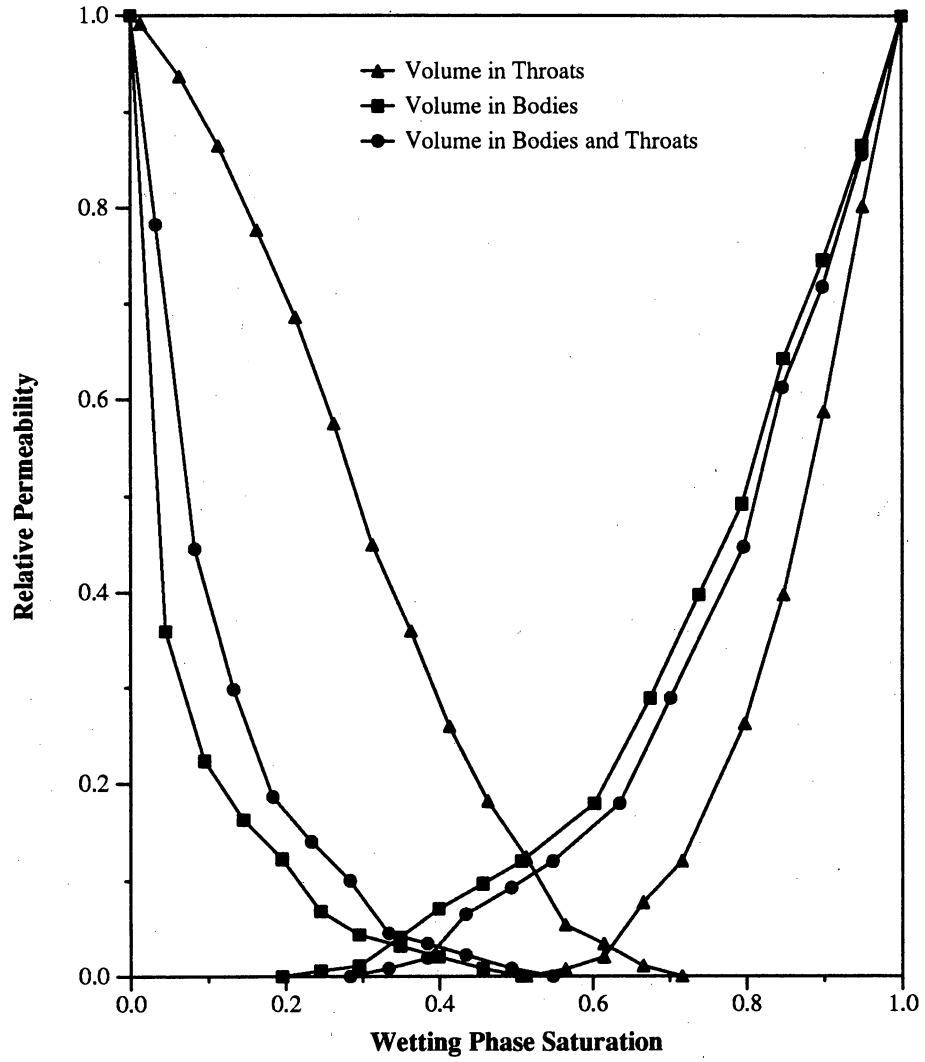Figure 24. Relative permeability curves using a 25 × 12 × 12 network with trapping, impermeable boundary conditions, and invasion through all six faces.
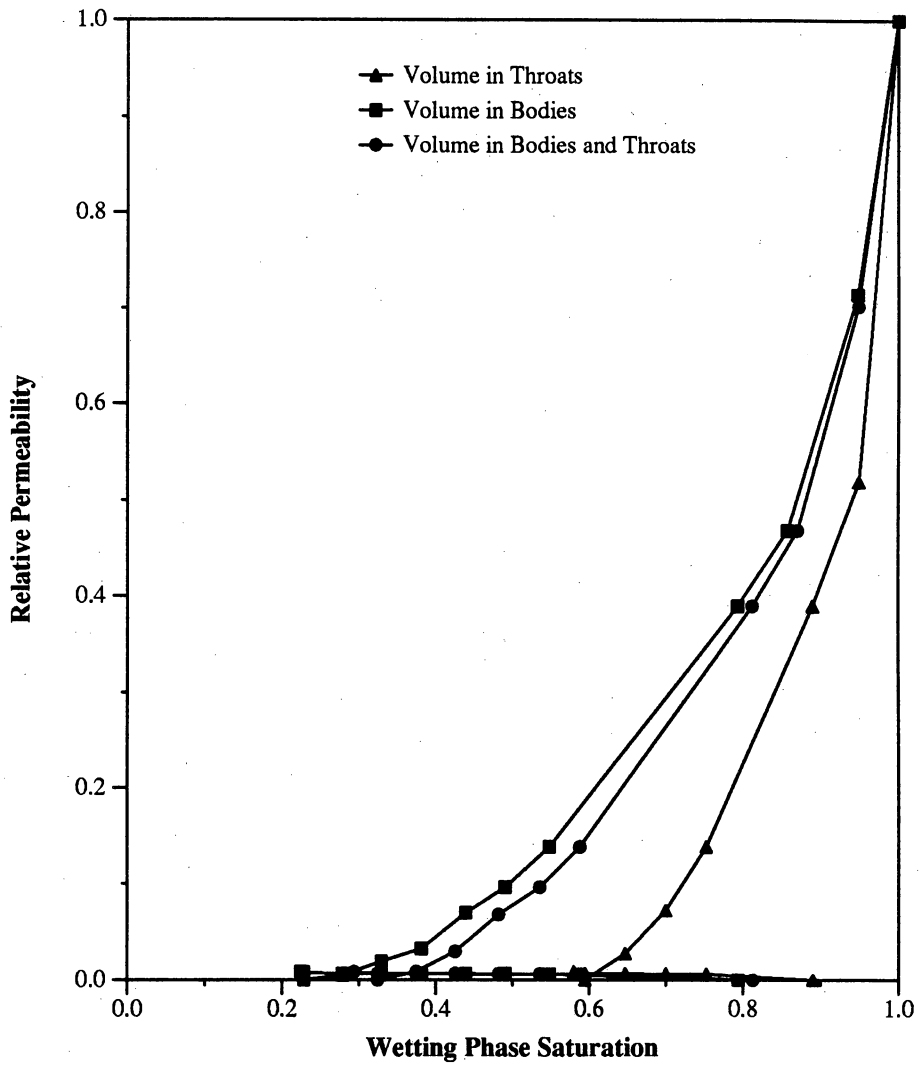
Figure 25. Relative permeability curves using a 25 × 12 × 12 network with trapping, periodic boundary conditions, and invasion through the inlet face.
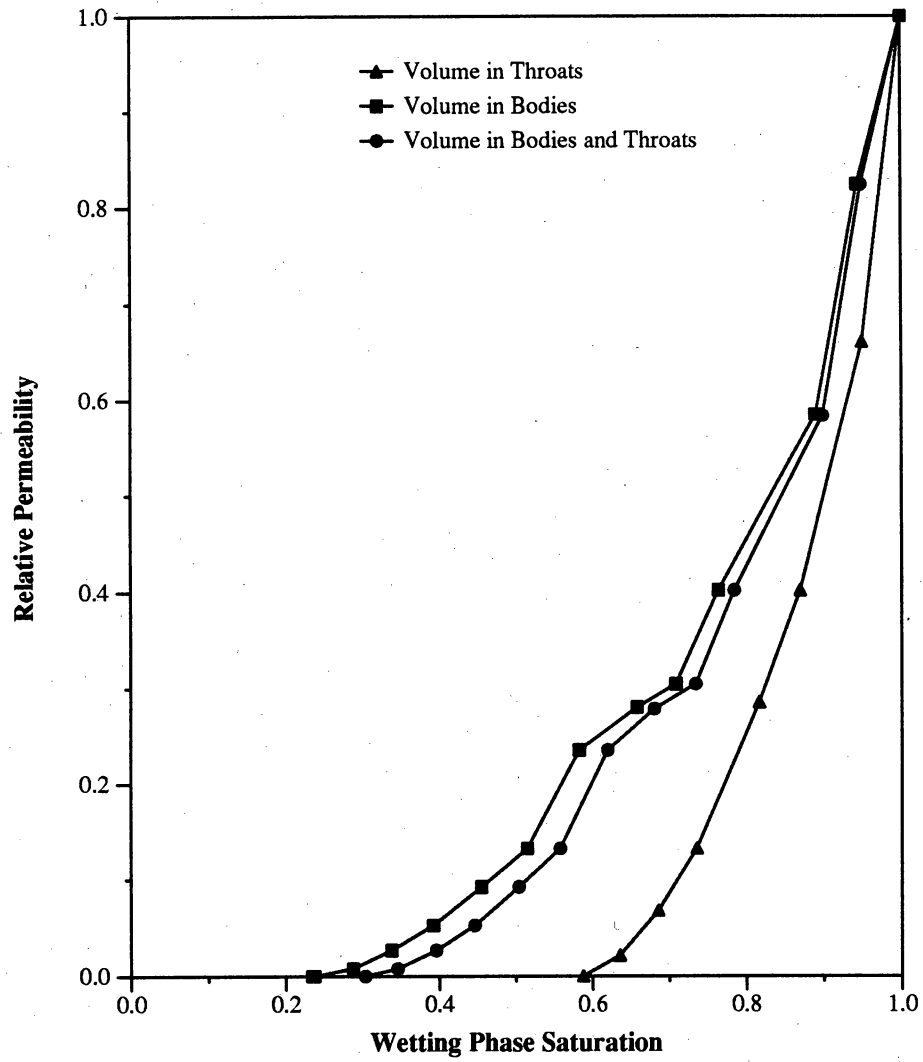
Figure 26. Relative permeability curves using a 25 × 12 × 12 network with trapping, periodic boundary conditions, and invasion through the inlet and outlet faces.
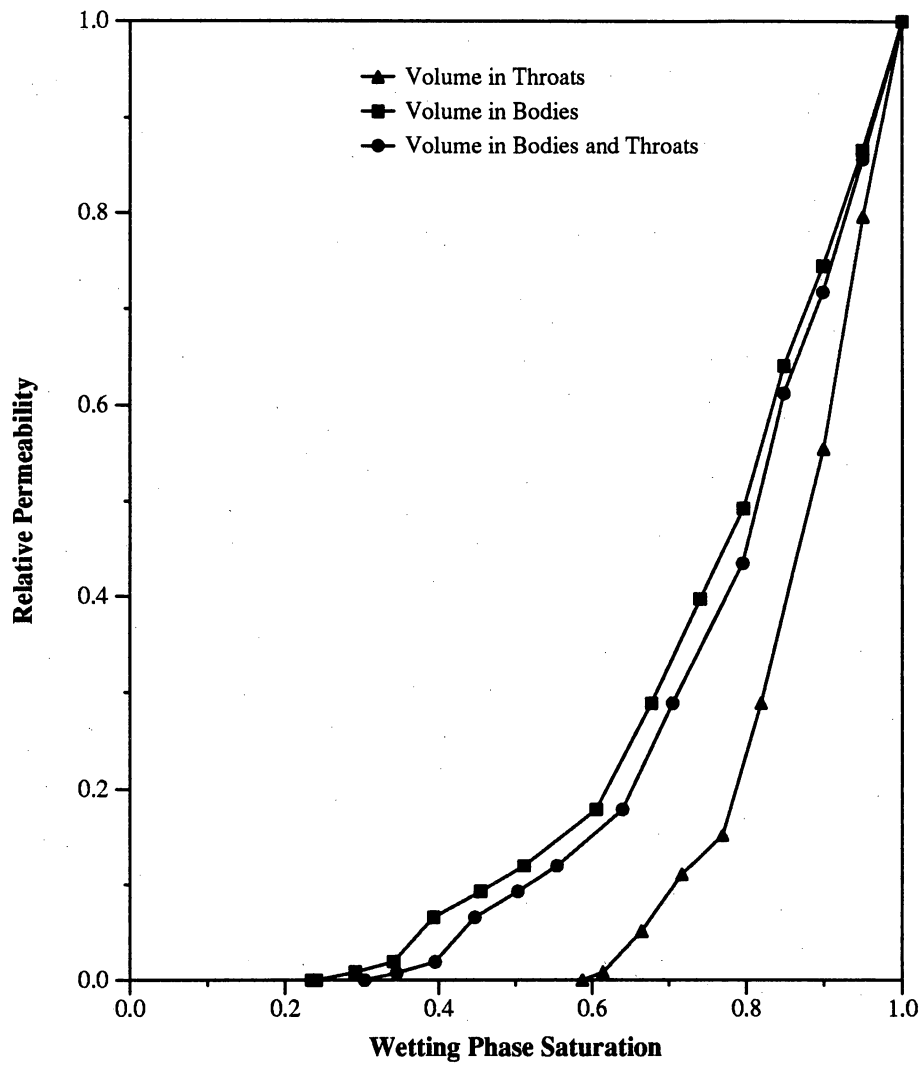
Figure 27. Relative permeability curves using a 25 × 12 × 12 network with trapping, periodic boundary conditions, and invasion through all six faces.
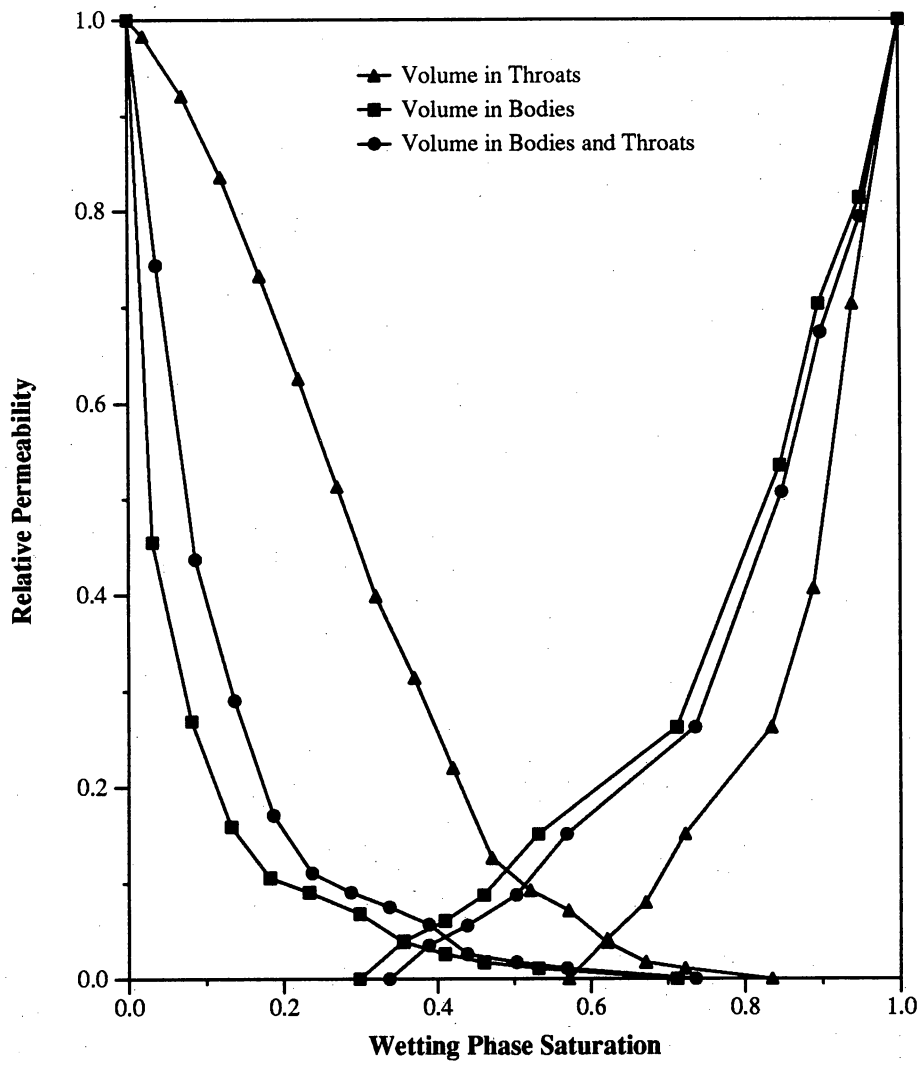
Figure 28. Relative permeability curves using a 25 × 12 × 12 network with no trapping, impermeable boundary conditions, and invasion through the inlet face.
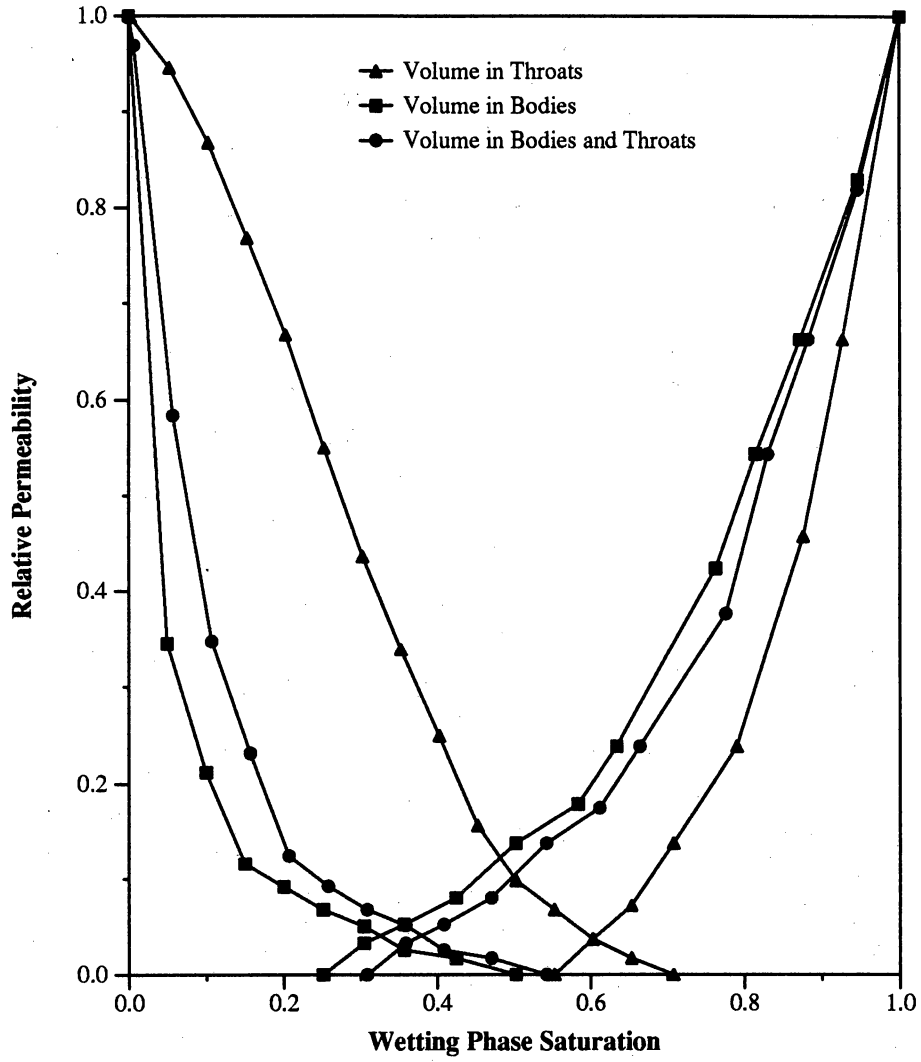
Figure 29. Relative permeability curves using a 25 × 12 × 12 network with no trapping, impermeable boundary conditions, and invasion through the inlet and outlet faces.
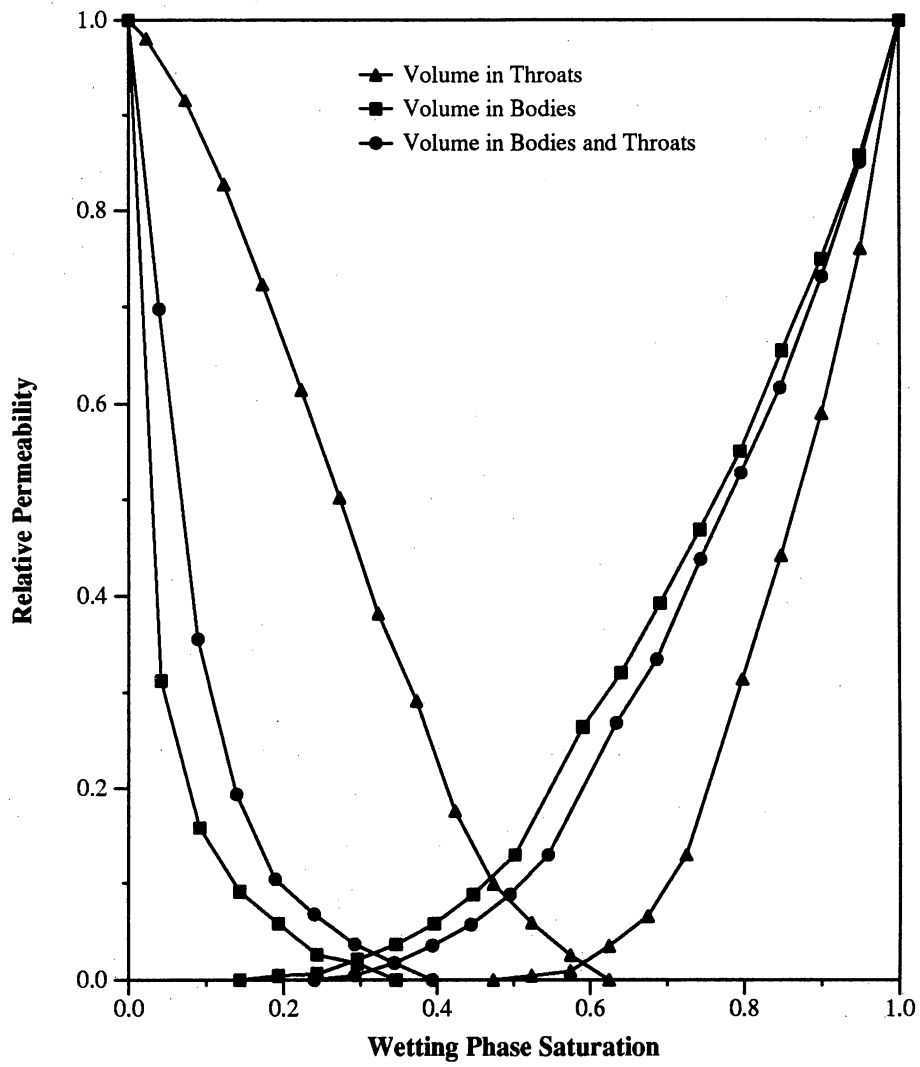
Figure 30. Relative permeability curves using a 25 × 12 × 12 network with no trapping, impermeable boundary conditions, and invasion through all six faces.

Figure 31. Relative permeability curves using a 25 × 12 × 12 network with no trapping, periodic boundary conditions, and invasion through the inlet face.

Figure 32. Relative permeability curves using a 25 × 12 × 12 network with no trapping, periodic boundary conditions, and invasion through the inlet and outlet faces.

Figure 33. Relative permeability curves using a 25 × 12 × 12 network with no trapping, periodic boundary conditions, and invasion through all six faces.

only in the throats, one where the volume is only in the bodies, and one where the volume is in both throats and bodies. For all runs, a 25 × 12 × 12 network was used.

The most obvious feature of the graphs is that the trapping assumption always yields extremely low or nonexistent nonwetting-phase permeability. For the no-trapping curves, the boundary conditions do not have much effect, and the only effect of invasion through more than one face seems to be a reduction in the wetting-phase saturation at which nonwetting-phase relative permeability becomes nonzero. Clearly the major difference in the no-trapping curves is in which pores the volume is placed. The case where the volume is only in the throats has much higher nonwetting-phase relative permeability than the other cases. The crossover point for this case occurs at a wetting-phase saturation greater than 50 percent. Still, the relative permeability at the crossover point is very low, around 5 percent.

Lin and Slattery (1982) used assumptions very much like this case since they had no bodies in their model. However, upon further study of their paper, we think that they allowed both phases to flow simultaneously in the same body. The other major difference in the two models is that they used a coordination number of 12, then reduced it by "removing" throats randomly. Implementing these two changes would almost certainly cause our relative permeability curves to approximate theirs more closely. However, it is an assumption of our model that the saturation should be controlled by the bodies as it was controlled successfully in the model of Mohanty and Salter (1982).

Blunt and King (1991) concur that the nonwetting-phase relative permeability is nonzero at all saturations using full trapping. They also present two graphs showing the results of their model using both uniformly and log-uniformly distributed, constant-length throats with uniformly distributed bodies. The significant difference between their model and ours was that they used the partial trapping assumption discussed earlier.

We have run the same cases using both no trapping and partial trapping as those of Blunt and King (1991). We digitized their two figures and compared their results with ours (figs. 34

through 37). The graphs differ as to the distribution used for throat radii and whether trapping was enforced for pore bodies.

For uniformly distributed throat radii, our results match reasonably well for both trapping rules. However, our nonwetting-phase relative permeability approaches 1 at a wetting-phase saturation of zero. Their curve approaches 1 at a wetting-phase saturation of about 7 percent. We are unsure why this is so.

For log-uniformly distributed throat radii, our results deviate from theirs in two significant ways. First, our nonwetting-phase relative permeability curve is up to 0.3 units below theirs in the 35- to 65-percent range. The curves, however, do match well for lower wetting-phase saturations. Second, our wetting-phase relative permeability curve is much lower for high wetting-phase saturations. In fact, comparing all of the wetting-phase curves in this range, it is seen that their log-uniform curve lies above the uniform curve, whereas ours lies below. It seems to us that for a log-uniform distribution there are proportionally fewer "large" sizes than for a uniform distribution. Therefore, a "large" throat will have more impact on relative permeability when using a log-uniform distribution. Since the larger throats are invaded first by the nonwetting phase, the wetting-phase relative permeability should decrease faster for a log-uniform distribution than for a uniform distribution.

We have written to Blunt and King expressing our concerns but have not yet received a reply.

In conclusion, the work that we have done this calendar year convinces us that our simulator is functioning correctly and that the core data measured at the Earth Sciences and Engineering Laboratory can be successfully matched with the current model.

Network Modeling of Diagenetic Processes

Petrophysical properties such as porosity, permeability, and formation factor are functions of size distribution of the deposited particles, the packing arrangement, and subsequent
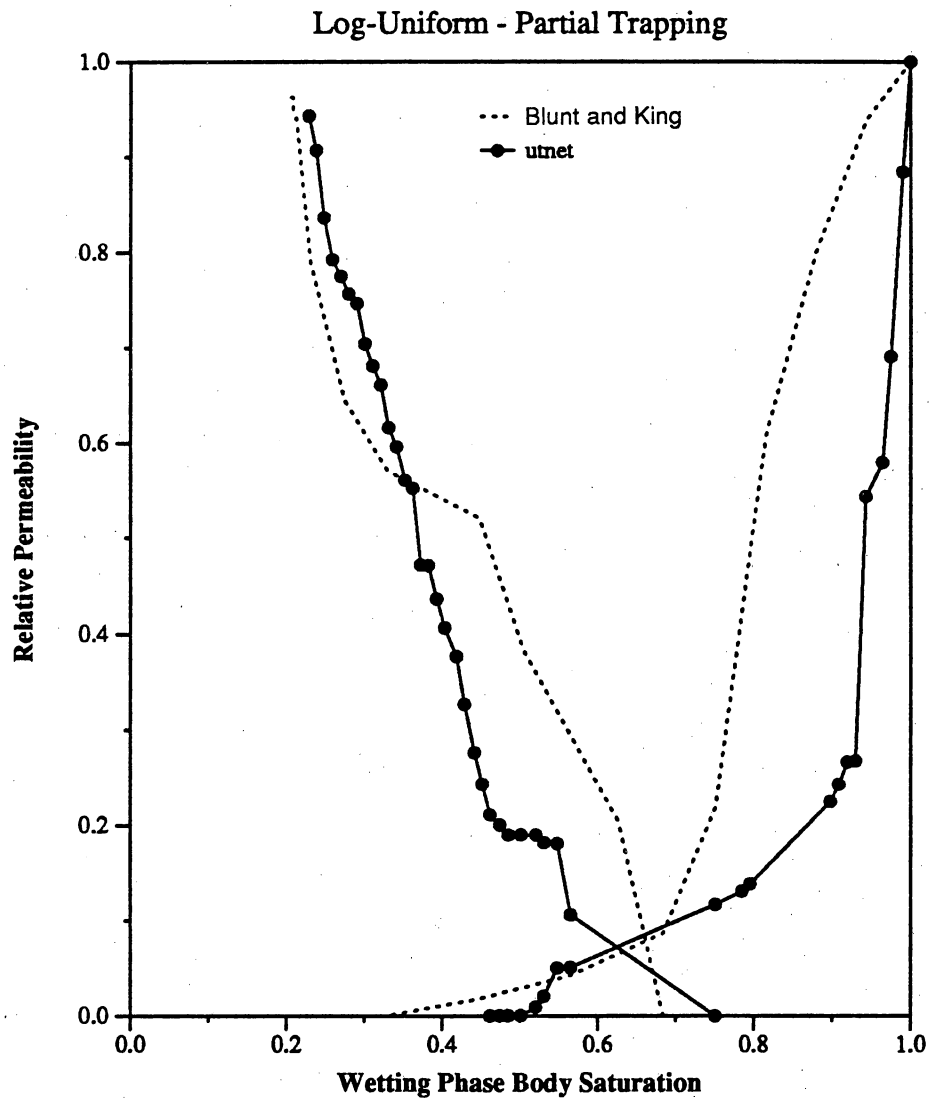
Figure 34. Comparison of the relative permeability results of our simulator with those of Blunt and King (1991) using log-uniformly distributed throat diameters with partial trapping.
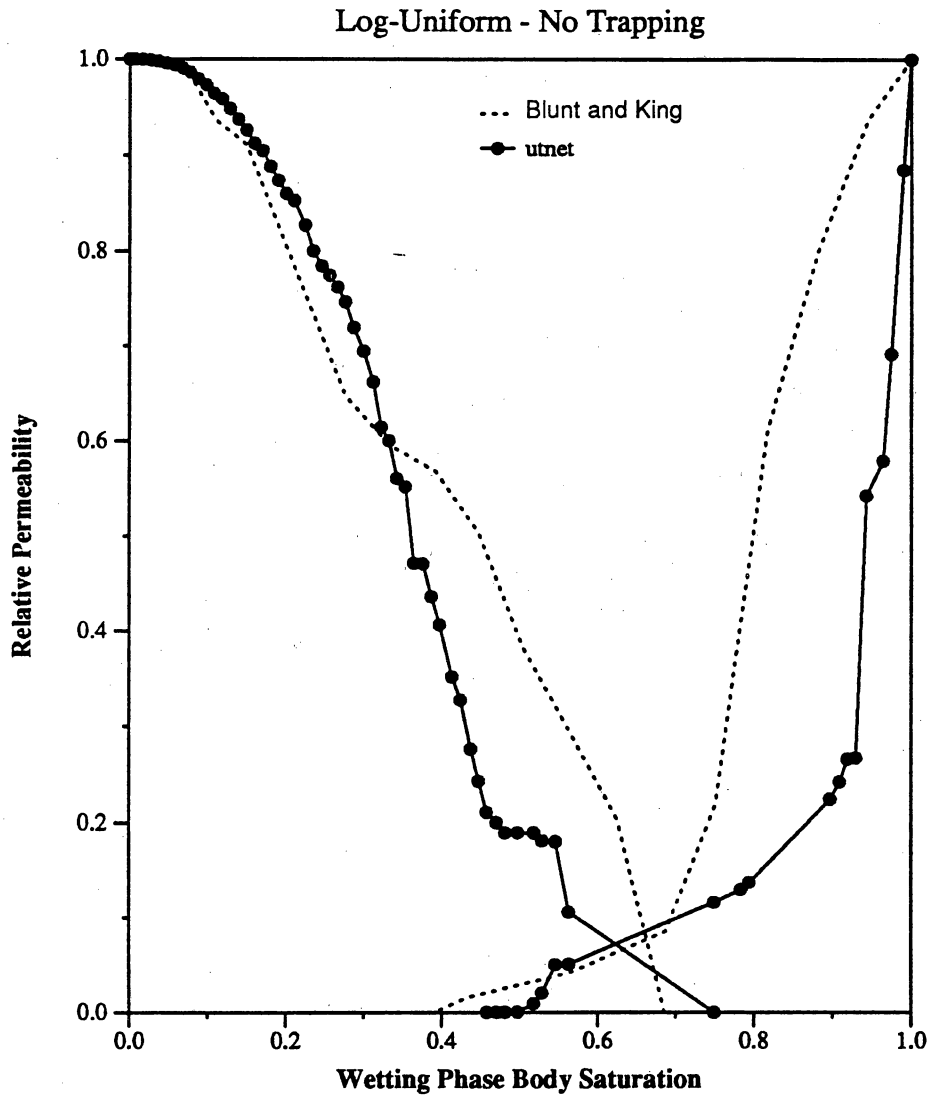
Figure 35. Comparison of the relative permeability results of our simulator with those of Blunt and King (1991) using log-uniformly distributed throat diameters without trapping.
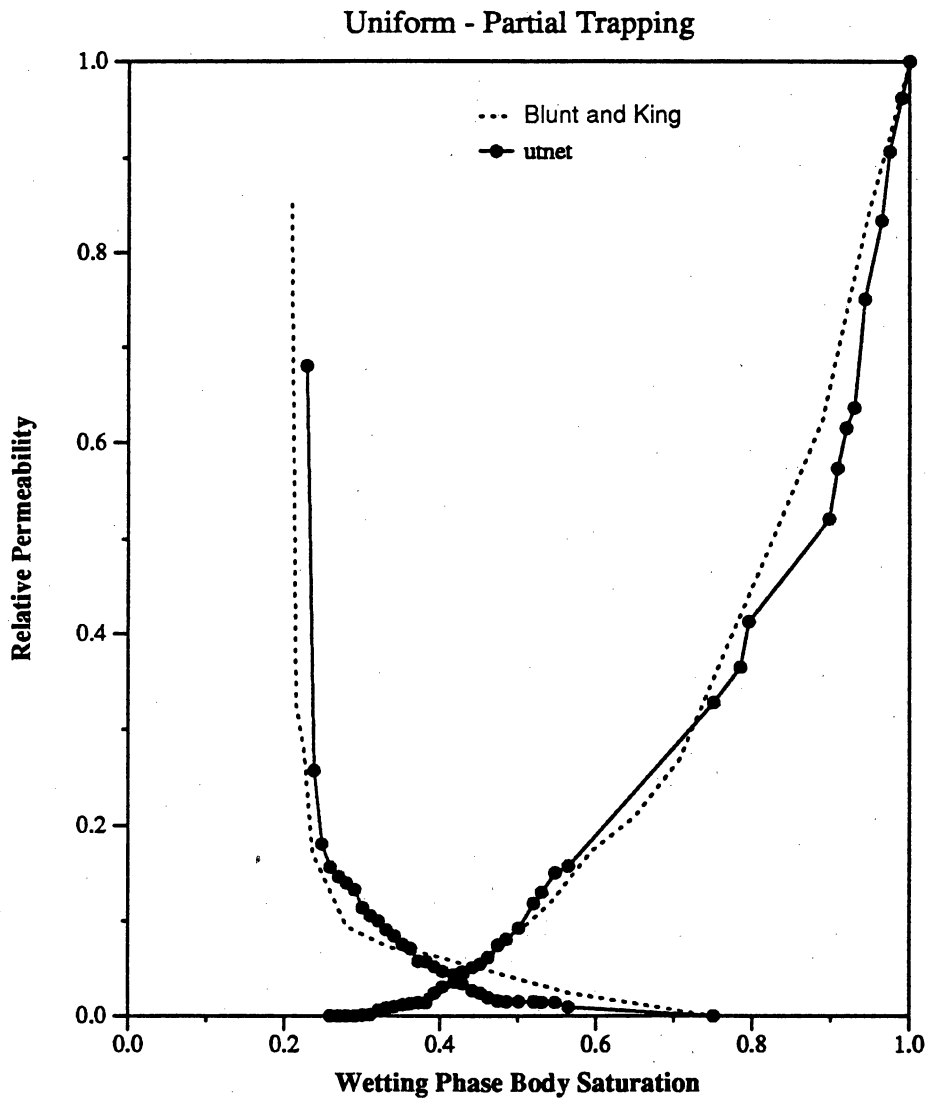
Figure 36. Comparison of the relative permeability results of our simulator with those of Blunt and King (1991) using uniformly distributed throat diameters with partial trapping.
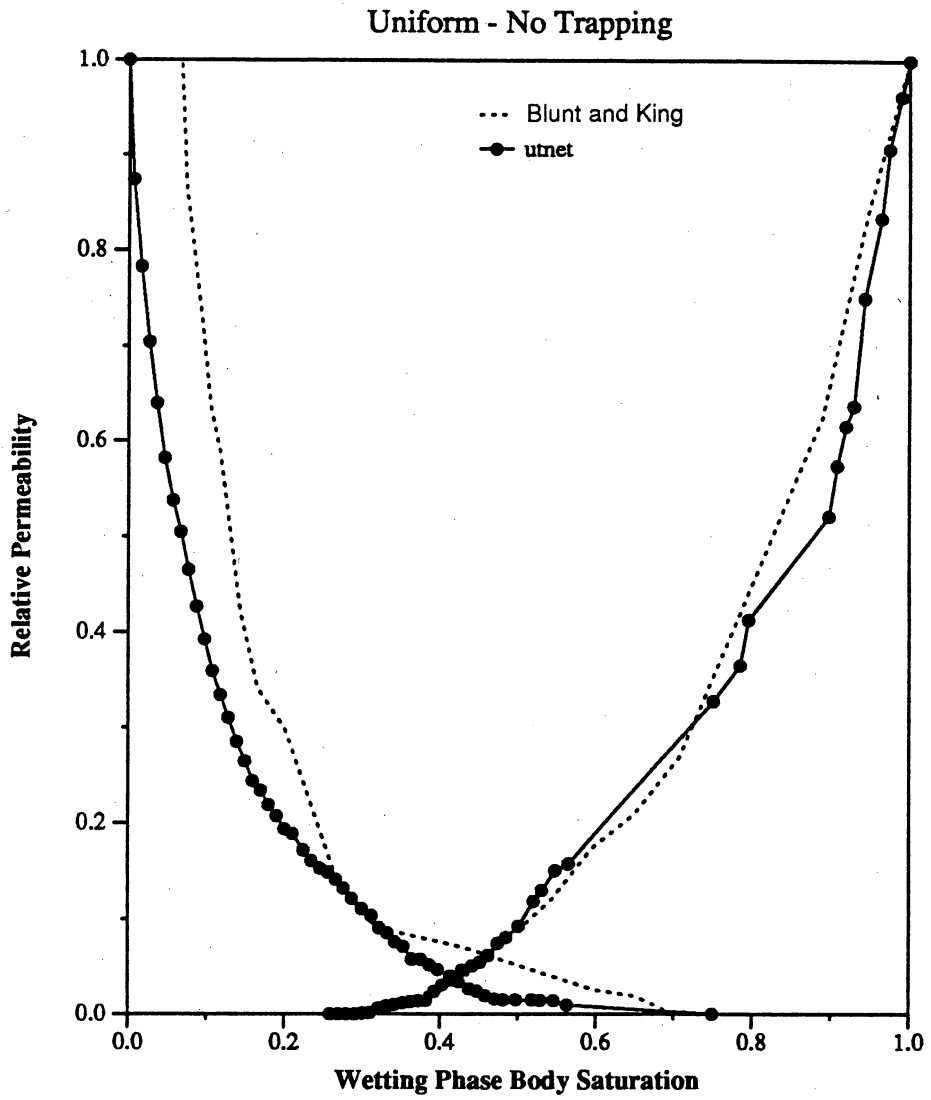
Figure 37. Comparison of the relative permeability results of our simulator with those of Blunt and King (1991) using uniformly distributed throat diameters without trapping.

diagenetic processes. In this section of the report, we describe initial approaches formulated to use the network model to replicate changes in petrophysical properties due to genetic and diagenetic processes. Because the two-phase portions of the network model are still under development, this discussion is restricted to the single-phase properties.

Past investigations have shown that porosity is not affected by particle size but strongly influenced by the sorting or size distribution of particles. Other diagenetic processes also influence the petrophysical properties. For example, compaction results in the reduction of porosity and permeability. Chemical precipitation to pore walls has a similar effect. Our initial studies were intended to determine how these two diagenetic processes influence petrophysical properties in a general sense and then to apply these results to the petrographic observations and data.

Cementation Model

Cementation is one of the diagenetic processes caused by precipitating of chemical matter due to the change of geological environments or by settling of clays later moved into the system. Although precipitation is likely to be spatially heterogeneous, for simplicity, we idealize the model as the thickness of cementation in pore bodies and pore throats to be the same.

Figure 38 shows a schematic diagram of idealized cementation reducing the pore space in a rock. In our network model, we simplify the pore body as a sphere and the pore throat as a cylinder, as shown in figure 39. To model the cementation process, for simplicity, we initially simulate the process in such a way that the diameters of all the pore bodies and pore throats are reduced uniformly by a constant amount Δd, so we have,

$$d_b{'} = d_b - \Delta d \tag{1}$$

$$d_t{'} = d_t - \Delta d \tag{2}$$

but the pore-throat length remains unchanged; that is,

$$l_t{'} = l_t \tag{3}$$
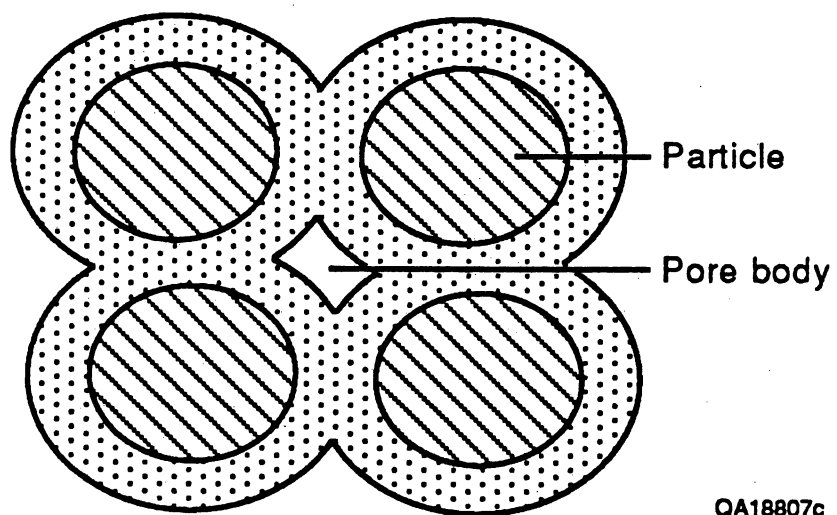
Figure 38. Cementation model of particle packing.
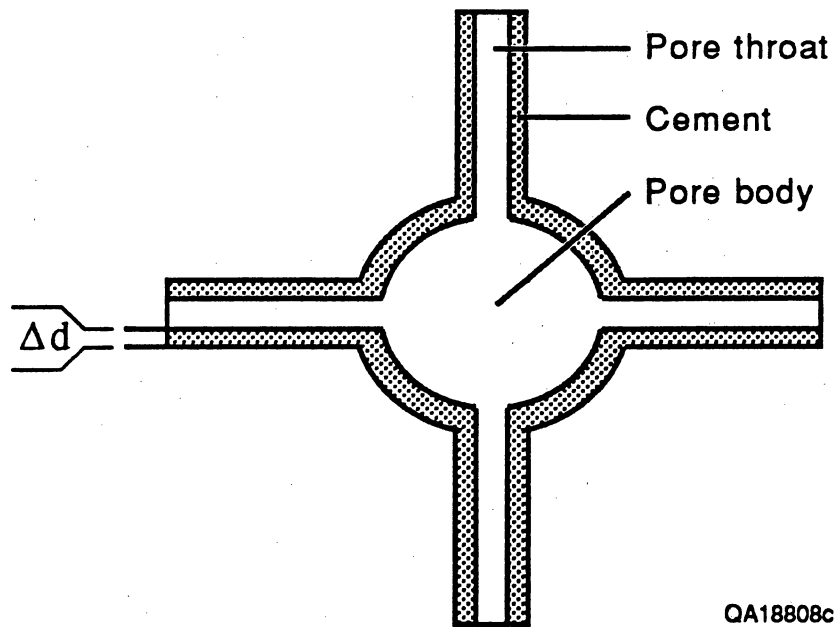
Figure 39. Cementation model of pore network.

where

d_b = pore-body diameter

d_t = pore-throat diameter

l_t = pore-throat length

Primed values refer to the cemented condition.

The relations to calculate porosity, permeability, and formation factor are developed in appendix B.

Example plots of formation factor versus porosity, permeability versus porosity, and permeability versus formation factor are shown in figures 40 through 42, respectively.

As can be seen from the plots, with increasing cementation porosity is reduced; correspondingly brine permeability decreases, and formation factor increases. Our approach to using these results on the Ferron is to determine what combinations of diagenetic and depositional processes affect both petrographic compositions and petrophysical properties. We will use this information as a guide to determining the type of pore-size-distribution changes that are required to match the network model with the actual petrophysical properties.

Compaction Model

Our initial simplified compaction model considers a volume of rock enduring stresses in all the directions, during which the solid particles experience plastic or elastic deformation such that the pore-throat length and the diameter of the pore bodies and pore throats shrink. For simplicity, we make the following assumptions:

The volumetric change of the solid particles is neglected.

The pore-throat length and the diameters of pore throats and pore bodies after compaction are proportional to those before compaction. The proportionality is f, such that

$$d_b' = f \, d_b \tag{4}$$
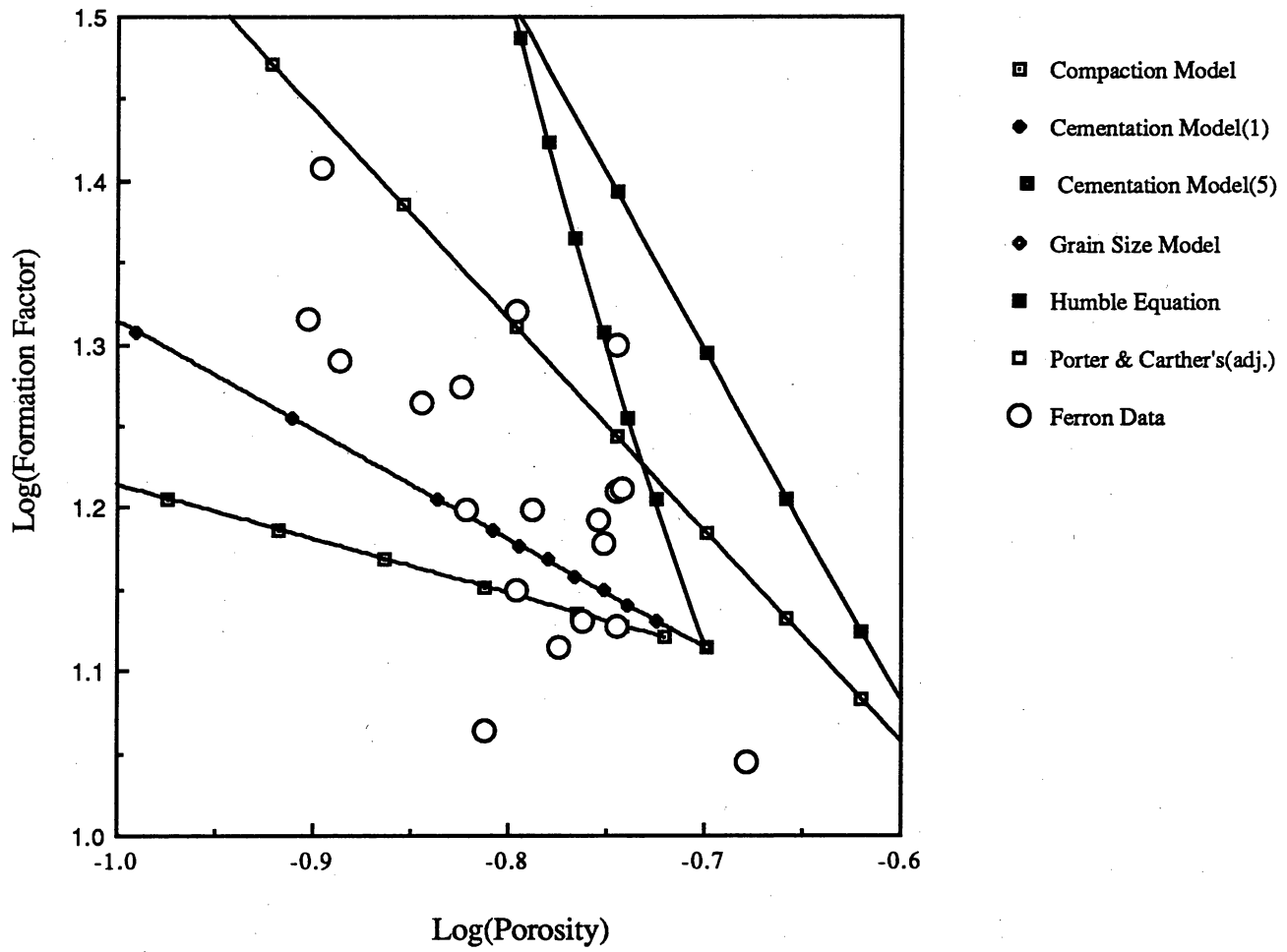
Figure 40. Comparison of results for different models of formation factor versus porosity compared to results of Ferron sandstone analyses.

78
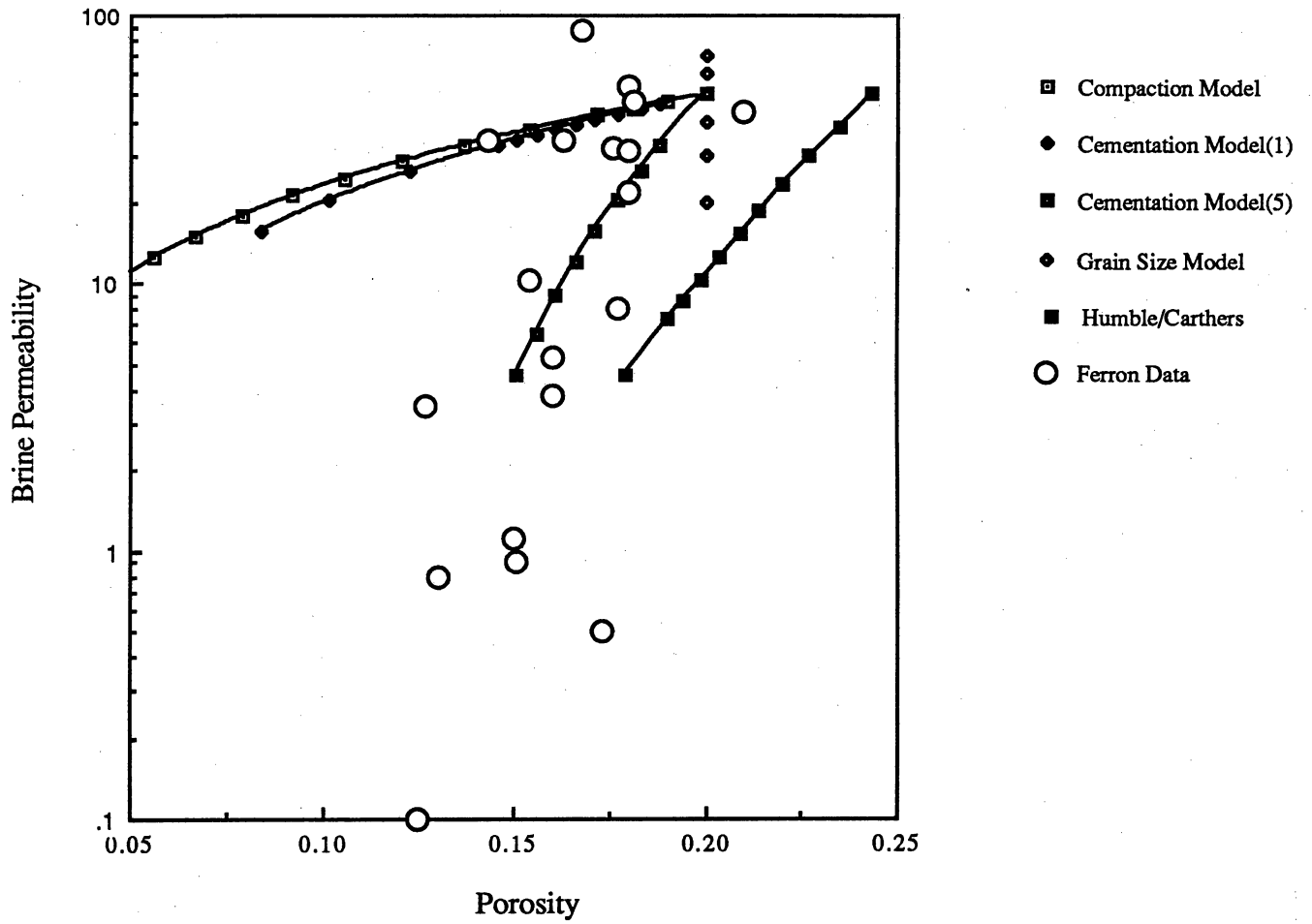
Figure 41. Comparison of results for different models of brine permeability versus porosity compared to results of Ferron sandstone analyses.
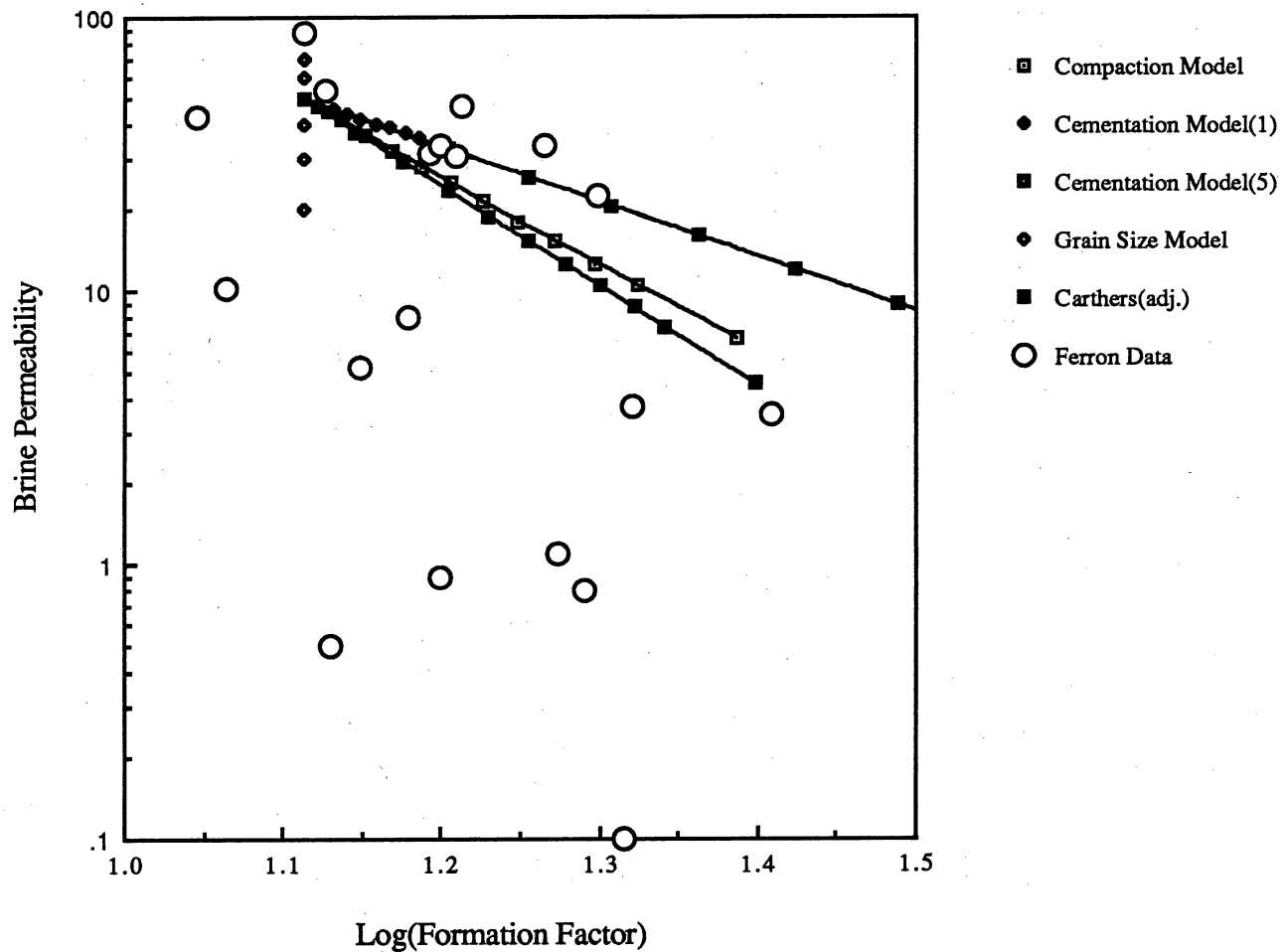
Figure 42. Comparison of results for different models of brine permeability versus formation factor compared with results of Ferron sandstone analyses.

$$d_t' = f\, d_t \tag{5}$$

$$l_t' = f\, l_t \tag{6}$$

These relationships and conserving rock volume result in (we have also neglected the dimensionless groups as in the cementation model)

$$\frac{\phi'}{\phi} = \frac{f^3}{1 + \phi(f^3 - 1)} \tag{7}$$

$$\frac{k'}{k} = \frac{f^3}{\sqrt[3]{1 + \phi(f^3 - 1)}} \tag{8}$$

$$\frac{F'}{F} = \frac{\sqrt[3]{1 + \phi(f^3 - 1)}}{f} \tag{9}$$

By changing the compaction factor, f, and determining the initial values of porosity, permeability, and formation factor, we can calculate set values of these petrophysical properties. Similar to cementation, different degrees of compaction introduce different degrees of reduction in porosity and permeability and increase of formation factor. Example plots of formation factor versus porosity, permeability versus porosity, and permeability versus formation factor are also show in figures 40 through 42, respectively.

This initial work on the diagenetic models provides a start in showing relative effects of different processes on pore network model response. Our work has now shifted to taking a closer look at the petrographic data being gathered by the Bureau to determine both further refinements of the modification rules and additional modification rules that will be necessary to replicate the correlations we observe between visual observations of pore structure and petrophysical data.

SUMMARY OF ACTIVITIES

During the first year of the project most activities were concentrated on developing methods for data collection. By the end of the first year, procedures for accomplishing the various tasks were fully developed, and we were ready to enter the main data collection phase of the project. The current year was highly productive in terms of collecting field data and analyzing samples for petrographic and petrophysical properties. Field activities during the past year were much more efficient because of the earlier experience, and the quality of both outcrop mapping and permeability measurements was improved over the first-year efforts. We had gathered enough petrologic and petrophysical information by the fall of 1991 to be able to start integrating results from the various tasks and to begin developing a general understanding of the processes and parameters that control gas reservoir properties. During the final year we will concentrate on data integration and interpretation.

Outcrop characterization activities during the 1991 field season extended the area of investigation to the seaward-stepping Ferron GS 2 sandstone and refined the procedure for measuring permeability. Field work was also extended to delta-front sandstones of GS 5 and to other exposures of GS 5 sandstones seaward of the area investigated during the 1990 field season. These results, when fully interpreted, will greatly increase our understanding of sandstone geometry in different fluvial-deltaic facies and different sequence stratigraphic settings.

Distributary-channel sandstones of Ferron GS 2 typically form amalgamated sandstone belts that consist of multiple-channel sand bodies. Because GS 2 was deposited during a time of relative sea-level fall, erosional truncation of older sands by younger deposits is common and bedform diversity is low. Air permeability ranges from less than 0.1 to more than 1,000 md. A plot of permeability versus cumulative frequency has a complex shape that signifies the presence of several permeability populations within the set of all distributary-channel sandstones. Subdividing the data set according to lithofacies type shows that individual

lithofacies can be represented by a single permeability distribution. As was the case for landward-stepping Ferron GS 5 distributary-channel sandstones, permeability correlation distances in GS 5 distributary-channel deposits are closely related to the dimensions of individual macroforms.

Petrographic examinations of GS 4 fluvial sandstones and GS 5 transgressive, delta-front, and distributary-channel sandstones at the Muddy Creek location are complete. Framework grain mineralogy, intergranular material, and cement composition show significant, systematic differences between fluvial, delta-front and transgressive, and distributary-channel sandstones. These differences in detrital and diagenetic mineralogy are reflected by systematic differences in mean permeability between the various facies.

Petrophysical measurements are proceeding on schedule. Analyses of the full suite of petrophysical properties have been completed on a total of 22 samples from GS 2, 4, and 5. These samples represent fluvial, distributary-channel, levee/crevasse splay, delta-front, and transgressive facies. Results of these measurements have been integrated with results of the petrographic examinations and are being examined for significant correlations. This information will provide the basis for developing relations between outcrop measurements and effective reservoir properties during the final phases of the research.

Significant progress has been made on the pore-level model and on developing a code that represents the petrography of analyzed specimens. Porosity, single-phase permeability, formation factor, and capillary pressure curves can be calculated for grain-size variation, compaction, and cementation scenarios. These scenarios were developed after thin sections of the sandstones were examined; the models will be refined as more petrographic and petrophysical information becomes available. A major activity during the past year was a critical evaluation of the model code and the assumptions inherent in the network model. This examination has led to improvements in the code. Our efforts during the final phase of the program will center on finding relations among reservoir properties and petrographic and

petrophysical data, particularly relations that allow us to predict effective gas permeability at irreducible water saturation from outcrop and petrographic information.

ANTICIPATED 1992 RESEARCH PROGRAM

During the final year of the contract period we will focus on three major issues: (1) map the three-dimensional geometry of flow units and bounding elements on a gas-reservoir scale, (2) develop a geographic relational data base that preserves information gained during this study in a form that can be used by interested parties, and (3) develop principles to translate field minipermeameter measurements to effective permeability values at irreducible water saturation and residual gas saturation in a three-dimensional reservoir model. Plans for accomplishing these goals, as well as other tasks to be accomplished, are discussed below.

1. Establish the three-dimensional geometry of facies and associated bounding elements at reservoir scale.

We can determine the reservoir-scale distribution of bounding elements three ways. First, several canyons dissect Ferron GS 2 near the I-70 roadcut and Ferron GS 5 near Short Canyon. These intersecting canyons provide outcrop exposures at various orientations to the direction of sediment transport. We will map flow units and bounding elements on the outcrop from photomosaic panels and determine actual dimensions of the architectural elements from measured vertical transects along the cliff faces. From this outcrop architecture we will prepare three-dimensional block diagrams of reservoir elements at gas-field scale.

Second, we will correlate facies and bounding elements from outcrop exposures to nearby cores. Two cores taken by the University of Utah Research Institute (UURI) are within 0.5 mi of Ferron GS 5 exposures in Muddy Creek Canyon, and one core taken previously by ARCO is near Ferron GS 2 exposures at Dry Wash Canyon. Tracing facies

and bounding elements from outcrop to core will indicate the lateral continuity of these reservoir elements.

Third, we have already completed preliminary mapping of Ferron sandstones between Muddy Creek and Picture Flats Canyons during the 1991 field season. We will construct a block diagram of flow units, baffles, and barriers between the two canyons, a distance of approximately 0.75 mi, on the basis of outcrop exposures in the two canyons and sandstone continuity between canyons.

2. Prepare a data base for storage and retrieval of permeability data.

We have selected ARC/INFO, a Geographic Information System (GIS), and INGRES, a relational data base management system, as our means to store, retrieve, and share data with other researchers. ARC/INFO allows us to process and present data to show a variety of spatial relations, whereas INGRES allows us to code and store permeability measurements and geologic attributes of sample points. The combination of ARC/INFO and INGRES has many advantages. Both systems are currently operating at the Bureau of Economic Geology, we have in-house expertise with both systems, and we are planning to expand our use of these systems in oil reservoir studies. ARC/INFO and INGRES are industry standards, readily available and widely accepted, so potential users can easily access our data and process it using other hardware and software systems.

We are currently establishing the basic structure of the data base. Our first data base structure follows the example of data bases established at the Bureau for oil reservoir studies. This structure will be modified as needed to reflect the specific nature of our outcrop study.

3. Develop transforms to relate field air permeability measurements to effective reservoir properties.

We will focus first on the most important transformations of air (minipermeameter) permeability (K_{air}) to brine permeability (K_{brine}) to effective gas permeability at irreducible water saturation (K_g). These are the most important properties for

determining the relationship between seals, barriers, and flow units. We have already spent a considerable amount of time studying the thin sections and have investigated through the literature the relationships between pore structure and petrophysical properties. In addition, the project has quantified sandstone compositions that include the following data: (1) fractions of sand, silt, and clay, (2) grain size and distribution parameters, (3) intergranular porosity, (4) mineralogy, (5) fractions of rock fragments, leached grains, and matrix, (6) cement composition, (7) fractions of clay rims, connected pores, and isolated pores, and (8) porosity type.

We intend to continue the general approach of the pore network model and let the thin-section observations and measured petrographic data guide our investigations into the relationships between petrophysical data and outcrop information (facies and air permeability). Our first approach will be to simply determine what variables seem to have the greatest effect on the ratio of brine-to-air permeability and gas-to-brine permeability. For example, the amounts and types of clays would seem to have some effect on the brine-to-air permeability ratio. Pore connectivity information might be expected to have an effect on the gas-to-brine permeability ratio.

Our second approach will be to apply statistical regression techniques. Although we much prefer to rely on physical insight to guide the transformations, statistical regression can be applied fairly readily and may provide additional insight into variables that might otherwise be overlooked. Our first approach here will be simply to do a regression of the brine-to-air and gas-to-brine permeability ratios against the quantitative petrographic data and air permeability. Our second approach will be to search for correlations within groups that have the same types of permeability distributions. Outcrop characterization efforts (this report) have successfully resolved subsets of all field permeability measurements that have similar permeability distributions. This confirms that air permeability is largely controlled by understandable physical and chemical processes. Preliminary regression results suggest that more regular relations

86

among petrographic and petrophysical properties can be resolved if samples are grouped according to depositional facies, lithofacies, and macroform type. We are optimistic that this approach will lead to development of transform principles that can then be built into a predictive reservoir model.

Once we have completed these studies on the permeability ratios, we plan to use the same approach with the other petrophysical data in the following order: irreducible water saturation, apparent capillary entrance pressure, residual gas saturation, brine-relative permeability at residual gas, formation factor, and saturation exponent.

4. Complete petrophysical measurements.

We will analyze an additional 20 to 40 samples, including approximately 20 taken from Ferron GS 2 and GS 5 in the UURI core. The data from core samples allow us to evaluate petrophysical differences between outcrop material and sandstones that have not been subjected to outcrop exposure and weathering. Other samples of bounding elements and flow units will be collected from outcrop during the 1992 field season.

5. Complete outcrop characterization of Ferron GS 2 and 5.

We will focus on the distal mouth-bar facies in GS 2 at the I-70 outcrop during the 1992 field season. We will also complete outcrop studies of Ferron GS 5 sandstones seaward of previously studied locations and test the usefulness of closer spacings between permeability measurements in Muddy Creek. During the first field season, we established vertical transects in Muddy Creek approximately 100 ft apart and measured permeability at vertical 1-ft intervals. Subsequently we found that closer spacings (50 ft between transects and measurements at 0.5-ft intervals) result in better resolution of permeability structure. We intend to determine how the closer spacing between data points would affect conclusions drawn from the Muddy Creek data sets. We will also complete a series of horizontal transects to determine permeability structure and to evaluate the continuity of high- and low-permeability zones between measured vertical sections.

6. Complete petrographic investigations.

    Examination of GS 5 samples from seaward sites in Picture Flats and Cedar Ridge Canyons will be finished by June 1992 for comparison with data from samples collected in Muddy Creek Canyon.

7. Log and measure permeability in units GS 2 and 5 of the UURI cores.

    Descriptions and analyses of this core will allow us to (1) compare outcrop and shallow subsurface samples, (2) obtain samples of bounding elements for petrophysical analysis, and (3) compare permeability profiles between core and outcrop.

8. Compare Ferron sandstones with selected reservoirs of the Lake Creek field (Wilcox Formation, Texas Gulf Coast).

    We will compare the geometry of flow units and baffles or barriers from Ferron sandstones with similar data for a selected interval (probably the G sand) of the Wilcox Lake Creek field.

REFERENCES

Allen, J. R. L., 1965, A review of the origin and characteristics of recent alluvial sediments: Sedimentology, v. 5, p. 89–191.

Blunt, M., and King, M. J., 1991, Simulation and theory of two-phase flow in porous media: submitted to Physical Review.

Donath, F. A., Holder, Jon, and Fruth, L. S., 1988, Simultaneous hydraulic/physical parameter measurement on rock specimens subjected to triaxial conditions: Advanced Triaxial Testing of Rock, ASTM STM 977, p. 143–154.

Folk, R. L., 1974, Petrology of sedimentary rocks: Austin, Texas, Hemphill Publishing Company, 182 p.

Friend, P. F., 1983, Towards a field classification of alluvial architecture or sequence: Sedimentology, v. 6, p. 345–354.

Gardner, M. H., 1991, Sequence stratigraphy of the Ferron Sandstone, east-central Utah, *in* Tyler, Noel, Barton, M. D., and Fisher, R. S., eds., Architecture and permeability structure of fluvial-deltaic sandstones: a field guide to selected outcrops of the Ferron Sandstone, east-central Utah: The University of Texas at Austin, Bureau of Economic Geology guidebook prepared for 1991 field trips, p. 4–55.

Goggin, D. J., 1988, Geologically-sensible modeling of the spatial distribution of permeability in eolian deposits, Page Sandstone (Jurassic), northern Arizona: The University of Texas at Austin, Ph.D. dissertation, 418 p.

Haldorsen, H. H., and Lake, L. W., 1984, A new approach to shale management in field-scale models: Society of Petroleum Engineers Journal, v. 24, p. 447–457.

Jackson, R. G., II, 1976, Depositional model of point bars in the lower Wabash River: Journal of Sedimentary Geology, v. 46, p. 579–594.

Kirkpatrick, S., 1973, Percolation and conduction: Reviews of Modern Physics, v. 45, p. 574–588.

Kittredge, M. G., 1988, Analysis of permeability variation—San Andres Formation (Guadalupian) Algerita Escarpment, Otera County, New Mexico: The University of Texas at Austin, M.S. thesis, 361 p.

Lin, C-Y., and Slattery, J. C., 1982, Three-dimensional, randomized, network model for two-phase flow through porous media: American Institute of Chemical Engineering Journal 28, p. 311–324.

Miall, A. D., 1985, Architectural-element analysis, a new method of facies analysis applied to fluvial deposits: Earth-Science Reviews, v. 222, p. 261–308.

Mohanty, K. K., and Salter, S. J., 1982, Multiphase flow in porous media 2. Pore-level modeling: SPE Paper 11018 presented at the 1982 Society of Petroleum Engineers Annual Technical Conference and Exhibition, New Orleans, September 26–29.

Reid, R. C., and Sherwood, T. K., 1966, The properties of gases and liquids: New York, McGraw-Hill, 646 p.

Ryer, T. A., 1981a, Deltaic coals of the Ferron Sandstone Member of the Mancos Shale predictive model for Cretaceous coal-bearing strata of the western interior: American Association of Petroleum Geologists Bulletin, v. 65, no. 11, p. 2323–2340.

_____ 1981b, The Muddy and Quitchupah projects: a project report with descriptions of cores of the I, J, and C coals beds from the Emery coal field, central Utah: U.S. Geological Survey Open-File Report 81-460, 34 p.

_____ 1982, Possible eustatic control on the location of Utah Cretaceous coal fields: Utah Geological and Mineralogical Survey, Bulletin 118, Proceedings, 5th ROMOCO Symposium, p. 89–93.

_____ 1983, Transgressive-regressive cycles and the occurrence of coal in some Upper Cretaceous strata of Utah: Geology, v. 111, p. 207–210.

Stalkup, F. I., and Ebanks, W. J., Jr., 1986, Permeability variation in a sandstone barrier island-tidal delta complex, Ferron Sandstone (Lower Cretaceous), central Utah: Society of Petroleum Engineers Paper 15532, p. 1–8.

Tyler, Noel, Fisher, R. S., Barton, M. D., Miller, M. A., Holder, Jon, and Gray, K. E., 1991, Quantification of flow unit and bounding element properties and geometries, Ferron Sandstone, Utah: implications for heterogeneity in Gulf Coast Tertiary deltaic reservoirs: The University of Texas at Austin, Bureau of Economic Geology, annual report prepared for the Gas Research Institute under contract no. 5089-260-1902, 127 p.

van Veen, F. R., 1977, Prediction of permeability trends for water injection in a channel-type reservoir, Lake Maracaibo, Venezuela: SPE Paper 6703 presented at the 52nd Annual Society of Petroleum Engineers Fall Technical Conference, Denver, October 9–12.

Weber, K. J., 1982, Influence of common sedimentary structures on fluid flow in reservoirs models: Journal of Petroleum Technology, March, p. 665–672.

_____ 1986, How heterogeneity affects oil recovery, in Lake, L. W., and Carroll, H. B., eds., Reservoir characterization: Orlando, Academic Press, p. 487–544.

APPENDIX A

LABORATORY MEASUREMENTS

A1. System Description

The final configuration of the two-phase flow system used for the laboratory measurements is shown in figure A-1. Basic elements of the system design, presented in the FY 1990 Annual Report, are repeated here for completeness. The measurements are carried out in a high-pressure testing vessel having capabilities for simultaneous pore fluid circulation and measurements of permeability, electrical resistivity, and static and dynamic moduli, on triaxially loaded $2^1/8$-inch $\times$ 4-inch cylindrical test specimens. Axial load is applied by a hydraulic ram, collar-coupled to the pressure vessel. Differential axial load is indicated by the output of a load cell in series with the loading piston. An inline equalizer compensates for the axial force due to the confining pressure, and for the change in confining fluid volume due to the movement of the axial load piston into the vessel. Axial strain is determined from the output of a linear transducer connected between the vessel wall and the loading piston. Confining and load-ram pressures are applied by motor-driven syringe pumps. A linear displacement transducer attached to the confining fluid pump continuously monitors changes in total specimen volume.

Liquid pore pressure and circulation control are provided by separate motor-driven syringe pumps upstream and downstream from the specimen, and the pressures are measured by independent upstream and downstream pore pressure transducers. A separate pressure line to the upstream pore pressure transducer eliminates pressure drops across the small-diameter tubing leading from the vessel exterior to the specimen. Flow measurements carried out with a hollow dummy test specimen show that pressure drops across the remaining internal pore fluid components between the upstream and

93
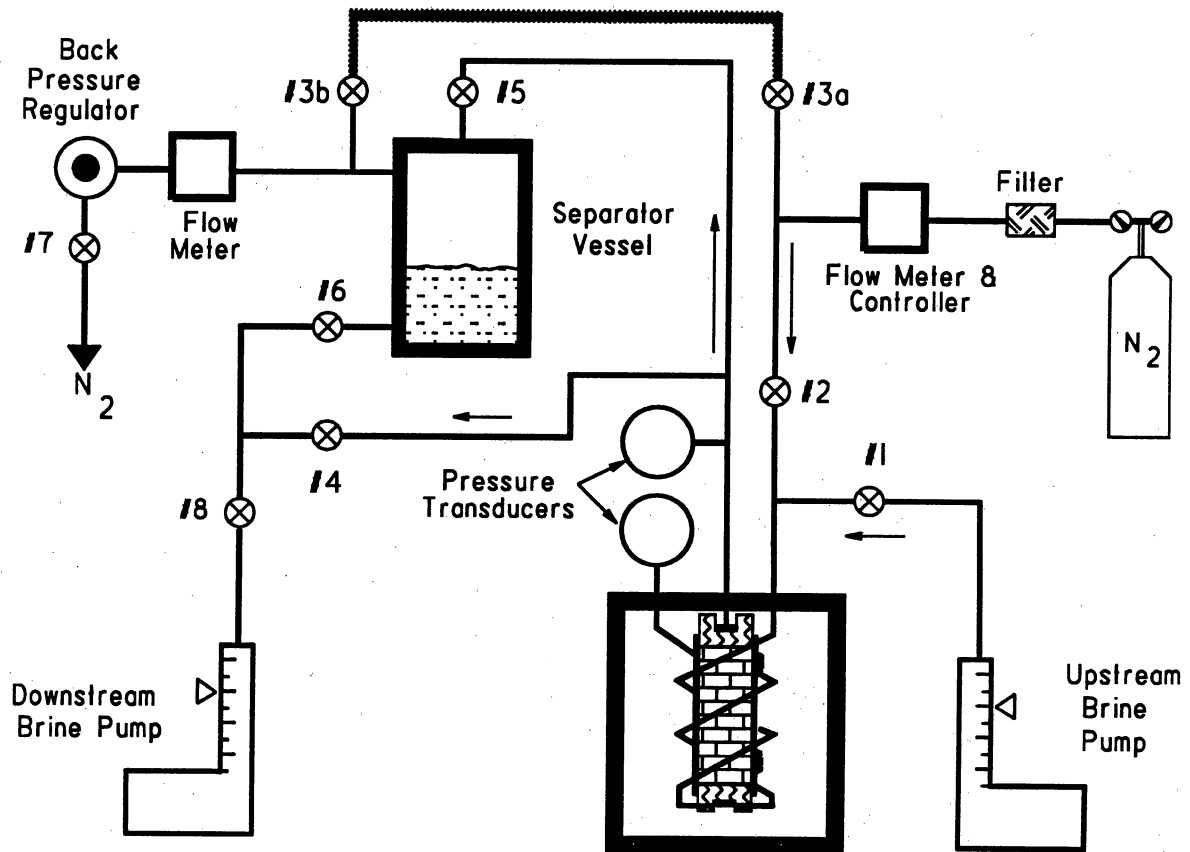
Figure A1. System configuration for laboratory petrophysical property measurements during two-phase flow.

downstream pore pressure transducers are less than the system resolution of about 0.2 psi.

Electrical displacement transducers are used to continuously monitor upstream and downstream pore fluid pump volumes. The pumps have internal provision for servocontrol at a constant flow rate. Gas flow is provided by a nominal 2,000 psi nitrogen tank, controlled and metered by a high-pressure mass flow control unit. All transducer outputs are input to a microcomputer-based data acquisition system, which also provides closed-loop servocontrol of confining pressure, axial load, and upstream and downstream pore pressure.

Permeability measurements are carried out under constant flow conditions, using the upstream and downstream transducers and the direct measurements of fluid flow volumes. Brine from the upstream syringe pump is mixed with the metered flow of nitrogen from the mass flow meter, and the mixture flows to the lower specimen end platen. The nitrogen/brine mixture exits from the top of the specimen and flows to the gas/liquid separator vessel. Brine from the separator vessel flows into the downstream syringe pump operating at the same flow rate as the upstream brine pump. An electrical sensor in the separator vessel is used to maintain the fluid volume at a constant level, and variations in brine saturation in the specimen during two-phase flow are determined by mass balance of the measured pump volumes. The downstream gas flow is routed through a flow meter to a gas back-pressure regulator, which determines the downstream pressure for both nitrogen and brine. Valves provide for single- and mixed-phase flow of nitrogen and brine through the specimen.

The specimen endcaps house ceramic transducers for the generation and detection of pulses for shear and compressional wave velocity measurements along the axis of the specimen. The top endcap is electrically isolated from the vessel so that the endcaps can serve as current electrodes for a uniform axial electric current in the specimen, for electrical resistivity measurements concurrent with single- and two-phase fluid flow.

Feed-through potential electrodes along the circumference of the test specimen provide for four-terminal resistivity determinations. An alternating-current phase-sensitive detection system operating at a frequency of 1 kHz is used for the potential measurements, so that only the in-phase contributions from the resistive processes within the specimen are measured. The resistance of the specimen is determined directly by comparison with the potential drop across a calibrated standard resistance. Details of the specimen assembly and the measurement instrumentation for electrical resistivity determinations are given in Donath and others (1988).

Several system calibrations are required for the petrophysical property determinations. Calibrations for the absolute brine permeability, static deformation, and wave velocity measurements are described in the FY 1990 Annual Report. The pore pressure transducers are calibrated at approximately 6-month intervals, or following any overpressurization due to specimen jacket failures, by comparison with a dead-weight tester. The total volume of pore fluid system external to the pumps and separator vessel has been determined from measurements of brine pump volumes necessary to fill the system, under test conditions, with a steel dummy test specimen. The brine pump displacement transducers, which were added in FY 1991, have been calibrated with direct fluid volume measurements.

Additional calibration requirements pertain to the gas flow system and brine saturation determinations during two-phase flow. The gas flow rate meters are calibrated at approximately 2-month intervals, and whenever the full-scale range is changed by interchanging an internal flow restrictor, by comparison with a wet-test flow meter standard. The brine content of the pore fluid lines at different flow conditions was determined, as a function of gas and brine flow rates, by direct measurements of brine pump volume changes during two-phase flow through a Lucite dummy specimen with a small, known pore fluid volume, in which a set of parallel pore fluid pathways were precisely machined to match the pore fluid spreader ports in the specimen endcaps.

A2. Test Procedures

For each of the test specimens a set of petrophysical property measurements, consisting of air and/or gas permeabilities, electrical resistivity, and shear and compressional wave velocities, are carried out for single-phase flow in the gas- and brine-saturated specimen, and for two-phase flow at several values of partial brine saturation. The following standardized sequence of pore fluid saturations is used for the tests.

1. Gas Flow at Gas Saturation.

The room-humidity dry specimen is placed in the vessel, and a reference axial displacement transducer value is determined for the unstressed specimen. A confining pressure of 5,000 psi is applied with zero pore pressure. A nominal 1,000 psi pore pressure is applied with the nitrogen gas system, and a small gas flow rate is established using the mass flow controller. The downstream pore pressure is fixed at a constant level by the pressure regulator, such that the mean pore pressure is approximately 1,000 psi. The confining pressure is then increased to 6,000 psi, and the confining pressure servocontrol system is activated. The effective pressure of 5,000 psi is maintained throughout the test sequence. The gas-saturated specimen is stabilized, with gas flow, overnight. The initial suite of petrophysical property measurements is then carried out.

2. Brine Flow at Brine Saturation.

Brine saturation of the specimen is preceded by the extraction of nitrogen gas from the pore space with a vacuum pump connected directly to the downstream outlet at the top of the apparatus. The confining pressure is lowered to 5,000 psi during this evacuation, in order to maintain the 5,000 psi effective pressure. Following an evacuation of about 1 hour, brine (6 percent NaCl, by weight) from the upstream pump is introduced into the bottom specimen platen. While the downstream (top) of the specimen is being evacuated, deaerated brine is injected into the specimen bottom at a

rate of less than one pore volume per hour. The downstream vacuum is maintained until a solid stream of brine is observed in the vacuum line. The vacuum is then released, the brine pore pressure is raised to the 1,000 psi test level, and the upstream pore pressure pump is placed under constant pressure servocontrol. Servocontrol of the confining pressure, at 6,000 psi, is restored, and the downstream pore pump is set to intake pore fluid at a constant rate. The upstream pore pressure control is adjusted to provide a mean pressure of 1,000 psi while the system stabilizes. A comparison of total pore fluid pump volumes before and after saturation is carried out to give a preliminary measurement of pore fluid volume. System stability, indicated by a constant pressure drop across the specimen, requires from 2 hours to overnight and a through-put of at least two pore volumes of brine. After stabilization, the measurement suite is again carried out. For the initial 20 test specimens a sample of pore fluid was extracted downstream from the sample brine-saturated specimen for a fluid resistivity determination. In all cases the resistivity has been the same, within experimental uncertainty, as the original brine solution, and only spot checks of pore fluid resistivity are now being carried out.

3. Two-Phase Flow during Brine Drainage.

In preparation for two-phase flow the upstream brine pump is refilled and the downstream pump is emptied, and final zero reference values of pore pressure differential and mass flow meter outputs at zero flows are determined. While maintaining brine flow through the brine-saturated specimen, the downstream separator vessel is valved into the system, the system is stabilized, the level of the air-brine interface in the separator is adjusted to the reference value, and a careful determination of the initial total brine pump volume is carried out for subsequent mass balance calculations of brine saturation. Nitrogen flow is initiated, at a rate sufficient for a pressure drop across the specimen at or below approximately 10 percent of the mean

pore pressure. When the system stabilizes, generally following the passage of 2 to 10 pore volumes of gas through the specimen, the petrophysical properties are measured.

4. Gas Flow at Irreducible Water.

Brine flow from the upstream pump is stopped, and the nitrogen flow rate is readjusted, if necessary, to provide a measurable pressure drop. When the system restabilizes, at the irreducible water saturation established by the flow conditions used, the petrophysical property measurements are carried out. If necessary, the upstream brine pump is refilled, and the downstream pump is emptied.

5. Two-Phase Flow during Brine Imbibition.

Brine flow is restarted, and the flow rate is increased until an adequate pressure drop is established. Whenever possible, the gas flow rate remains the same as that used for the irreducible water measurements. The system is allowed to stabilize, and the measurement set is carried out.

6. Brine Flow at Residual Gas.

Nitrogen flow is stopped, and the brine flow is increased to provide an adequate pressure drop. Flow is continued until the system is stabilized, at the residual gas saturation established by the flow conditions, typically overnight. The petrophysical property measurements are carried out.

7. Static Deformation Measurements.

After the measurements at residual gas saturation have been carried out, brine flow is halted, and a triaxial deformation at a constant strain rate of approximately 10^{-6} per second is carried out. The downstream pore fluid lines remain connected to the separator vessel during the deformation, to maintain drained pore fluid conditions. The deformation is limited to a total axial strain of approximately 0.5 percent, which is below the onset of significant dilatantcy or other permanent, nonelastic behavior for all

specimens tested. The static moduli are not sensitive to the partial saturation value, and this one set of values provide an adequate description of the specimen's static pseudo-elastic behavior.

This sequence is carried out over a period of 4 to 7 days. At the conclusion of the measurement sequence, the partially saturated specimen is removed, vacuum-saturated with brine, and weighed. The specimen is then oven-dried and reweighed to determine the bulk specimen porosity, ϕ.

For each of the saturation stages, the following suite of petrophysical property measurements is carried out. Nitrogen permeabilities are determined from average values of gas flow rates and pressure drops during the time interval over which flow is stable. Brine flow rates used for the brine permeability calculations are determined from changes in the upstream pore fluid pump volume over the same interval. The 1-kHz current flow is activated, and the electrical resistivity is measured. A small reference axial load is applied to seat the axial displacement transducer, and the P- and S-wave transit times are determined from the corresponding first arrival times on the oscilloscope. The complete wave signals are also digitized and stored for subsequent analysis and refinements of arrival times; see the discussion of Laboratory Measurement Results, below. The brine level in the separator vessel is adjusted to the reference value, and a reading of brine pump volumes is recorded. Brine content in the pore volume is calculated by mass balance. The net volume of brine expelled from the specimen, V_{out}, is determined from the corresponding brine pump volumes and their initial values and the calibrated correction for the volumes of pore-fluid system brine displaced by the gas. Pore volume brine saturation, S_w, is then determined from

$$S_w = \phi - V_{out} / V_s ,$$ (A-1)

where V_s is the specimen volume.

Data reduction procedures for the brine permeability, formation factor, and wave velocity measurements are given in the FY 1990 Annual Report. Gas permeability is

determined using the same expression as that used for brine permeability, using gas viscosities and mass flow rates corresponding to the mean specimen pore pressure, p, in kpsi. The viscosity, μ_g, in centipoise, is determined from a least-squared curve fit to measurements reported by Reid and Sherwood (1966):

$$\mu_g = \sqrt{3.31 \times 10^{-4} + 9.23 \times 10^{-6}\, p + 2.21 \times 10^{-5}\, p^2 + 9.14 \times 10^{-7}\, p^3}\ . \qquad \text{(A-2)}$$

The gas flow rate outputs from the mass flow meters, Q_{SLPM}, are in terms of liters per minute of nitrogen at atmospheric pressure. The flow rates, Q_g, at mean specimen pore pressure, p, are determined by least-squared curve fit to density ratio data, also in Reid and Sherwood (1966):

$$Q_g = [\, -0.001 + 0.0835\, p - 0.00347\, p^2\,] \cdot Q_{SLPM} \qquad \text{(A-3)}$$

A3. Test Results

Tests for four of the specimens were not completed. The test for the Set 2 Block 10 sample of fluvial facies material was aborted because several months would have been required for flow stabilization at this very low permeability (<1 md). Jacket ruptures in both specimens from a second Set 4 block of laminated material prematurely ended the tests and rendered the specimens unusable for subsequent testing. A system malfunction during testing of the Set 2 Block 4 specimen of delta-front material led to imbibition conditions during the drainage phase of the measurements, and the results from that test are not usable.

Measured pore storage and transport properties are summarized in table 5. Variations in formation factors and relative permeabilities with relative brine saturation of the pore volume are shown in figures A-2 to A-25, a and b, respectively. The formation factors are plotted in a log-log format to facilitate a visual best-fit to Archie's Law:

$$F = A\, S_w{}^n. \qquad \text{(A-4)}$$
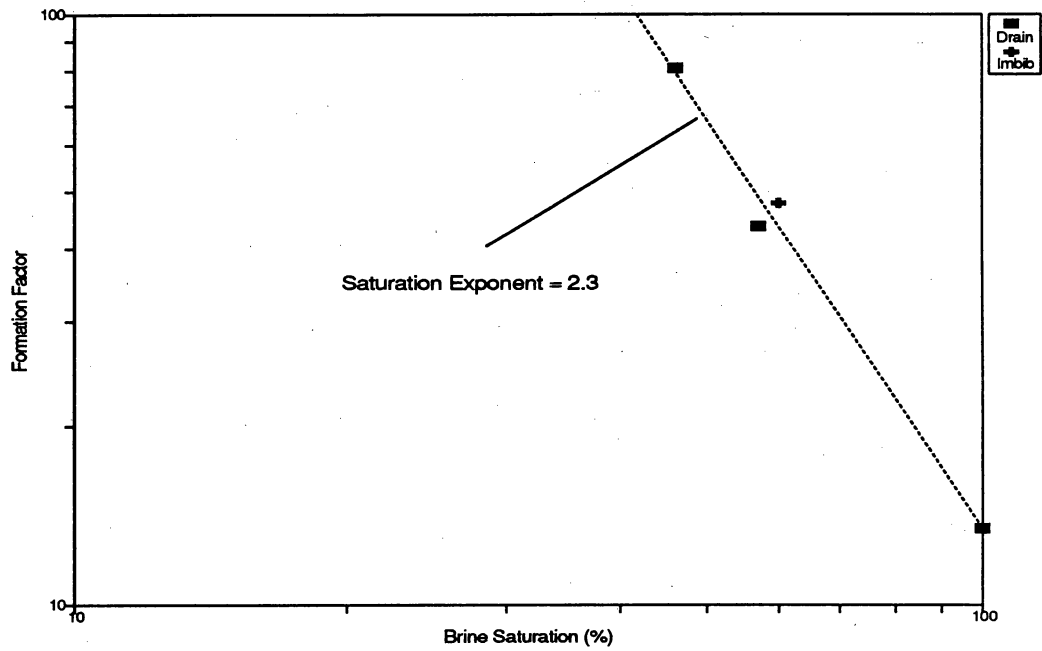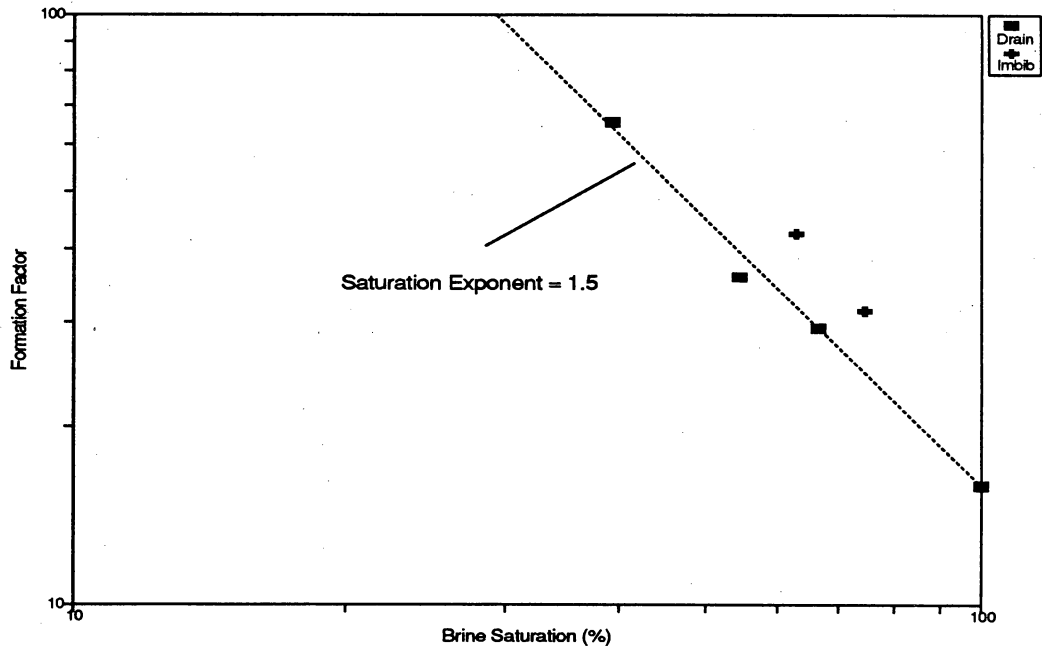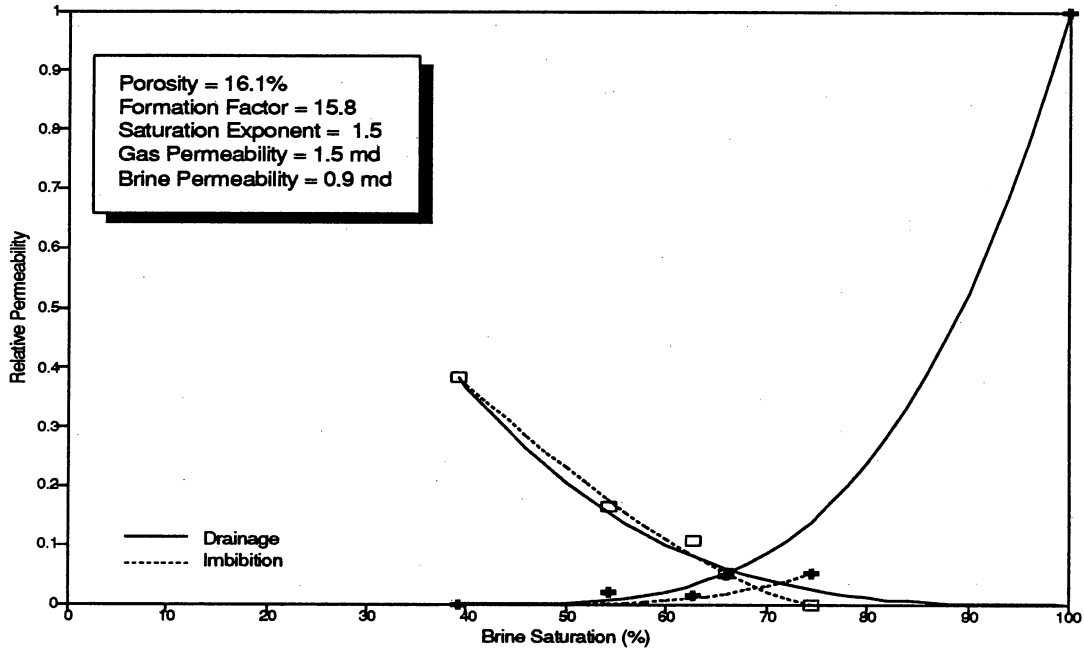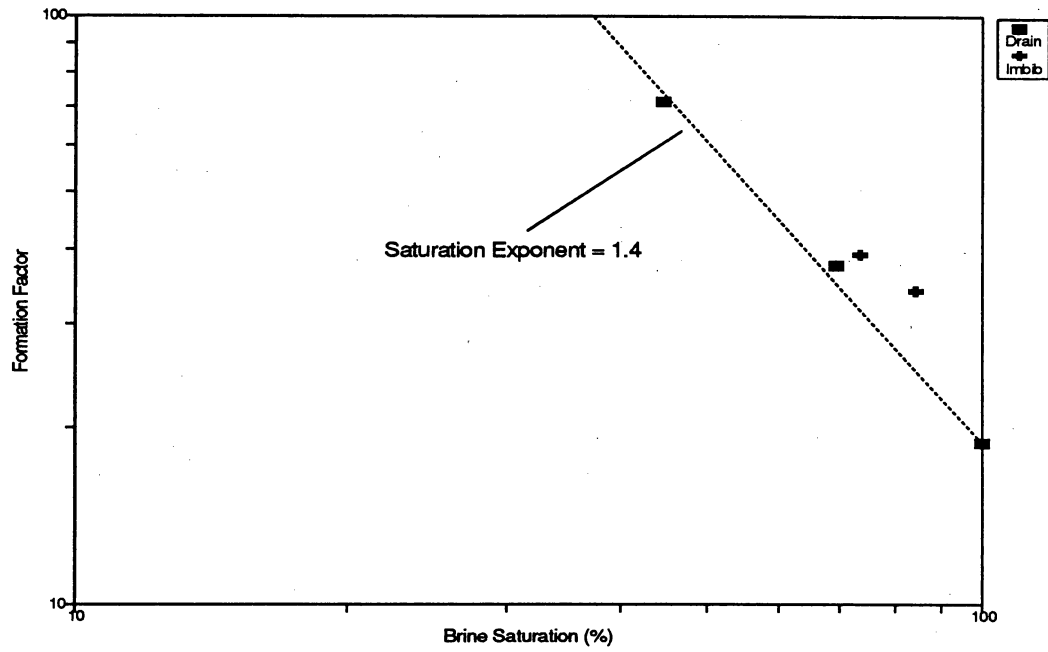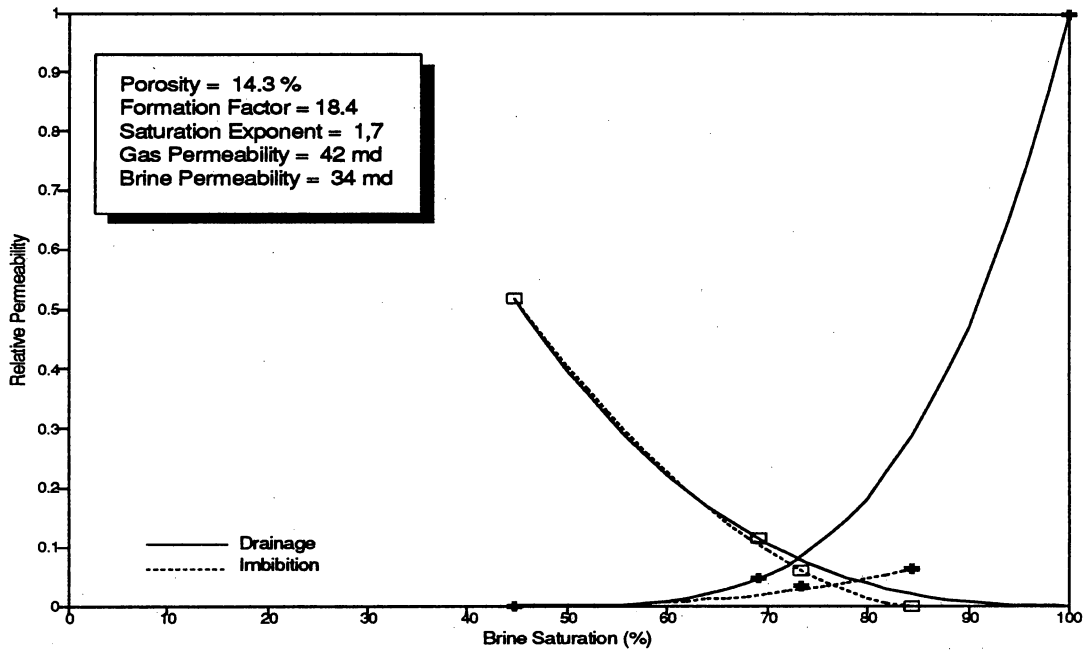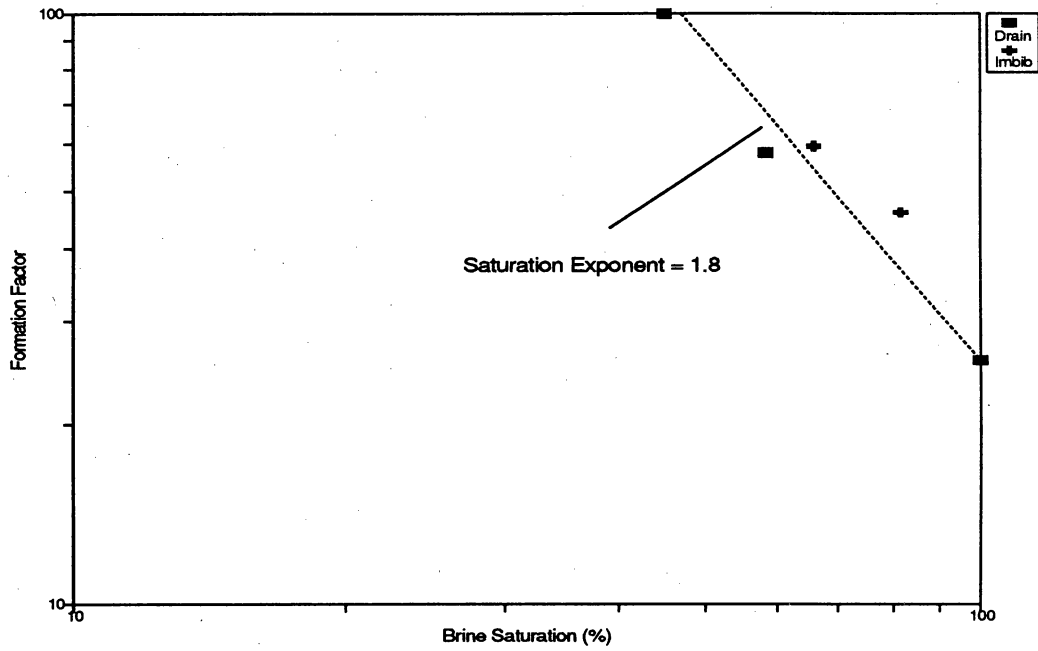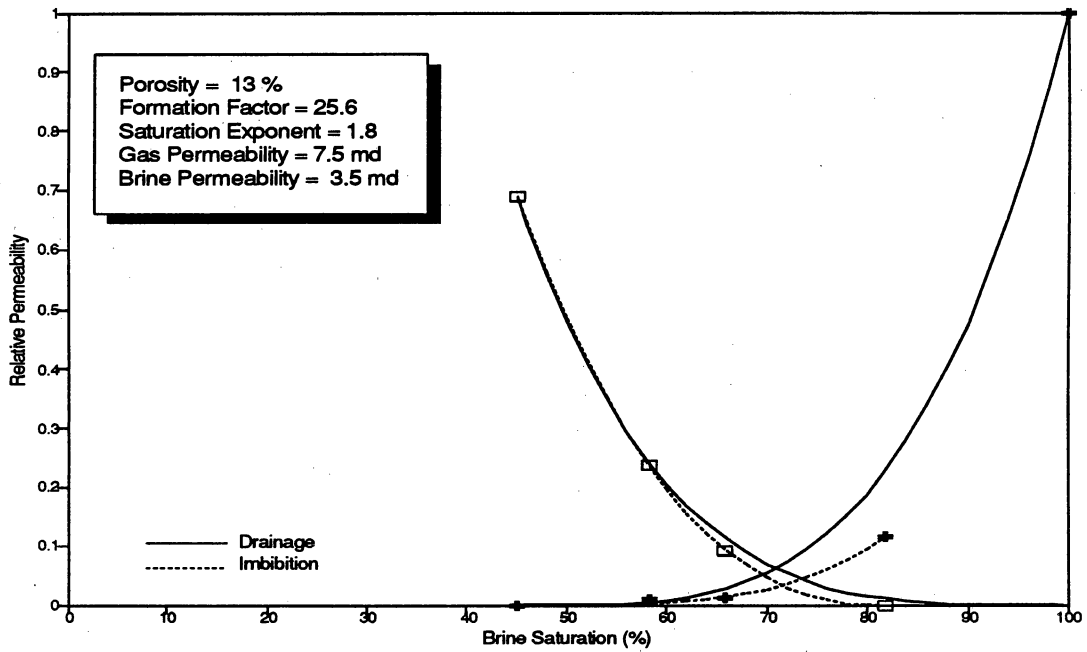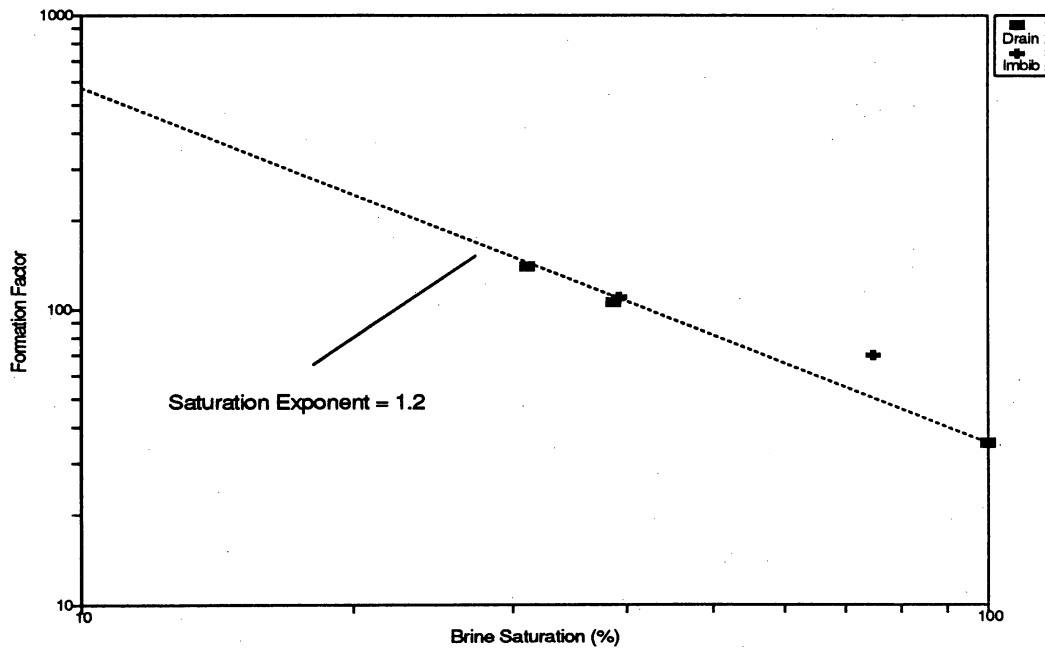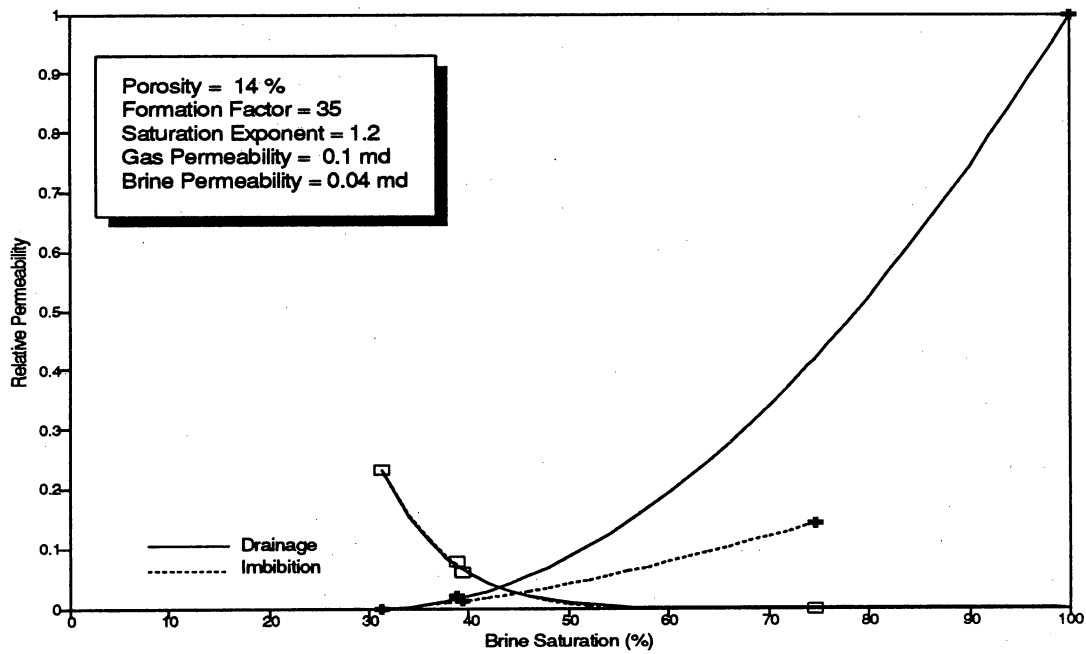
(a)
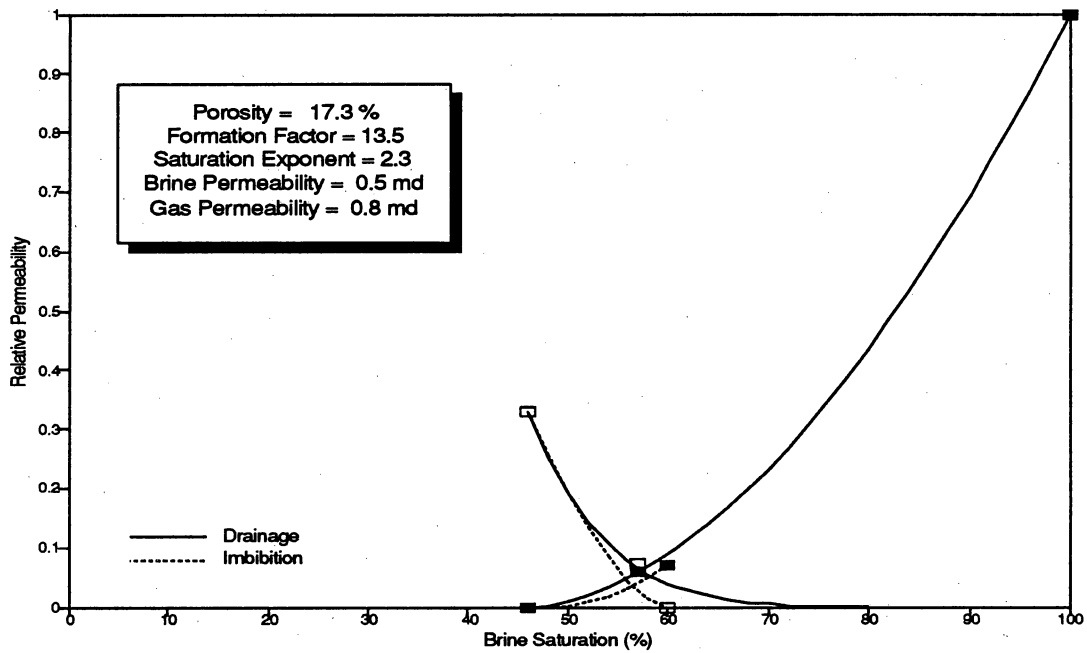
(b)

Figure A2. Variations in formation factor (a) and relative gas and water permeabilities (b) as functions of pore volume brine saturation for a distributary channel facies from the top of a contorted zone in the Muddy Creek outcrop of Ferron Unit 5 (Set 2, Block 1).
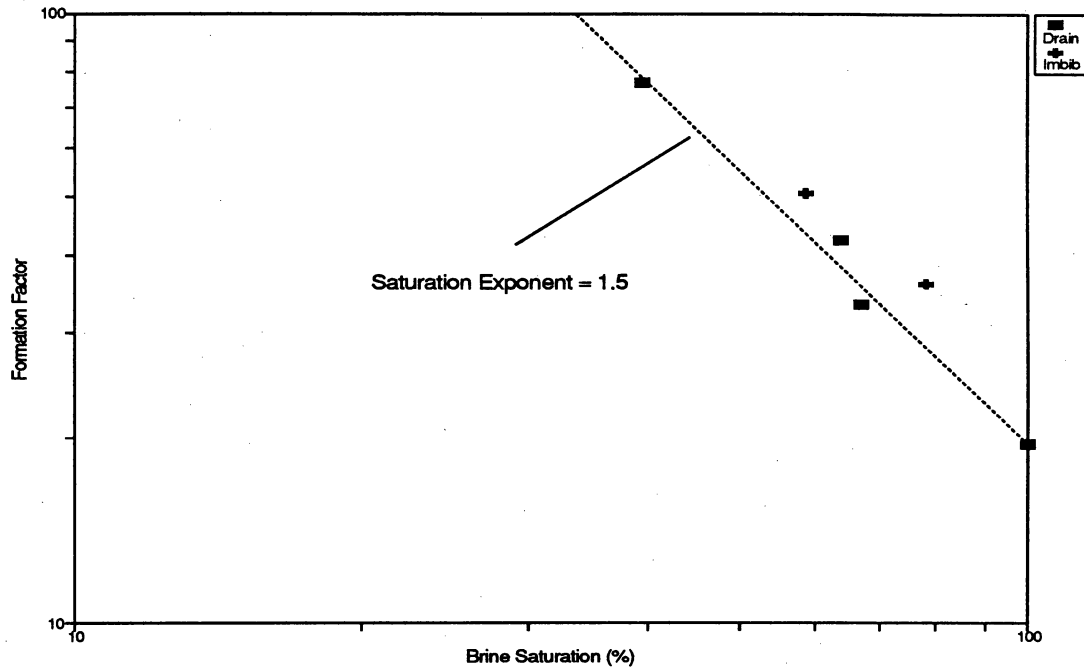
(a)
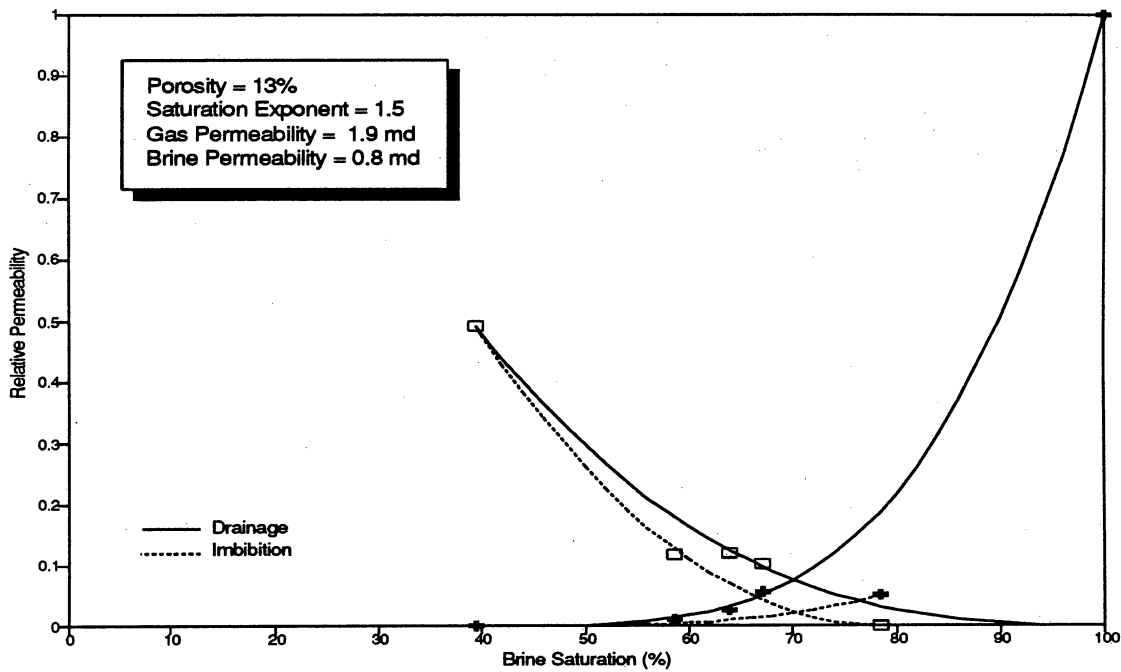
(b)

Figure A3. Variations in formation factor (a) and relative gas and water permeabilities (b) as functions of pore volume brine saturation for a distributary channel facies from a horizontally laminated zone in the Muddy Creek outcrop of Ferron Unit 5 (Set 2, Block 2).
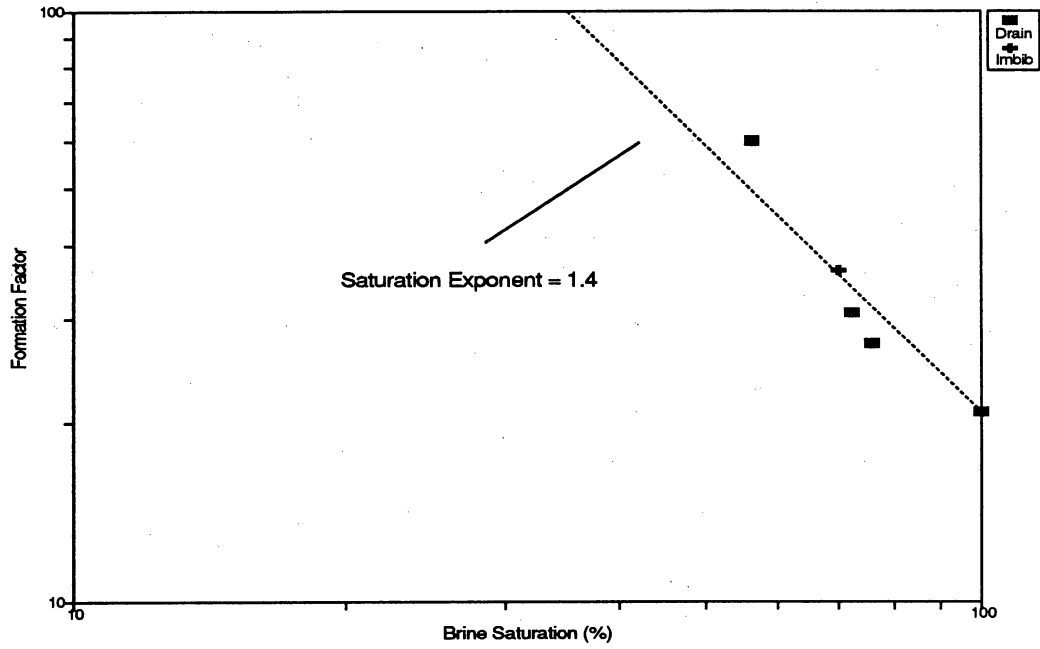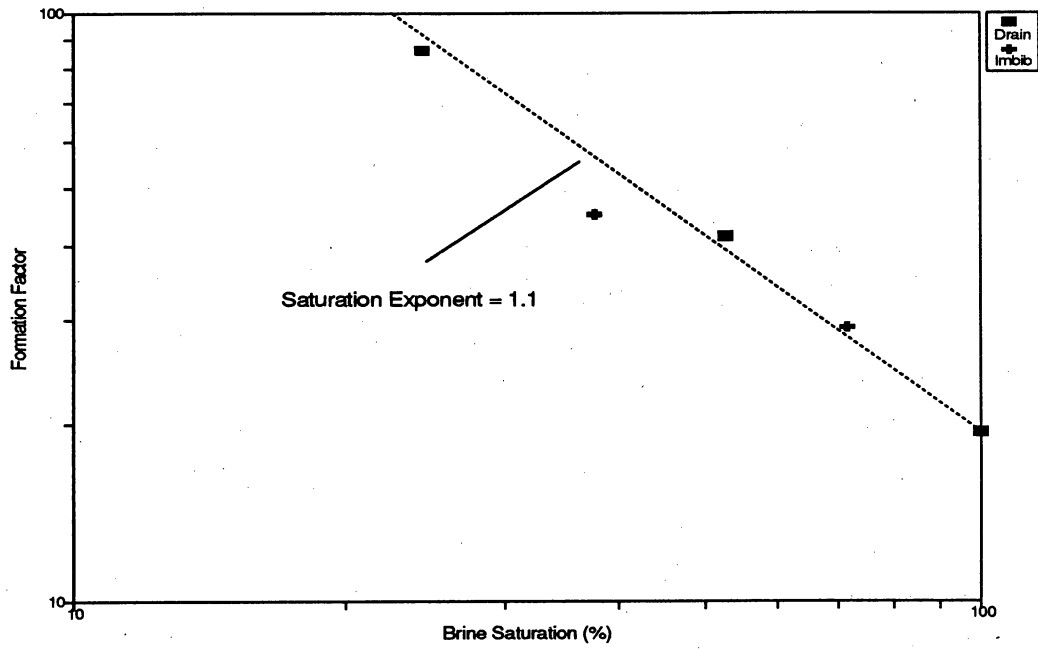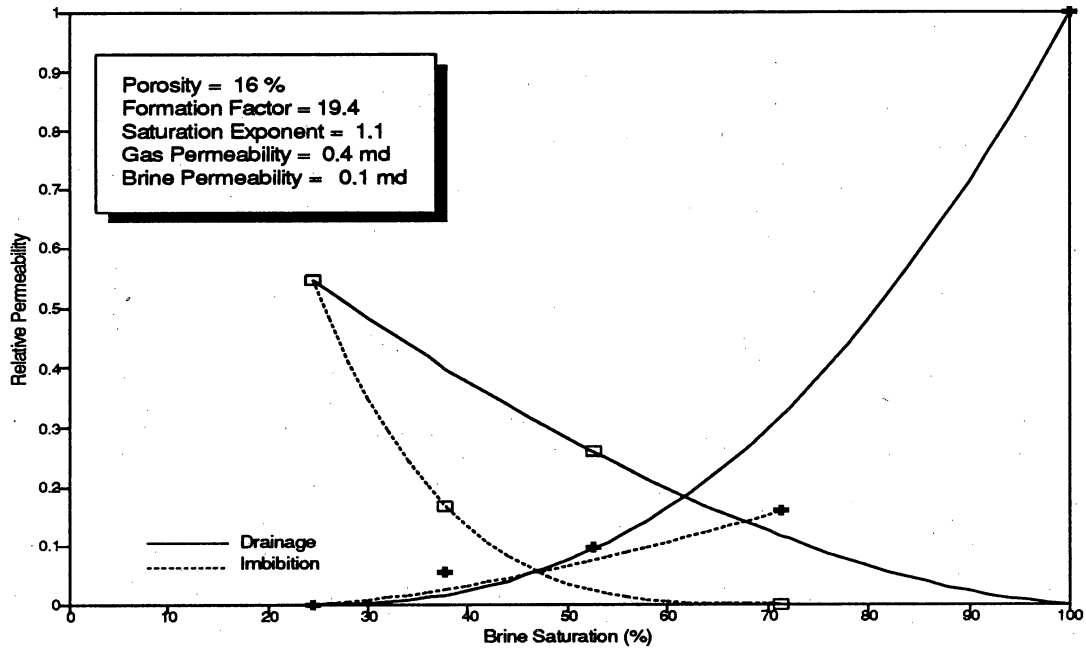
(a)
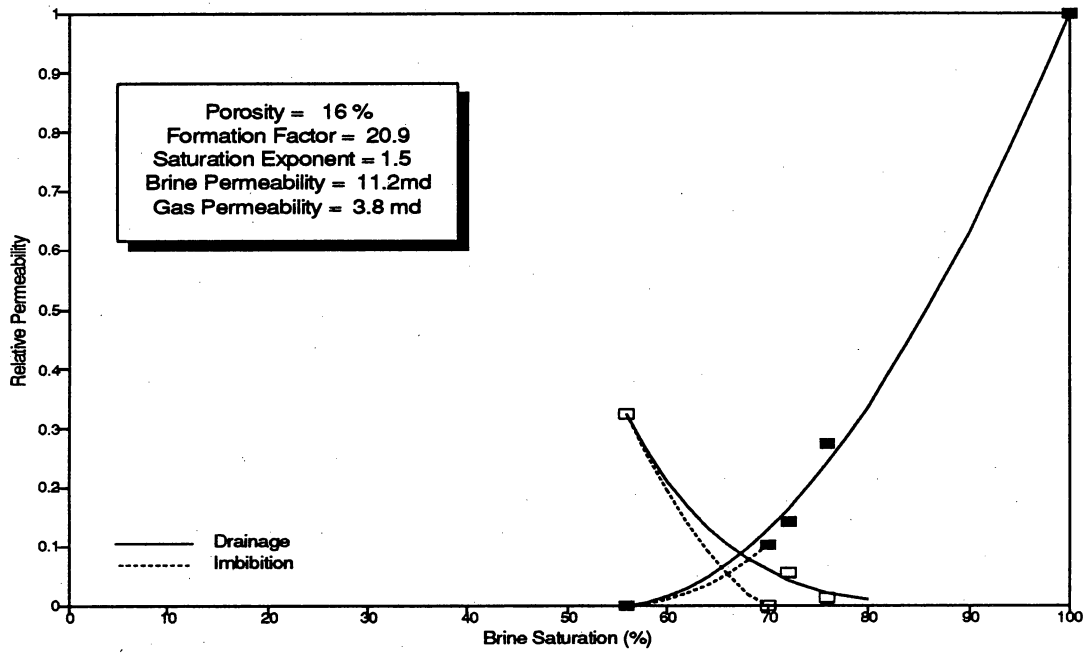
(b)

Figure A4. Variations in formation factor (a) and relative gas and water permeabilities (b) as functions of pore volume brine saturation for a distributary channel facies from a trough cross-bedded zone in the Muddy Creek outcrop of Ferron Unit 5 (Set 2, Block 3).
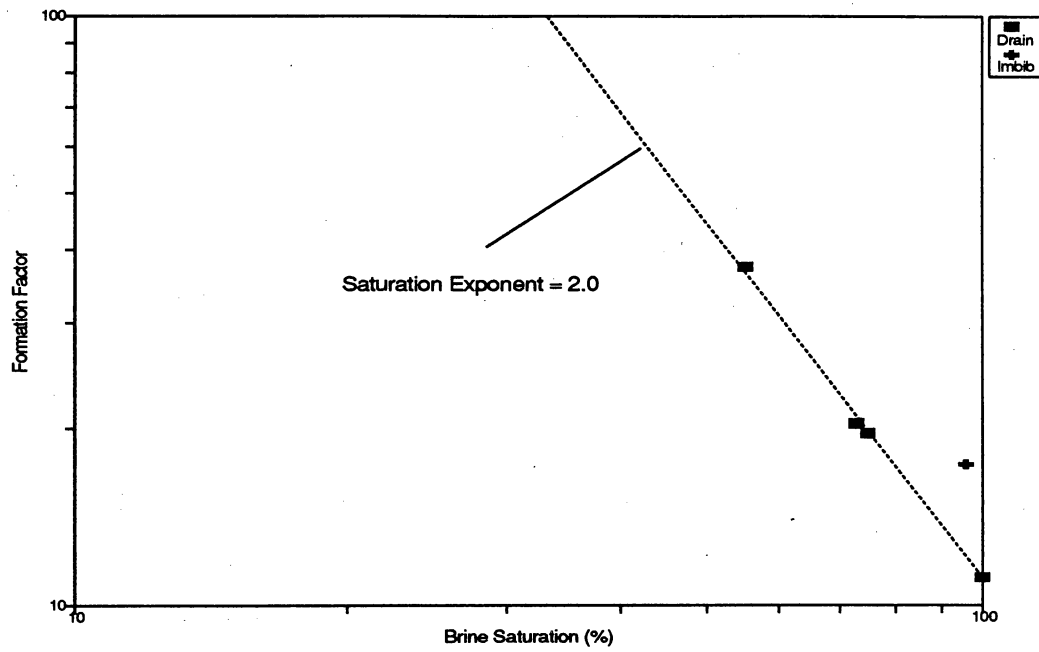
(a)
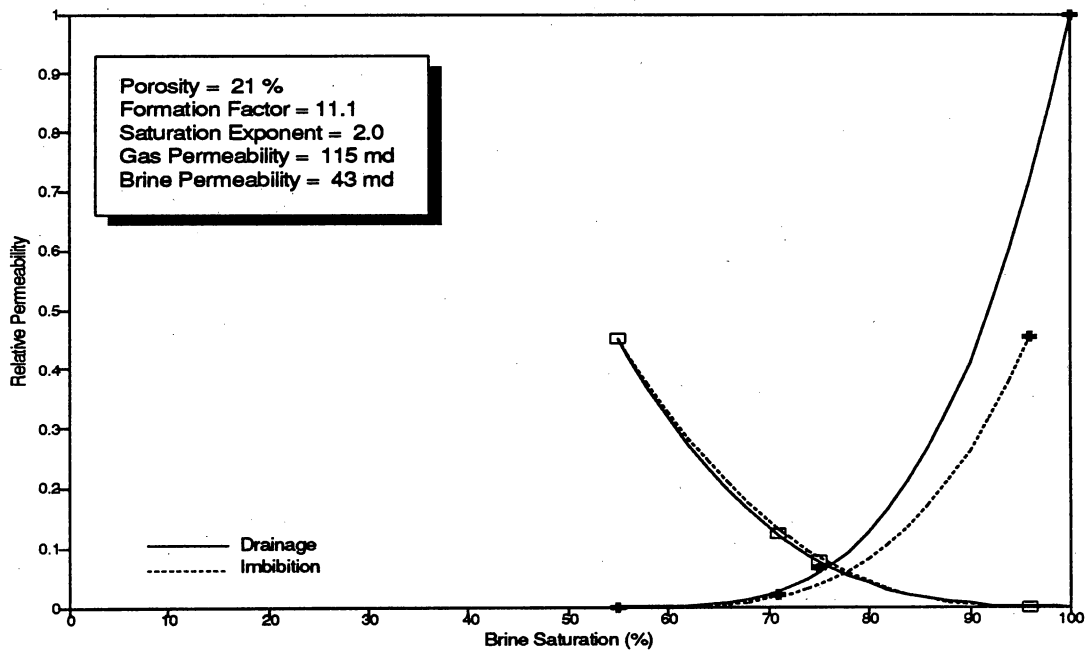
(b)

Figure A5. Variations in formation factor (a) and relative gas and water permeabilities (b) as functions of pore volume brine saturation for a distributary channel facies from a planar cross-bedded zone in the Muddy Creek outcrop of Ferron Unit 5 (Set 2, Block 5).
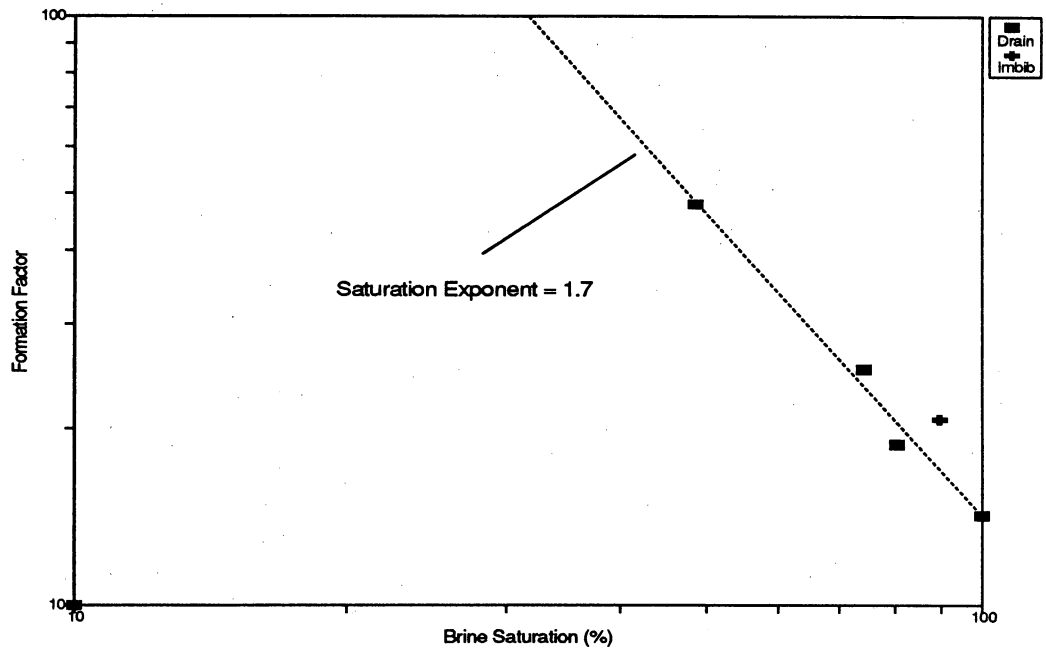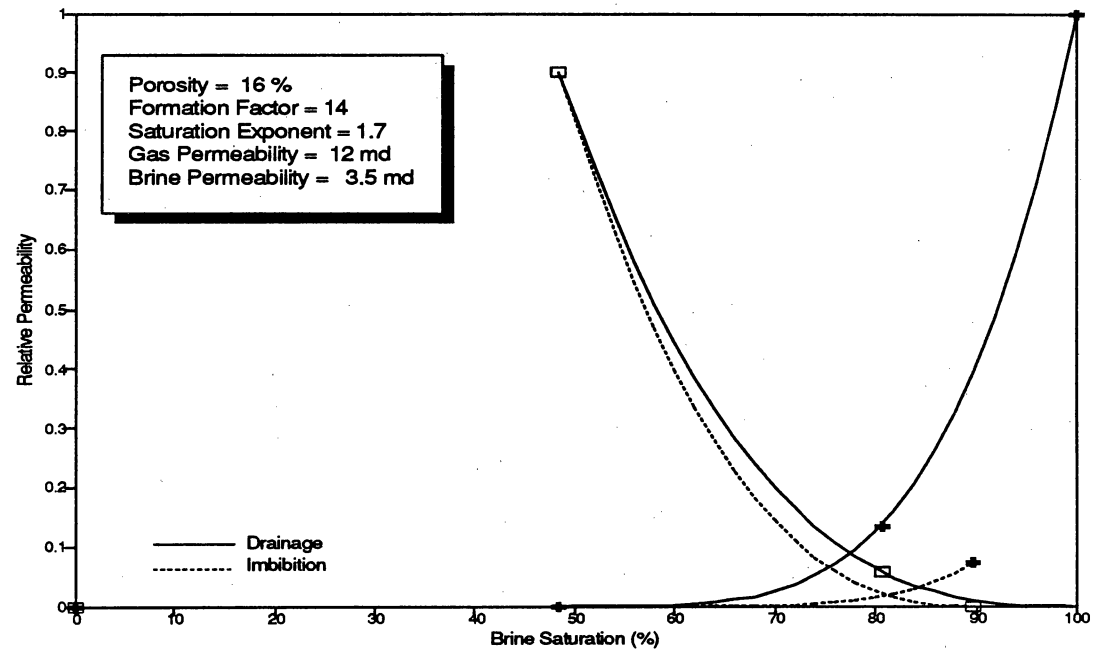
105
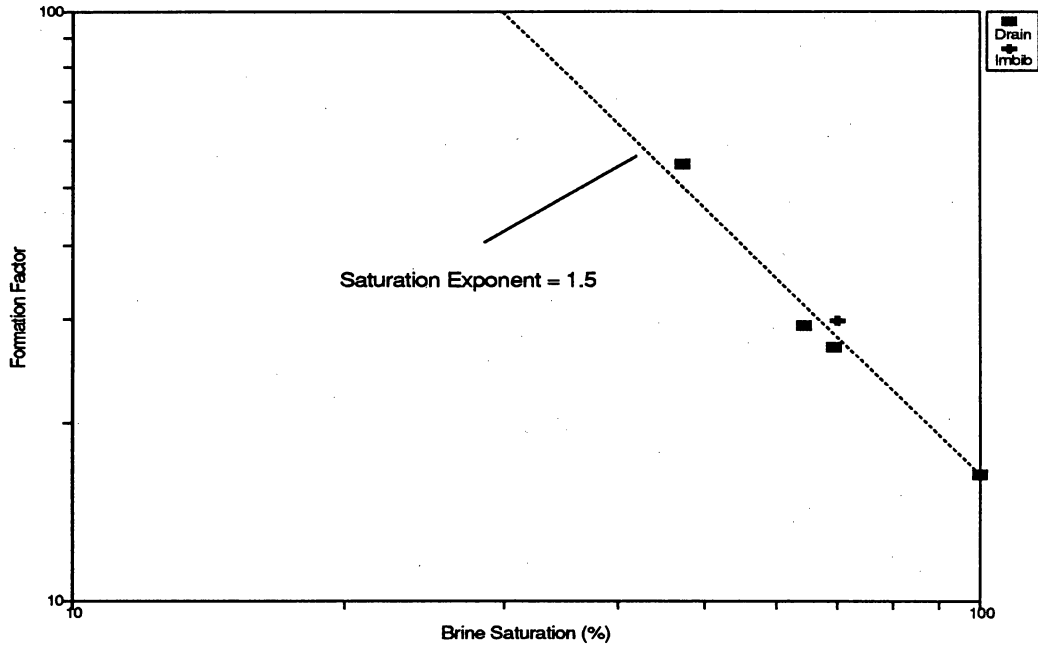
(a)
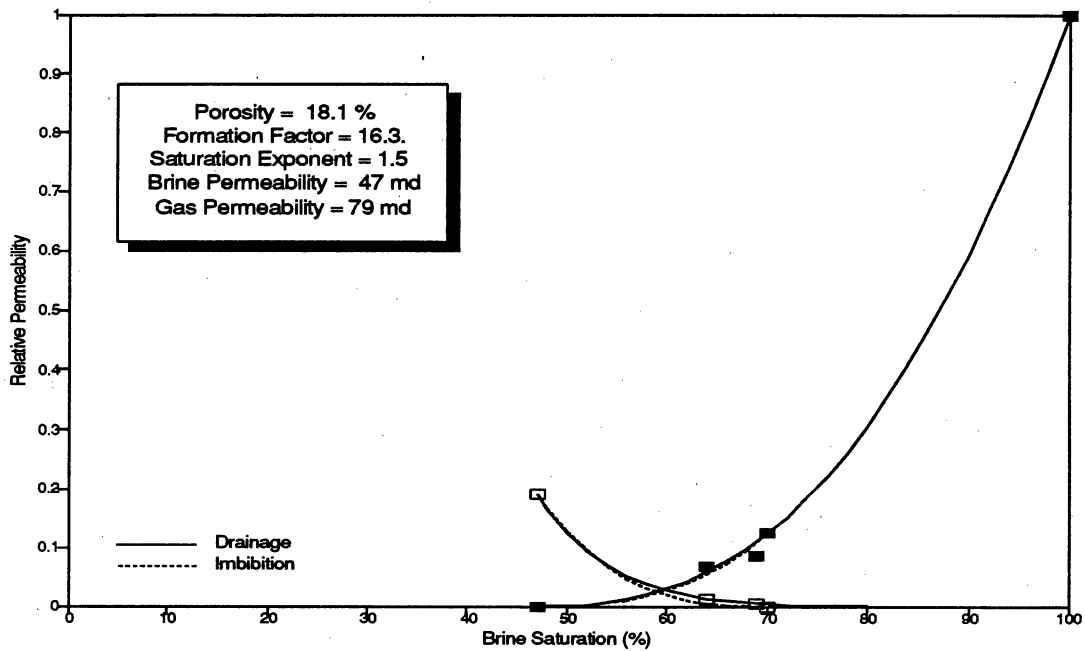
(b)

Figure A6. Variations in formation factor (a) and relative gas and water permeabilities (b) as functions of pore volume brine saturation for a sample from the base of a distributary channel facies in the Muddy Creek outcrop of Ferron Unit 5 (Set 2, Block 9).

106
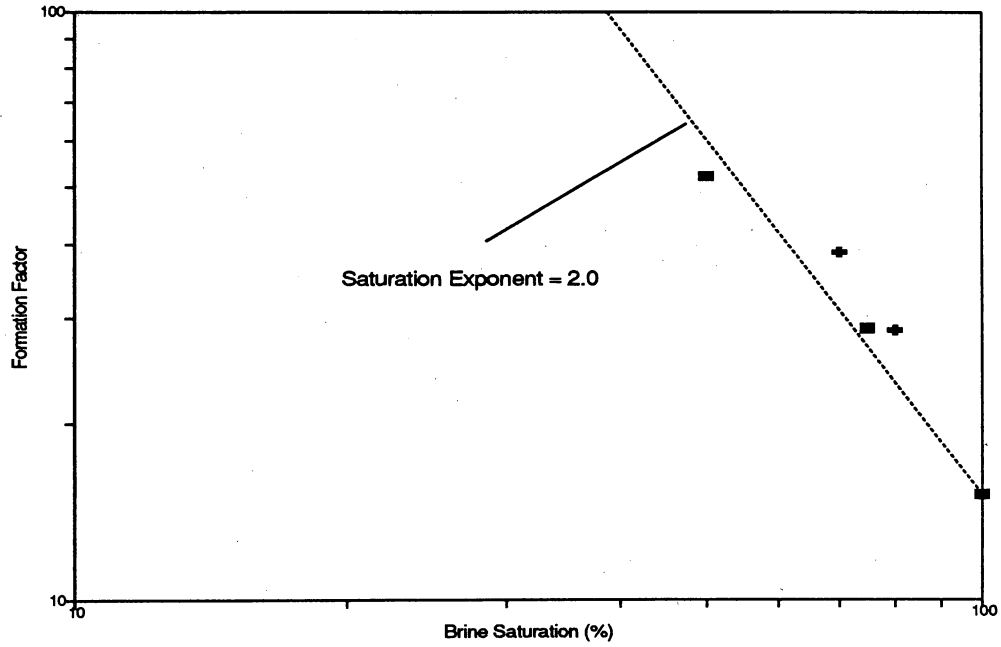
(a)
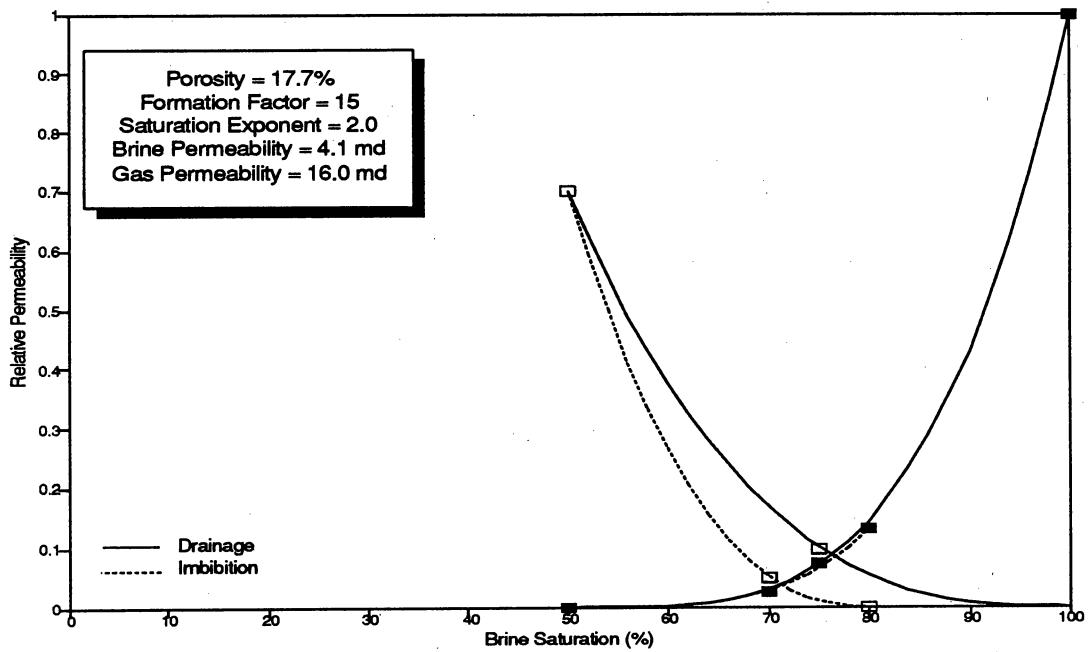
(b)

Figure A7. Variations in formation factor (a) and relative gas and water permeabilities (b) as functions of pore volume brine saturation for a sample from the upper part of a distributary channel facies in the Muddy Creek outcrop of Ferron Unit 5 (Set 2, Block 11).
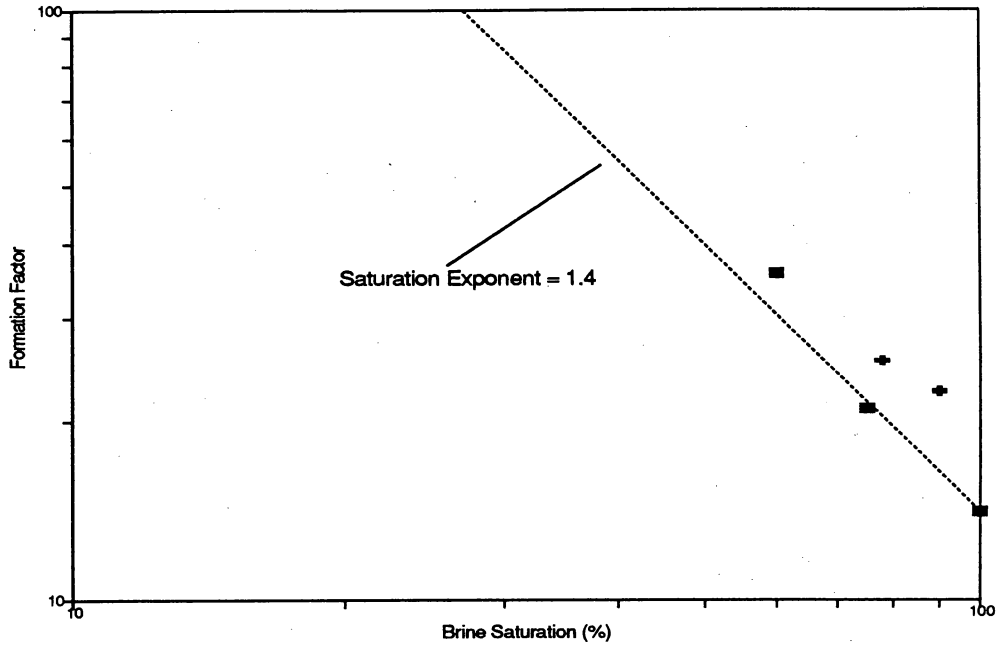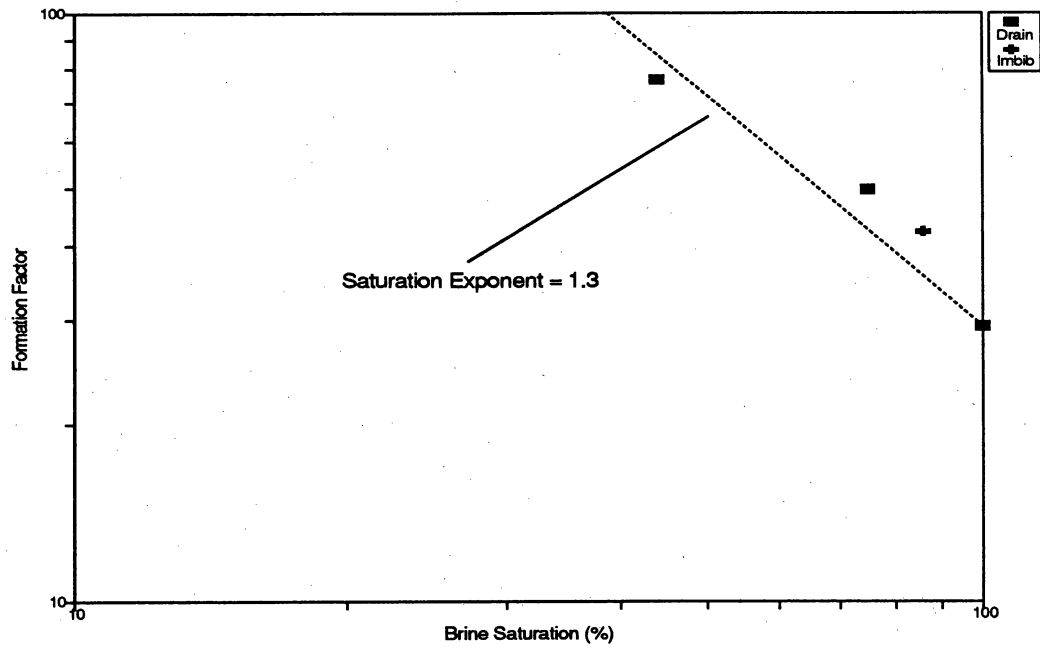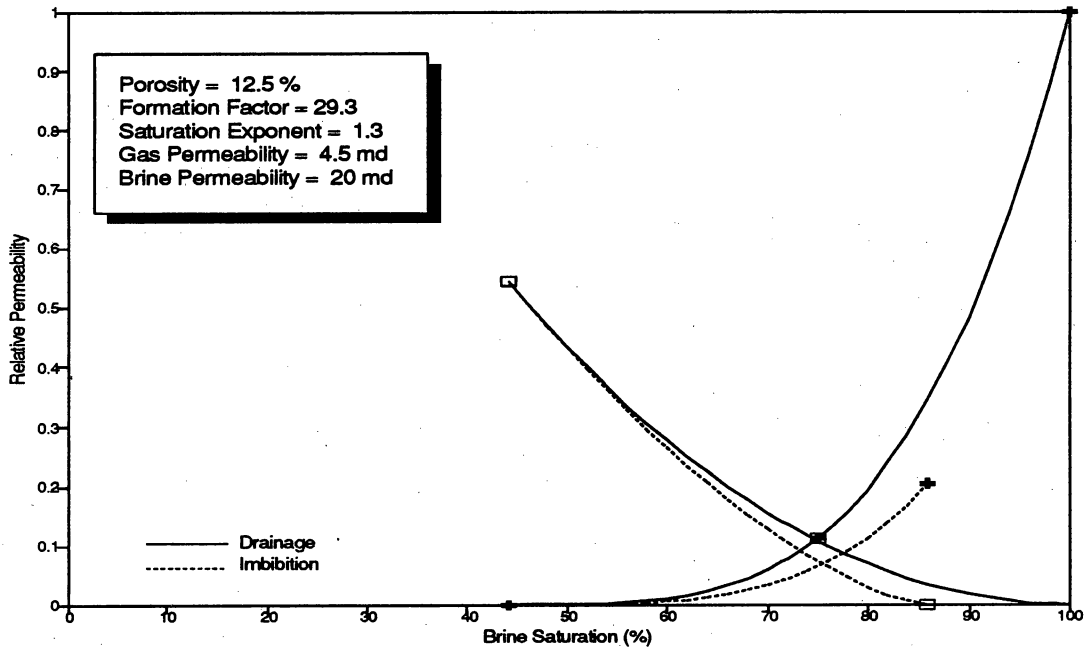
(a)
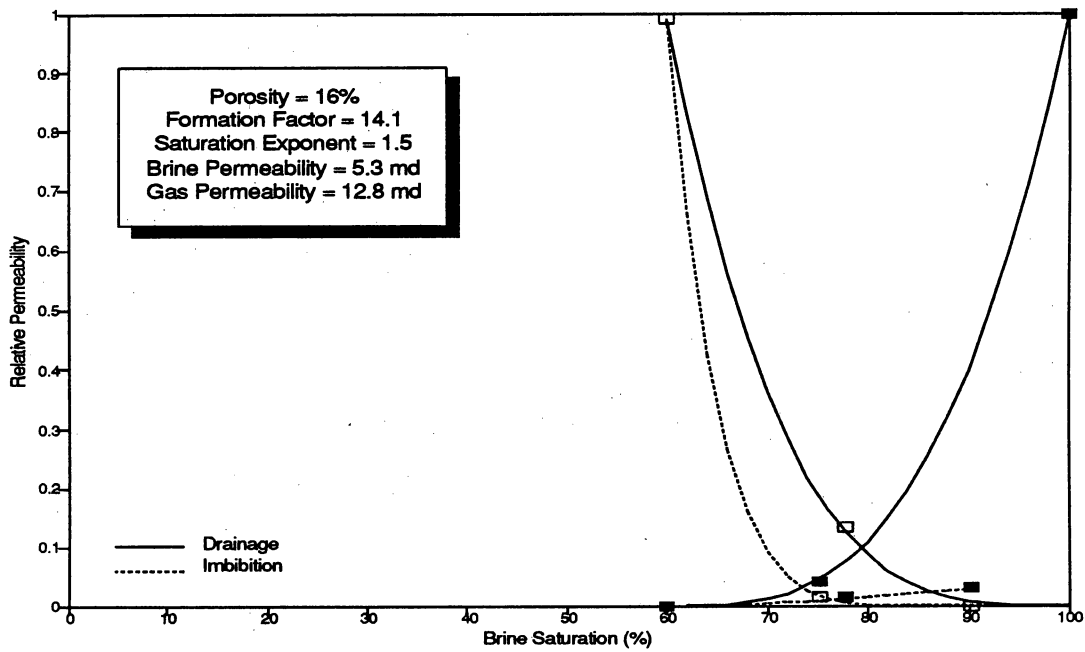
(b)

Figure A8. Variations in formation factor (a) and relative gas and water permeabilities (b) as functions of pore volume brine saturation for a distributary channel facies from a point bar in the Muddy Creek outcrop of Ferron Unit 5 (Set 2, Block 12).

108
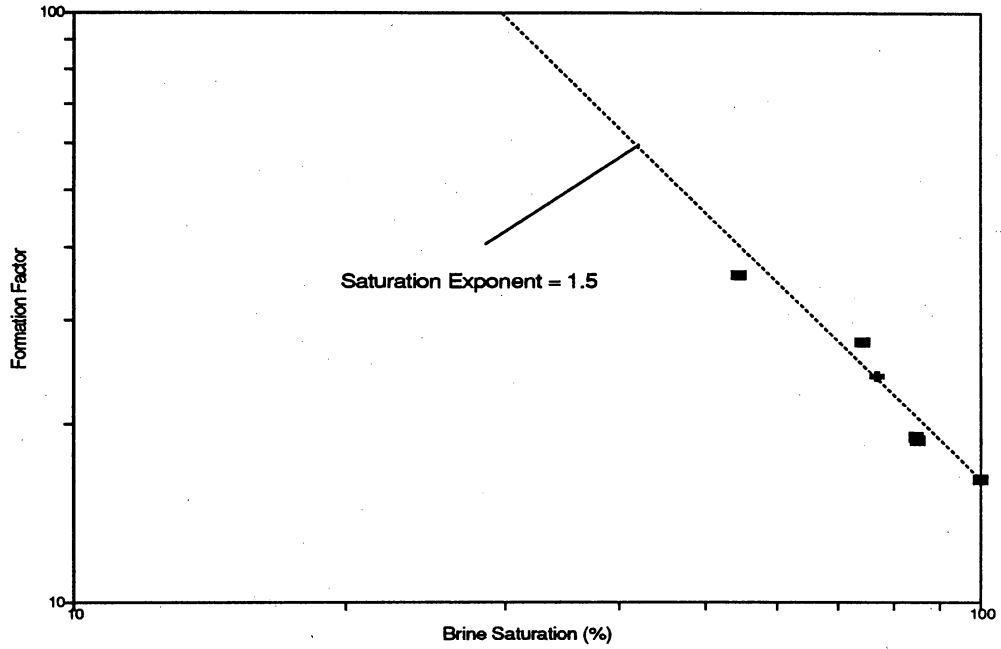
(a)
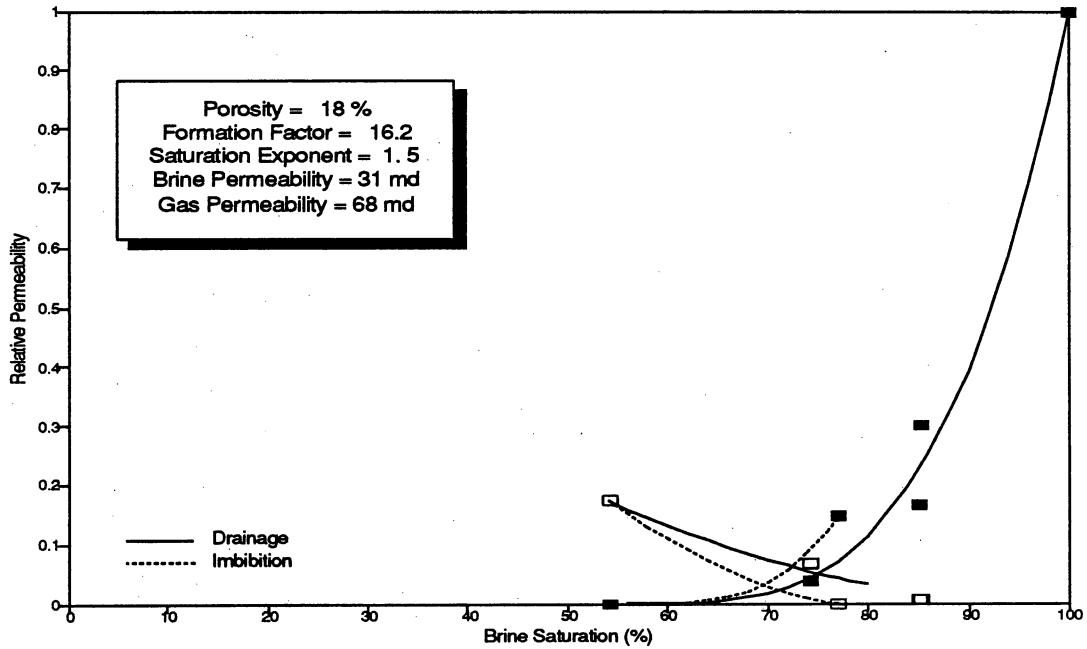
(b)

Figure A9. Variations in formation factor (a) and relative gas and water permeabilities (b) as functions of pore volume brine saturation for a facies from the lower part of a distributary channel in the Muddy Creek outcrop of Ferron Unit 5 (Set 2, Block 13).
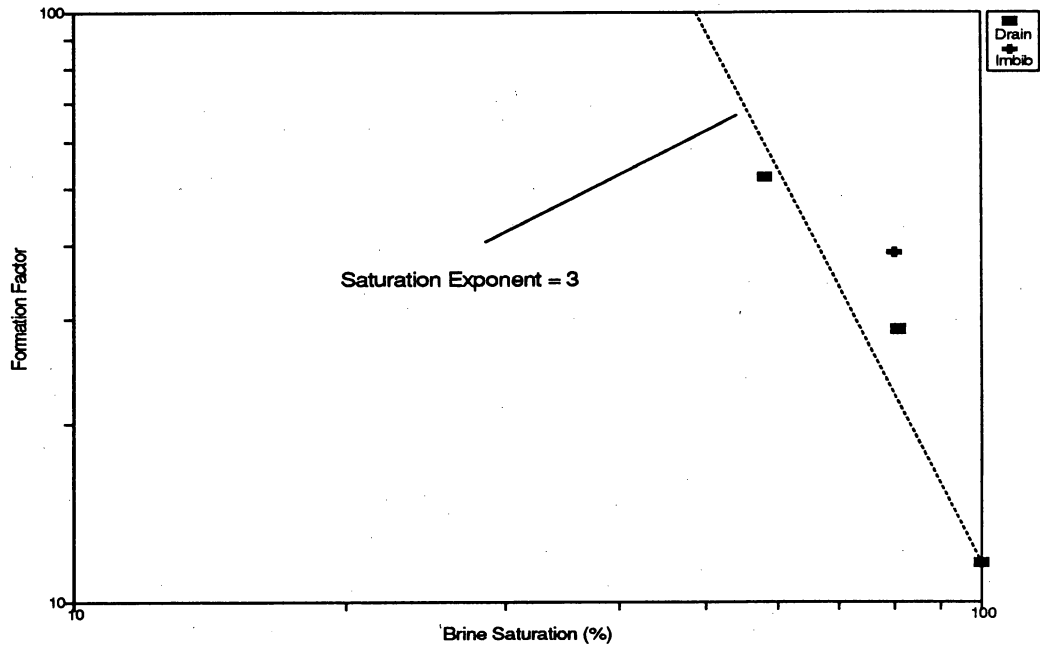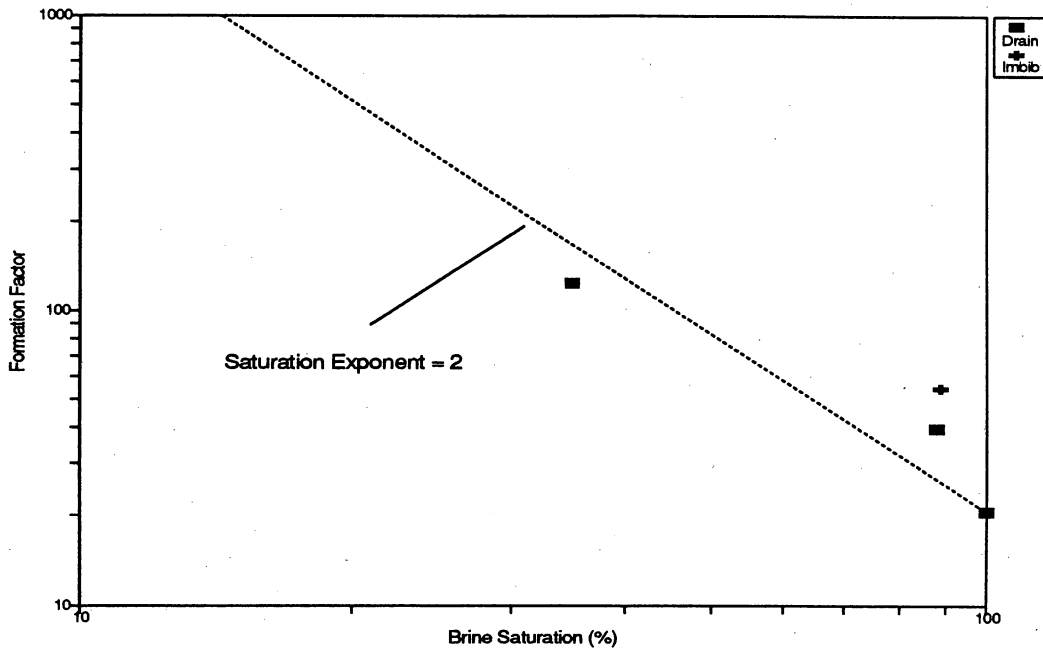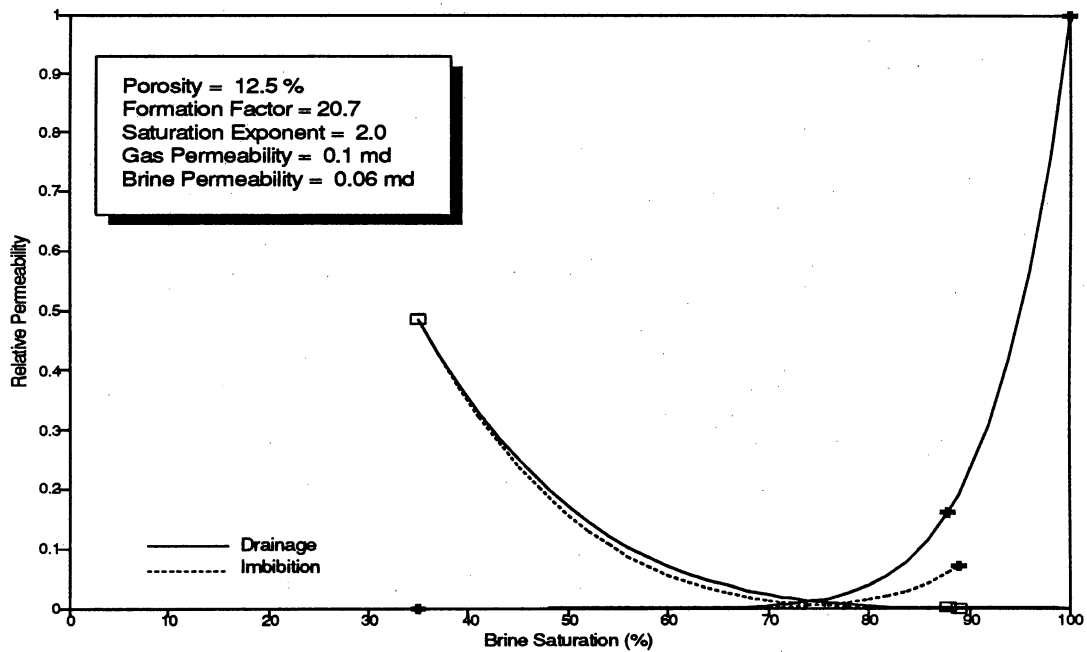
(a)
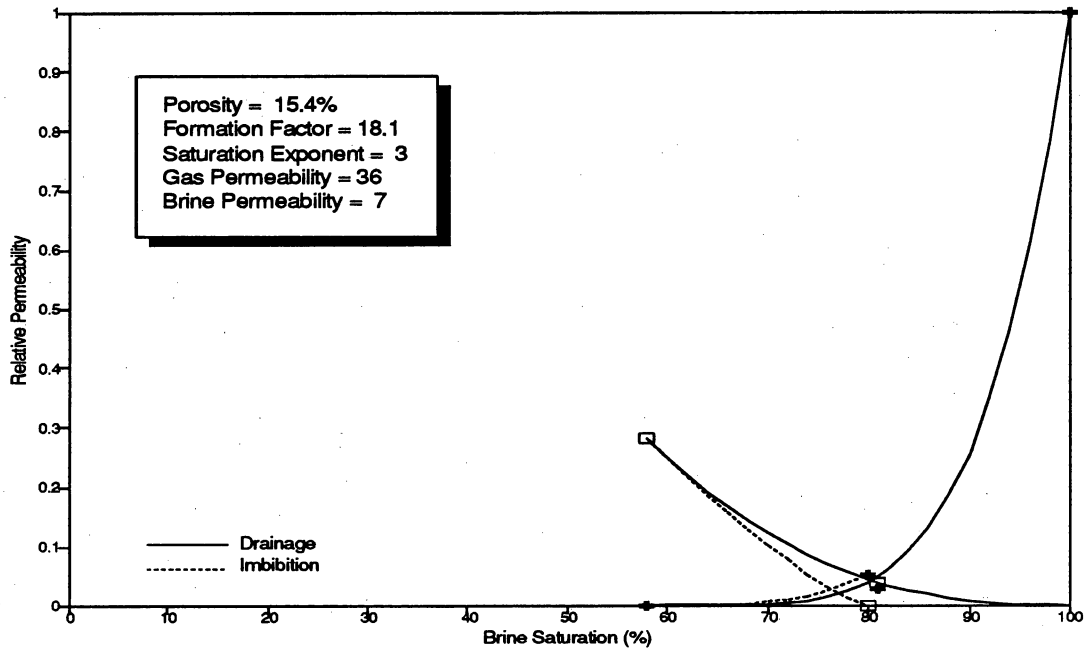
(b)

Figure A10. Variations in formation factor (a) and relative gas and water permeabilities (b) as functions of pore volume brine saturation for a massive sandstone facies in the Picture Flats outcrop of Ferron Unit 5 (Set 3, Block 4).
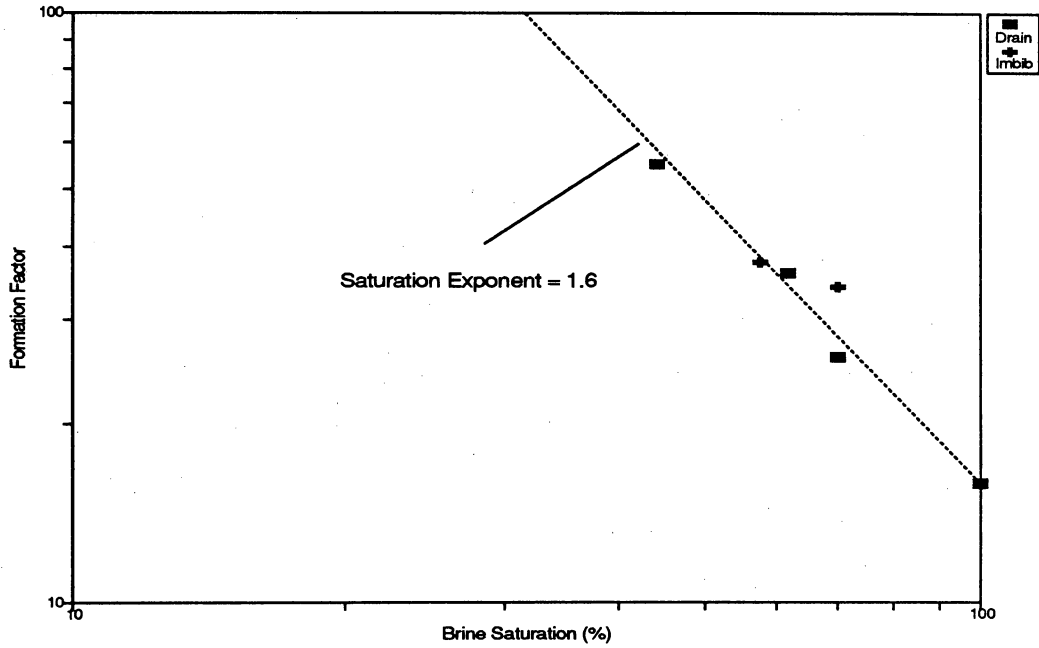
(a)
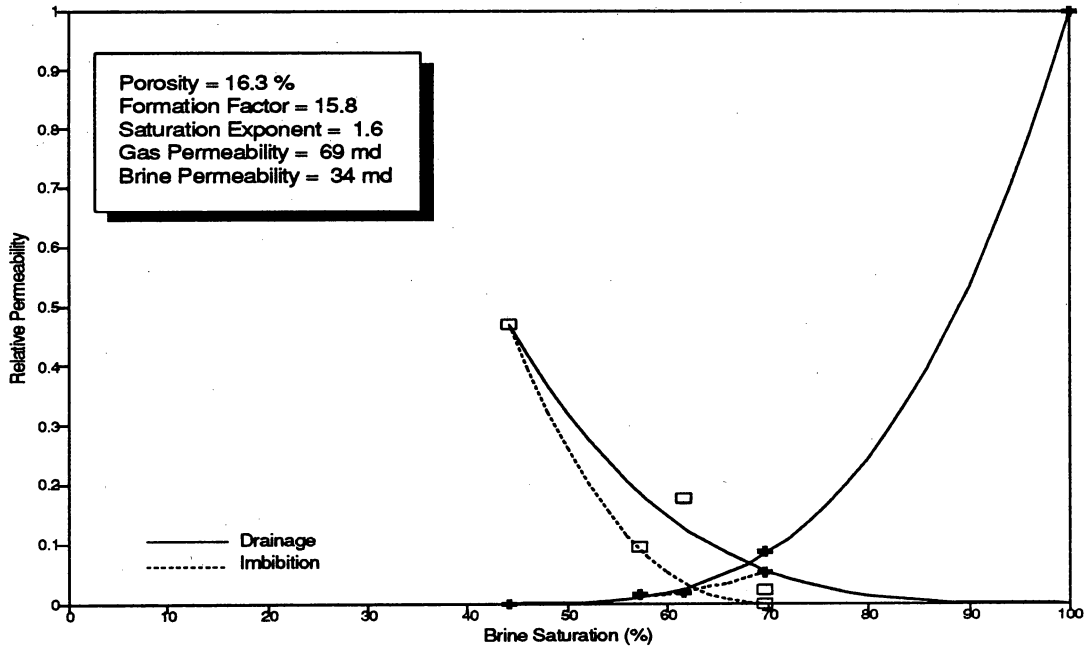
(b)

Figure A11. Variations in formation factor (a) and relative gas and water permeabilities (b) as functions of pore volume brine saturation for a sample from the top of a distributary channel in the Picture Flats outcrop of Ferron Unit 5 (Set 3, Block 5).
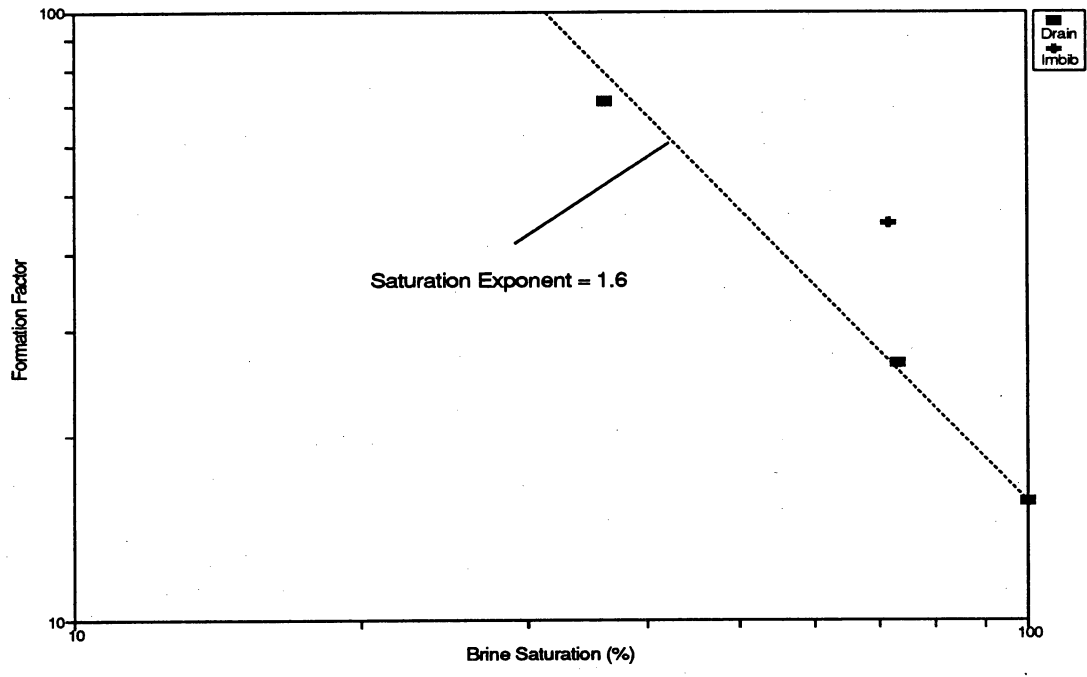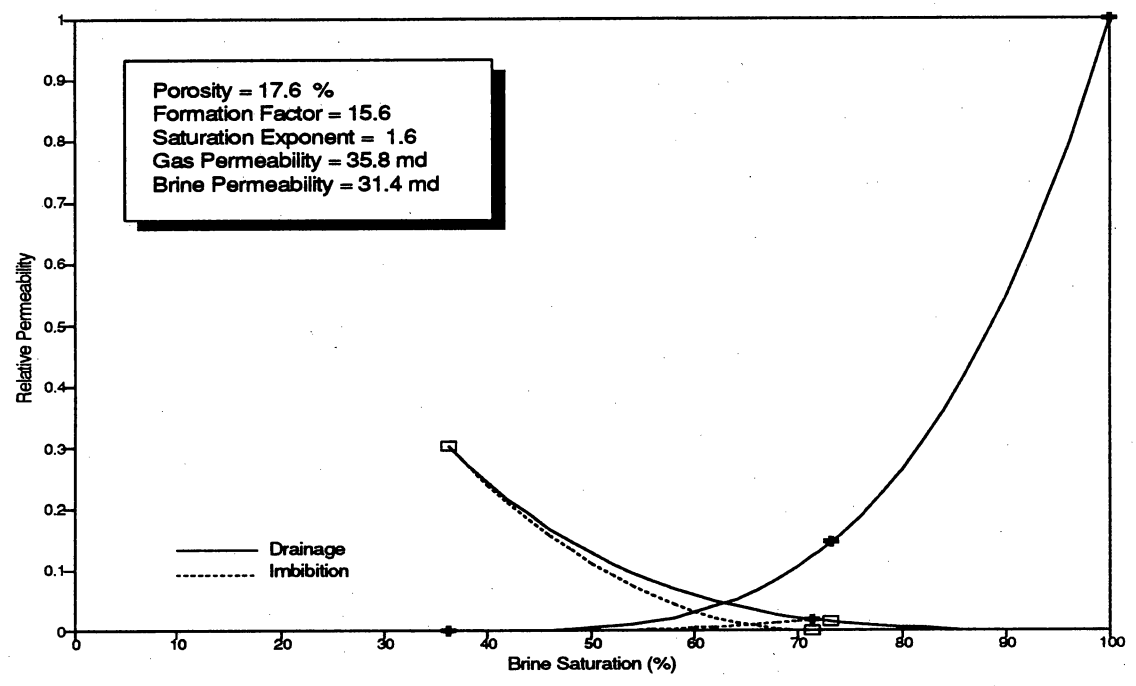
111
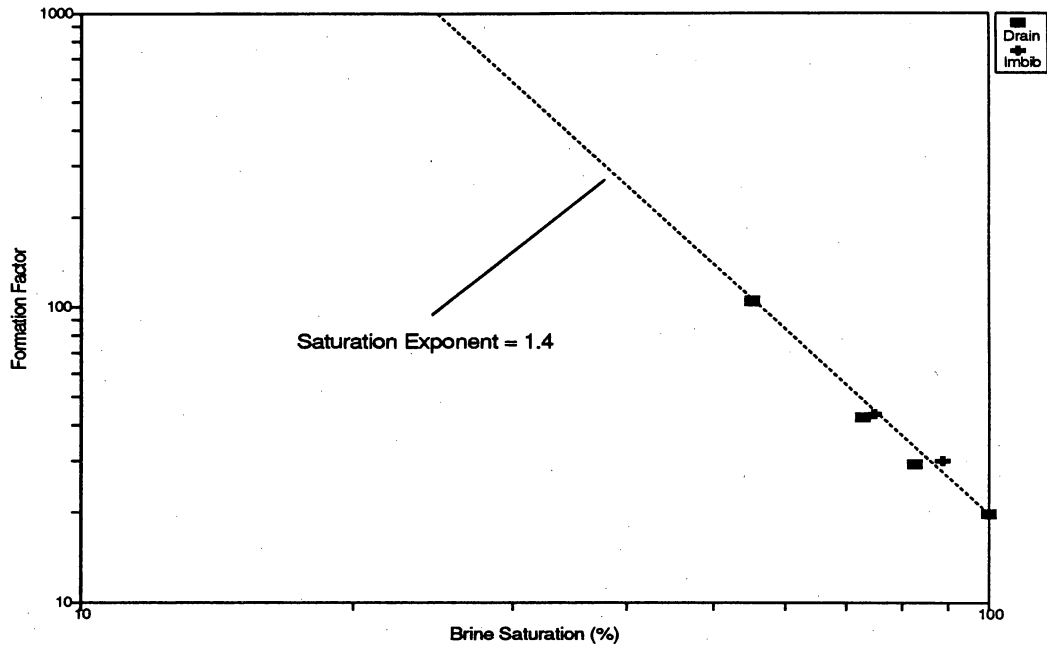
(a)
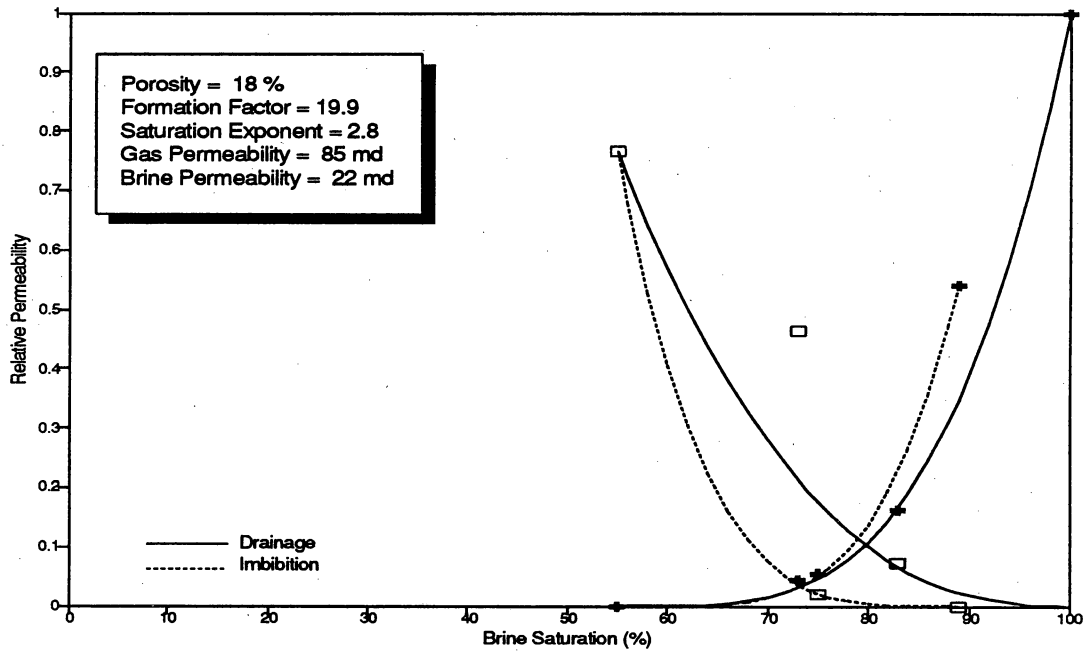
(b)

Figure A12. Variations in formation factor (a) and relative gas and water permeabilities (b) as functions of pore volume brine saturation for a sample with mud clasts from the base of a distributary channel in the Picture Flats outcrop of Ferron Unit 5 (Set 3, Block 6).
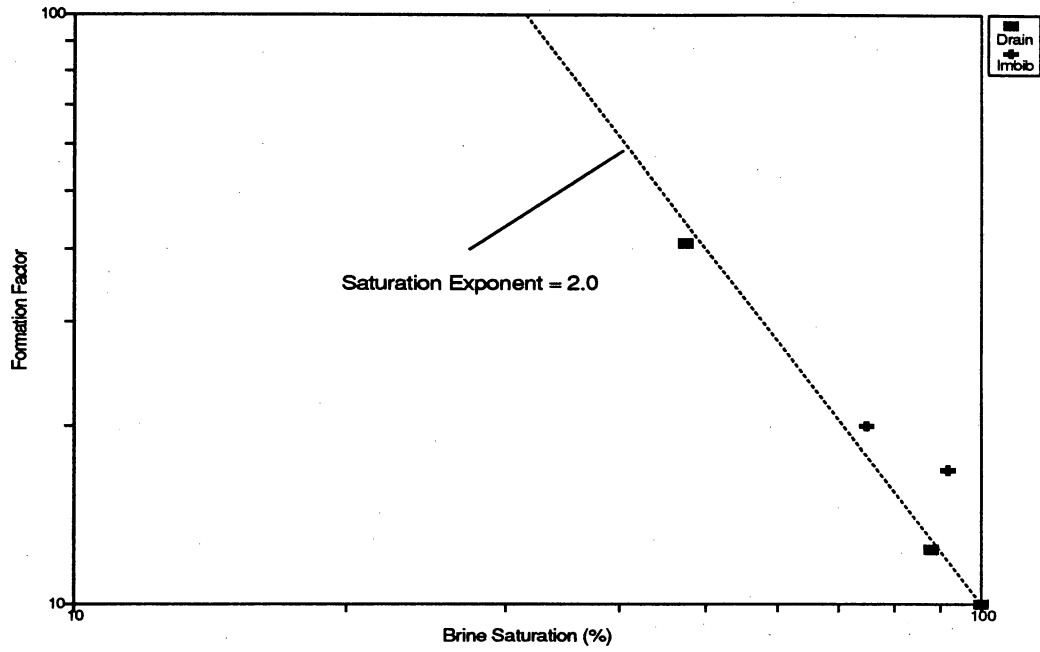
112
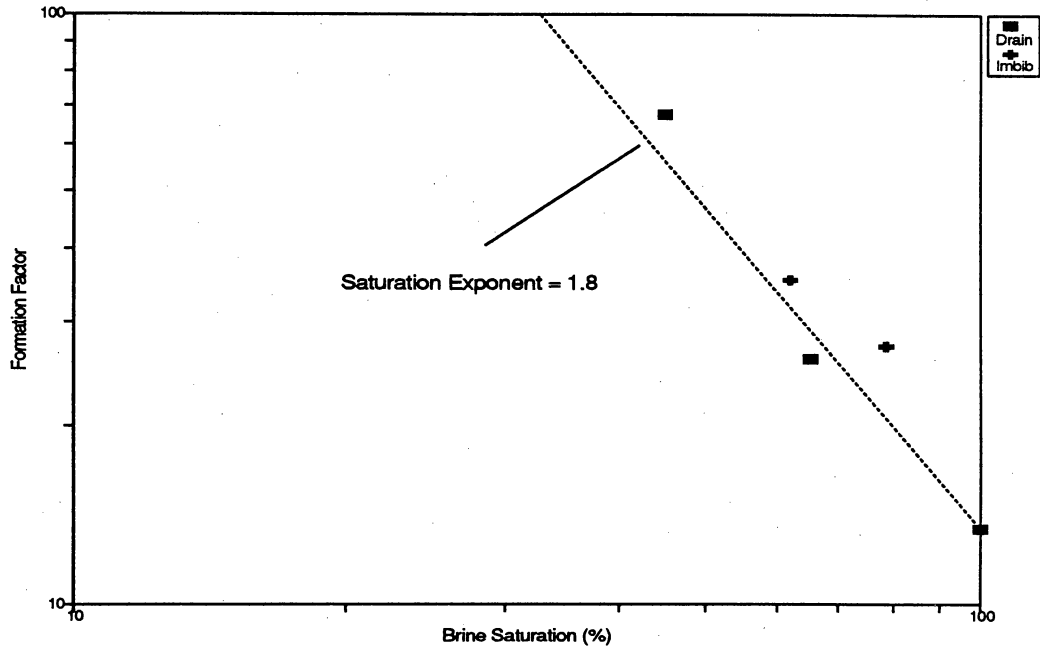
(a)
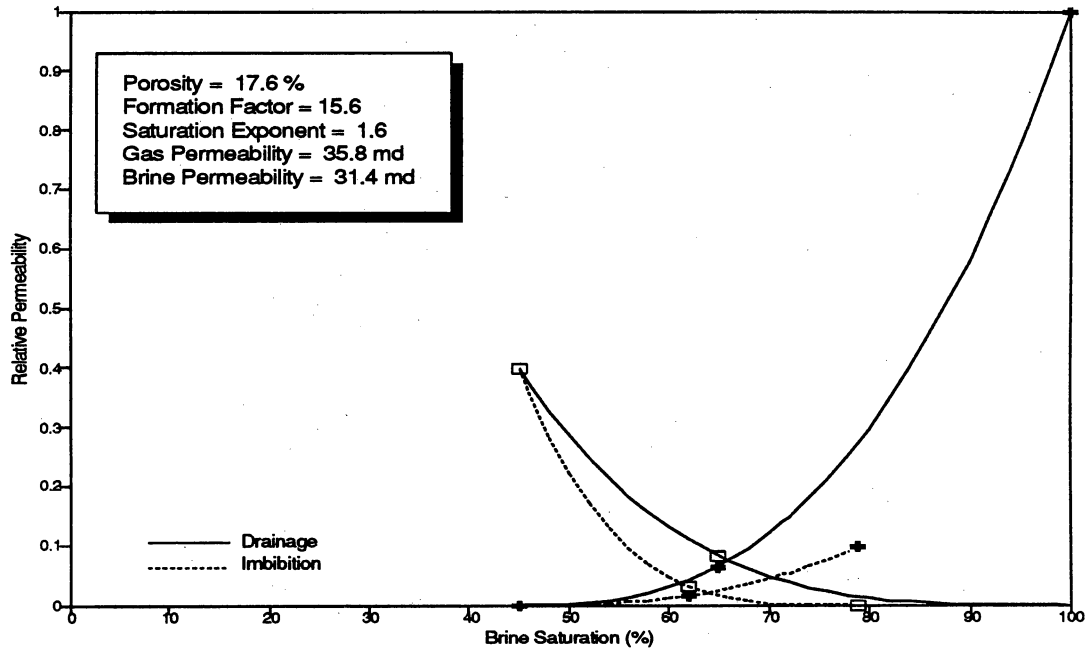
(b)

Figure A13. Variations in formation factor (a) and relative gas and water permeabilities (b) as functions of pore volume brine saturation for a distributary channel facies from a zone of small scale trough cross bedding in the Picture Flats outcrop of Ferron Unit 5 (Set 3, Block 7).
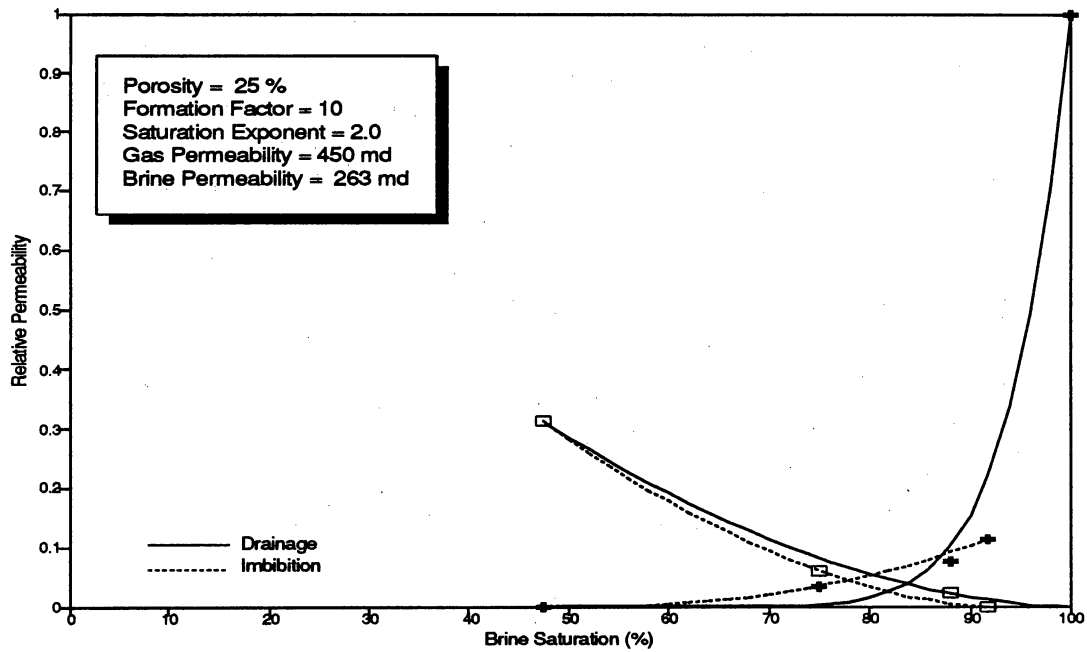
113
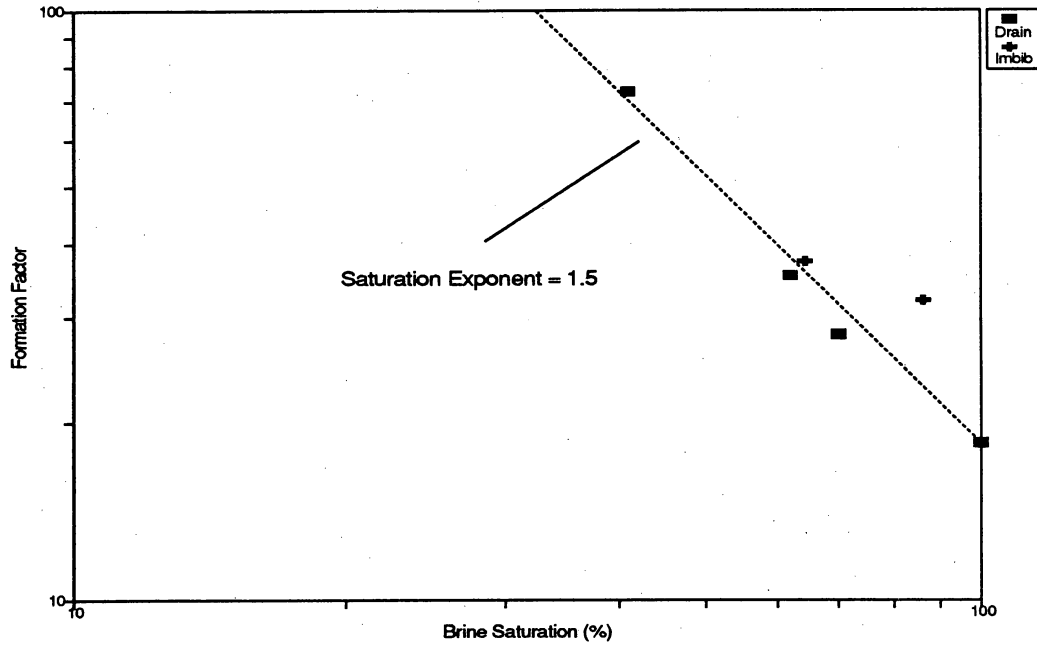
(a)
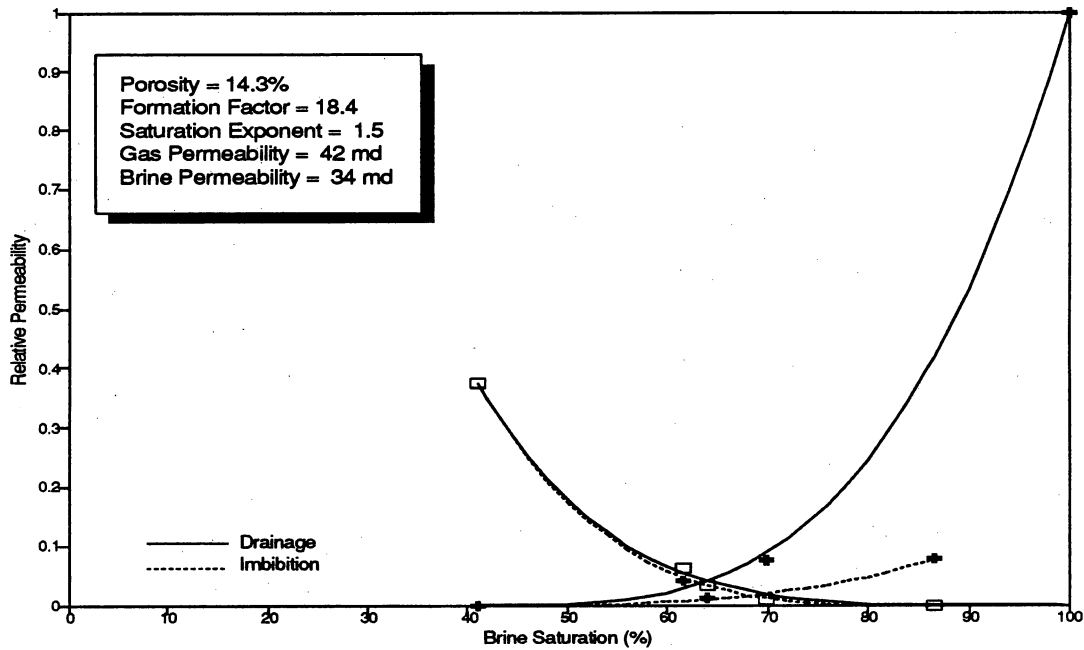
(b)

Figure A14. Variations in formation factor (a) and relative gas and water permeabilities (b) as functions of pore volume brine saturation for a sample from a levee/crevasse-splay deposit in the Picture Flats outcrop of Ferron Unit 5 (Set 3, Block 8).

114
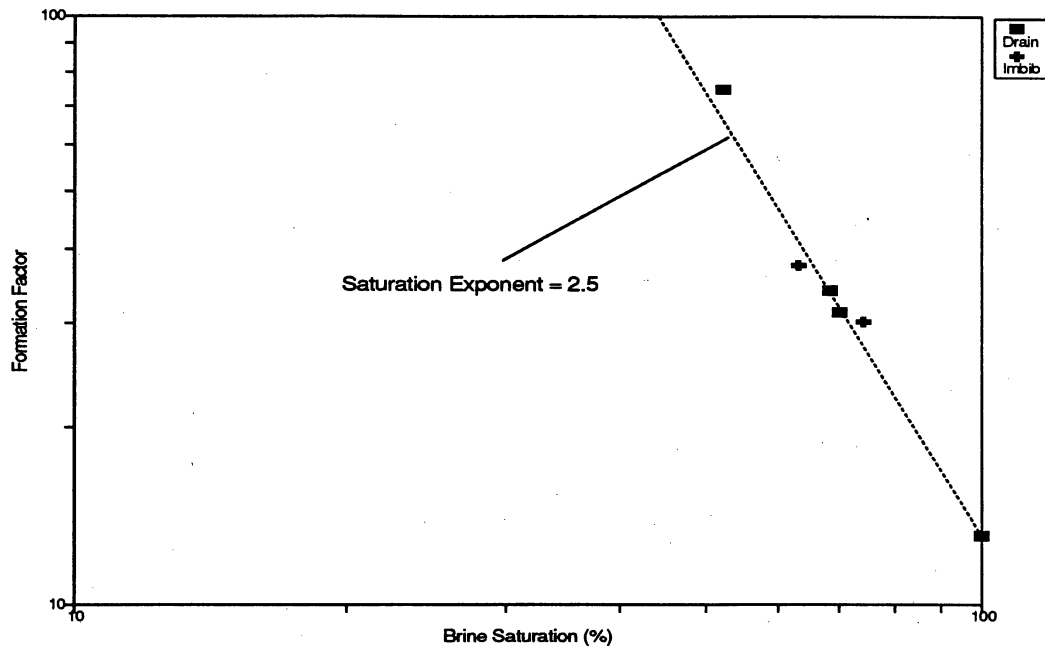
(a)
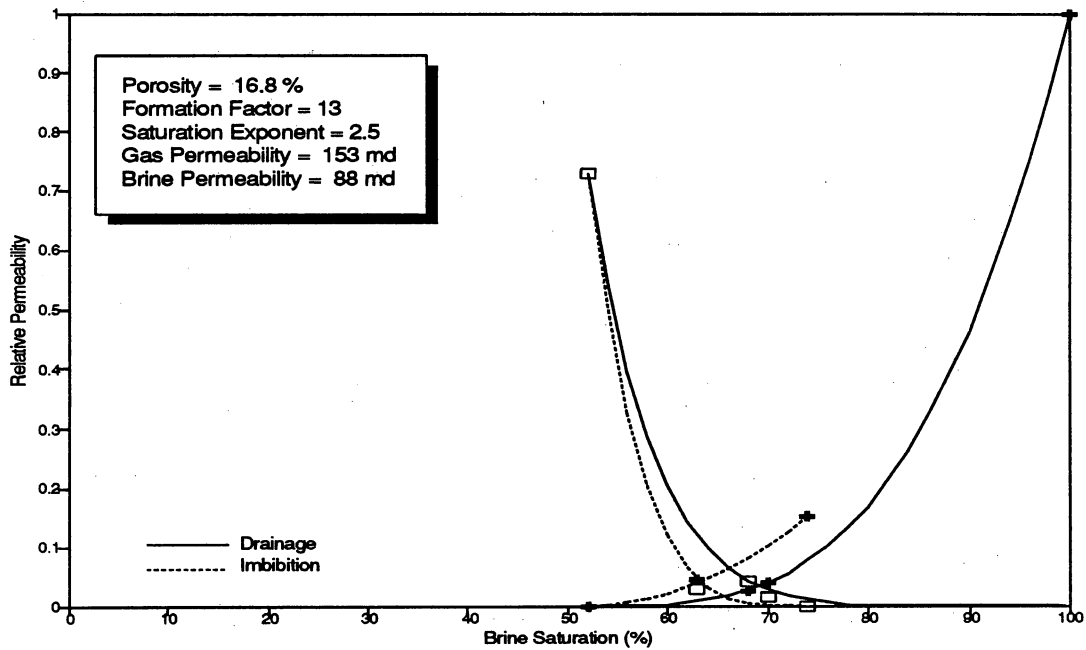
(b)

Figure A15. Variations in formation factor (a) and relative gas and water permeabilities (b) as functions of pore volume brine saturation for a sample from a mouth bar deposit in the Picture Flats outcrop of Ferron Unit 2 (Set 3, Block 9).

(a)

Porosity = 16.1%
Formation Factor = 15.8
Saturation Exponent = 1.5
Gas Permeability = 1.5 md
Brine Permeability = 0.9 md

(b)

Figure A16. Variations in formation factor (a) and relative gas and water permeabilities (b) as functions of pore volume brine saturation for a lower fluvial depositional facies from the top of a channel in the Muddy Creek outcrop of Ferron Unit 4 (Set 2, Block 6).

116

(a)

(b)

Figure A17. Variations in formation factor (a) and relative gas and water permeabilities (b) as functions of pore volume brine saturation for a fluvial depositional facies from the Muddy Creek outcrop of Ferron Unit 4 (Set 2, Block 8).

(a)

(b)

Figure A18. Variations in formation factor (a) and relative gas and water permeabilities (b) as functions of pore volume brine saturation for a levee deposit in the Picture Flats outcrop of Ferron Unit 4 (Set 3, Block 1), with flow along laminations (Specimen A).

118

(a)

(b)

Figure A19. Variations in formation factor (a) and relative gas and water permeabilities (b) as functions of pore volume brine saturation for a levee deposit facies in the Picture Flats outcrop of Ferron Unit 4 (Set 3, Block 1), with flow across laminations (Specimen C).

119

(a)

(b)

Figure A20. Variations in formation factor (a) and relative gas and water permeabilities (b) as functions of pore volume brine saturation for a ripple laminated facies in the Muddy Creek outcrop of Ferron Unit 2 (Set 4, Block 2), with flow along laminations (Specimen A).

120

(a)

(b)

Figure A21. Variations in formation factor (a) and relative gas and water permeabilities (b) as functions of pore volume brine saturation for a ripple laminated facies in the Muddy Creek outcrop of Ferron Unit 4 (Set 4, Block 2), with flow across laminations (Specimen B).

121

(a)

(b)

Figure A22. Variation in formation factor (a) and relative gas and water permeabilities (b) as functions of pore volume brine saturation for bioturbated delta front facies in the Muddy Creek outcrop of Ferron Unit 5 (Set 1, Block 6).

122

(a)

Porosity = 12.5%
Formation Factor = 20.7
Saturation Exponent = 2.0
Gas Permeability = 0.1 md
Brine Permeability = 0.06 md

(b)

Figure A23. Variation in formation factor (a) and relative gas and water permeabilities (b) as functions of pore volume brine saturation for a delta front facies in the Picture Flats outcrop of Ferron Unit 5 (Set 3, Block 2).

Figure A24. Variation in formation factor (a) and relative gas and water permeabilities (b) as functions of pore volume brine saturation for a sample from the top of a shore face in the Picture Flats outcrop of Ferron Unit 5 (Set 3, Block 3).

(a)

Porosity = 25 %
Formation Factor = 10
Saturation Exponent = 2.0
Gas Permeability = 450 md
Brine Permeability = 263 md

(b)

Figure A25. Variation in formation factor (a) and relative gas and water permeabilities (b) as functions of pore volume brine saturation for a Berea Sandstone sample.

125

The values of the corresponding saturation exponents, n, are listed in table 5. The smoothed lines shown in the plots for relative gas and water permeabilities, k_{gr} and k_{wr}, respectively, are visual fits of the measured points to expressions in the form

$$k_{gr} = k_{gr}(S_{wi}) \cdot [\, 1 - \Phi_R{}^m \,] \tag{A-5}$$

and

$$k_{wr} = k_{wr}(\text{max}) \cdot \Phi_R{}^m, \tag{A-6}$$

where the normalized saturations, Φ_R, are defined by

$$\Phi_R = \frac{[\, S_w - S_{wi} \,]}{[\, S_w(\text{max}) - S_{wi} \,]} \tag{A-7}$$

$k_{wr}(max)$ is equal to 1 or $k_{wr}(S_{gr})$, and $S_w(max)$ is equal to 100 percent or $1 - S_{gr}$, for drainage or imbibition, respectively.

Benchtop permeameter measurements of brine permeabilities were carried out on the post-test specimens from Set 2 Block 11 and Set 3 Block 7 and on the reference Berea sandstone. The condition of the specimens had been altered from that corresponding to the table 5 measurements, by the subsequent static deformation and oven-drying, and the permeameter results are not included in the tabulation. However, in all cases the permeameter results agreed with the brine permeabilities in table 5, to within 30 percent. A separate benchtop permeability measurement was also carried out on the Berea specimen using distilled water, for which the permeability was more than a factor of two lower than the value for brine flow. This substantiates the visual observation of significant clay content in this specimen, and documentation of system performance by comparisons of measurements on this specimen with the body of published data from generally cleaner Berea material may not be possible.

The test sequences for Set 3, Blocks 3 and 9, and the Berea specimen were interrupted following the initial brine saturation and following the measurements at irreducible water saturation, and the test specimen was removed from the test vessel and weighed to determine the pore volume brine content. Some water loss during

Table A1. Summary of laboratory static and dynamic mechanical properties, measured simultaneously with the pore fluid transport properties of table 5. The brine/gas ratios refer to the brine- or gas-saturated specimen, and the relative velocities at irreducible water (S_{wi}) are relative to the gas-saturated values.

Spec #	Porosity	Young's Mod(Mpsi)		Poisson's Ratio		Brine / Gas Rat		Rel Vel @Swi	
	%	Static	Dynamic	Static	Dynamic	P-Wave	S-Wave	P-Wave	S-Wave
(Set 1)									
6	12.5	2.4	4	0.25	0.17	1.13	1.03	0.97	1
(Set 2)									
2	14.5	3	4.3	0.29	0.2	1.05	1	0.98	1.03
3	16	2.3	3.8	0.15	0.18	1.1	0.94	0.97	1.01
5B	20.7	1.8	3.4	0.12	0.19	1.02	0.97	0.98	0.99
6	15.1	2.2	4	0.21	0.19	1.03	0.95	0.97	1.01
8	15	2.2	3.8	0.3	0.19	1.06	0.95	0.96	0.99
9	18.1	2	3.3	0.3	0.24	1.08	0.97	0.96	1.02
11	17.7	1.8	3.6	0.13	0.09	1.03	0.94	0.96	0.97
12	16	3	4.2	0.15	0.18	1.03	0.95	0.97	1.01
13	18	2.5	3.9	0.25	0.19	1.05	0.96	0.98	1.02
(Set 3)									
1 A	12.7	3.9	5.4	0.2	0.14	1.05	0.97	0.98	1.02
1 C	14.2	2.3	4.4	0.24	0.13	1.06	0.97	0.96	1
2	12.5		5.7		0.13	1.09	0.97	0.97	1.04
3	17.6	4						0.99	1.04
4	15.4	2.8	4.3	0.22	0.14	1.06	0.96	0.97	1.02
5	16.3	3.5	5.4	0.3	0.13	1.01	0.95	0.98	0.99
6	18	3	4.8	0.1	0.12	1.04	0.97	0.97	1.01
7	18.1		4.5		0.17	1.02	0.96	0.97	1.02
9	16.8	3.7	4.9	0.22	0.09	1.08	0.91	0.95	0.98
(Set 4)									
2 A	17.2	1.9	3.5	0.26	0.1	1.05	0.92	0.93	1.04
2 C	16.8	1.9	4.1	0.3	0.13	1.04	0.94	0.96	1.01
Berea									
	25.4	3.1	3.9	0.2	0.12	1.02	0.93	0.97	1.06

sample extraction was unavoidable, but the saturation values were all within 10 percent of the values calculated by mass balance; all saturations determined by direct weighing were higher than the mass balance determinations. This agreement corresponds to a brine volume measurement uncertainty of less than 4 mL.

The measurements carried out on the specimen from Set 2 Block 2, illustrated in figure A-26, were carried out to assess the effects of initial specimen pressurization on measured permeability. The arrows in the figure indicate the measurement sequence. An initial laboratory gas flow measurement was carried out for confining and pore pressures of only 300 and 200 psi, respectively, for which the permeability was almost 2 md. After the pore and confining pressures were increased to the test values of 1 and 6 kpsi, respectively, the permeability had decreased to about 1 md, and it remained at this level after the effective pressure was cycled between the original 100 psi and the test level of 5 kpsi in several different configurations of pore and confining pressures. It is likely that a disproportionately large fraction of compaction-related permeability decrease occurs during the initial pressurization of the specimen, which could be the source of the remaining discrepancy between the 5-md minipermeameter value and the initial 2-md laboratory value.

Results are listed in table A1 for the static and (gas-saturated) dynamic Young's and Poisson's ratios, the ratios of brine-saturated compressional (P-wave) and shear wave (S-wave) velocities to the gas-saturated values, and the relative shear and compressional-mode wave velocities at irreducible water saturations (normalized to their brine-saturated values). The specimens are designated by the set and block numbers used in table 5. No velocity measurements or triaxial deformations were carried out for the first specimen tested, from Block 1 of Set 2; the results from the Set 3 Block 7 specimen deformation are not usable because of a malfunction in confining pressure servocontrol during the test; no velocity measurements were carried out for the specimen from Block 8 of Set 3 because of a malfunction of the signal transducers in the vessel; and no
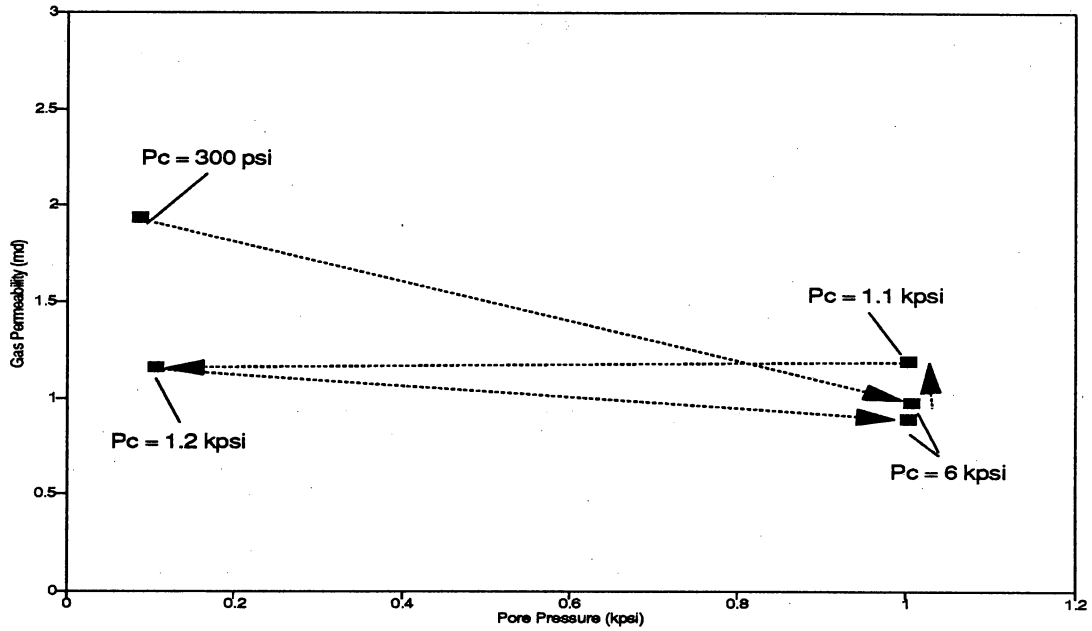
Figure A26. Initial sequence of laboratory gas permeability measurements carried out on the test specimens for Block 2 of Set 2. The arrows indicate the measurement sequence; the specimen was unpressurized prior to the initial measurement.

velocity measurements were carried out for the gas-saturated specimen from Block 3 of Set 3.

Plots of the brine-saturation variations in wave velocities, and in the dynamic bulk and shear moduli, are shown in figures A-27 to A-48, a and b, respectively. The shear moduli are determined from the product of density, δ, and the square of the shear velocity, v_s. The bulk moduli, B_d, are determined from the (isotropic material) expression

$$B_d = \delta \bullet [\, v_p{}^2 - \frac{4}{3} v_s{}^2], \qquad\qquad\qquad (A\text{-}8)$$

where v_p is the compressional-mode wave velocity.

For all tests carried out after June 1991 (approximately half of the specimens listed in table 5), the signals for the wave velocity measurements were digitized and stored. Representative signals for one of the tests, for the Set 2 Block 6 specimen, are shown in figures A-49 and A-50, for shear and compressional-mode waves, respectively. The first arrivals of the compressional mode signals are well defined, but, as indicated in figure A-50, the determination of the first arrival of the shear wave signal is often complicated by the presence of precursor signals, mostly compressional mode signals generated by mode conversions within the specimen. The first arrival of the shear wave signal is clearly indicated for the gas-saturated specimen, very obscure for the brine-saturated specimen, and progressively better defined as brine saturation decreases in the specimen. By successive comparisons of the wave forms the shear wave arrival can be traced with confidence between the different saturations, but without the composite waveforms arrival times can easily be in error by one or more wave periods. Post-test comparisons of the waveforms with the oscilloscope arrival time measurements recorded during the tests were used to refine the travel time determinations for those tests for which signals were digitized.

The general patterns of variations evident from figures A-27 through A-48 are approximately linear increases in compressional velocity and bulk modulus, and small
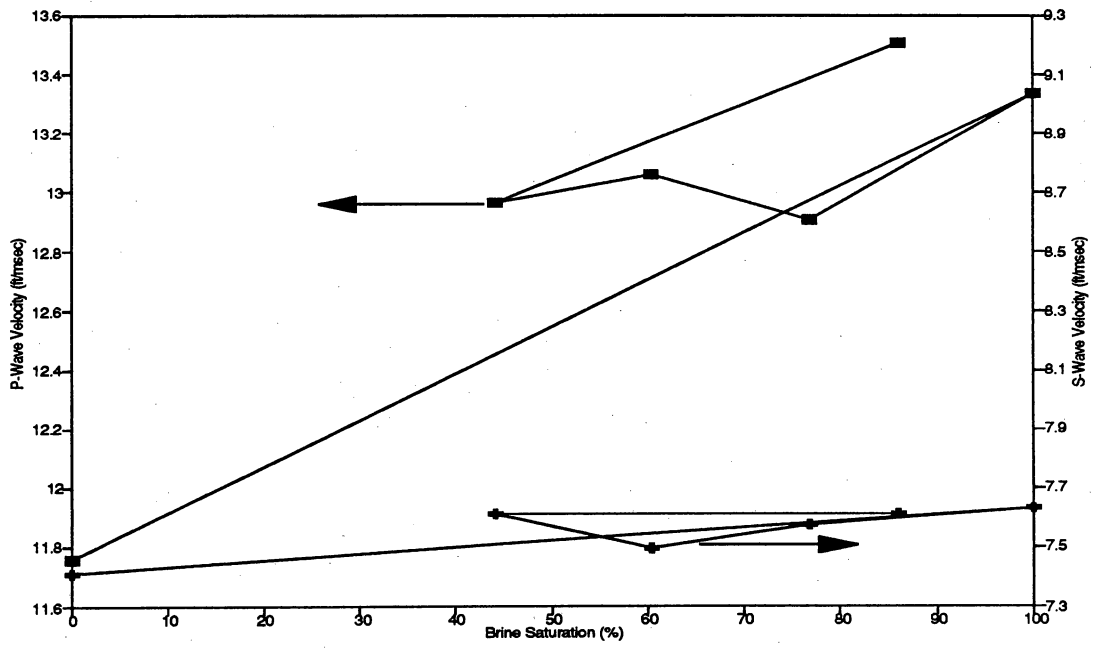
(a)
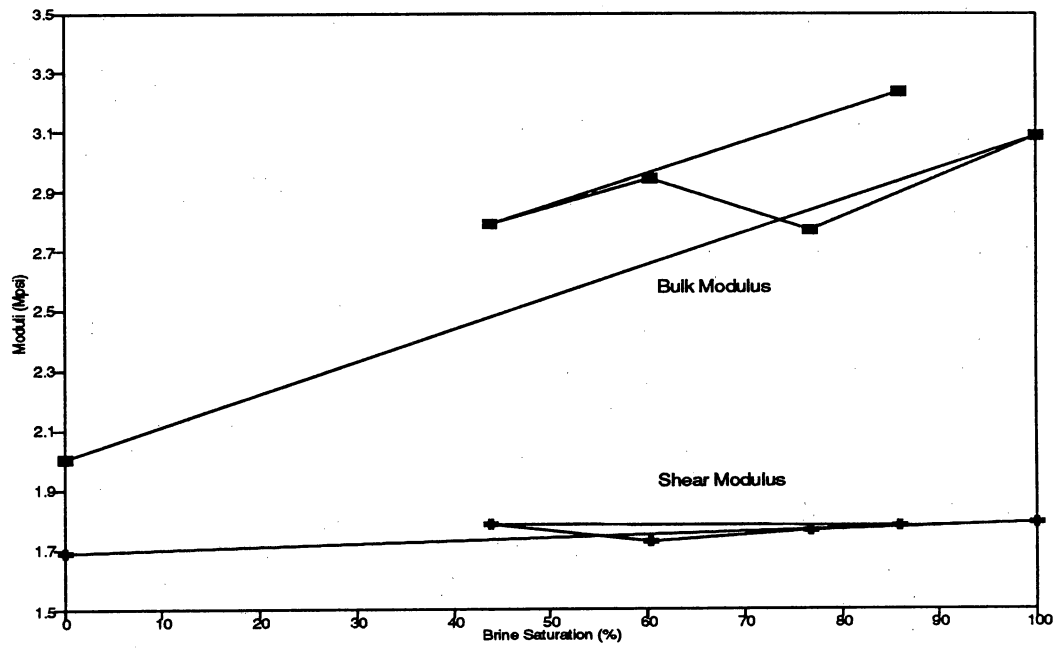
(b)

Figure A27. Variations in wave velocities (a) and moduli (b) with brine saturation for the specimen from Block 6 of Set 1.
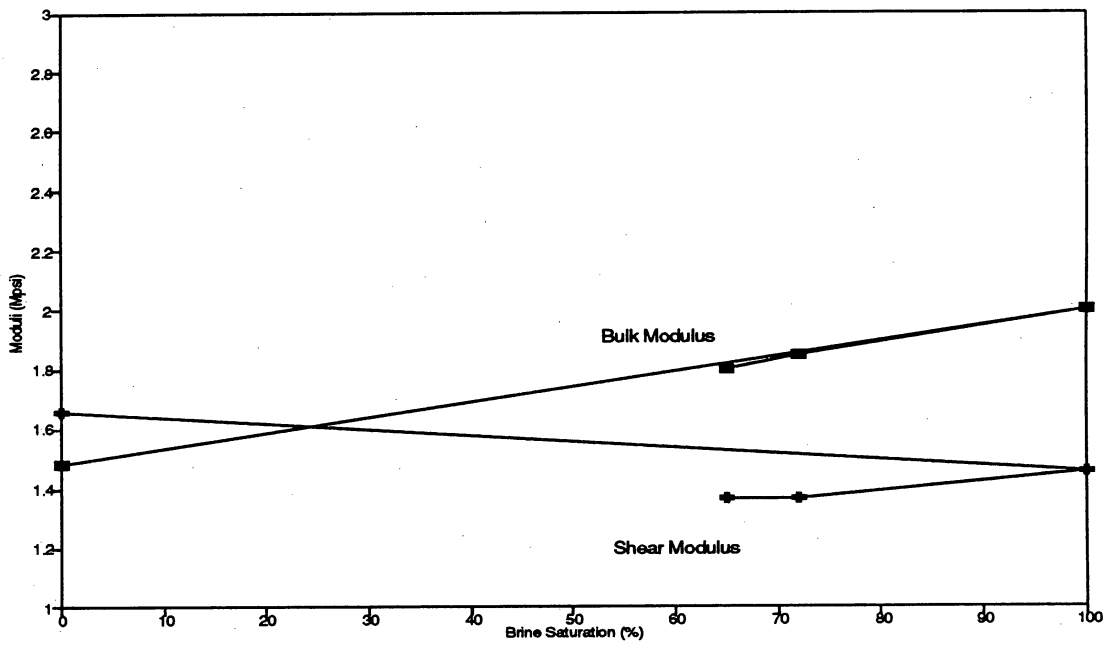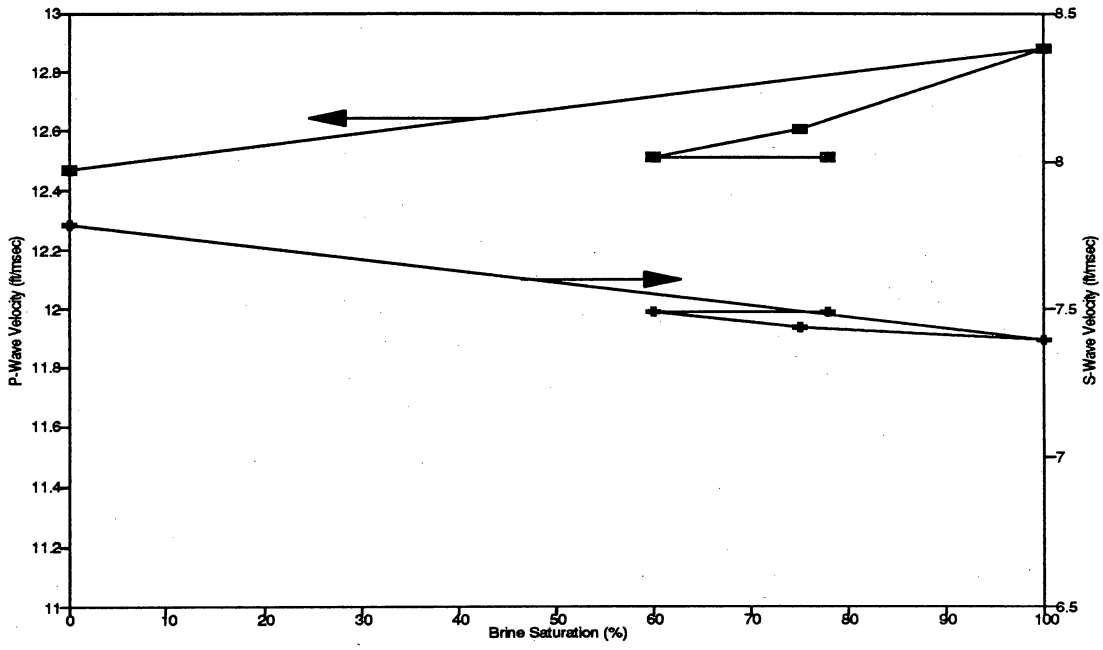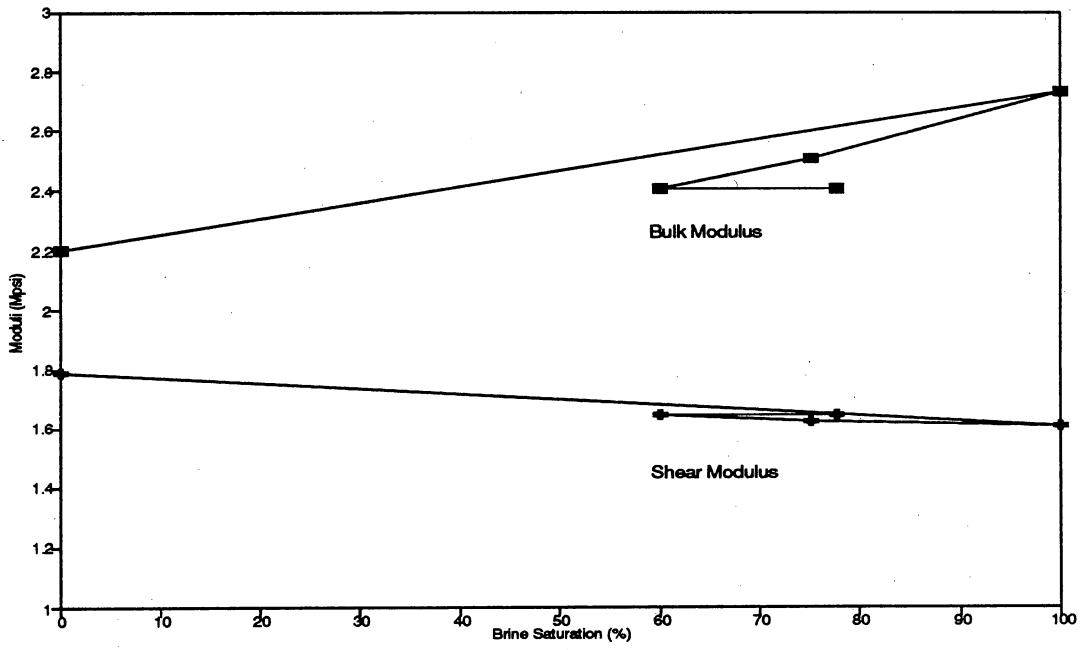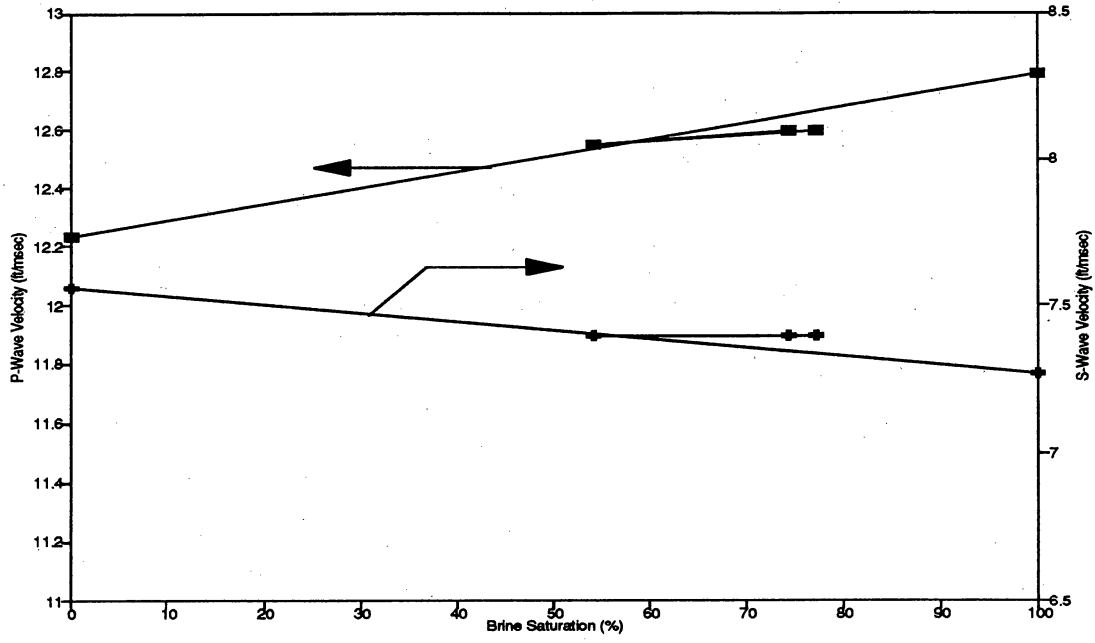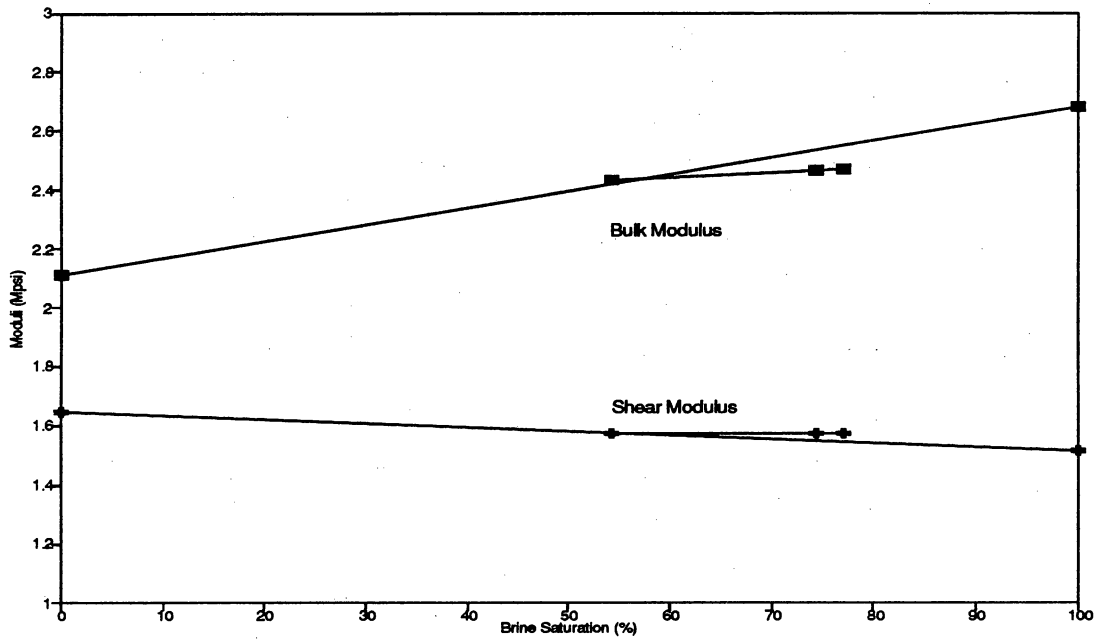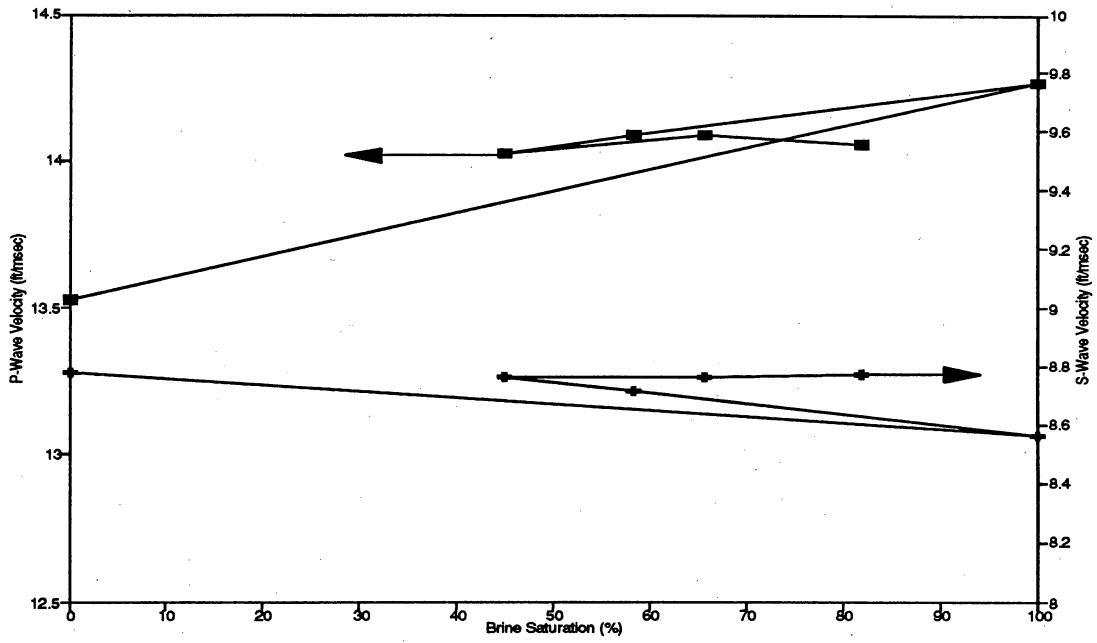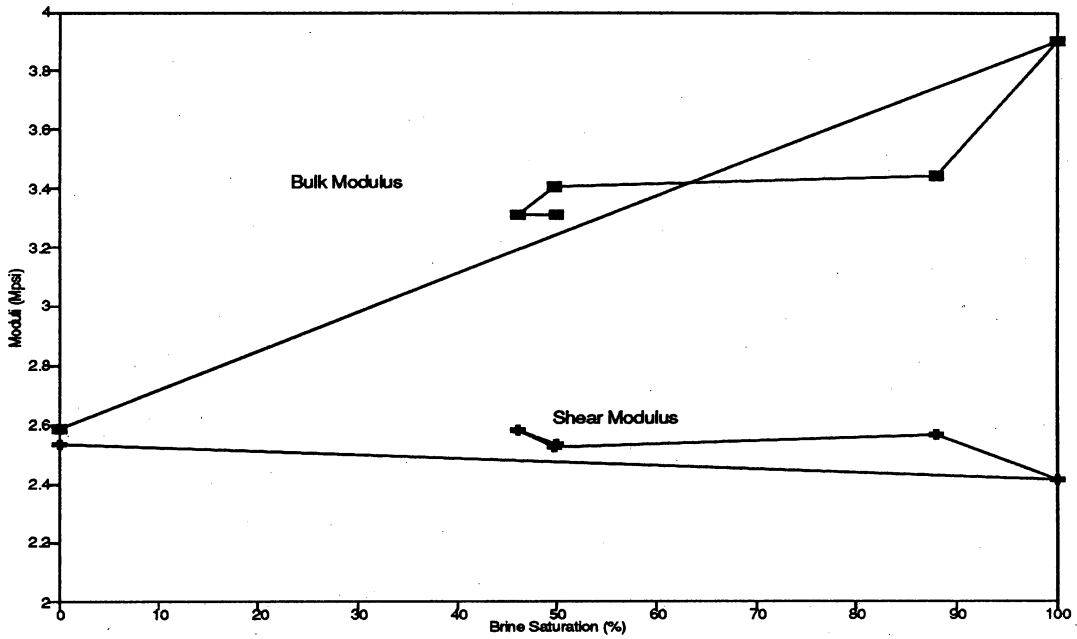
131
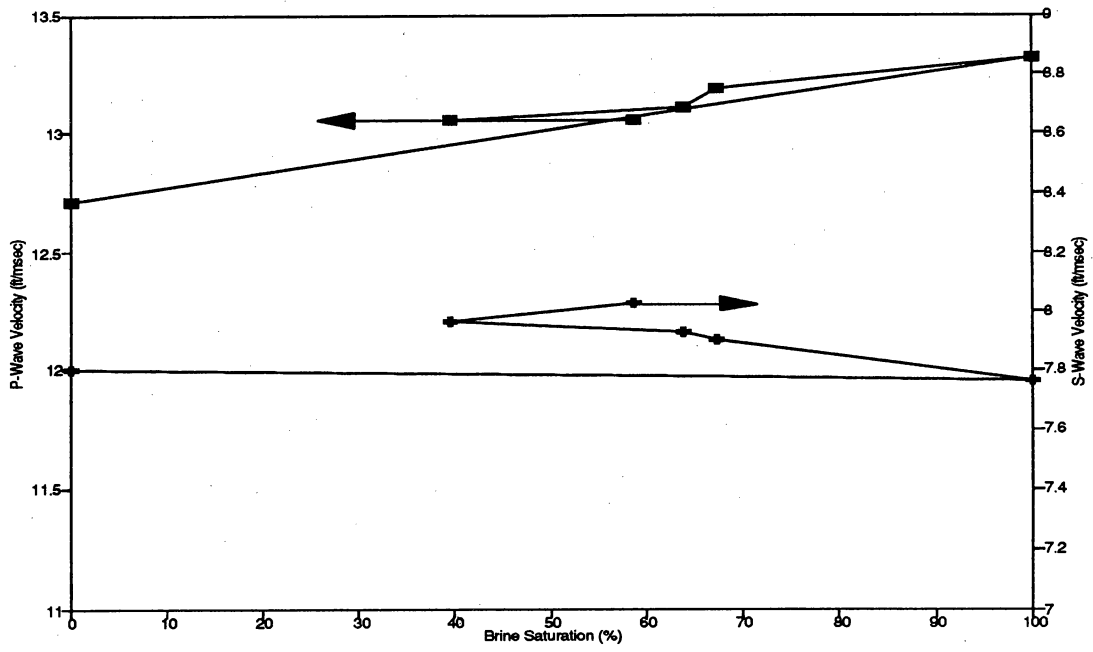
(a)
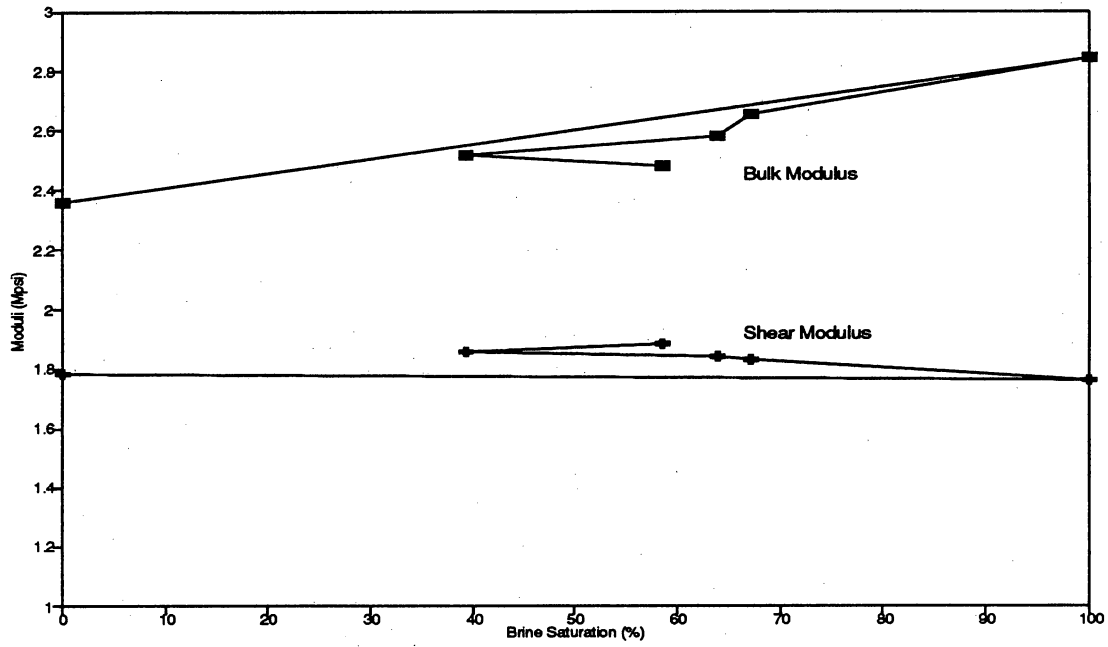
(b)

Figure A28. Variations in wave velocities (a) and moduli (b) with brine saturation for the specimen from Block 2 of Set 2.
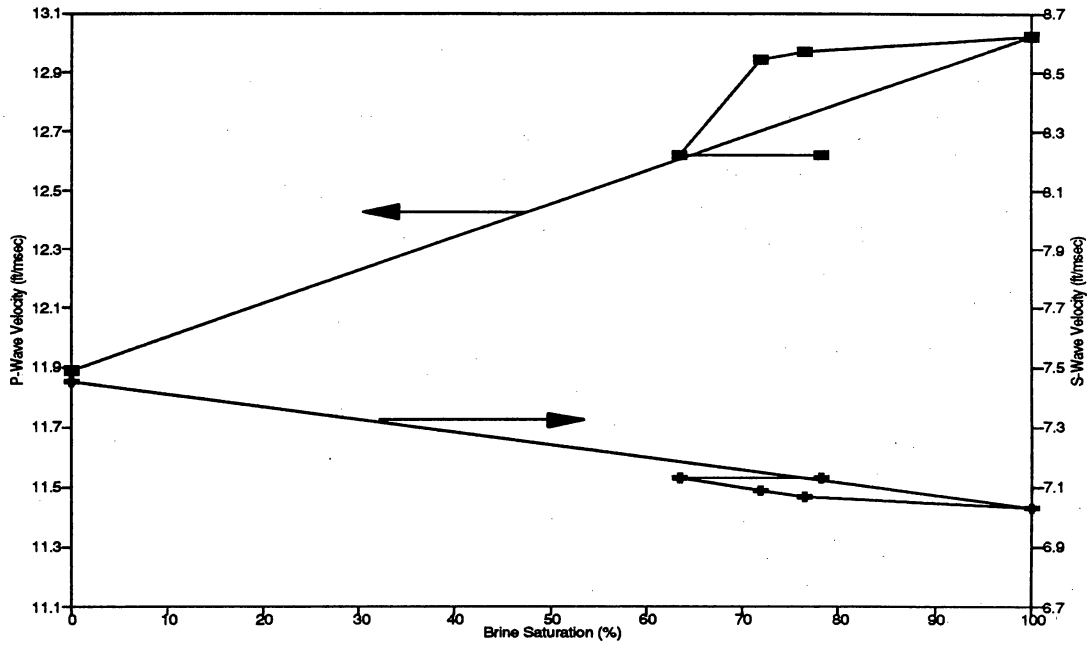
(a)
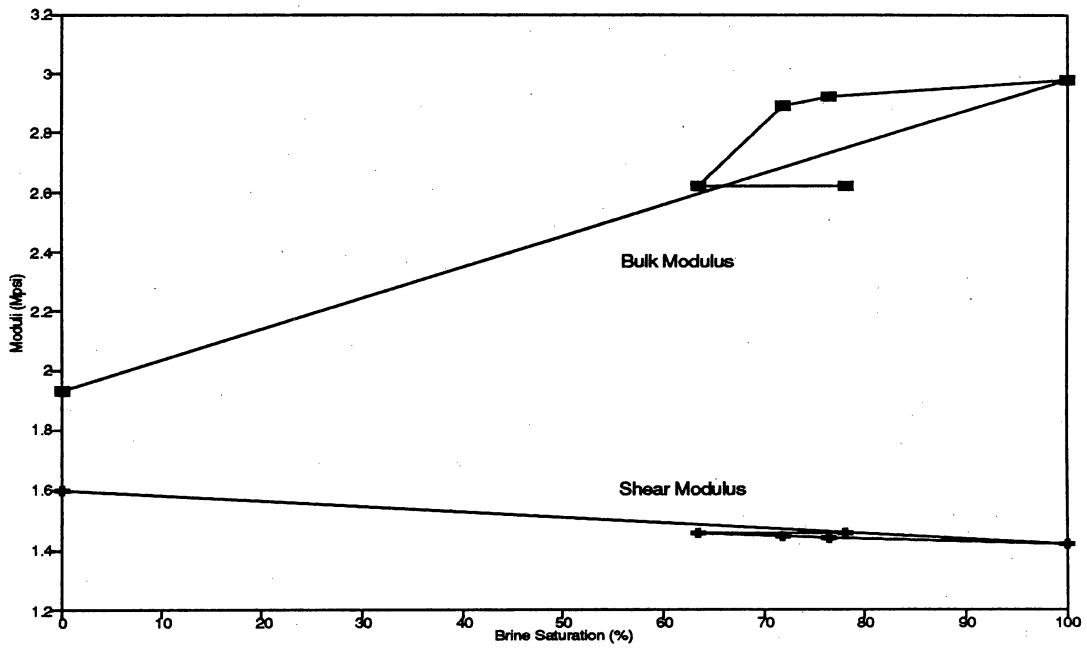
(b)

Figure A29. Variations in wave velocities (a) and moduli (b) with brine saturation for the specimen from Block 3 of Set 2.
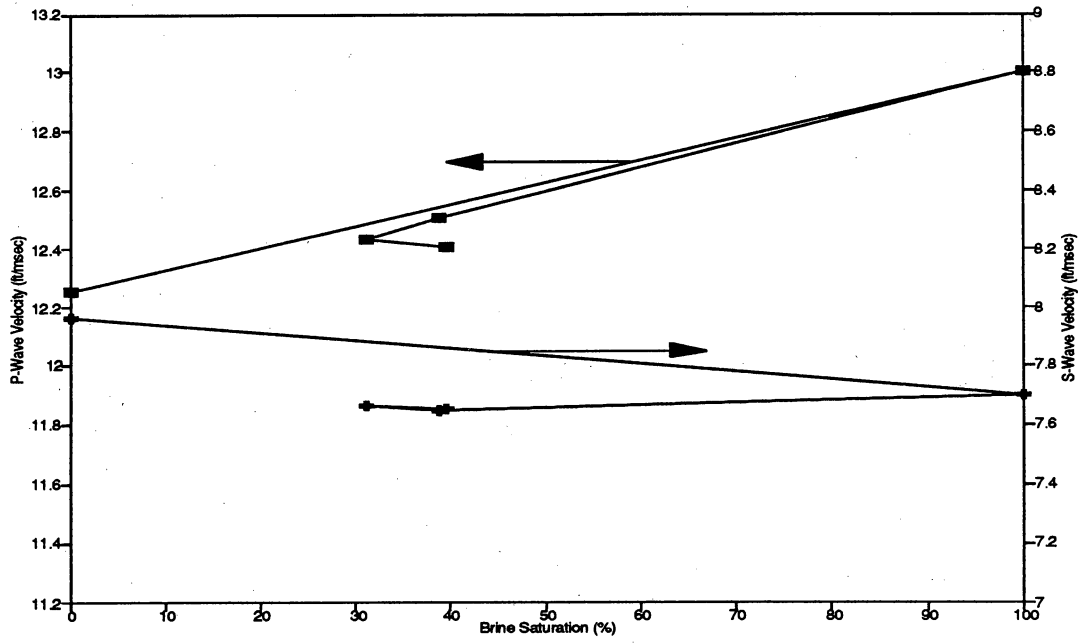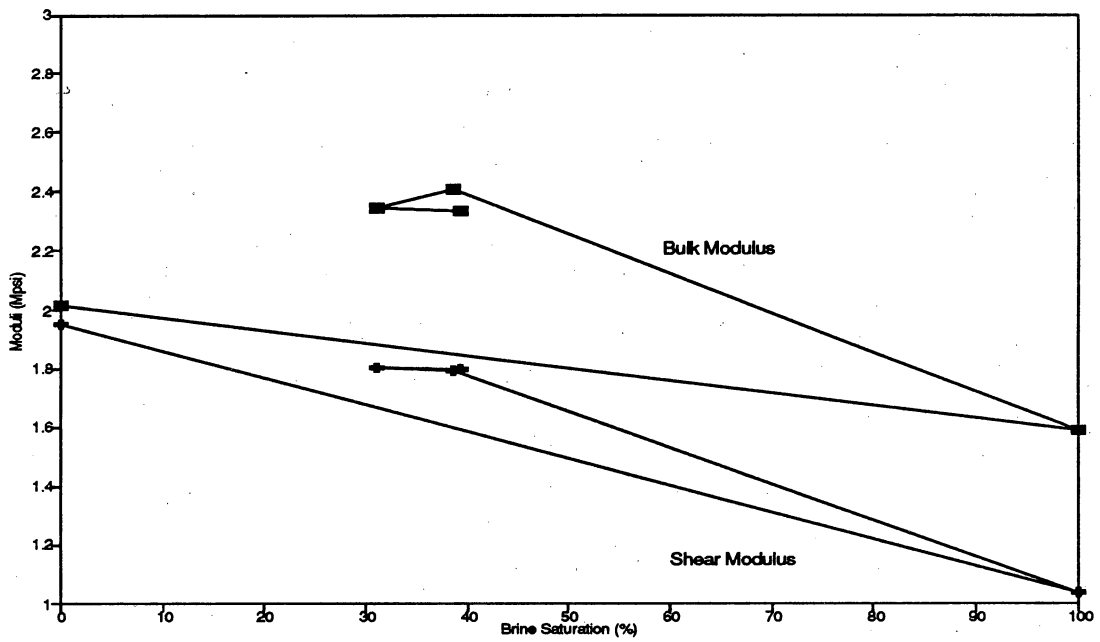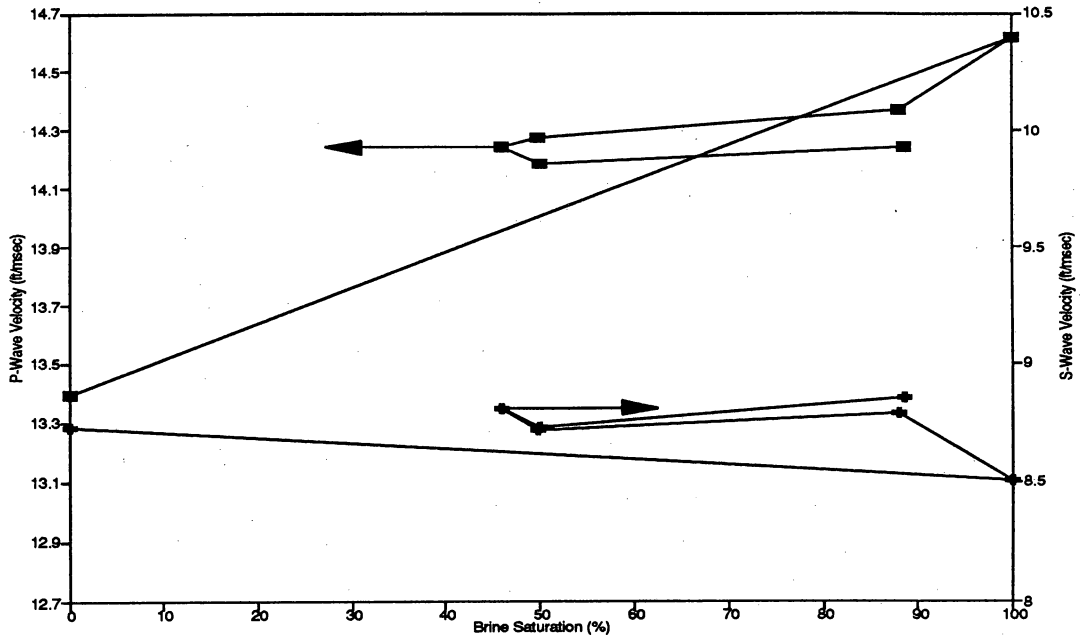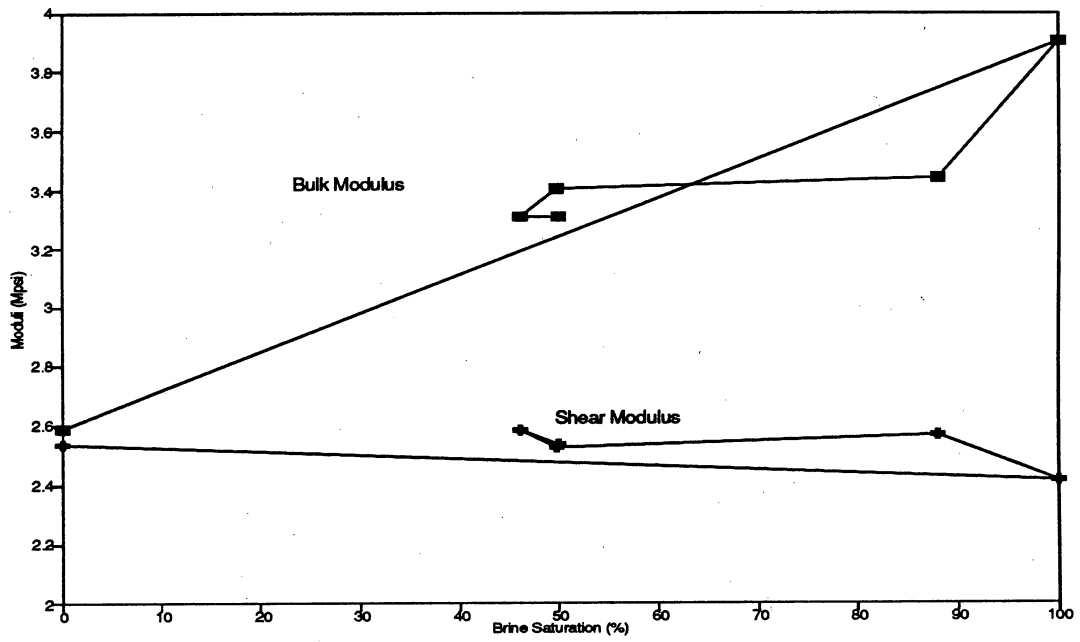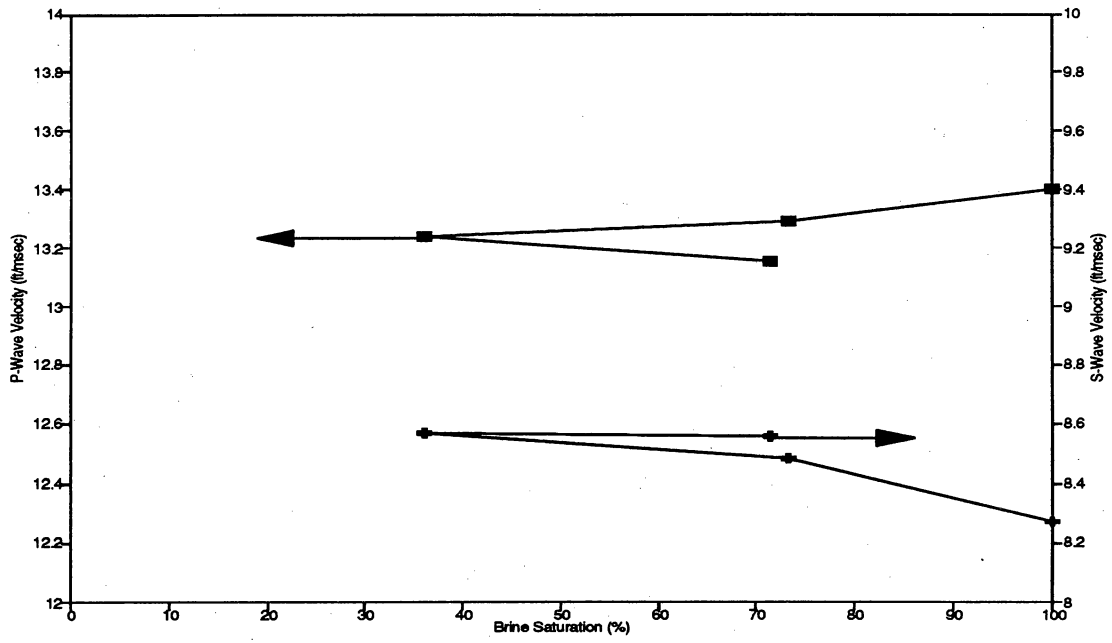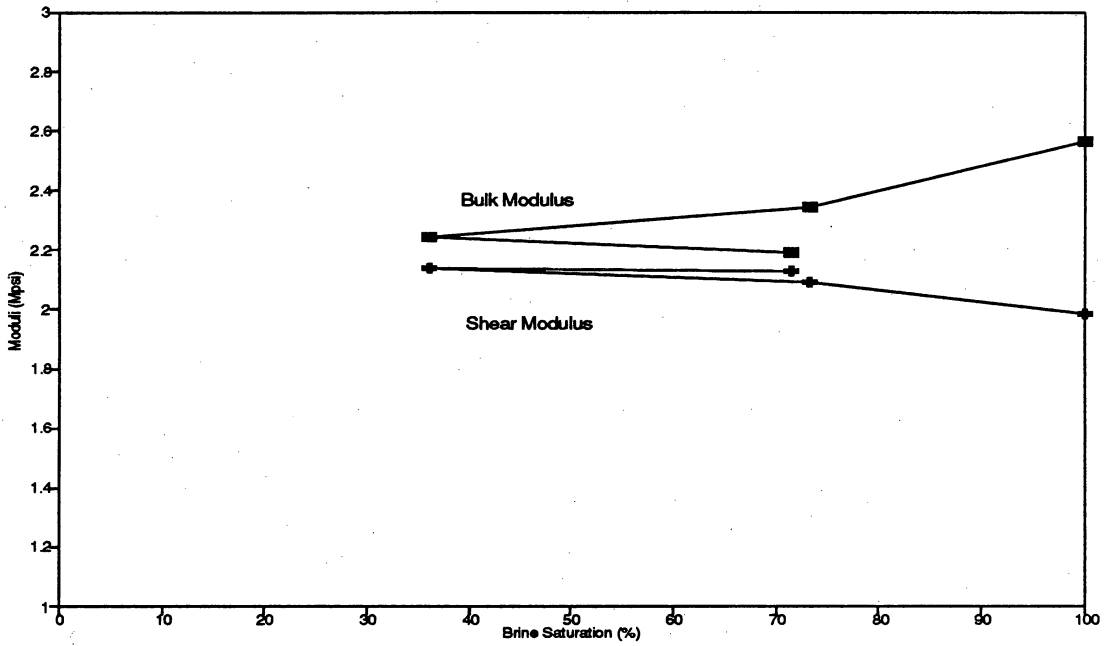
133
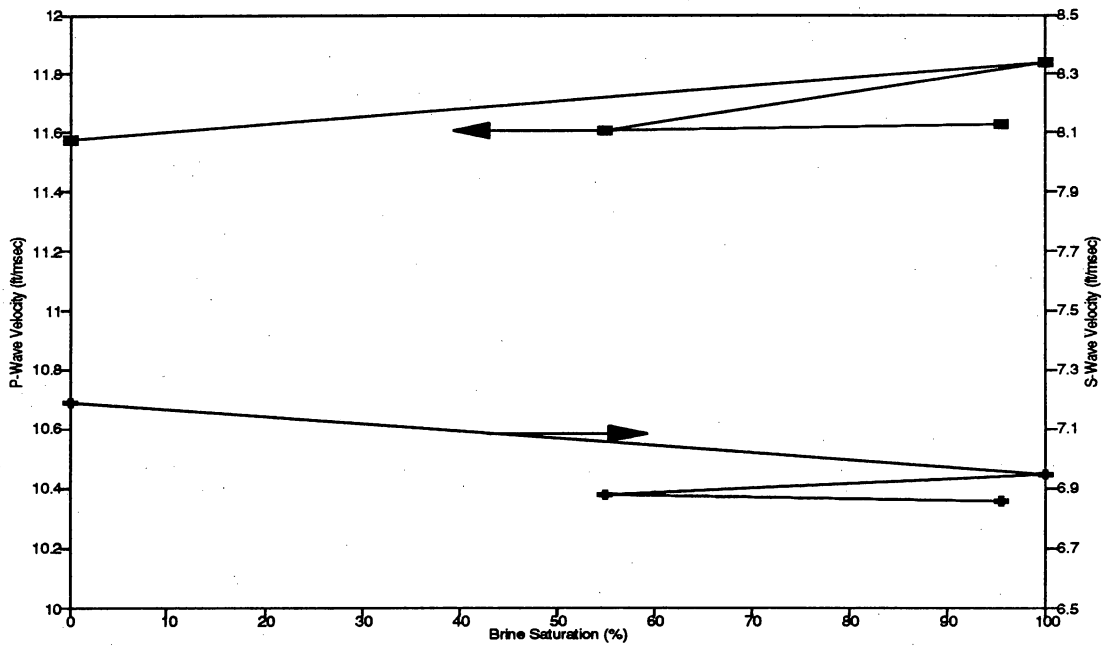
(a)
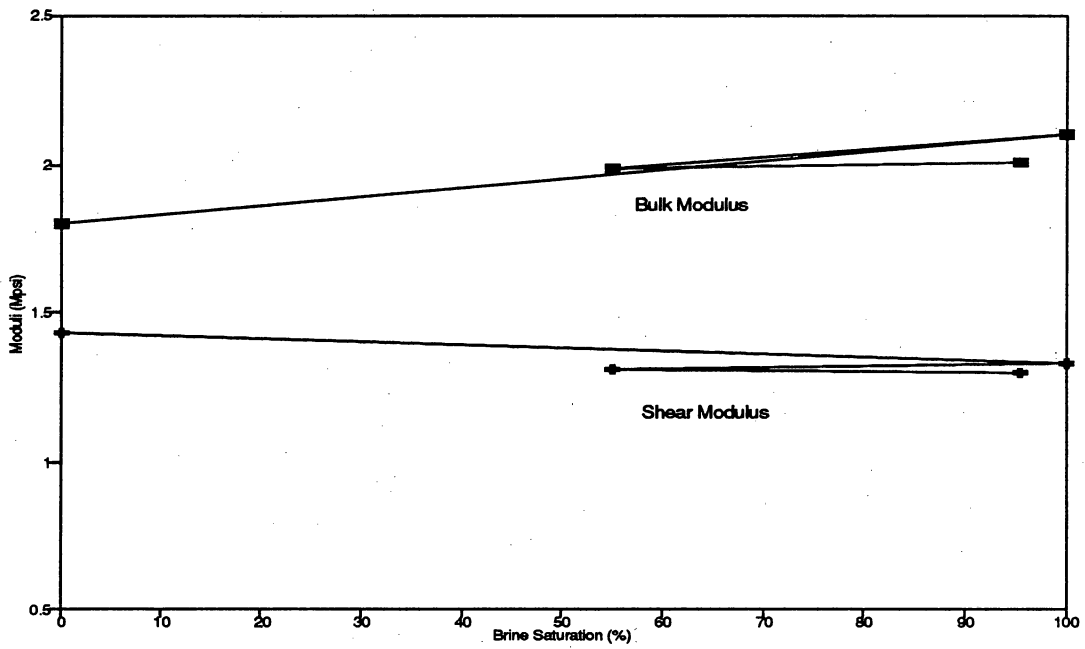
(b)

Figure A30. Variations in wave velocities (a) and moduli (b) with brine saturation for the specimen from Block 5 of Set 2.
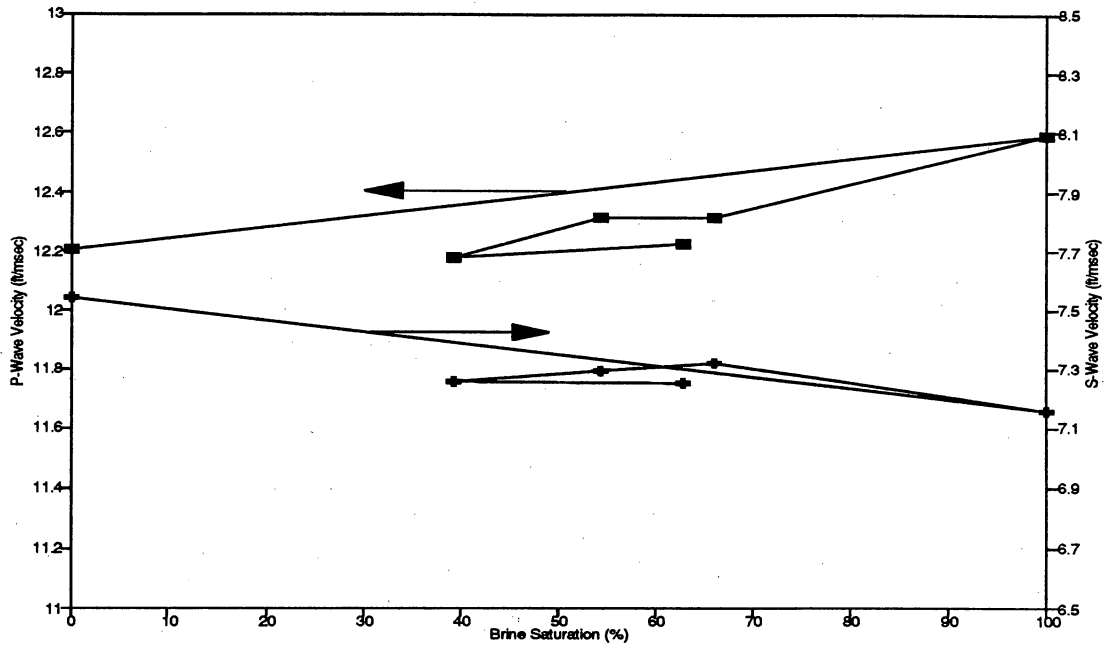
(a)
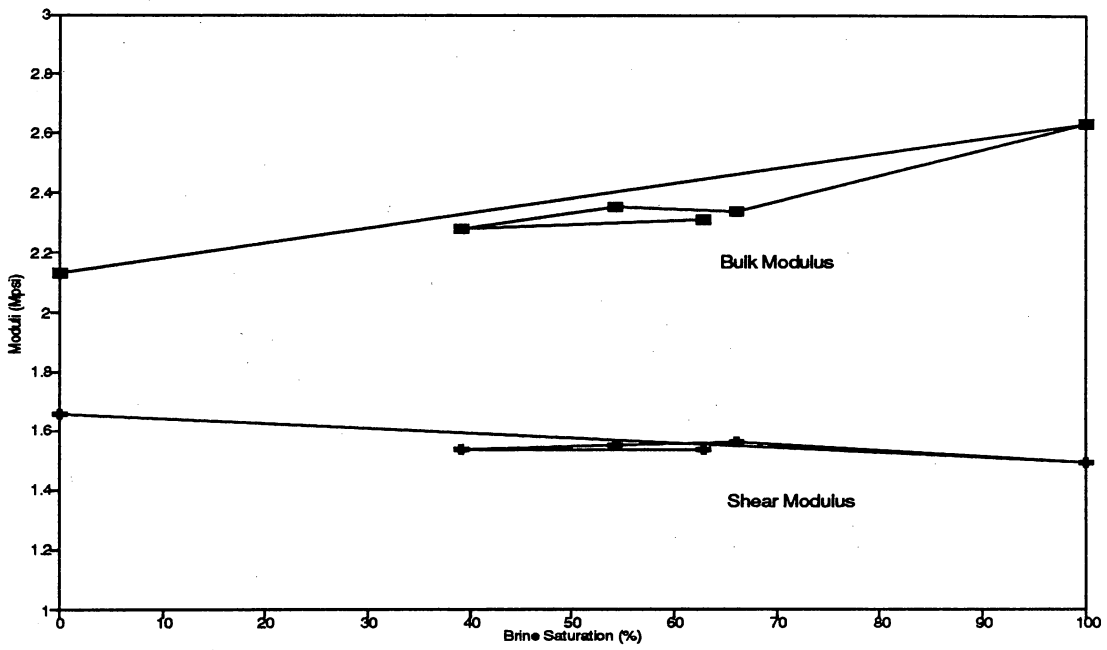
(b)

Figure A31. Variations in wave velocities (a) and moduli (b) with brine saturation for the specimen from Block 6 of Set 2.
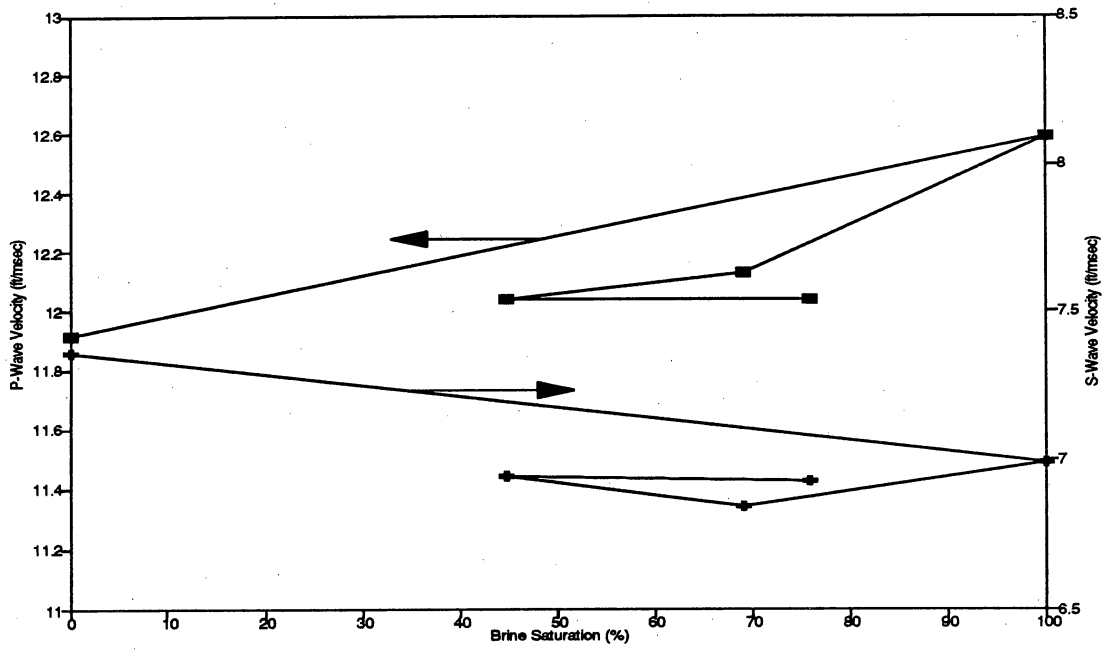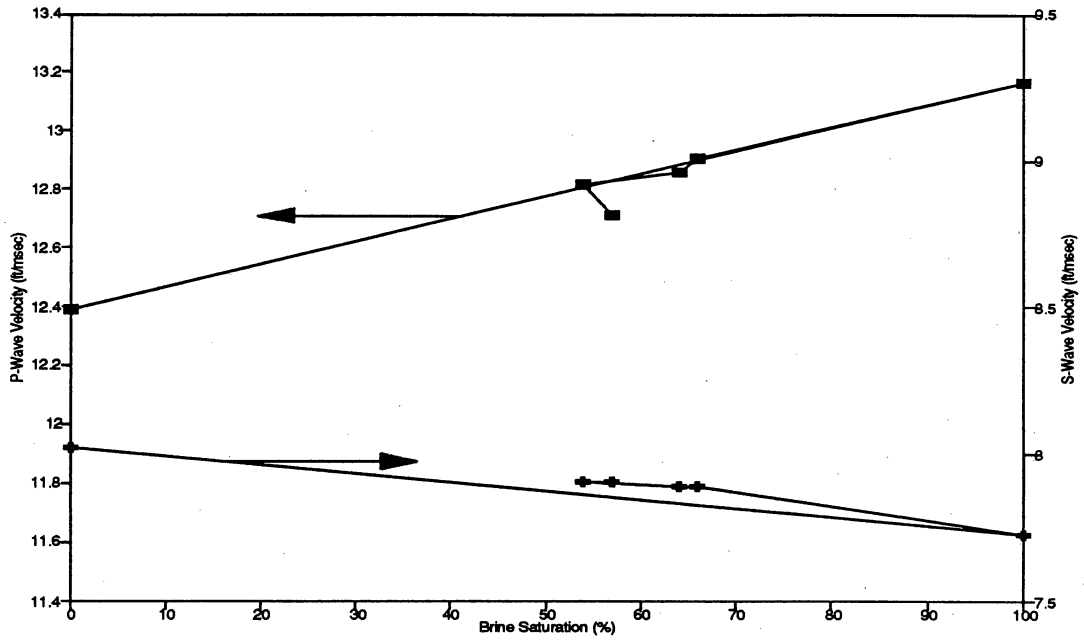
(a)
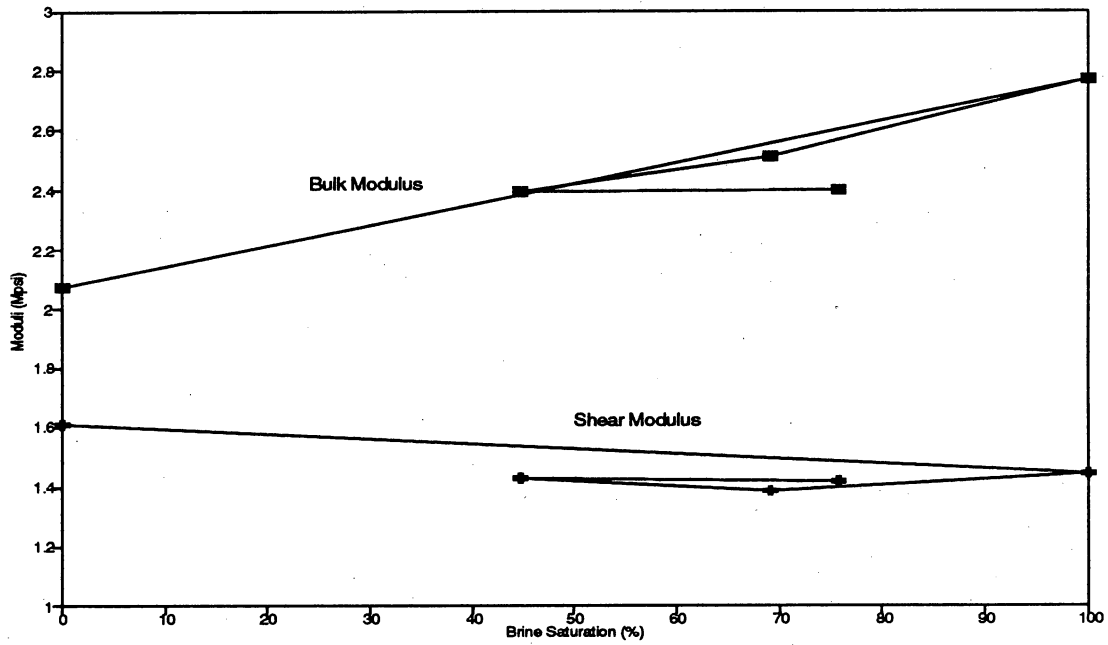
(b)

Figure A32. Variations in wave velocities (a) and moduli (b) with brine saturation for the specimen from Block 8 of Set 2.
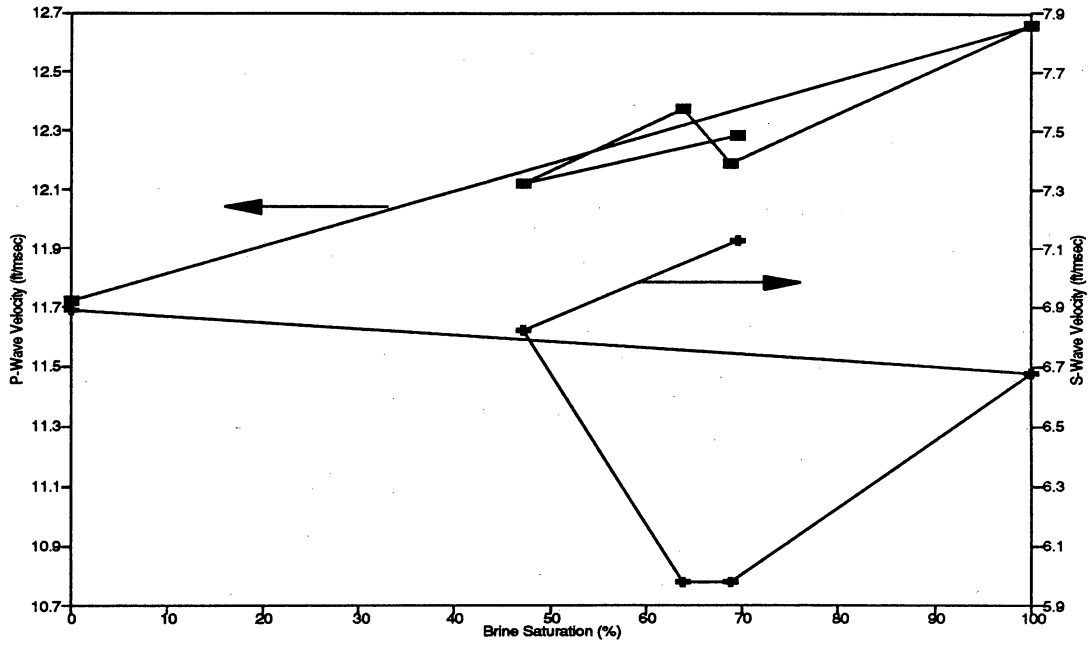
(a)
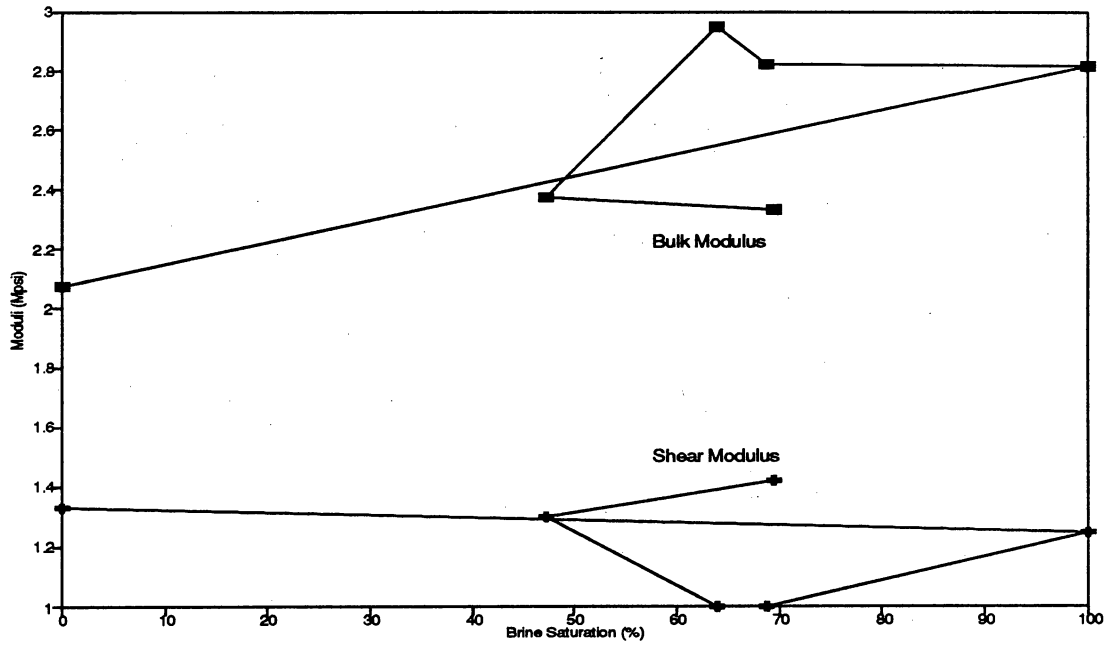
(b)

Figure A33. Variations in wave velocities (a) and moduli (b) with brine saturation for the specimen from Block 9 of Set 2.
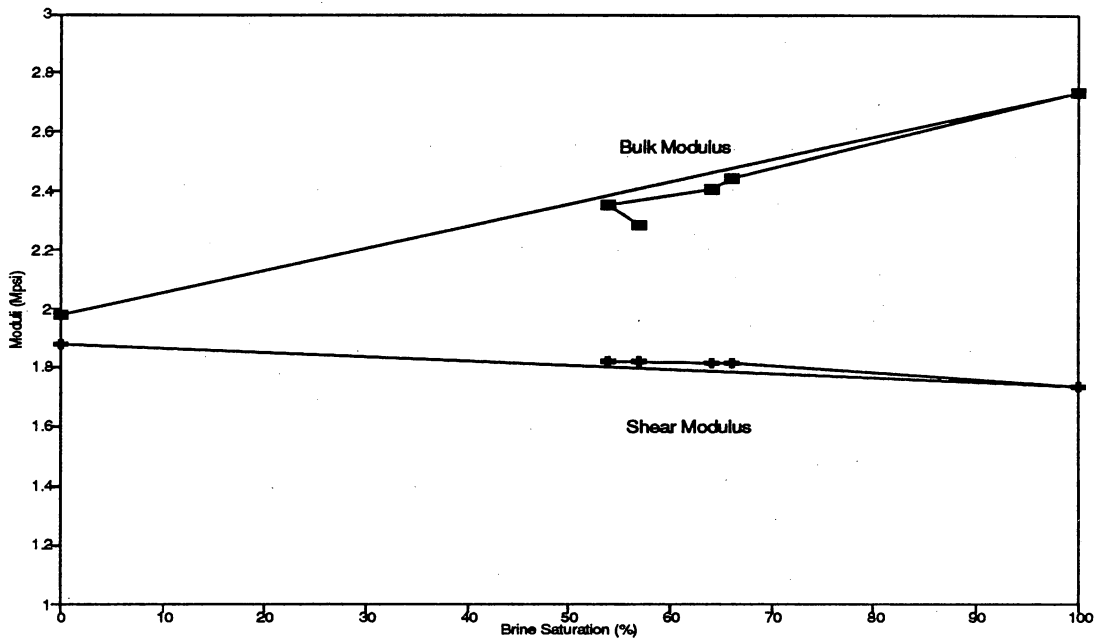
137
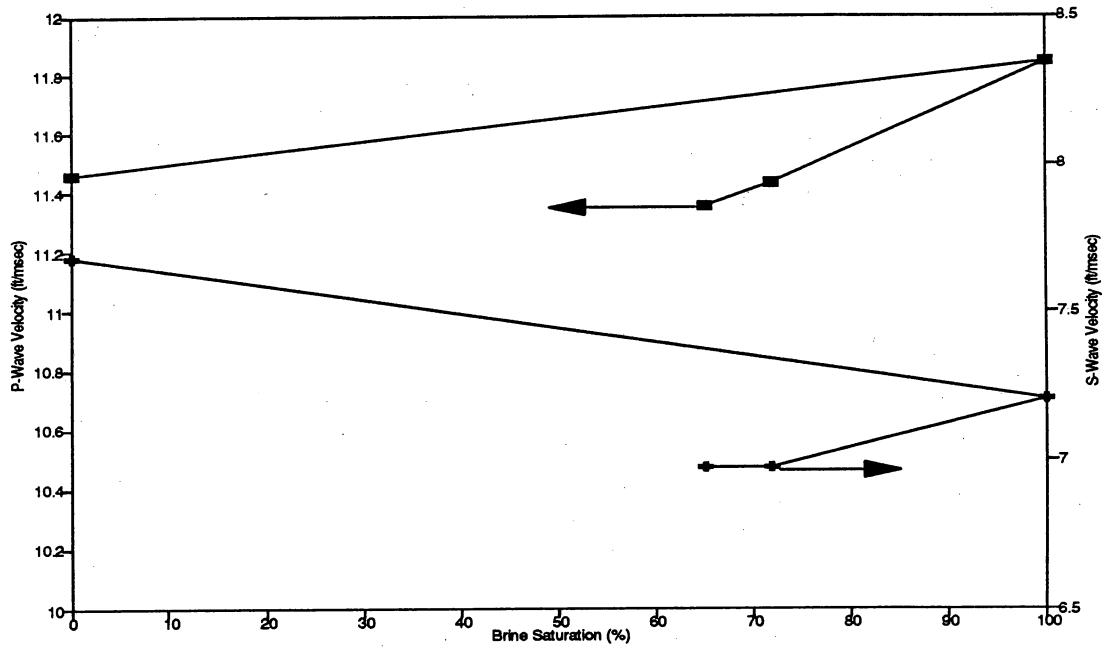
(a)

(b)

Figure A34. Variations in wave velocities (a) and moduli (b) with brine saturation for the specimen from Block 11 of Set 2.

(a)

(b)

Figure A35. Variations in wave velocities (a) and moduli (b) with brine saturation for the specimen from Block 12 of Set 2.

139
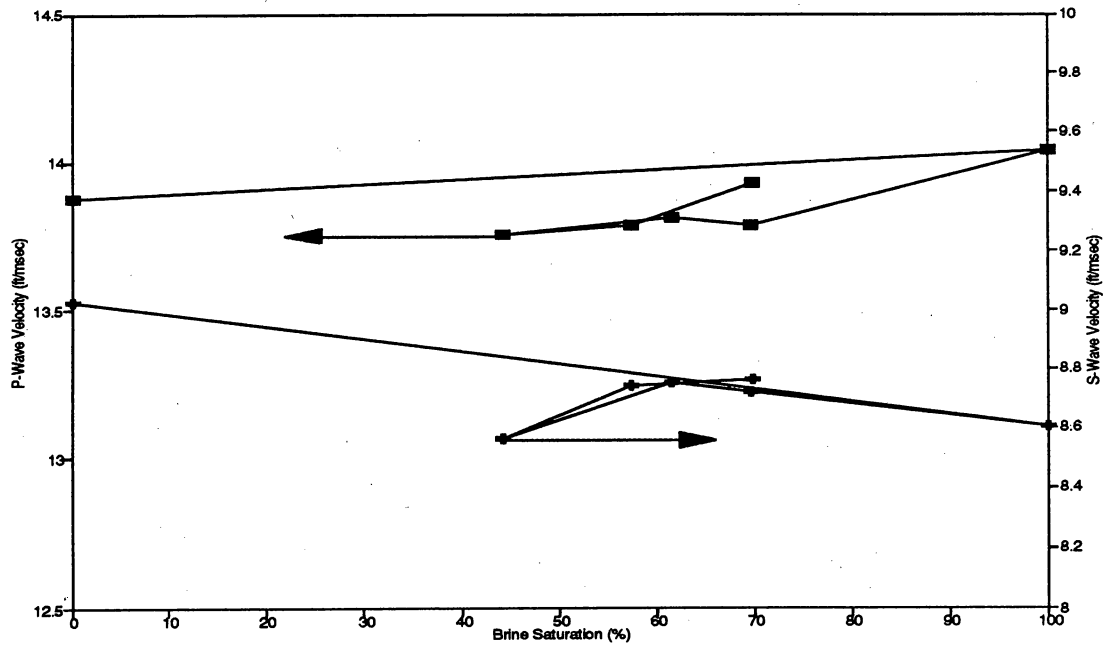
(a)

(b)

Figure A36. Variations in wave velocities (a) and moduli (b) with brine saturation for the specimen from Block 13 of Set 2.

Figure A37. Variations in wave velocities (a) and moduli (b) with brine saturation for the specimen from Block 1 of Set 3 (Specimen A).

(a)

(b)

Figure A38. Variations in wave velocities (a) and moduli (b) with brine saturation for the specimen from Block 1 of Set 3 (Specimen C).
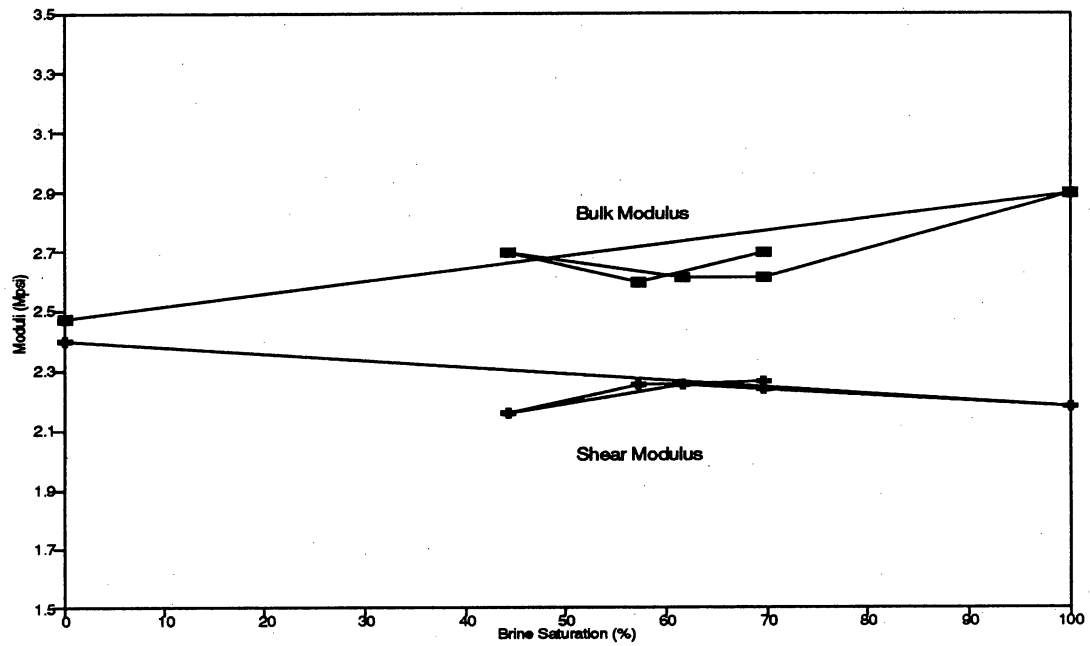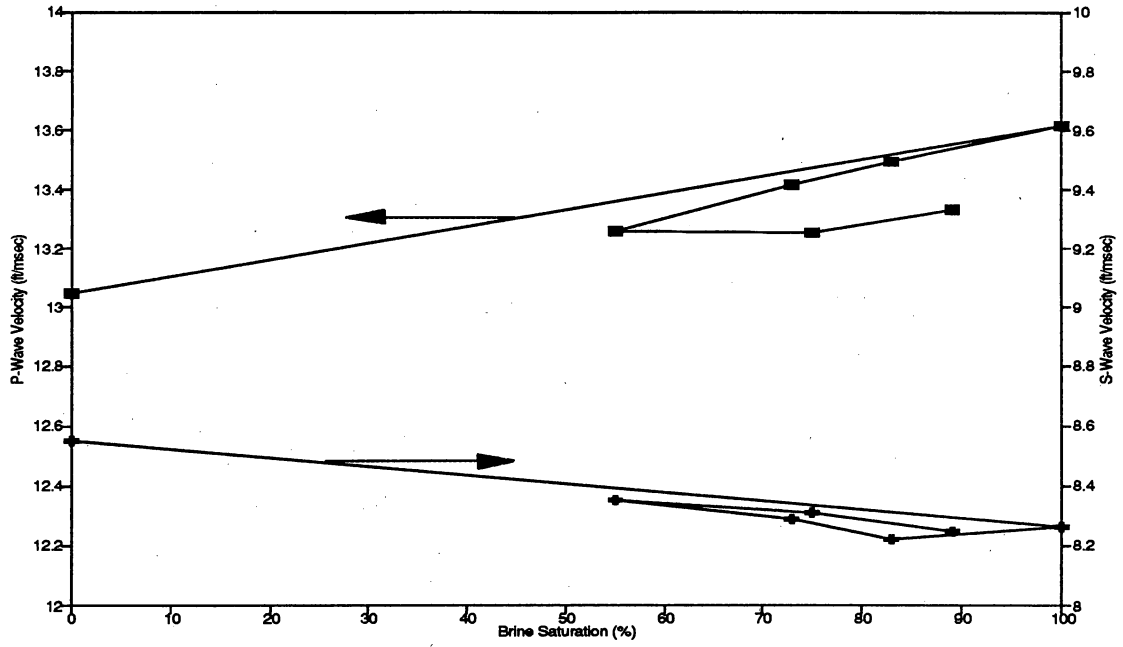
(a)

(b)

Figure A39. Variations in wave velocities (a) and moduli (b) with brine saturation for the specimen from Block 2 of Set 3.
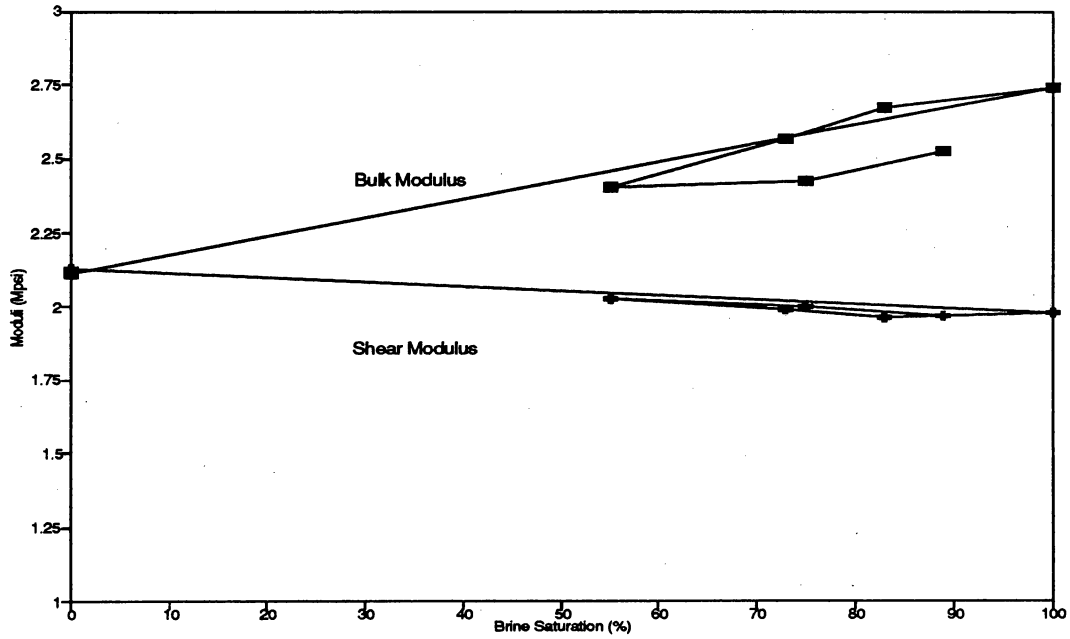
143

(a)

(b)

Figure A40. Variations in wave velocities (a) and moduli (b) with brine saturation for the specimen from Block 3 of Set 3.

144

(a)

(b)

Figure A41. Variations in wave velocities (a) and moduli (b) with brine saturation for the specimen from Block 4 of Set 3.

145

(a)

(b)

Figure A42. Variations in wave velocities (a) and moduli (b) with brine saturation for the specimen from Block 5 of Set 3.
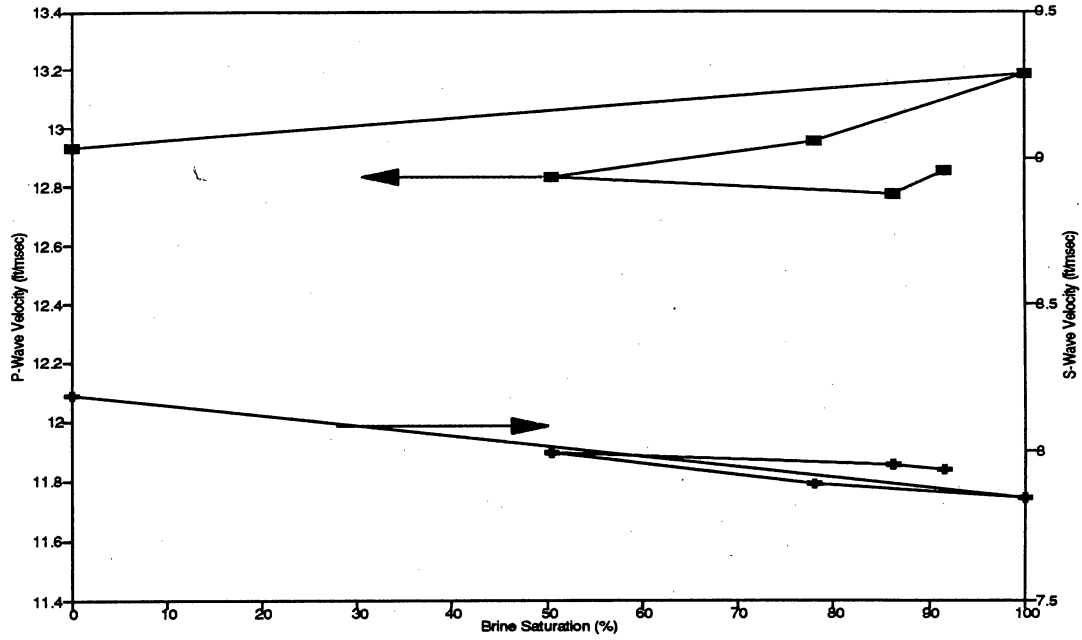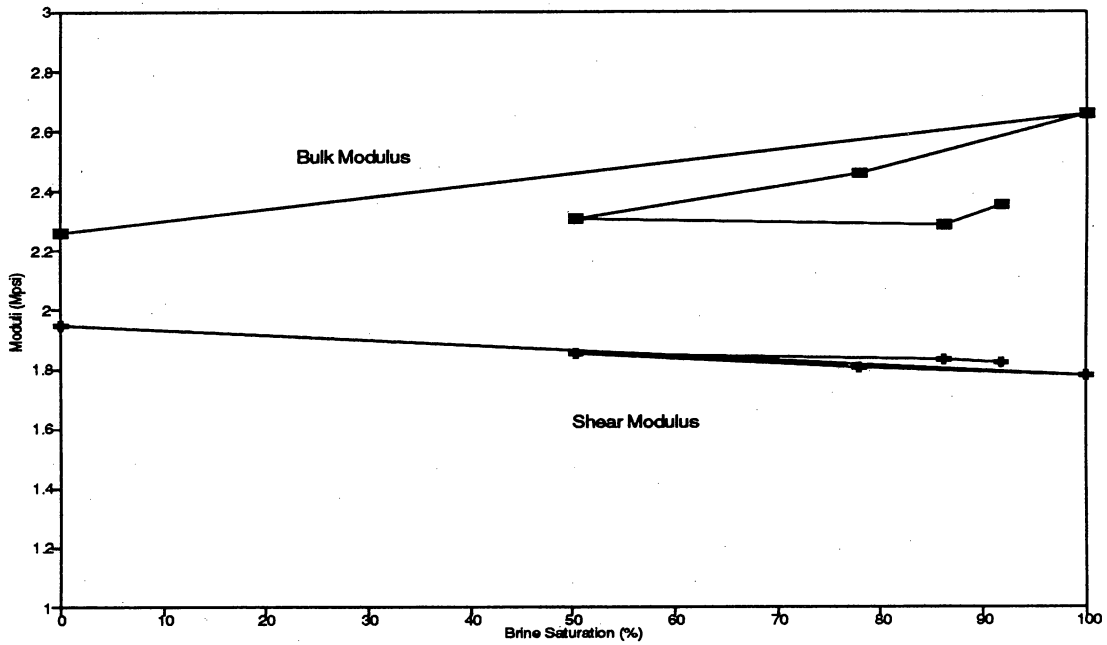
146

(a)

(b)

Figure A43. Variations in wave velocities (a) and moduli (b) with brine saturation for the specimen from Block 6 of Set 3.
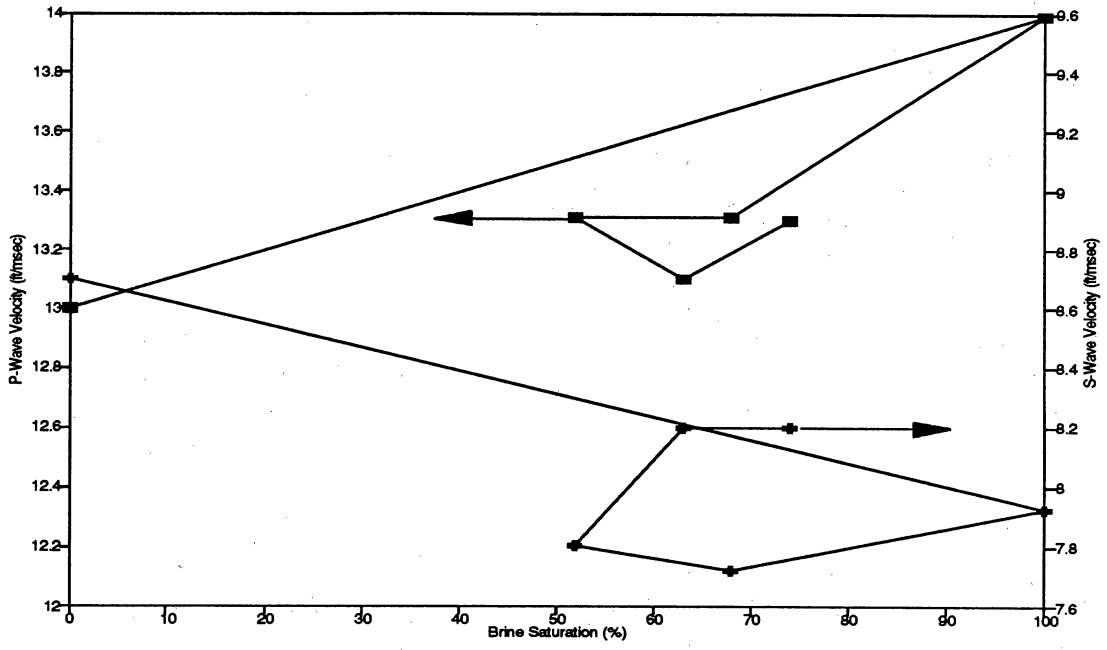
(a)

(b)

Figure A44. Variations in wave velocities (a) and moduli (b) with brine saturation for the specimen from Block 7 of Set 3.

(a)

(b)

Figure A45. Variations in wave velocities (a) and moduli (b) with brine saturation for the specimen from Block 9 of Set 3.
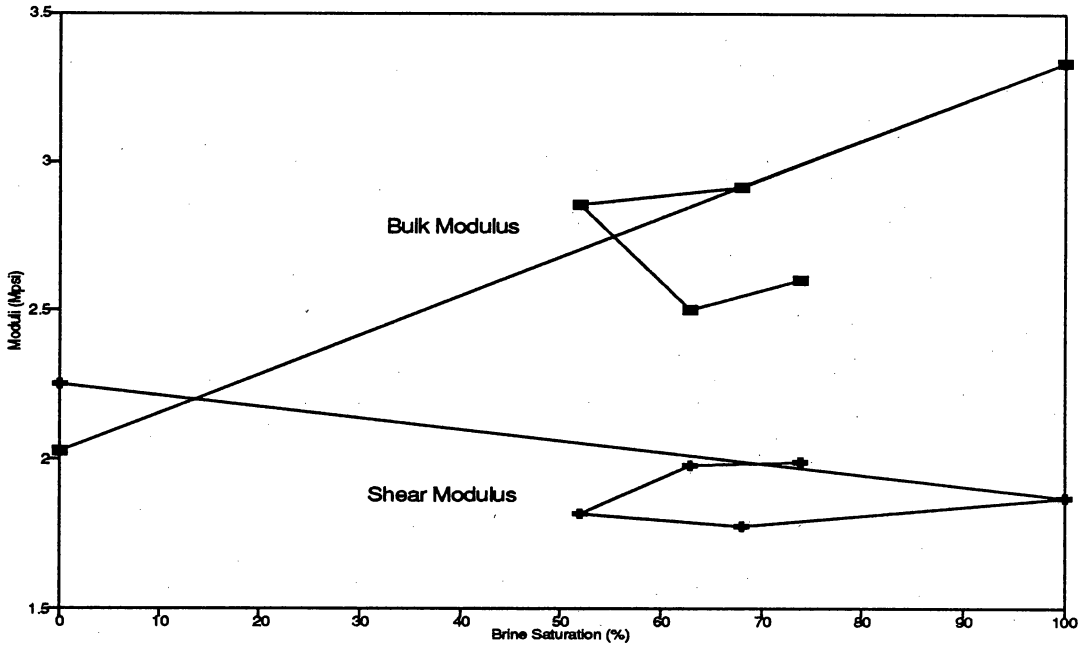
(a)

(b)

Figure A46. Variations in wave velocities (a) and moduli (b) with brine saturation for the specimen from Block 2A of Set 4.
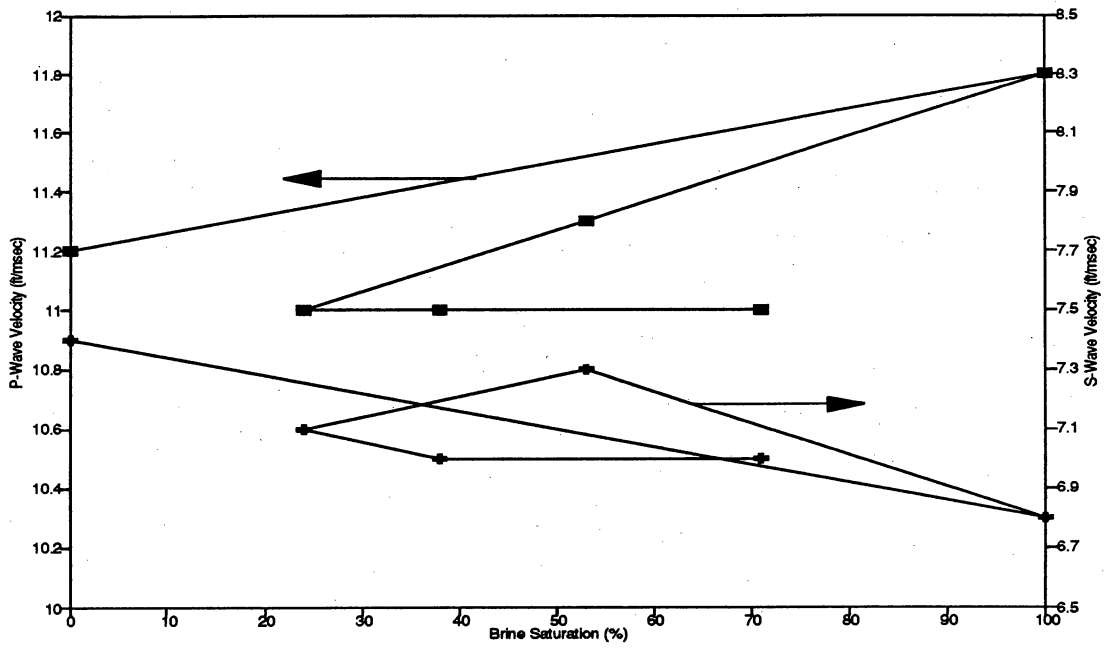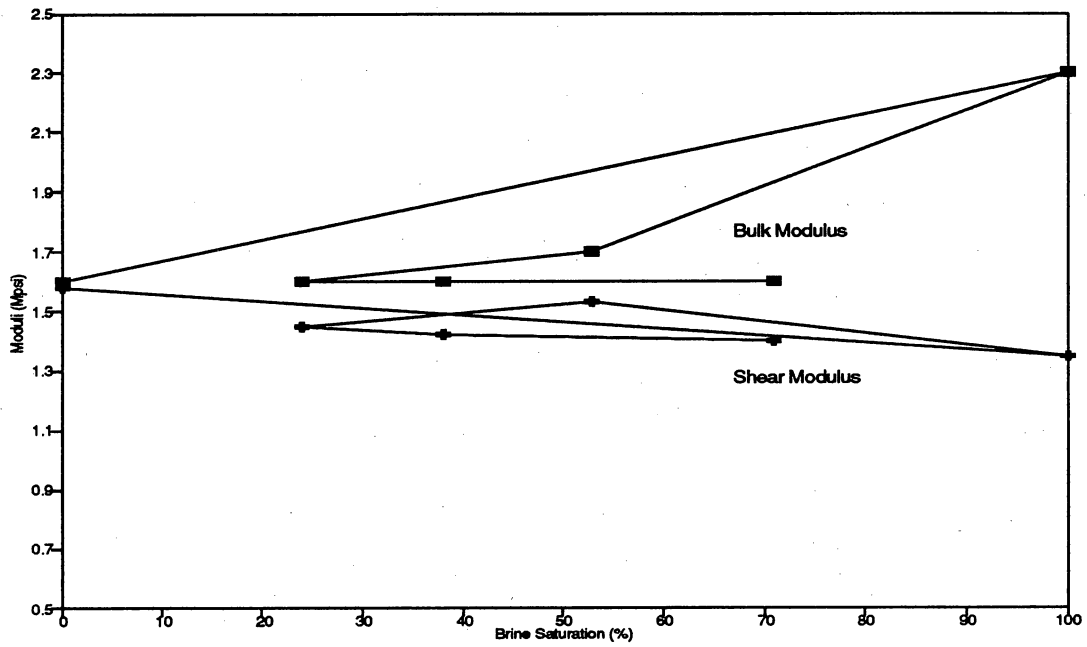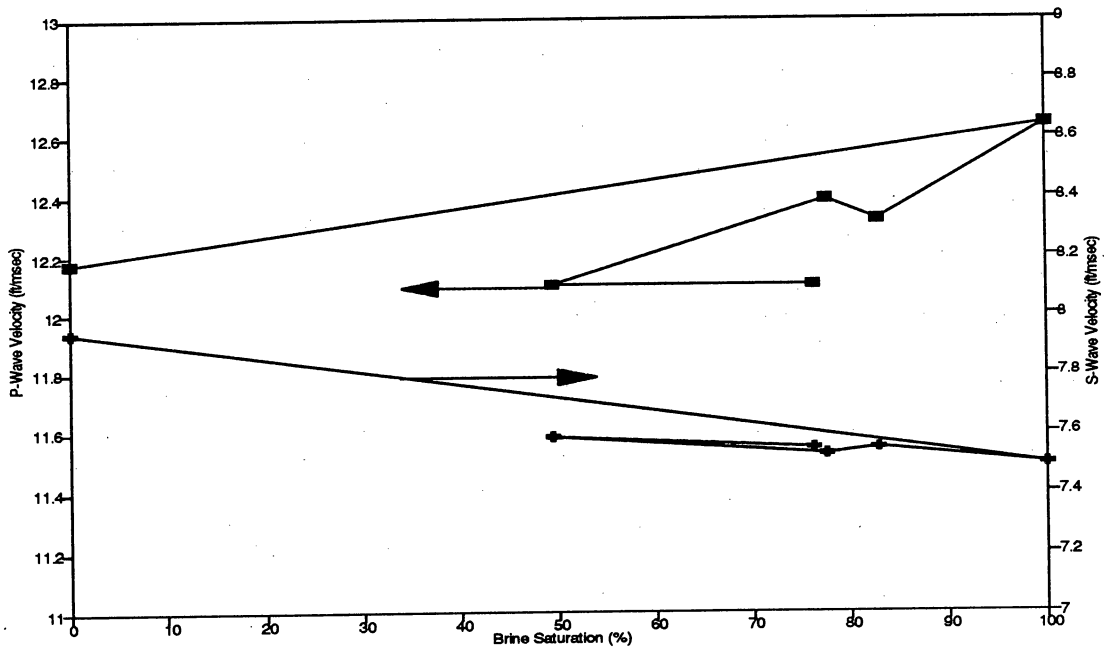
(a)
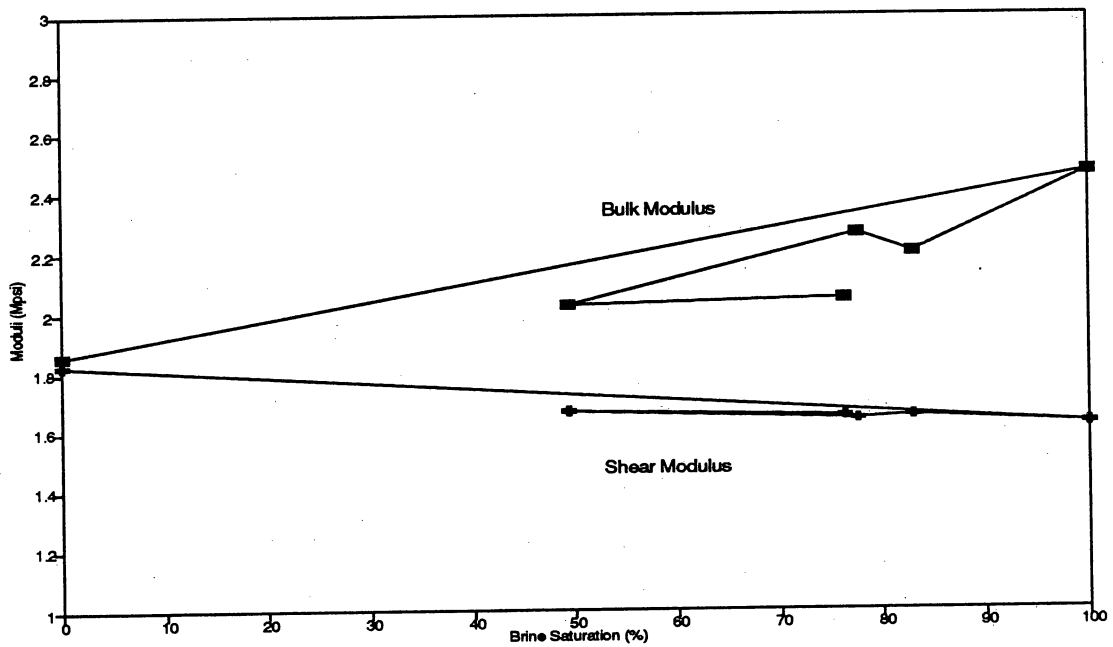
(b)

Figure A47. Variations in wave velocities (a) and moduli (b) with brine saturation for the specimen from Block 2C of Set 4.
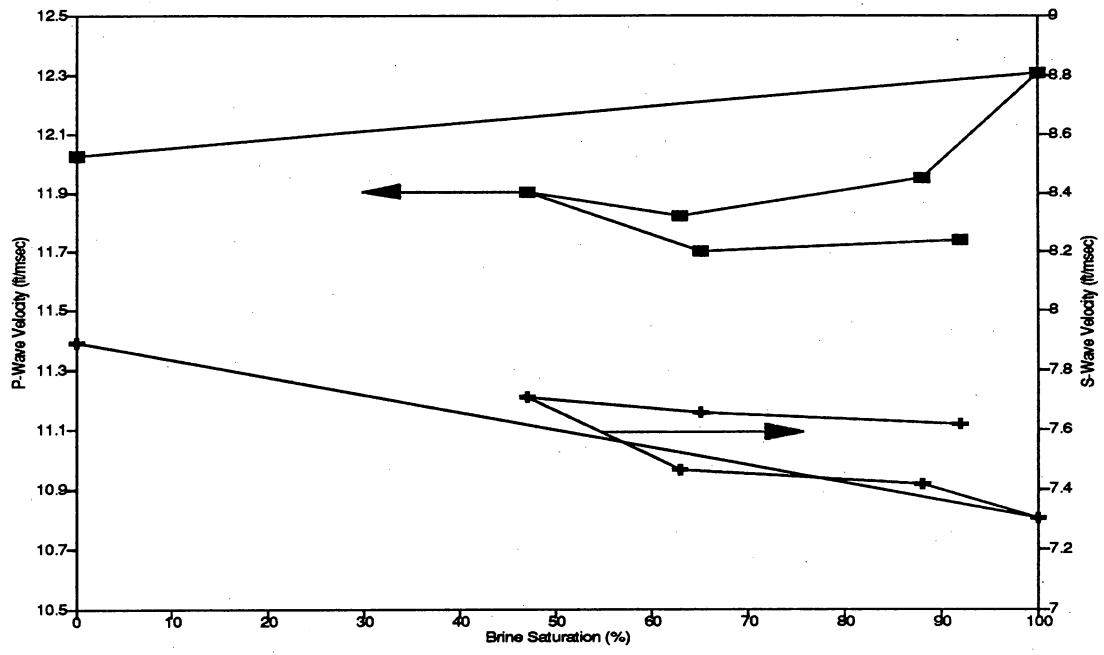
(a)
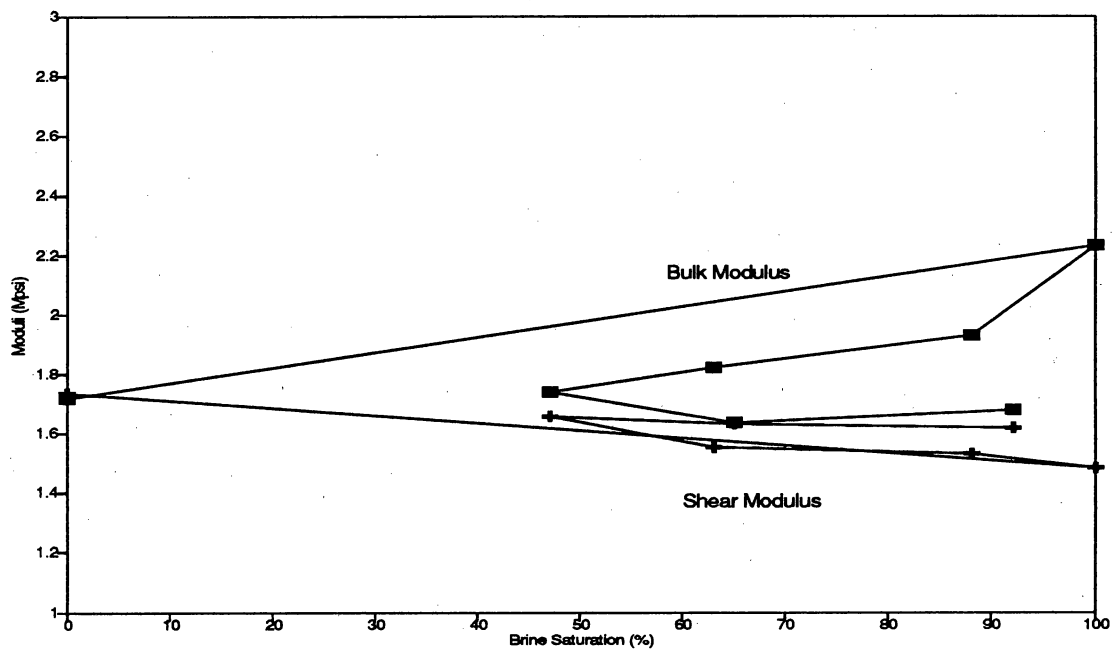
(b)

Figure A48. Variations in wave velocities (a) and moduli (b) with brine saturation for the specimen from Berea.
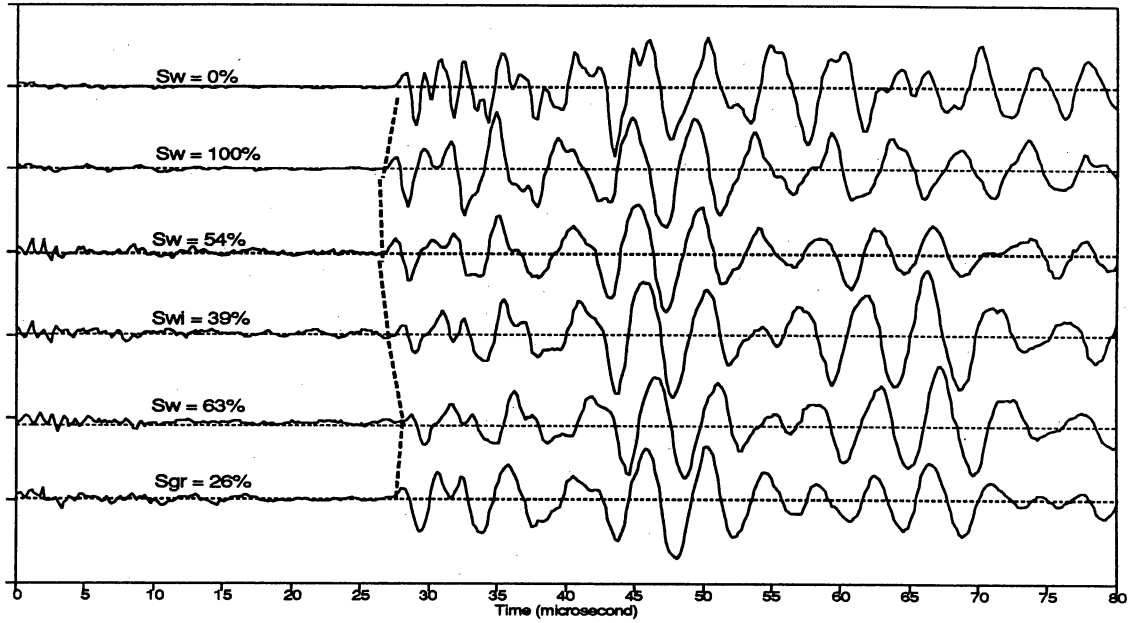
Figure A49. Sequence of signal traces of digitized compressional mode waveforms for the Set 2 Block 6 specimen. The dashed line indicates the locus of first arrivals, and the pore volume brine saturation is listed for each trace.

153

Figure A50. Digitized Set 2 Block 6 shear mode waveforms, during the same sequence as for Figure A49.

changes in shear modulus, with brine saturation. The bulk and shear moduli characterize material response to purely volumetric and to volume-conserving deformations, respectively, and the significantly larger variations in bulk moduli reflect their sensitivity to the compressibility of the pore fluid. Much of the decrease in shear wave velocity with brine saturation is due to variations in specimen density.

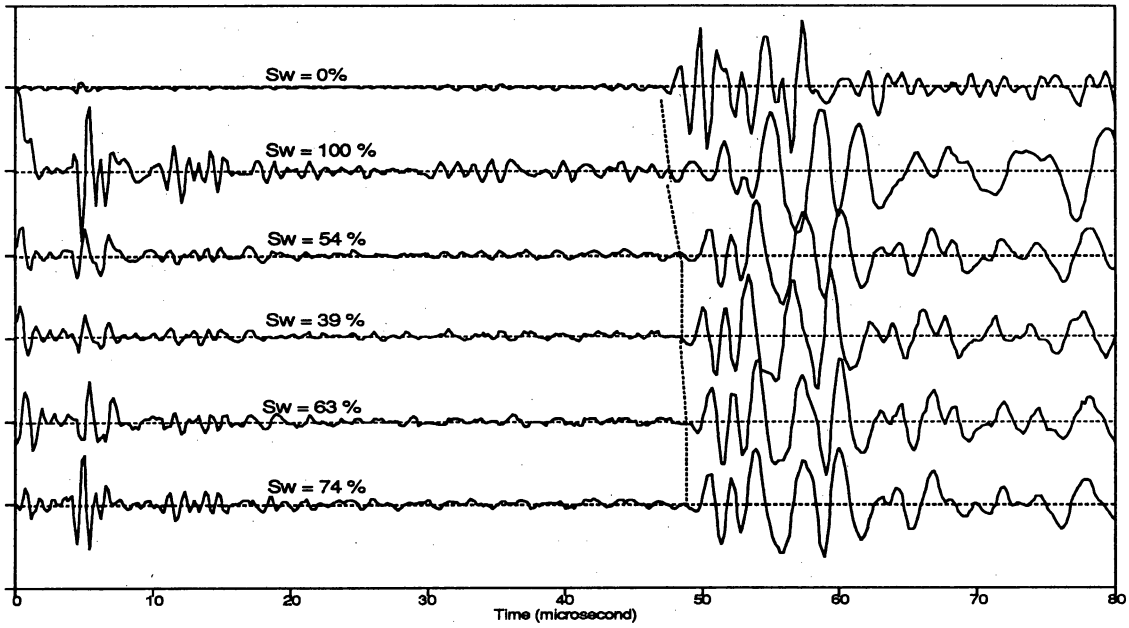The trends in behavior are similar for both drainage and imbibition phases, and significant departures from smooth behavior observed for some of the specimens (for example, Set 3 Block 9 and Set 2 Block 9) are probably due to erroneous determinations of shear wave first arrivals (stored waveforms were not available for these specimens). The travel time variations can be determined with significantly greater accuracy with digital signal processing of the stored waveforms, and the digital data necessary for such processing are available. However, this will not be carried out in this program unless dictated by program objectives. The results summarized in table A-1 and in figures A-27 through A-48 should be regarded as preliminary.

The static deformation measurements of differential axial stress and volumetric strain as a function of axial strain tests shown in figure A-51, for the same specimen as that used for the dynamic moduli shown in figures A-49 and A-50, are representative. There is little evidence for dilatant behavior at these very low deformations, and the static moduli are determined by (visual) fits to the predilatant portion of the stress and volumetric strain curves. The estimated uncertainty in static moduli from these fits is on the order of 10 percent for both Young's moduli and Poisson's ratios.
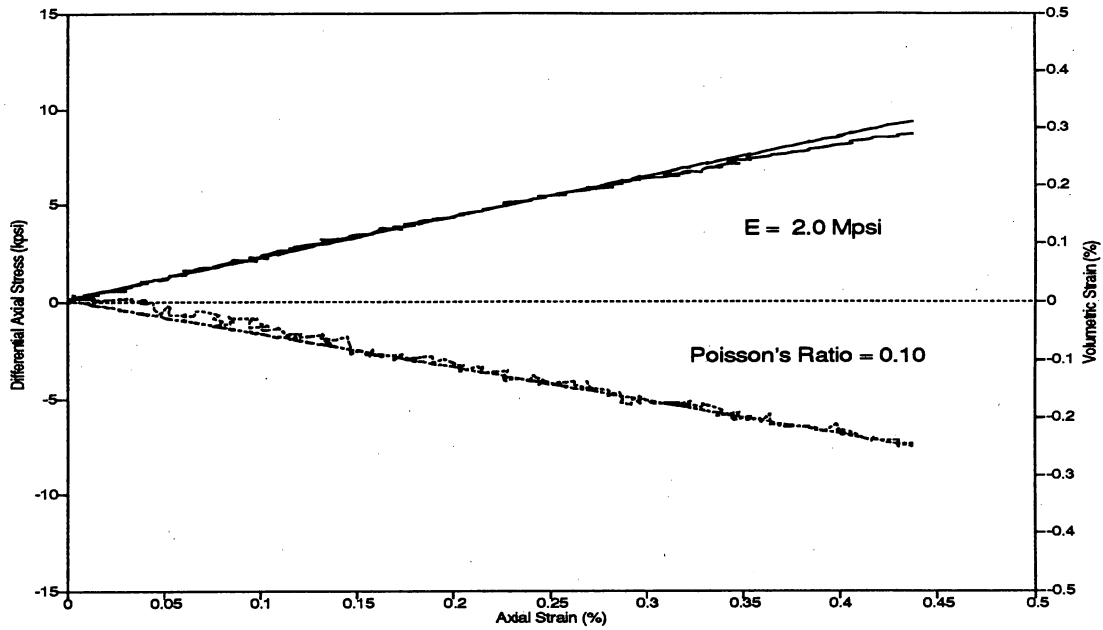
Figure A51. Representative static deformation curves for differential axial stress and volumetric strain, as functions of axial strain, from measurements on the Set 2 Block 6 specimen.

APPENDIX B

PORE NETWORK MODEL

We here briefly describe some of the debugging process used to resolve the relative permeability issue. The problem was that the nonwetting-phase relative permeability curve was extremely low and became lower as the network size increased. For a 20 × 20 × 20 network, the nonwetting-phase relative permeability at the irreducible wetting phase saturation was less than 0.01.

Two things could have been wrong: the invasion sequence and/or the permeability calculation. Because the invasion sequence code was awkward as written in FORTRAN, it was recoded in C. The two major advantages that C provides for the new algorithm are dynamic memory allocation and pointers. Since the maximum number of throats that were accessible candidates for invasion could not be determined a priori, FORTRAN arrays of size equal to the number of pores were used. This is clearly a waste of memory and could prohibit the running of very large networks. Furthermore, because the list of candidates is best kept sorted by size, a linked list is the natural data structure to use. To emulate a linked list, additional FORTRAN arrays had to be used. As mentioned above, this was at best awkward. Believing that it would be more costly in the long run to debug and maintain the FORTRAN implementation, the simpler C version was written. After this, we are confident that the invasion sequence is working correctly.

The other potential problem was the relative permeability calculation. This involves setting up the system of equations to be solved and then solving them. The routine that sets up the matrix was checked. A bug was found whereby some of the throats were not "connected" to the correct bodies. Next, the previous method of dealing with the isolated fraction, that fluid that does not have pressure communication to the exterior, was examined. The previous method was to use some small conductivity in throats that had menisci (which are static in our model). This was necessary because the isolated fraction can cause the matrix to be singular. A

157

singular matrix implies that there is no unique solution, an obvious result since there are bodies filled with fluid without exterior pressure communication. It was not certain how small conductivity could be and still avoid spurious results. Therefore, it was decided to actually determine which throats contained fluid in the isolated fraction. This was done by first setting up the matrix as we had previously done; however, a conductivity of zero was used for throats with menisci instead of the small number used before. Since that matrix describes the fluid connectivity from inlet to outlet, it is possible to find the isolated fraction by first finding the nonisolated fraction. This routine was also written in C, again because of the need for dynamic memory allocation as well as the use of bit arithmetic. Once the isolated fraction is found, the affected bodies have their pressures set to −1 by zeroing out all elements of the matrix row for that body except the diagonal element, which is set to 1, and then setting the right-hand side element to −1. This maintains the bandedness of the matrix and allows the same fast solver to be used at all saturations.

After eliminating the possibility of a singular matrix and the issue of mass rate error introduced by small conductivities in the throats with menisci, the solution of the system of equations was checked. As this solver is used in the department's large chemical flooding simulator, its accuracy was easily validated.

The relationships used to calculate porosity, permeability, and formation factor are given below:

$$\phi = \frac{\pi}{6} \frac{\langle d_b^3 \rangle}{(\lambda \, \overline{d_b})^3} \tag{B-1}$$

$$k = \frac{\pi}{128} \frac{\overline{d_t}^4}{\overline{l_t} \, (\lambda \, \overline{d_b})} \left\langle \frac{d_{tD}^4}{l_{tD}} P_D \right\rangle_{entrance} \tag{B-2}$$

$$\frac{1}{F} = \frac{\pi}{4} \frac{\overline{d_t}^2}{\overline{l_t} \, (\lambda \, \overline{d_b})} \left\langle \frac{d_{tD}^2}{l_{tD}} V_D \right\rangle_{entrance} \tag{B-3}$$

where

ϕ = porosity

k = permeability

F = formation factor

$\overline{d_b}$ = mean pore-body diameter

$\overline{d_t}$ = mean pore-throat diameter

$\overline{l_t}$ = mean pore-throat length

λ = constant indicating tortuosity/orthogonality of the pore system

$\lambda\overline{d_b}$ = average bulk length per pore body

$\langle\,\rangle$ refers to average values.

We can then calculate the porosity, permeability, and formation factor after the cementation process:

$$\phi' = \frac{\pi}{6}\,\frac{\langle d_b'^3\rangle}{(\lambda'\,\overline{d_b'})^3} \tag{B-4}$$

$$k' = \frac{\pi}{128}\,\frac{d_t'^4}{\overline{l_t'}\,(\lambda'\,\overline{d_b'})}\left\langle\frac{d_{tD}'^4}{l_{tD}'}\,P_D'\right\rangle_{entrance} \tag{B-5}$$

$$\frac{1}{F'} = \frac{\pi}{4}\,\frac{\overline{d_t'^2}}{\overline{l_t'}\,(\lambda'\,\overline{d_b'})}\left\langle\frac{d_{tD}'^2}{l_{tD}'}\,V_D'\right\rangle_{entrance} \tag{B-6}$$

It is apparent that the cementation process does not change bulk lengths, so

$$(\lambda\,d_b',\,\overline{}) = (\lambda\,\overline{d_b}) \tag{B-7}$$

and

$$\frac{\phi'}{\phi} = \frac{\langle d_b'^3\rangle}{\langle d_b^3\rangle} \tag{B-8}$$

159

$$\frac{k'}{k} = \frac{\overline{d_t'}^4}{\overline{d_t}^4} \left\{ \frac{\left\langle \dfrac{d_{tD}'^4}{l_{tD}'} P_D' \right\rangle_{entrance}}{\left\langle \dfrac{d_{tD}^4}{l_{tD}} P_D \right\rangle_{entrance}} \right\} \qquad (B.9)$$

$$\frac{F'}{F} = \frac{\overline{d_t'}^2}{\overline{d_t}^2} \left\{ \frac{\left\langle \dfrac{d_{tD}'^2}{l_{tD}'} V_D' \right\rangle_{entrance}}{\left\langle \dfrac{d_{tD}^2}{l_{tD}'} V_D \right\rangle_{entrance}} \right\} \qquad (B.10)$$

where the subscript "entrance" refers to an average over the entrance face of the porous medium.

From previous studies, we have found that the entrance dimensionless groups are all near unity. This leads us to ignore these terms as a first approximation.

From the pore-size parameters and the petrophysical properties of porosity, permeability, and formation factor for the uncemented situation, we can thus calculate the porosity, permeability, and formation factor values for different degrees of cementation.

$$\frac{k'}{k} = \frac{\overline{d_t'^4}}{\overline{d_t^4}} \left\{ \frac{\left\langle \dfrac{d_{tD}'^4}{l_{tD}'} P_D' \right\rangle_{entrance}}{\left\langle \dfrac{d_{tD}^4}{l_{tD}} P_D \right\rangle_{entrance}} \right\} \tag{B.9}$$

$$\frac{F'}{F} = \frac{\overline{d_t'^2}}{\overline{d_t^2}} \left\{ \frac{\left\langle \dfrac{d_{tD}'^2}{l_{tD}'} V_D' \right\rangle_{entrance}}{\left\langle \dfrac{d_{tD}^2}{l_{tD}'} V_D \right\rangle_{entrance}} \right\} \tag{B.10}$$

where the subscript "entrance" refers to an average over the entrance face of the porous medium.

From previous studies, we have found that the entrance dimensionless groups are all near unity. This leads us to ignore these terms as a first approximation.

From the pore-size parameters and the petrophysical properties of porosity, permeability, and formation factor for the uncemented situation, we can thus calculate the porosity, permeability, and formation factor values for different degrees of cementation.